Exploring the nature and strength of S-H···O hydrogen bond employing gas-phase laser spectroscopy and quantum chemistry calculations

विद्या वाचस्पति की
उपाधि की अपेक्षाओं की आंशिक पूर्ति में प्रस्तुत शोध प्रबंध

A thesis submitted in partial fulfillment of the requirements of the degree of Doctor of Philosophy

By/ द्वारा
Surajit Metya
सूरजित मेट्या

Registration No. / पंजीकरण सं. :
20173536
२०१७३५३६

Thesis Supervisor/ शोध प्रबंध पर्यवेक्षक:
Professor Aloke Das
प्रोफेसर अलोक दास

भारतीय विज्ञान शिक्षा एवं अनुसंधान संस्थान पुणे
INDIAN INSTITUTE OF SCIENCE EDUCATION AND RESEARCH PUNE

2024

Dedicated to my parents,

Late Mr. Gopal Chandra Metya

and

Mrs. Kabita Metya

भारतीय विज्ञान शिक्षा एवं अनुसंधान संस्थान पुणे
INDIAN INSTITUTE OF SCIENCE EDUCATION AND RESEARCH PUNE
डॉ. होमी भाभा मार्ग, पुणे 411008, महाराष्ट्र, भारत | Dr. Homi Bhabha Road, Pune 411008, Maharashtra, India
T +91 20 2590 8001 W www.iiserpune.ac.in
IISER PUNE

Declaration

I declare that this written submission represents my ideas in my own words, and wherever other's ideas have been included, I have adequately cited and referenced the original sources. I also declare that I have adhered to all principles of academic honesty and integrity and have not misrepresented, fabricated, or falsified any ideas/data/facts/sources in my submission. I understand that violation of the above will cause disciplinary action by the Institute and can also evoke penal action from the sources which have thus not been properly cited or from whom proper permission has not been taken when needed.

Date: 15/01/2023

Surajit Metya

Mr. Surajit Metya

20173536

भारतीय विज्ञान शिक्षा एवं अनुसंधान संस्थान पुणे
INDIAN INSTITUTE OF SCIENCE EDUCATION AND RESEARCH PUNE
डॉ. होमी भाभा मार्ग, पुणे 411008, महाराष्ट्र, भारत | Dr. Homi Bhabha Road, Pune 411008, Maharashtra, India
T +91 20 2590 8001 **W** www.iiserpune.ac.in
IISER PUNE

Certificate

Certified that the work incorporated in this thesis entitled "**Exploring the nature and strength of S-H···O hydrogen bond employing gas phase laser spectroscopy and quantum chemistry calculations,**" submitted by Mr. Surajit Metya represents his original work, which was carried out by him at IISER Pune under my guidance and supervision during the period from 2017 to 2023. The work presented here or any part of it has not been included in any other thesis submitted previously for the award of any degree or diploma from any other University or Institution. I further certify that the above statements made by him regarding his thesis are correct to the best of my knowledge.

Date: 15/01/2024

Aloke Das
Prof. Aloke Das

(Research Supervisor)

Acknowledgment

I want to sincerely thank **Professor Aloke Das**, my research supervisor, for being incredibly helpful and providing thoughtful guidance, inspiration, and encouragement throughout my doctoral studies. His knowledge and hard work have played a crucial role in helping me achieve the study objectives. I truly appreciate his support and involvement, without which my doctoral journey would not have been possible. I am grateful for his efforts in helping me improve my experimental skills and become a better researcher. Not only has he assisted me in refining my research techniques, but he has also contributed to enhancing my speaking and writing abilities. The lessons I've learned from him will undoubtedly be valuable as I venture into independent research.

I take great pleasure in expressing my gratitude to the members of my research advisory committee, **Prof. Pankaj Mandal** and **Prof. G.V. Pavan Kumar**, for their valuable and constructive suggestions that have significantly enhanced the quality of my results. I take great pleasure in expressing my gratitude to the members of my research advisory committee, Prof. Pankaj Mandal and Prof. G.V. Pavan Kumar, for their valuable and constructive suggestions that have significantly enhanced the quality of my results.

I want to thank my collaborators, **Prof. Jer-Lai Kuo** and **Mr. Qian-Rui,** from the Institute of Atomic and Molecular Science, Academia Sinica, Taiwan. Without their assistance, my research work would not have been complete.

I want to extend my sincere thanks to the former members of our lab, **Dr. Sumit Kumar**, **Dr. Santosh Kumar Singh**, **Dr. Kamal Kumar Mishra**, and **Dr. Satish Kumar**. They played a significant role in acquainting me with lab instruments and experimental techniques during my initial days, offering guidance and assistance throughout the experiments whenever it was required. Learning both the computational and experimental aspects of the work within a short time wouldn't have been possible without their valuable contributions. I want to express my heartfelt and special thanks to the **late Mr. Kshetrimayum Borish** for his companionship and joyful activities. Even though he is no longer with us, the memories of our time together have been a meaningful part of this journey, and I am grateful for the camaraderie and shared experiences. I also want to express my sincere gratitude to my current lab mates, **Mr. Prakash Panwaria**, **Mr. Sourav Mandal**, and **Mr. Supravat Roy**, for their assistance in my research work and help in preparing my thesis.

I would like to convey my gratitude to **Prof. K. N. Ganesh** and **Prof. Jayant B. Udgaonkar**, former Directors, as well as the current Director of IISER Pune, **Prof. Sunil Bhagwat**, for fostering a high-quality research environment.

I wish to express my gratitude to **Prof. M. Jayakannan**, the former Chair of Chemistry, and **Prof. Hosahudya N. Gopi**, as well as the current Chair of Chemistry, **Prof. Nirmalya Ballav**, for their support and guidance.

I sincerely thank the Department of Chemistry **staff members** for their tremendous help.

I would like to thank IISER Pune for giving me the JRF and SRF scholarships.

My appreciation goes out to all my IISER friends for their companionship and support. I also want to thank all my friends outside of IISER for their unfailing support and companionship, which have brought enormous richness into my life.

In memory of my **father**, whose support and encouragement shaped my academic journey, I dedicate this thesis to him. Though he is no longer with us, his influence continues to inspire me. I also dedicate this work to my **mother**, without whom I would not be here today. Her love, guidance, and sacrifices have been my pillars of strength. This thesis stands as a token of gratitude to both my parents, acknowledging their profound impact on my life and education.

Contents

List of acronyms i
List of Figures ii-ix
List of Tables x-xi
Synopsis xii-xv
List of Publication xvi

Chapter 1: Introduction

- 1.1 Non-covalent interactions and their significance: 1
- 1.2 Nature of Non-covalent interactions 1
- 1.3 Types of non-covalent interaction 4
- 1.4 Hydrogen Bonding 7
  - 1.4.1 History of the concept of Hydrogen Bonding 7
  - 1.4.2 Conventional concept of hydrogen bonding 9
  - 1.4.3 Experimental and theoretical approach to studying hydrogen bonding 10
  - 1.4.4 Modulation of Hydrogen bond strength 13
- 1.5 Unconventional Hydrogen bonding 15
  - 1.5.1 Significance of Sulfur-centered hydrogen bonding 18
  - 1.5.2 Sulfur as hydrogen bond acceptor (X-H⋯S) vs donor (S-H⋯X) 19
- 1.6 Aim of thesis 21

Chapter 2: Experimental and Computational Method

- 2.1 Experimental method 24
  - 2.1.1 Supersonic jet expansion 24
  - 2.1.2 Resonantly enhanced multiphoton ionization (REMPI) spectroscopy and Time of Flight (TOF) mass spectrometry 29
  - 2.1.3 Laser systems used for the experiments 34
  - 2.1.4 Experimental Set-Up 38
  - 2.1.5 Experimental Scheme 40
  - 2.1.6 Spectroscopic Techniques 42

2.2 Computational Methods 45
  2.2.1 Geometry optimization and frequency calculation 46
  2.2.2 Natural Bond Orbital (NBO) analysis 47
  2.2.3 Energy Decomposition Analysis 48
  2.2.4 Quantum Theory of Atoms in Molecules (QTAIM) calculation 48

Chapter 3: S–H···O Hydrogen Bond Can Win over O–H···S Hydrogen Bond: Gas-Phase Spectroscopy of 2 Fluorothiophenol···H2O Complex

3.1 Introduction 51
3.2 Result and Discussion 53
  3.2.1 Conformational Landscape of 2-FTP···H2O complex 53
  3.2.2 Electronic Spectra of the 2-FTP monomer and 2-FTP···H2O complex 57
  3.2.3 IR Spectra of the 2-FTP Monomer and 2-FTP··· H2O Complex 62
  3.2.4 Analysis of the Non-covalent Interactions in the 2-FTP···H2O complex 67
3.3 Conclusions 72

Chapter 4: Modulation of the strength of weak S-H···O hydrogen-bond: Spectroscopic study of the complexes of 2-Flurothiophenol with methanol and ethanol

4.1 Introduction 75
4.2 Result and Discussion 76
  4.2.1 Electronic spectra of 2-FTP···MeOH and 2-FTP···ETOH complexes 76
  4.2.2 Quantum chemistry calculations of the 2-FTP···MeOH and 2-FTP···ETOH complexes 82
  4.2.3 IR spectra of the 2-FTP···MeOH and 2-FTP···ETOH complexes and assignment of the observed conformers 97
  4.2.4. Theoretical evaluation of the non-covalent interactions present in the observed conformers of the 2-FTP···MeOH and 2-FTP···EtOH complexes. 107
4.3 Conclusion 114

Chapter 5: Interplay between proton affinity and steric repulsion on S-H···O hydrogen bond: Spectroscopic study and quantum chemical calculations

5.1 Introduction 117
5.2 Result and Discussion 119
  5.2.1 Conformational landscape of 2-FTP···Et_2O complex 119
  5.2.2 Mass-selected Electronic Spectra of the 2-FTP···Et_2O complex 126
  5.2.3 IR spectra of 2-FTP···Et_2O and assignment of the conformers 129
  5.2.4 Analysis of the non-covalent interactions in 2-FTP···Et_2O 134
  5.2.5 Extension of theoretical studies on the nature and strength of the S-H···O hydrogen bonding 137
5.3 Conclusion 143

Chapter 6: Summary and Future Directions

6.1 Conclusion 146
6.2 Future directions 147
References 151

List of Acronyms

1C-R2PI	1 Color-Resonant Two-Photon Ionization
2C-R2PI	2 Color-Resonant Two-Photon Ionization
ALMO	Absolutely-Localized Molecular Orbital
Ar	Argon
AIM	Atoms-In-Molecules
aVNZ	aug-cc-pVNZ
BSSE	Basis set superposition error
BE	BSSE+ZPE corrected binding energy
CSD	Cambridge Structural Database
CT	Charge Transfer
DFT	Density Functional Theory
Disp	Dispersion
E_{rel}	Relative Energy
Es	Electrostatics
EDA	Energy Decomposition Analysis
Ex	Exchange
He	Helium
He-Ne	Helium-Neon
HB	Hole Burn
IP	Ionization Potential
LMO	Localized Molecular Orbital
MS	Mass Spectrometry
MP2	Moller-Plesset Second-Order Perturbation Theory
NBO	Natural Bond Orbital
OPA	Optical Parametric Amplifier
OPO	Optical Parametric Oscillator
Pol	Polarization
PDB	Protein Data Bank
PV	Pulse Valve
Rep	Repulsion
RIDIRS	Resonant Ion-Dip Infrared Spectroscopy
REMPI	Resonantly Enhanced Multi-Photon Ionization
TOF	Time Of Flight
ZPE	Zero Point Energy

List of Figures

Figure 2.1. A schematic diagram of the supersonic expansion. 26

Figure 2.2. Comparison of the velocity distribution curve of effusive (blue-solid) and supersonic beam (red-dotted). 27

Figure 2.3. Schematic diagram of (a) one-color resonant two-photon ionization (1C- R2PI) spectroscopy (b) two-color resonant two-photon ionization (2C-R2PI) spectroscopy (c) a representative REMPI spectrum. 30

Figure 2.4. Schematic diagram of time of flight mass spectroscopy. 32

Figure 2.5. Schematic diagram of the Nd:YAG laser pumped dye laser. 34

Figure 2.6. Schematic diagram of Nd:YAG pumped OPO-OPA system IR laser (Laser Vison). 36

Figure 2.7. Photograph of the laboratory of home-built jet-cooled REMPI Time of Flight Mass spectrometer. 39

Figure 2.8. A schematic diagram of the experimental set-up. 40

Figure 2.9. (a) Schematic diagram of UV-UV hole-burning spectroscopy. (b) Mass spectra of a molecule due to pump and probe UV lasers. (c) UV-UV hole-burning spectrum (Bule color) corresponds to the R2PI spectra (Red color). 43

Figure 2.10. (a) Schematic diagrams of the RIDIRS technique and (b) an IR spectrum as a depletion of ion signal. 44

Figure 2.11. (a) Schematic diagrams of IR-UV hole-burning spectroscopy and (b) IR UV hole-burning spectrum (blue) correspond to the R2PI spectra (red). 45

Figure 3.1. Various low-energy conformers of the (a) 2-FTP monomer and (b) 2-FTP···H2O complex optimized at the MP2/6-311++G(d,p) and cp-MP2/6-311++G(d,p) levels of theory, respectively. E_{rel} stands for the relative electronic energy of the monomer, while BE denotes the binding energy of the complex. Both E_{rel} and BE are zero-point energy corrected, while BE is additionally counterpoise (cp) corrected at every step during the geometry optimization. 53

Figure 3.2. TOF Mass spectrum of mixed vapor of 2-FTP and H_2O measured at 35221 cm^{-1} (origin band of the 2-FTP···H_2O complex) employing 1C-R2PI spectroscopy. 57

Figure 3.3. Mass-selected electronic spectra of the (a) cis-2-FTP monomer showing the origin band and (b) 2-FTP···H_2O complex measured by 1C-R2PI technique. (c,d) UV–UV hole-burning spectra of the conformers A and B of the 2-FTP···H_2O complex measured by probing the 35221 (A_0^0) and 35232 (B_0^0) cm^{-1} bands, respectively, in the electronic spectrum. The number in the parentheses below each band of the hole-burning spectra in parts c and d denotes the intermolecular vibrational frequency of the complex in cm^{-1}. A tentative assignment of the low-frequency intermolecular vibration is provided in Table 3.4. Assignment of the bands marked with asterisks in Figure 3.3(b) could not be done through UV–UV hole-burning due to their weak intensity. 58

Figure 3.4. Electronic spectra measured at the (a) 2-FTP monomer mass channel (in the absence of cluster formation with H_2O), (b) 2-FTP monomer mass channel (under the clustering condition), and (c) 2-FTP···H_2O mass channel. (d) and (e) are the UV-UV hole-burning spectra of the 2-FTP···H_2O complex. 60

Figure 3.5. Comparison of the electronic spectra of the 2-FTP···H2O complex recorded by 1C R2PI technique using (a) argon (Ar) and (b) He-Ne (70%-30%) carrier gases. 61

Figure 3.6. IR spectra of the (a) 2-FTP monomer, (c) conformer A of 2-FTP···H2O, and (e) conformer B of 2-FTP···H2O measured by RIDIR spectroscopy. (b,d,f) Theoretical scaled IR stick spectra of the 2-FTP monomer, T1, and C1 conformers of the 2-FTP···H2O complex, respectively, calculated at the cp-MP2/6-311++G(d,p) level of theory. O−H (s) and O−H (as) in parts (d) and (f) denote symmetric and asymmetric O−H stretching frequencies, respectively. The scaling factors for the harmonic S−H and O−H frequencies are discussed in the text. 63

Figure 3.7. Experimental and Calculated S-H and O-H Stretching frequencies of all the conformers of the 2-FTP···H_2O complex. Frequencies are calculated at the cp-MP2/6-311++G (d,p) level of theory. S-H stretching frequencies are scaled with a factor of 0.9375, derived from the ratio of experimental and calculated S-H stretching frequency of the 2-FTP monomer. Similarly, O-H frequencies are scaled by a factor of 0.9378 obtained from the observed and calculated antisymmetric O-H frequencies of free water. 65

Figure 3.8. Molecular graphs of C1 and T1 conformers of the (a) 2-FTP···H_2O and (b) 2 FP···H_2O complex obtained from QTAIM calculation performed on the cp-MP2/6-311++G(d,p) level optimized geometries. Electron density (ρ) and its Laplacian (∇2 ρ) values at the bond critical points (BCPs) of the hydrogen bonds present in the two conformers are provided in the figure. (b) 67

Figure 3.9. (a,b) NCI plot of reduced density gradient (RDG, a.u.) as a function of the electron density multiplied with the sign of the second eigenvalue of the electron density Hessian matrix [sign $(\lambda_2)\rho$, (a.u.)] for the C1 and T1 conformers of 2-FTP⋯H_2O. (c,d) NCI isosurface plots showing the non-covalent interactions present in the C1 and T1 conformers. Gradient isosurface follows a blue-green-red color scheme over the range of $-0.04 < \text{sign}(\lambda_2)\rho < 0.04$, where blue, green, and red colors denote very strong attraction, weak attraction, and strong repulsion, respectively. RDG minima and corresponding non-covalent interactions represented by NCI isosurfaces are marked by squares and circles. The NCI calculations are performed on the cp-MP2/6-311++G(d,p) level geometries. 68

Figure 3.10. NBO overlap for the (a) S−H⋯O and O−H⋯F hydrogen bonds in the C1 conformer of 2-FTP⋯H_2O, (b) S−H⋯O and C− H⋯O hydrogen bonds in the T1 conformer of 2-FTP⋯H_2O (c,d) are conventional O-H⋯O hydrogen bonds in the C1 and T1 conformers of 2- FP (2-fluorophenol)⋯H_2O complexes, respectively. NBO 2nd order perturbation energy value for individual non-covalent interaction is provided with the NBO plot. NBO calculations are performed on the MP2/6-311++G(d,p) level optimized geometries. 69

Figure 3.11. Decomposition of the total interaction energies of the C1 and T1 conformers of 2-FTP⋯H_2O at the M06-2X/aug-cc-pVTZ level of theory on the cp-MP2/6-311++G(d,p) optimized geometries using the LMO-EDA method. The total interaction energy (E) of the complex is decomposed into electrostatics (ES), exchange (EX), repulsion (REP), and polarization (POL) components. 71

Figure 4.1. TOF mass spectra of (a) 2-FTP⋯MeOH complex recorded at 35277 cm^{-1} and (b) 2-FTP⋯EtOH complex recorded at 35307 cm^{-1}. 77

Figure 4.2. Electronic spectra measured in the mass channels of the (a) cis-2-FTP monomer and (b) 2-FTP⋯MeOH dimeric complex using 1C-R2PI technique. UV-UV hole-burning spectra corresponding to the three conformers of 2-FTP⋯MeOH, named A, B, and C, are shown in the panels (c), (d), and (e), respectively. Hole-burning spectra were measured by probing the bands marked with asterisks (*) in the electronic spectrum presented in Figure 4.2 (b). The origin bands for the conformers A, B, and C of the complex appear at 35232 cm^{-1}, 35208 cm^{-1}, and 35202 cm^{-1}, respectively. Intermolecular vibrational frequencies (in cm^{-1}) of the conformers of the complex are marked underneath each of the vibronic bands in the spectra depicted in the panels c, d, and e. 78

Figure 4.3. Electronic spectra measured in the mass channels of the (a) cis-2-FTP monomer and (b) 2-FTP⋯EtOH dimeric complex using 1C-R2PI technique. UV-UV hole-burning spectra of 79 the two conformers of the 2-FTP···EtOH complex designated as A (0_0^0 band at 35269 cm^{-81}) and B (0_0^0 band at 35251 cm^{-1}) are presented in panels c and d, respectively. Hole-burning spectra were obtained by probing the bands marked with asterisks in the electronic spectra presented in Figure 4.3(b). Intermolecular vibrational frequencies (in cm^{-1}) of the conformers of the complex are marked underneath each of the vibronic bands in the spectra depicted in the panels c and d.

Figure 4.4. Mass-selected electronic spectra of (a) 2-FTP monomer in the absence of any complexing partner (b) 2-FTP monomer recorded at the fragmented monomer mass channel in cluster formation condition with methanol (c) 2-FTP···MeOH complex observed at the complex mass channel. A_0^0, B_0^0, *and* C_0^0 are the origin band for the $S_1 \leftarrow S_0$ transition for the three conformers of the 2-FTP···MeOH complex. 81

Figure 4.5. Mass-selected electronic spectra of (a) 2-FTP monomer in the absence of EtOH, (b) 2-FTP in the presence of EtOH and recorded in the monomer mass channel, and (c) 2-FTP···EtOH complex measured at the complex mass channel. A_0^0, *and* B_0^0 are the origin bands of the corresponding A and B conformers of the 2-FTP···EtOH complex. 81

Figure 4.6. Structures of six low-energy conformers of 2-FTP···MeOH complex optimized at the M06-2X/6-311++G(d,p) level of theory. BE stands for the BSSE and ZPE corrected binding energy in kJ/mol. Different colored dotted lines in the structures represent different non-covalent interactions present there. Distance (in Å) between two atoms involved only in the primary S-H···O hydrogen bonding interaction is provided with the structures. Geometrical parameters for the all interactions are given in Table 4.1. 82

Figure 4.7. Graphical representation of the Binding energies of the conformers of the 2-FTP···MeOH complexes at different level of theory. 85

Figure 4.8. Structures of ten low-energy conformers of 2-FTP···EtOH complex optimized at the M06-2X/6-311++G(d,p) level of theory. BE stands for the BSSE and ZPE corrected binding energy in kJ/mol. Different colored dotted lines in the structures represent different non-covalent interactions present there. Distance (in Å) between two atoms involved only in the primary S-H···O hydrogen bonding interaction is provided with the structures. Geometrical parameters corresponding to all the interactions are presented in Table 4.2. The structures of Tg^- and Cg^- are mirror images of those of Tg^+ and Cg^+, respectively. Thus, the Tg$^-$ and Cg$^-$ are identical in structure and energy to the Tg^+ and Cg^+, respectively. The Tg^- and Cg^- structures, corresponding to the Tg^+ and Cg^+ structures presented in this figure, are provided in Figure 4.9. 87

Figure 4.9. Structure of the *g*$^{-}$ version of the conformers of 2-FTP···EtOH complexes, calculated at M06-2X/6-311++G(d,p) level of theory. BE represents the BSSE and ZPE corrected binding energy in KJ/mol. 88

Figure 4.10. Graphical representation of the Binding energies of the conformers of the 2-FTP···EtOH complexes at different level of theory. 94

Figure 4.11. Experimental IR spectra of the (a) 2-FTP monomer, (c,e,f) conformers A, B, and C of the 2-FTP···MeOH complex, respectively, measured in the S-H and O-H stretching regions by RIDIR spectroscopy. (b,d,g-k) Theoretical scaled IR spectra of the 2-FTP monomer and T1, T2, C1, C2, T3, and C3 conformers of the 2-FTP···MeOH complex, respectively, calculated at the M06-2X/6-311++G(d,p) level of theory. The scaling of the calculated harmonic S-H frequencies in the complex is done with respect to the experimental S-H frequency of the 2-FTP monomer [Figure 4.11(a)] while the calculated harmonic O-H frequencies in the complex are scaled with reference to the O-H frequency of bare MeOH in the gas-phase. 98

Figure 4.12. Gas-phase IR spectra of (a) 2-FTP and (c, e, f) three experimentally observed conformer of 2-FTP···MeOH complex. (b, d, g-k) are the theoretically calculated [**A.**] IR spectra at M06-2X /6-311++G(d,p) level of theory with a scaling factor of 0.944 taken from the data base for this specific level of theory. [**B.**] anharmonic vibrational stretching frequencies at S-H and O-H region using DVR method at DLPNO-CCSD(T)/aug-cc-pVTZ-F12 level of theory using the optimized structure at M06-2X /6-311++G(d,p) level of theory. 101

Figure 4.13. Experimental IR spectra of the (a) 2-FTP monomer, (c,g) conformers A and B of the 2-FTP···EtOH complex, respectively, measured in the S-H and O-H stretching regions by RIDIR spectroscopy. (b,d-f,h-n) Theoretical scaled IR spectra of the 2-FTP monomer and T$g^{+/-}$(2), T$g^{+/-}$(1), T$g^{+/-}$(3), T*a*(2), T*a*(1), C$g^{+/-}$(1), C$g^{+/-}$(2), C$g^{+/-}$(3), C*a*(1), and C*a*(2) conformers of the 2-FTP···EtOH complex, respectively, calculated at the M06-2X/6-311++G(d,p) level of theory. The scaling of the calculated harmonic S-H frequencies in the complex is done with respect to the experimental S-H frequency of the 2-FTP monomer [Figure 4.13(a)] while the calculated harmonic O-H frequencies in the complex is scaled with reference to the O-H frequency of bare EtOH in the gas-phase. 102

Figure 4.14. Gas-phase IR spectra of (a) 2-FTP and (c,g) two experimentally observed conformer of 2-FTP···EtOH complex. (b, d-f, h-n) are the theoretically calculated [**A.**] IR spectra at M06-2X /6-311++G(d,p) level of theory with a scaling factor of 0.944 taken from the data base for this specific level of theory. [**B.**] anharmonic vibrational stretching 105 frequencies at S-H and O-H region using DVR method at DLPNO-CCSD(T)/aug-cc-pVTZ-F12 level of theory using the optimized structure at M06-2X /6-311++G(d,p) level of theory.

Figure 4.15. Correlation between the red-shift in the experimental stretching frequency corresponding to the S-H bond and proton-affinity (PA) of the acceptor part. 106

Figure 4.16. NBO overlap for different non-covalent interactions present in the observed T1, T2, and C1 conformers of the 2-FTP···MeOH complex calculated at the M06-2X/6-311++G(d,p) level of theory. NBO second-order perturbation energy [$E^{(2)}$] values in kJ/mol are also provided with each of the interactions shown in the figure. 108

Figure 4.17. NBO overlap for different non-covalent interactions present in the observed Tg^+ and T*a* conformers of the 2-FTP···EtOH complex calculated at the M06-2X/6-311++G(d,p) level of theory. NBO second-order perturbation energy [$E^{(2)}$] values in kJ/mol are also provided with each of the interactions shown in the figure. 110

Figure 4.18. Topology of the electron density of the (a) T1, T2, and C1 conformers of the 2-FTP···MeOH (b) Tg^+(1), Tg^+(2), Tg^+(3), T*a*(1), and T*a*(2) conformers of the 2-FTP···EtOH complexes obtained from QTAIM calculations performed on the M06-2X/6-311++G(d,p) level optimized structures. The electron density (ρ) and its Laplacian ($\nabla^2\rho$) at the BCPs of only the primary non-covalent interaction i.e., S-H···O hydrogen bond for all the conformers of the two complexes are provided with the molecular graphs. 111

Figure 4.19. Correlation between the red-shift in experimental S-H stretching frequency and (a) NBO second order perturbation energy ($E^{(2)}$) and (b) electron density (ρ) at the bond critical point S-H···O contacts. NBO perturbation energy and the electron density are calculated at M06-2X/6-311++G(d,p) level of theory. 112

Figure 4.20. Decomposition of the total interaction energies of the T1, T2, and C1 conformers of the 2-FTP···MeOH complex using LMO-EDA method at the M06-2X/6-311++G(d,p) level of theory. The total interaction energy (TOTAL) is decomposed into electrostatics (ES), exchange (EX), repulsion (REP), polarization (POL), and dispersion (DISP). 113

Figure 4.21. Decomposition of the total interaction energies of the Tg^+(1), Tg^+ (2), Tg^+ (3), T*a*(1), and Ta(2) conformers of the 2-FTP···EtOH complex using LMO-EDA method at the M06-2X/6-311++G(d,p) level of theory. The total interaction energy is decomposed into electrostatics (ES), exchange (EX), repulsion (REP), polarization (POL), and dispersion (DISP). 114

Figure 5.1 (a) 3D representation of diethylether (Et_2O) that shows the two dihedral angles $\phi_1 = C_1 - C_2 - O_3 - C_4$ and $\phi_2 = C_2 - O_3 - C_4 - C_5$ along which conformers are generated. (b-d) three conformers of Et_2O optimized at the M06-2X/6-311++G(d,p) level. Relative electronic energies are provided in kJ/mol unit. (e-j) optimized geometries of the complexes of 2-FTP and Et_2O at the M06-2X/6-311++G(d,p) level of theory. Geometries (e-g) belong to the *trans* complex category according to the complexation with *trans*-2-FTP and (h-j) belong to the *cis* complex category according to the complexation with *cis*-2-FTP. Colored Dotted lines on the 2-FTP···Et_2O complexes represent the non-covalent interactions. Geometrical parameters for the various non-covalent interactions are provided in Table 5.1. 120

Figure 5.2 Graphical representation of the binding energies of the conformers of the 2-FTP···Et_2O complexes calculated at different levels of theory. 126

Figure 5.3 TOF Mass spectrum of mixed vapor of 2-FTP and Et_2O measured at 35240 cm^{-1} (most intense electronic band of the 2-FTP···Et_2O complex) employing 1C-R2PI spectroscopy. 127

Figure 5.4 Mass selected electronic spectra of the (a) 2-FTP monomer and (b) 2-FTP···Et_2O complex recorded utilizing 1C-R2PI spectroscopic technique with He-Ne carrier gas. (c, d) UV-UV hole-burning spectra for the conformers A and B of the 2-FTP···Et_2O complex recorded by fixing the probe energy correspond to $A_0^0 + 10$ (35240 cm^{-1}) and B_0^0 (35066 cm^{-1}) bands. Numbers are given in (c) correspond to the bands that represent the intermolecular vibration of the conformer A. Band at +338 cm^{-1} in (d) is the 6a intramolecular vibration of 2-FTP. 128

Figure 5.5 Experimental IR spectra of the (a) 2-FTP monomer, (c, h) conformers A and B of the 2-FTP···Et_2O complex, respectively, measured in the S-H regions by RIDIR spectroscopy. (b, d-g, i-j) Theoretical scaled IR spectra of the 2-FTP monomer and Ttt, Ctg, Ttg, Tgg, Ctt, and Cgg conformer of 2-FTP···Et_2O complex, respectively, calculated at M06-2X/6-311++G(d,p) level of theory. Scaling of the S-H frequencies is done with respect to the experimentally observed S-H frequency of the 2-FTP monomer. 130

Figure 5.6 Fitted line along the blue square represents the correlation between of the strength of the S-H···O hydrogen bonding interaction in terms of the red-shift with the proton affinity of the hydrogen bond acceptor. The fitted line along the red circle represents the correlation between the strength of the O-H···O hydrogen bonding and the proton affinity of the hydrogen bond acceptors. Asterisks are given for the value taken form the reference (249,301). 133

Figure 5.7 NBO overlap for the various non-covalent interactions, including S-H···O hydrogen bonding interactions and other secondary interactions present in the conformers of the 2-FTP···Et_2O complex calculated at M06-2X/6-311++G(d,p) level of theory. 135

Figure 5.8 Topology of the electron density of the conformers of the 2-FTP···Et_2O complex calculated performing QTAIM calculation with the optimized geometries at M06-2X/6-311++G(d,p) level of theory. Red circles on each of the conformers are highlighting the bond critical point (BCP) corresponding to S-H···O hydrogen bonding interactions. Total electron density (ρ) and the laplacian of the electron density ($\nabla^2\rho$) at the bond critical points are mentioned for the S-H···O hydrogen bonding interactions of each conformer. 136

Figure 5.9 Scaled harmonic stretching frequencies in the S-H region of the most stable conformers of the complexes of 2-FTP with acyclic ethers optimized at the M06-2X/6-311++G(d,p) level of theory. Blue color stick spectra correspond to the *trans* conformers of the complex formed with *trans*-2-FTP, while the red color stick spectra represent the *cis* conformer of the complexes formed with *cis*-2-FTP. Calculated stretching frequencies are scaled with respect to the experimental S-H stretching frequency of the 2-FTP monomer. 138

Figure 5.10 Correlation of the NBO steric repulsion energy and binding energy of the complexes with the proton affinity of the hydrogen bond acceptors calculated at M06-2X/6-311++G(d,p) level of theory. 139

Figure 5.11 Scaled harmonic stretching frequencies in the S-H region of the most stable conformers of the complexes of 2-FTP with cyclic ethers optimized at the M06-2X/6-311++G(d,p) level of theory. Blue color stick spectra correspond to the *trans* conformers of the complex formed with *trans*-2-FTP, while the red color stick spectra represent the *cis* conformer of the complexes formed with *cis*-2-FTP. Calculated stretching frequencies are scaled with respect to the experimental S-H stretching frequency of the 2-FTP monomer. 141

Figure 5.12 (a, b) correlation between the electron density and the NBO interaction energies with the proton affinity for the complexes of 2-FTP with acyclic ethers and (c, d) correlation between electron density and the NBO interaction energies with the proton affinity for the complexes of 2-FTP with cyclic ethers calculated at the M06-2X/6-311++G(d,p) level of theory. 142

List of Tables

Table 3.1 Zero-point energy (ZPE) and BSSE corrected binding energy (BE) calculated at different levels of theory for all the conformers of 2FTP···H2O complex. 54

Table 3.2 Detailed geometrical parameters for the most stable conformers of the monomers and complexes calculated in cp-MP2/6-311++G (d,p) level of theory. 56

Table 3.3 Energy barrier between the cis and trans conformers of the 2-FTP monomer. 58

Table 3.4 Observed and calculated low-frequency intermolecular vibrations of the T1 and C1 conformers of the 2-FTP···H2O complex. Excited state (S1) vibrational frequencies are calculated at the CIS/6-311++G(d,p) level of theory using the optimized geometry obtained at the cp-MP2/6-311++G(d,p) level of theory 59

Table 4.1 Geometrical parameter of different conformers of 2-FTP···MeOH complex calculated at M062X/6-311++G(d,p) level of theory. Distances are given in Å unit and angles, and dihedral angles are reported in (◦) unit. 83

Table 4.2 Geometrical parameter of different conformers of 2-FTP···EtOH complex calculated at M062X/6-311++G(d,p) level of theory. Distances are given in Å unit and angles, and dihedral angles are reported in (◦) unit. 89

Table 4.3a Six intermolecular vibrational modes in the excited electronic state (S_1) of the T1, T2, and C1 conformers of the 2-FTP···MeOH complex calculated at the CIS/6-311++G(d,p) level of theory. 94

Table 4.3b Tentative assignment of the low-frequency intermolecular vibrations (cm^{-1}) observed in the electronic spectra (Figure 4.2) of the three conformers of the 2-FTP···MeOH complex. 95

Table 4.4a Six intermolecular vibrational modes in the excited electronic state (S_1) of the T1, T2, and C1 conformers of the 2-FTP···EtOH complex calculated at the CIS/6-311++G(d,p) level of theory. 96

Table 4.4b Six intermolecular vibrational modes in the excited electronic state (S_1) of the T1, T2, and C1 conformers of the 2-FTP···EtOH complex calculated at the CIS/6-311++G(d,p) level of theory. 96

Table 5.1 Geometrical parameters of the various conformers of both the 2-FTP and Et_2O monomers along with the 2-FTP···Et_2O complex calculated at the M062X/6-311++G(d,p) level of theory 122

Table 5.2 Six intermolecular vibrational modes in the ground electronic state (S_0) of the conformers of the 2-FTP···Et_2O complex calculated at the M06-2X/6-311++G(d,p) level of theory 125

Table 5.3 Tentative assignment of the low-frequency intermolecular vibrations (cm^{-1}) observed in the electronic spectra (Figure 5.4) of the two conformers of 2-FTP···Et_2O complex 128

Table 5.4 Scaled harmonic stretching frequencies (in cm^{-1} unit) of the conformers of 2-FTP···Et_2O complex calculated at various levels of theory 132

Table 5.5 Comparison of the NBO second-order perturbation energy and the AIM parameters calculated at M06-2X/6-311++G(d,p) level of theory with the red-shift in the experimentally observed S-H stretching frequency 137

Synopsis

Non-covalent interactions are pervasive in our immediate surroundings, affecting everything from living things to non-living objects. These relationships are not only essential but also the basis for life on Earth. Numerous types of non-covalent interactions occur, depending on their characteristics, strength, and atoms involved. Among these, hydrogen bonding is the most widely recognized and crucial non-covalent interaction. Since the discovery of the hydrogen bonding a hundred years ago, its concept has been modified very much. This thesis provides an understanding of the hydrogen bonding involving sulfur as a hydrogen bond donor and oxygen as a hydrogen bond acceptor, i.e., S-H⋯O using gas-phase laser spectroscopy coupled with quantum chemistry calculations.

Even though hydrogen bonding interactions have been thoroughly studied in the past, researchers continue to find it to be the most fascinating topic to investigate. The idea of hydrogen bonding was built more than a century ago with the concept of formation of the attractive interaction between an electronegative element (hydrogen bond acceptor) and a hydrogen atom, which is covalently bonded with another electronegative element (hydrogen bond donor). Subsequent research revealed that extremely electronegative elements like oxygen (O), nitrogen (N), and fluorine (F) are not the only ones which take part in hydrogen bonding interactions. Less electronegative elements such as carbon (C), sulfur (S), selenium (Se), and phosphorus (P), among others, are also observed to participate in the hydrogen bonding interactions, which create a distinct category known as unconventional hydrogen bonding. To accommodate such unconventional hydrogen bonding interactions, IUPAC redefined the definition of hydrogen bonding in 2011.[1]

Unconventional hydrogen bonds based on sulfur are essential components of biological molecules, pharmaceuticals, and materials. Sulfur makes up around 0.3% of the mass of the human body and is essential for proteins, vitamins, and enzymes. Proteins include the amino acids cysteine (Cys) and methionine (Met), both of which contain sulfur. On the other hand, the efficiency and selectivity of catalysis, as well as supramolecular assembly, are significantly influenced by sulfur-centered hydrogen bonding. Studies on the SCHB involving N-H⋯S/O-H⋯S hydrogen bonding reveal that these are just as strong as conventional hydrogen bonding.[2-5]

Sulfur exhibits versatility in forming hydrogen bonds as it acts as both an acceptor and donor. Existing literature primarily explores N-H⋯S or O-H⋯S hydrogen bonding, where sulfur acts as an acceptor. However, sulfur-centered hydrogen bonding, with sulfur as the donor, remains less explored. Computational studies, including cheminformatics and bioinformatics, acknowledge S-H⋯X (X=O, N, S, or π) hydrogen bonding.[6] Additionally, a few experimental evidences of spectroscopic studies on S-H⋯X are reported that reveal red-shifts in the S-H stretching frequencies.[7-9]

The objectives of the thesis include:

i) Investigating the characteristics and the strength of hydrogen bonds involving sulfur, wherein sulfur serves as a hydrogen bond donor and oxygen serves as a hydrogen bond acceptor.

ii) Exploring the modulation of the weak S-H⋯O hydrogen bond by altering the complexing partners with varying proton affinities.

iii) Comparing the modulation of S-H⋯O hydrogen bonding with conventional hydrogen bonding and comprehending the additional factors influencing the strength of the S-H⋯O hydrogen bond.

Chapter 1 briefly overviews the significance, characteristics, and classifications of non-covalent interactions. We have talked about how the idea of hydrogen bonding has evolved over the time to accept unconventional hydrogen bonding in addition to the conventional hydrogen bonding. We have also reviewed the previous spectroscopic studies on unconventional hydrogen bonds with a focus on sulfur-centered hydrogen bonding (SCHB). We have detailed the importance of sulfur-centered hydrogen bonding in biomolecules, materials, drugs, and other areas. The chapter concludes with the aim of the thesis.

Chapter 2 provides a comprehensive idea of various gas-phase laser (UV/IR) spectroscopic methods based on supersonic jet cooling and Time of flight mass spectrometry. A brief overview of various computational methods that have been employed in the investigations of the nature and strength of the S-H···O hydrogen bonding is also provided in this chapter.

Chapter 3 describes gas-phase spectroscopic study on the nature and strength of S-H···O hydrogen bonding interactions employing one color resonant 2-photon ionization (1C-R2PI), UV-UV hole-burning, and IR-UV double resonance spectroscopy combined with quantum chemistry calculations. Here, our detailed spectroscopic and computational study on 2-FTP (2-Fluorothiophenol)···H_2O demonstrates that S-H···O hydrogen bond is weak in strength. The present work signifies that the S–H···O hydrogen bond can have preference over the O–H···S hydrogen bond depending on the pKa values or proton affinities of the hydrogen bonding partners in a complex, although the O–H···S hydrogen bond is much stronger than the S–H···O hydrogen bond.

In **Chapter 4**, we have shown that the S-H···O hydrogen bond, which is weak in general, can be strengthened by choosing the hydrogen bond acceptors of higher proton affinities.

Here, we have demonstrated the modulation of the strength of the S–H···O hydrogen bond by studying the 2-FTP···MeOH and 2-FTP···EtOH complexes using gas-phase laser spectroscopy and calculations. We have observed that the strength of the S-H···O hydrogen bond increases significantly as the hydrogen bond acceptor is changed from H_2O to MeOH and EtOH and a linear correlation between the strength of the hydrogen bond and proton affinity of the acceptors.

In **Chapter 5,** we have studied 2-FTP···Et_2O complex to explore the strength of the S-H···O hydrogen bond by substituting both the hydrogens in H_2O by ethyl group. Here, Et_2O can act solely as a hydrogen bond acceptor. It is observed from the gas-phase spectroscopic investigations and quantum chemical calculations that the linear correlation curve between the strength of the S-H···O hydrogen bond and proton affinity of the hydrogen bond acceptors is less steeper than that obtained in the case of the conventional hydrogen bonding i.e., O-H···O, N-H···O, etc. This observation signifies that the S-H···O hydrogen bond, being weaker than conventional hydrogen bonds, is significantly influenced by the steric effect and dispersion interaction as the hydrogen bond acceptors of higher proton affinities are used as complexing partners. Investigation of the nature and strength of the S-H···O hydrogen bonding was further extended by theoretical studies on several complexes of 2-FTP with a series of cyclic and acyclic ethers.

Chapter 6 deals with the summary and future direction of the thesis.

List of Publications

- **Surajit Metya**, Supravat Roy, Sourav Mandal and Aloke Das*," Interplay between proton affinity and steric repulsion on S-H···O hydrogen bond: Spectroscopic study and quantum chemical calculations," (Manuscript under preparation)

- **Surajit Metya**, Supravat Roy, Sourav Mandal, Qian-Rui, Jer-Lai Kuo*, and Aloke Das*, "Modulation of the strength of weak S-H···O hydrogen-bond: Spectroscopic study of the complexes of 2-Flurothiophenol with methanol and ethanol" (Manuscript under preparation)

- **Surajit Metya**, and Aloke Das, "S–H··· O Hydrogen Bond Can Win over O–H···S Hydrogen Bond: Gas-Phase Spectroscopy of 2-Fluorothiophenol···H2O Complex." *J. Phys. Chem. A*, **2022**, 126, 9178-9189.

- Kamal K. Mishra, Kshetrimayum Borish, Gulzar Singh, Prakash Panwaria, **Surajit Metya**, M. S. Madhusudhan, and Aloke Das., "Observation of an Unusually Large IR Red-Shift in an Unconventional S–H···S Hydrogen-Bond." *J. Phys. Chem. Lett.,* **2021**, 12, 1228-1235.

- Manzoor Ahmad, **Surajit Metya**, Aloke Das, and Pinaki Talukdar. "A sandwich azobenzene–diamide dimer for photoregulated chloride transport." *Chem. Eur. J.*, **2020**, *26*, 8703-8708.

Chapter 1

Introduction

1.1 Non-covalent interactions and their significance:

Non-covalent interactions weave their influence throughout the expanse of our world, extending their reach from living organisms to inanimate entities. These interactions are not just necessary but the foundation that sustains life on Earth.[10-11] The significance becomes most evident in the presence of liquid water, which owes its stability to numerous hydrogen bonding interactions occurring in ambient conditions.[12-13] Even the fundamental molecules of life, DNA, find their structural forms in the intricate interplay of nucleic acids and bases through hydrogen bonding and π- π stacking.[11, 14-16]

These non-covalent forces are equally crucial in the structural stability and functionality of the biomolecules and materials. It is well known that the building block of life, DNA, which carries the code of hereditary information for synthesis and functionality of all other essential biomolecules such as proteins and enzymes, depends on various non-covalent interactions for structural stability and functionality.[17-18] The typical helical structure of DNA is maintained by double hydrogen bonds between adenine and thymine bases and triple hydrogen bonds between guanine and cytosine bases.[19] In biology, these interactions emerge as essential determinants in forming various molecular recognitions, such as protein-DNA, drug-DNA, and protein-protein interactions.[20-24] Protein-DNA interactions are a vital event in a living system, which is the underlying mechanism of several crucial tasks like DNA replications. Similarly, in materials, non-covalent interactions significantly influence various processes such as self-assembly, stereoselectivity, arrangement of molecular clusters, solid-state reaction, etc.[25-30]

1.2 Nature of Non-covalent interactions

Theoretical investigations conducted over the time on the characteristics of non-covalent interaction return an idea that tells energetic stabilization of such interaction possess along a specific orientation. Like true chemical bonds, these interactions also follow Morse-type potential energy surface.[31] However, the difference is that the equilibrium distance is much longer, and the minimum energy value is smaller than a pure covalent bond. The classical mechanical concept provides an approximation of the interaction energy based on electrostatic interaction when two molecules, A and B, are far apart from each other in space.[32-33]

$$E_{el} = \frac{1}{4\pi\varepsilon_0}\frac{q_A q_B}{r} - \frac{1}{4\pi\varepsilon_0}\frac{q_A \mu_B}{r^2} cos\theta - \frac{1}{4\pi\varepsilon_0}\frac{\mu_A \mu_B}{r^3}\,(2cos\theta_1 cos\theta_2 - sin\theta_1 sin\theta_2 cos\phi) - \cdots \quad (1.1)$$

In this equation, the first term corresponds to the *charge-charge* interaction, expressed as the Coulomb interaction. The second term represents the *charge-dipole* interaction, where θ signifies the angle of the dipole in relation to the axis connecting the centers of mass of A and B. The third term denotes the *dipole-dipole* interaction, with θ_1 and θ_2 representing the angles of two dipoles relative to the axis of interaction, and ϕ is the dihedral angle between two dipoles. Here, q and μ represent the charge and dipole, respectively, and r is the distance between A and B. Equation (1.1) can also be represented as

$$E_{el} = E_{(q,q)} + E_{(q,\mu)} + E_{(\mu,\mu)} + \cdots \quad (1.2)$$

When both of these, A and B, are charged partially $E_{(q,q)}$ contribution dominates, but if one of them is charged and the other is neutral but has a significant dipole $E_{(q,\mu)}$ dominates in the total E_{el}. Finally, if both the A and B molecules are neutral but have a significant dipole moment $E_{(\mu,\mu)}$ Contribution plays a major role. If the dipoles are not fixed dipoles but rather can rotate freely, equation (1.1) will be modified by averaging over the angles:

$$E_{el} = \frac{1}{4\pi\varepsilon_0}\frac{q_A q_B}{r} - \frac{1}{(4\pi\varepsilon_0)^2}\frac{1}{6kT}\frac{q_A^2 \mu_B^2}{r^4} - \frac{1}{(4\pi\varepsilon_0)^2}\frac{1}{3kT}\frac{\mu_A^2 \mu_B^2}{r^6} - \cdots \quad (1.3)$$

Here, k is the Boltzmann constant, and T is the absolute temperature.

Fascinating studies on the decomposition of the total interaction energy, when two molecules come together to make aggregation, have been done based on various theories from the quantum mechanical approach. The perturbative method is one of the accepted strategies for understanding the interaction when the wavefunctions of the two interacting molecules are non-negligibly overlapped.[34] This procedure gives the total interaction energy (E_{int}) are the sum of the different energies like electrostatic, exchange-repulsion, polarisation, dispersion etc. However, the procedure has been developed over time with further improvement. Kitaura and Morokuma method is one of the most popular of them.[35-36]

$$E_{int} = E_{el} + E_{er} + E_{pol} + E_{ct} + E_{disp} \quad (1.4)$$

Terms in equation (1.4) represent *electrostatic*, *exchange-repulsion*, *polarisation*, *charge-transfer,* and *dispersion* contribution, respectively.

The electrostatic contribution has been discussed previously in this section. The *exchange-repulsion* contribution implies the stabilization due to exchange energy, which comes from the exchange of symmetry between the wave functions of two indistinguishable particles.[37] For the electron-like Fermion particles with asymmetric wavefunction, this interaction is destabilizing according to the theory of the Pauli exclusion principle. However, in the physical sense, this interaction contribution destabilizes molecular aggregation as the distance between two molecules decreases, which is proportional to r^{-12}. *Polarisation* or *dipole-induced-dipole* contribution between a polar and non-polar molecule adds an attractive contribution to the total interaction energy.[38-39] Polar molecules, having a permanent dipole moment because of uneven electron cloud distribution, repel the electron density in the non-polar molecule and generate a temporary dipole moment. This induced dipole in the non-polar molecule attracts the corresponding permanent dipole in the polar molecule. The strength of these interaction contributions depends upon the magnitude of the electric field due to the permanent dipole and polarizability of the non-polar molecule. The electric field generated due to the polar molecule is proportional to the r^{-4}. *Charge-transfer* contribution involves the delocalization of electron density between donor and acceptor molecules.[39] *Dispersion* contributions among the non-polar molecule are proportional to the r^{-6}, and have been quantified with the London formula. An instantaneous dipole moment is formed due to the fluctuation in the electron cloud, which in turn induces the other nearby non-polar molecules and makes an instantaneous dipole-induce dipole type interaction. This is a very short rage interaction.[39-41]

1.3 Types of non-covalent interaction

Non-covalent interactions are of various types depending on the strength and occurrence. The strength of these interactions can vary from a few to several tens of kJ/mol. These interactions can be categorized based on the atoms of the atoms involved in building these interactions. A few important non-covalent interactions are hydrogen bonding interaction, London-dispersion (Van-dar-Waal) interaction, π-π interaction, n→ π* interaction, halogen bonding, chalcogen bonding, pnicogen bonding, tetrel bonding etc.

Electrostatic or ionic bonding is the strongest type of non-covalent interaction. Ion-ion or ion-dipole contribution is mainly associated with this interaction. An example of this interaction is any ionic salt like NaCl, which forms due to the strong electrostatic interaction of the oppositely charged ions Na^+ and Cl^-.

The most explored and most important non-covalent interaction is hydrogen bonding interactions because of its extensive appearance in biological, chemical, and even physical processes. It is characterized as a robust non-covalent interaction, generally occurs when a hydrogen atom, covalently bonded with a highly electronegative element like (O, F, N, etc.), comes closer to interacting with another highly electronegative element. From the theoretical point of view, electron density redistribution takes place to stabilize the entire process when the molecular orbitals of each pair overlap. Energy associated with this quantifies the strength of the hydrogen bonding interaction. Examples of hydrogen bonding interactions are found everywhere. N-H⋯O, O-H⋯O, N-H⋯N, etc., are typical examples of hydrogen bonding.[42-43]

Another important non-covalent interaction is Van-dar Waal or London dispersion interaction, which is present in all kinds of materials. This can occur between atoms or molecules that have no permanent dipole moment. Temporary fluctuation in the electron clouds generates instantaneous dipoles, which interact with each other. The size and shape of a molecule or system generally influence the strength of such interactions. These are the weakest type of non-covalent interaction, despite the fact that these are crucial for various things such as physical property, boiling point, solubility, viscosity, etc.[44-45]

π-π stacking interaction is an important non-covalent interaction that occurs mainly due to the overlap of the π orbitals of aromatic rings. This type of interaction most frequently occurs when a large molecule or molecular assembly binds a small molecule in a cavity or pocket. These are also important for the stability and functions of biological systems. π-π interaction does not favor when the aromatic rings are parallel to each other as this conformation is electrostatically repulsive. Instead, these interactions become more favorable if a balance between attractive and repulsive forces can be achieved when aromatic rings are offset or perpendicular to each other.[46-47]

n→p* interaction is a recent discovery of an important weak non-covalent interaction vital in bio-molecules. This weak interaction develops because of the electron density redistribution between a lone pair and a π-antibonding orbital of carbonyl (C=O) or aromatic ring (C=C). The strength of such interaction is very weak and limited to only a few kJ/mol.[48-49]

Halogen bonding is another significant non-covalent interaction that develops due to the interaction between an electron-deficient halogen (typically iodine, bromine, or chlorine) and a nucleophile. In such cases, electron density on the halogen atom is distributed in such a way that a region formed with lesser electron density, which is called a σ-hole. This σ-hole acts like an electrophile and is prone to bind with a nucleophile. These types of non-interaction are now essential in molecular design, drug discovery, and crystal engineering.[50-51]

Similarly, another σ-hole interaction is also observed in chalcogen elements (sulfur, selenium, and tellurium). These elements inside the molecules interact with the Lewis bases or nucleophiles, which is called chalcogen bonding. These interactions opened a new window for various disciplines in chemistry like crystal engineering, molecular recognition, drug discovery, etc.[52-53]

Group-15 and group-14 elements of the periodic table are also promising candidates to build up weak non-covalent interaction via Pnicogen bonding and tetrel bonding, respectively. When an electron density region builds up on these elements, they participate in the formation of weak non-covalent interaction with Lewis bases and nucleophiles.[54]

1.4 Hydrogen Bonding

Hydrogen bonding is a special type of long-range dipole-dipole interaction.[55] It is the most crucial and popular non-covalent among all the non-covalent interactions. The concept of hydrogen bonding was developed more than a century ago.[56] But still, it is as interesting as before. This versatile, non-covalent interaction is spread in all the disciplines of science. Starting from the molecular assemblies in supramolecular chemistry,[57-58] controlling the structural stability and functionality of crucial bio-molecules everywhere hydrogen bonding plays a significant role.[59-60] Hydrogen bonding interaction is the heart of application-based research like biochemistry, medicinal chemistry, material science, crystal engineering, etc.[61-64]

1.4.1 History of the Concept of Hydrogen Bonding

While widely acknowledged as the most significant non-covalent interaction, the concept has encountered some controversy regarding its origin. A large part of the scientific community contends that it was invented in the early 19th century. The first reported document of this non-covalent interaction came in 1902 through the observation of ammonium salts by Werner and Hanstzsch.[65] In that report, the authors introduced the term '*Nebenvalenz,'* denoting the secondary valency in German. IN 1912, Moore and Winmill employed a new phase, '*weak union*,' to articulate the inferior basic characteristic of trimethylammonium hydroxide in contrast with the tetramethylammonium hydroxide.[66] At the same time or in the early stages of 1913, Pfeiffer's study on 1-hydroxyanthraquinone yielded a report echoing similar findings. Within this report, Pfeiffer introduced the term '*Innere Komplexasalzbildung*' (internal complex salt-bridge) to describe this non-covalent interaction elegantly.[67] Lattimer and

Rodebush, in 1920, proposed an explanation for the properties of highly associated liquids such as water and hydrogen fluoride, etc.[68] According to their proposal, a free electron pair on the oxygen atom of one water molecule could potentially apply enough force to a hydrogen atom, which is stabilized by a pair of electrons on a different water molecule, resulting in the bonding of the two molecules. This conceptualization implies that the hydrogen nucleus is situated between two octets, forming a weak 'bond.' Also, in the footnote of their report, Latimer and Rodeush attributed this idea to being initially proposed by M. L. Huggins, who first introduced the term "*Hydrogen Bridge*." The same thing was confirmed by the report of Lewis in 1923.[69] The term' Hydrogen Bridge' continues to be used alongside the more common expression "*Hydrogen Bond*" or "*H-bond*," introduced by Pauling in 1939 in his famous book '*The Nature of Chemical Bond*".[70] In order to explain the nature of hydrogen bonding, Pauling mentioned in his book that a large ionic force must be involved to build up this attraction force for two other atoms because hydrogen can make only one pure covalent bond as it has only one orbital. In 1960, the first detailed definition of hydrogen bonding was given by Pimentel and McClellan in their book '*The Hydrogen Bond*.' According to them:[71]

"A hydrogen bond exists between a functional group A-H and an atom or a group of atoms B in the same or a different molecule when

> *(a) There is evidence of bond formation (association or chelation)*
>
> *(b) There is evidence that this new bond linking A-H and B involves the hydrogen atom already bonded to A."*

This definition was crafted without imposing any limitations on the chemical properties of the donor or acceptor, as well as the geometric orientation and energy of bond formation. In line with this definition, hydrogen bonding is recognized to occur between any A-H group and any atom B, whether it is within the same molecules or between different molecules. This can be symbolized as:

$$\mathbf{A - H \cdots B} \qquad (0.5)$$

Where A and B can be any atom or group.

Based on the interaction energy, hydrogen bonding was categorized into 'Strong' and 'Weak' groups by Jeffrey and Saenger.[72] Later, it was modified into three groups: strong, moderate, and weak. A more detailed classification of hydrogen bonding was made by following Linus Pauling's definition, which was based on the electronegativity of the involved donor and acceptor atoms. Classification introduced two categories: conventional hydrogen bonding and unconventional hydrogen bonding.

1.4.2 Conventional concept of hydrogen bonding

In the previous section, the symbolic representation of hydrogen bonding, built upon the concept of Pauling's definition, is represented as A-H⋯B, where A and B are the donor and acceptor atoms. According to the conventional concept of hydrogen bonding, the hydrogen bond is mostly an electrostatic interaction that develops due to the formation of a partial charge on the involved atom.[42, 59] Significantly partial charge development can only be possible through significant polarisation of electron density. This is done when A, being a highly electronegative element like oxygen (O), nitrogen (N), or fluorine (F), attracts the electron density, resulting in the formation of partial charge on the hydrogen atom like $A^{\delta-}$-$H^{\delta+}$. Similarly, *B* is also a highly electronegative atom or electron-dense region which forms $B^{\delta-}$. This partially charged opposite polar hydrogen atom and the B atom attract each other.[73-74] However, several experimental and theoretical works reveal that not only the highly electronegative elements but also the less electronegative elements are capable of making hydrogen bonding. The formation of hydrogen bonding can be identified as a shortening of the distance between H and Y atom H···Y. Distance is expected to be less than the sum of the van der Wall radii.[55, 75-76] Conventionally formed hydrogen bonds are strong in nature, having bond strength up to 10 to 50 kJ/mol.[72, 77]

1.4.3 Experimental and theoretical approach to studying hydrogen bonding

The conventional definition of hydrogen bonding makes it obvious that A-H···B type interaction boning forms with a signature of weakening of the A-H covalent bond.[77] This phenomenon is reflected in the vibrational stretching frequency of the A-H bond. A substantial red-shift is frequently observed in the case of hydrogen-bonded covalent bonds.[39, 75-76] Eventually, this red-shift value describes the strength of the hydrogen bonding. Though observation is not always true, it is discussed in detail later. Besides this, a noticeable increment of the band intensity is generally observed related to the vibrational spectra of the corresponding covalent bond. Numerous experimental and theoretical investigations have been done to understand the nature of hydrogen bonding.[39, 76] Infrared and Raman spectroscopy were the most utilized spectroscopic methods from the beginning, as these are directly related to the stretching frequency change due to the formation of hydrogen bonding.

Besides this, nuclear magnetic resonance (NMR), especially ^{1}H-NMR spectroscopy, is a very powerful tool for studying hydrogen bonding as well as other non-covalent interactions. This technique distinguished the protons' environment from the chemical shift measurement. In 1951, Arnold and Packard studied the change in chemical shift of O—H and CH_2 protons in ethanol at different temperatures in the range of 150°K to

350°K.[78] They have also observed a similar variation of the chemical shift associated with ethanol dilution. In the spectroscopic database, the chemical shift for the aliphatic alcohols O-H proton varies in between 0.5 to 6 ppm, and aromatic O-H proton falls in the range of 4 to 12 ppm.[79] Resonances of exchangeable protons in OH or NH groups cannot be distinctly assigned to a specific region on the δ scale, as the various factors, including hydrogen bonding among themselves, highly influence their positions. Typically, a higher ppm shift is observed due to a deshielding of protons in hydrogen bond formation. This result, however, contradicts the conventional concept of hydrogen bonding, where electron density delocalizes to the anti-bonding orbital. This paradox is ascribed to the counterintuitive impact of the electrical dipole field inherent in the hydrogen bond, which explains that hydrogen bonding is not a simple electrostatic interaction.[79]

Crystallographic methods are also prevalent methods of studying hydrogen bonding as they are among the most superior techniques for understanding the structure.[80-82] Hydrogen-bonded solids are often studied using crystallographic techniques. This information is readily available in the Cambridge Structural Database (CSD). Several surveys have established the correlations between the geometries of hydrogen bonds in solid-state structures and the characteristics of the donor and acceptor groups, shedding light on the influence of the donor and acceptor groups' nature and environment. Noteworthy trends have emerged from these investigations.

Recently, after the discovery of the REMPI technique, several high-resolution spectroscopic methods have been built up based on that, which are powerful tools for understanding hydrogen bonding precisely.[83-86] Adaptation of high-resolution spectroscopic approaches like Resonant two-photon ionization (R2PI), IR-UV double resonance, microwave, matrix isolation, Laser induced fluorescence (LIF), etc.,.[87-94]

Modern high-resolution spectroscopic approach reveals the strength and nature of the hydrogen bonding with magnificent accuracy. These tools have also become indispensable for investigating various non-covalent interactions, including unconventional hydrogen bonding. Lots of hydrogen-bonded homo and hetero dimers have been studied utilizing various high-resolution spectroscopic techniques accompanying the ab initio electronic structure calculations as well as DFT-based calculations. A typical example, water dimer, which forms by O-H⋯O hydrogen bonding, was studied by Huang and Miller using the molecular-beam electric resonance spectroscopic technique. Their study represents a huge red-shift (about 100 cm^{-1}) in the stretching frequency of hydrogen-bonded O-H.[95] This experimental result closely matched the previously done theoretical ab initio study and the quantum mechanical simulation study.[96-100] Later, several studies were reported on water dimers, and it was established that O-H⋯O is a strong hydrogen bonding having bond energy approx. 13 kJ/mol.[101-102] Similarly, a large number of reports are in the literature where an extensive study has been done involving the homo and hetero dimer of methanol, ethanol, Phenol, formic acid, acetic acid, formaldehyde, etc.[103-108] Another popular example of conventional hydrogen bonding is N-H⋯O interaction. This is the most common type of hydrogen-boding generally observed in the 3-dimension structure of a protein, making an interaction between backbone N-H and C=O groups. T. Zwier and co-workers extensively explored the N-H⋯O hydrogen bonding in indole and water complexes using various mass-selected spectroscopic techniques.[109] The outcome of their investigation mentions a red-shift in N-H stretching frequency by 87 cm^{-1}, indicating a strong hydrogen-bonded complex. Hydrogen bonding involving aromatic O-H is another interesting chapter of this non-covalent interaction. Matrix–isolation study of Phenol-water and Phenol dimer by G. Yu. Gor et al. shows a huge red-shift in the phenolic O-H

(179 for Phenol-water complex and 146 for phenol dimer) appears due to the formation of hydrogen bonding where Phenol acts as a hydrogen bond donor.[110]

Quantum mechanical calculation is essential to understanding the nature and strength of hydrogen bonding. Three-dimensional geometry and corresponding parameters of the structure are the primary tools for comparison of the nature and strength of hydrogen bonding and are also equally important for its applications. Geometry optimization using wavefunction theory of density functional theory is widespread nowadays. The gold standard calculation, including coupled cluster singles doubles and perturbative triples [CCSD(T)], provides the most accurate information about hydrogen bonding and other non-covalent interactions. A large number of studies have been done with very expensive quantum calculations.[111-114] Understanding of the change in electronic topology because of the hydrogen bonding or any other non-covalent interaction is a very powerful approach in terms of theoretical study. Quantum theory on atoms in molecule (QTAIM) calculation is a popular application in this purpose.[115-116] This calculation offers a conclusive response to the ambiguity of bond formation between two atoms with the bond critical point (BCP) calculations. Electron density and the Laplacian of electron density at the BCP provide the idea of the existence of the non-covalent interaction and also strengthen the interaction if present. Natural bond orbital (NBO) calculation is another widely used quantum chemical calculation.[117-119] This calculation returns the second-order perturbation energy of electronic delocalization while the donor and acceptor orbitals overlap. This energy value qualitatively reflects the strength of the interaction.

1.4.4 Modulation of Hydrogen bond strength

The strength of the hydrogen bonding depends upon several factors. First of all, the position of the donor/acceptor element in the periodic table, which means the electronegativity and proton affinity (PA) of the element, is an important factor in the strength of the hydrogen bonding.[120] This proton affinity can be modulated by changing the bonded elements or group. Another important factor is pKa (acidity) of the hydrogen bond donor group. A combined effect of the pKa of the hydrogen bond donor and PA of the hydrogen bond acceptor can conclude the strength of the hydrogen bonding. Hussein and Millen studied the hydrogen-bonded complex of various alcohols with a series of free amines using IR spectroscopy of the gaseous mixture of the molecules. Their findings revealed a red-shift in the O-H stretching frequency, with the degree of increase following the order $NH_3 < MeNH_2 < Me_2NH < Me_3N$ for all tested alcohols, including MeOH, EtOH, ^{i}PrOH, ^{t}BuOH, and TFE (trifluoroethanol).[121] In a separate study, C. Laurence et al., investigated a hydrogen bonding complex involving 4-fluorophenol as a hydrogen bond donor and serving water and a series of alcohols as hydrogen bond acceptors.[122] They have observed a linear correlation between the hydrogen bonding strength and the proton affinity of acceptor molecules. Gibbs free energy of hydrogen bond formation (pK_{HB}) gradually increased for the linear chain alcohols in the order Me < Et < ^{n}Pr<^{n}Bu< ^{n}Oct and similarly for the branched-chain alcohols in the order Me<Et<^{i}Pr<^{t}Bu.[123] Any general correlation between the Gibbs free energy of hydrogen formation and the frequency shift cannot be made for all kinds of hydrogen bond acceptors, but a family-dependent relationship can be achieved. Family stands for the same donor or acceptor site or similar hybridization state. Steric repulsion also plays a crucial role in the modulation of the strength of the hydrogen bonding.

With the increase of the number of the alkyl group on the hydrogen bond acceptor atom increases the polarizability of the acceptor atom, which enhances the enthalpy of hydrogen bond formation and, at the same time, this also increases the steric effect that increases the hydrogen bond formation entropy. R. West et al., in a study of hydrogen bonding with Phenol and a list of ethers, observed that enthalpy of hydrogen bond formation as well as entropy both are linearly increased in the order Me < Et < *ⁱ*Pr < *ᵗ*Bu.[124] Later M. Berthelot and co-workers, in a FTIR study of hydrogen bonding in MeOH and 4-Fluorophenol with a large number of ethers and epoxides, observed that the red-shift in O-H stretching frequencies following an order Et_2O < $^tBu_2O$ < $^iPr_2O$.[125]

Cooperativity is a special property of hydrogen bonding, which has a huge influence on the strength of the hydrogen bonding. Upon formation of a linear chain network, hydrogen bonding interaction increases significantly.[126-127] The hydrogen-bonded water network is very popular. Several studies were done on this topic. In the Ar-matrix spectroscopic study of water dimer to water dodecamer, Lee et al. observed a red-shift of O-H stretching frequency that can enhance up to 500 cm^{-1}.[128]

1.5 Unconventional Hydrogen bonding

Up to this point, it has been discussed that elements with high electronegativity, such as oxygen, nitrogen, fluorine, etc., consistently form robust hydrogen bonds, playing a vital role in both biological and material chemistry. This concept involves the rearrangement of electrons between the donor and acceptor, resulting in a noticeable red-shift in the stretching frequencies of the X-H (where X = O, N, F) part of the hydrogen bond. Simultaneously, it has been noted that elements with lower electronegativity, such as carbon (C), sulfur (S), phosphorus (P), etc., can also engage in non-covalent interactions, which hold significant importance in both biological and material contexts.[43, 55, 129-131]

A commonly observed intermolecular interaction in molecular crystals, particularly prevalent in organic molecular crystals, is C–H···X interaction.[55] This interaction involves a C–H group from one molecule and an X atom from another, arranged in a manner that facilitates a short and significant H···X contact. From the early 1960s, the scientific community observed the very weak non-covalent interaction involving carbon.[132-133] The debate surrounding the classification of the C-H···O=C interaction as a hydrogen bond was explored by Jeffrey and Saenger in 1991.[59] While Pauling's definition rejects it, Pimentel and McClellan's definition accepts it, with further refinement by Steiner and Saenger in 1993 emphasizing specific charge criteria on the hydrogen and acceptor atom for hydrogen bond classification.[73] Thereafter, weak unconventional interactions due to short C-H···O contacts are appreciated as hydrogen bonds. C-H···X (X= O, N, π) are studied extensively, and the nature of this hydrogen bonding has been well explored. Desiraju and Steiner, in their book '*The Weak Hydrogen Bond, In Structural Chemistry and Biology*' categorized these weak hydrogen bonding by studying lots of C-H···X hydrogen bonding interaction.[55] These weak hydrogen bonds have different structural properties and nature than conventional strong hydrogen bonds. Weak hydrogen-bonded complexes are moderately electrostatic and exhibit a much less (<5% of the bond length) red-shift in stretching frequency. Weak hydrogen bond distance varies in the range of 2.0Å to 3.0Å, and the angle can be within the range of 90 to 180°.

Interestingly, aromatic π-electron density is observed to make a hydrogen-bonded interaction with the covalently bonded hydrogen atom.[134-135] Interactions are named π-type hydrogen bonding. Some well-known examples of this are benzene···water, benzene···MeOH, etc.[136-137] In benzene···benzene dimer, it was also observed that C-H can also participate in C-H···π hydrogen bonding. π type hydrogen bonding also offers a characteristic red-shift in X-H stretching frequencies. However, this is not true for C-H··· π hydrogen bonding.[138-139]

Sulfur-center hydrogen bonding is very common, and the idea of such interaction was also contemporary with the C-H⋯X interaction. In a spectroscopic study, Schleyer observed that Di-n-butyl sulfide and MeOH complex is formed with a similar red-shift (155 cm^{-1}) in O-H stretching frequency as it was in the case of Di-n-methyl ether and MeOH complex.[140] This study explains that the electronegativity requirement for the involved elements is not necessary for a strong hydrogen bonding interaction. Not only in intermolecular hydrogen bonding, but in some cases, sulfur can also make equally strong hydrogen bonds intramolecularly. Later, with the high-resolution spectroscopic study Biswal *et al*. observed that in sulfur-center hydrogen bonding (O-H⋯S, O-H⋯N, etc.), red-shift in stretching frequency is similar or sometimes more compared to conventional hydrogen bonding.[2, 130, 141] In unconventional hydrogen, bonding sulfur is very interesting as it can participate as an acceptor as well as a donor. Das and co-workers have shown the participation of selenium (Se) in unconventional hydrogen bonding, which is also marked with a strong hydrogen bonding tag in terms of red-shift in stretching frequency.[142]

Hydrogen bond acceptor elements in the periodic table are spread everywhere. Phosphorous center hydrogen bonding was recently reported using high-resolution FT-IR spectroscopy. The involvement of the transition metal in hydrogen bonding has also been established since the '90s. Metal hydrides are also capable of making hydrogen bonds because they are highly polarizable.[143]

With all the evidence of the hydrogen bond formation among the less electronegative elements, the IUPAC team redefined the hydrogen bond in 2011. The new definition is described as *'the hydrogen bond is an attractive interaction between a hydrogen atom from a molecule or a molecular fragment X-H in which X is more* *electronegative than H, and an atom or a group of atoms in same of different molecules, in which there is evidence of bond formation.'*[1]

1.5.1 Significance of Sulfur-centered hydrogen bonding

Sulfur-centered hydrogen bonding is highly popular in the unconventional hydrogen bonding domain. Sulfur has huge importance from biological and material aspects. For biological purposes, sulfur is a major inorganic element that plays a crucial role in proteins, vitamins, enzymes, and more.[144-145] In the human body, ~0.3% of the body mass is contributed by sulfur which places after calcium and phosphorous in terms of abundance. Sulfur has been utilized in dermatologic issues since ancient times. It is now also used in the treatment of acute exposure to radioactive materials.[146-147] Sulfur in the human body has a role as an antioxidant, which in turn reduces the production of reactive oxygen and nitrogen.[148-150] The daily requirement of sulfur for an adult human body is ~14mg/kg of body mass, which mainly comes from the sulfur-containing amino acids of protein-based foods.[151-152]

In proteins, two sulfur-containing essential amino acids are there, which are cysteine (Cys) and methionine (Met).[153] Cys has an S-H group at the amino acid's side chain, which can participate in hydrogen bonding as both donor and acceptor, whereas Met can participate as hydrogen bond acceptor. In a statistical study by Shang and co-workers using 500 high-resolution proteins, it was found that out of 2143 methionines, 232 methionines are hydrogen bonded with the O-H and N-H group in the form of X-H···S interaction, whereas out of 753 cysteines 465 are hydrogen bonded with are hydrogen bonded with O, N atoms as S-H···X.[154] Biswal and co-workers show that in gas-phase vibrational spectroscopy, N-H···S hydrogen bonding is equally strong like conventional hydrogen bonding N-H···O.[2] Biswal et al. also reported that backbone N-H···S_{Met} are involved in a specific folding pattern which is similar in the crystallographic protein data.[141]

Sulfur-centred hydrogen bonding also plays a huge importance in the supramolecular assembly. Ashwini et al., from the crystal structure study, show that the axial conformation of the of penicillins is stabilized due to N-H···S and C-H···O hydrogen bonding.[155] Reddi et al, observed in a study of the Methionine aminopeptidase (MetAP) enzyme a unique C-H···S hydrogen bonding between MetAP and its N-terminal methionine polypeptide substrate is playing crucial role in the specificity and efficiency of the catalysis.[156] Also, this C-H···S hydrogen bonding is involved in characteristic physical properties like melting points.

1.5.2 Sulfur as hydrogen bond acceptor (X-H···S) vs donor (S-H···X)

Sulfur-centered hydrogen bonding acquires significant attention within the realm of unconventional hydrogen bonding due to its immense importance from both a biological and materialistic perspective. Though such hydrogen bonding was initially thought to be a weak interaction,[157] extensive studies with modern high-resolution spectroscopy opened the scope of understanding such non-covalent interaction. Biswal and co-workers established the fact with experimental evidence that sulfur-centered hydrogen bonding can be as strong as conventional hydrogen bonding.[2, 130-131] From the studies of several binary complexes of sulfur-centered hydrogen bonding using REMPI spectroscopy, fluorescence-dip infrared (FDIR), resonant ion-dip infrared (RIDIR) spectroscopy, etc., accompanied with quantum chemical calculation, the interesting thing came out that sulfur-center hydrogen bonding is not electrostatic dominant in nature rather dispersion contribution plays a major role for the strength of such interaction. Vapor phase infrared spectroscopic investigation of methanol and Me_2S/Me_2O complex by Kjaergaard and co-workers report the red-shift in methanolic O-H of 113 cm^{-1} for Me_2S and 103 cm^{-1} for Me_2O complex.[158] Mons and co-workers have studied the amide N-H⋯S hydrogen bonding with a capped model dipeptide build-up with methionine (Met) and L-phenylalanine (Phe) where amide N-H is involved in hydrogen bonding with the side chain of the methionine residue.[141] This N-H⋯S hydrogen bond is involved in maximum red-shift in the N-H stretching frequency. Many other independent computational and experimental studies reported a similar result, which delivered a message that sulfur-centred hydrogen bonding can be significantly strong.

Sulfur is also capable of making hydrogen bonds, acting as both acceptor and donor. Previous studies that have proven to make conventional-like strong hydrogen bonding are generally N-H⋯S or O-H⋯S type hydrogen bonding. In those cases, sulfur functions as a hydrogen bond acceptor, while the donor of hydrogen bonds are the conventional type O-H or N-H groups. However, on the other hand, sulfur-center hydrogen bonding involving sulfur as a hydrogen bond donor is explored well. Cheminformatics or bioinformatics study of hydrogen bonding although apprised the exitance of S-H⋯X (X=O, N, S or π) hydrogen bonding.[154, 159] Computational study for understanding the strength and nature of such hydrogen bonding has been developed to some extent. In terms of experimental evidence, Wategaonkar and co-workers reported the study of the simplest molecules H_2S dimer and $H_2S\cdots H_2O$ and $H_2S\cdots MeOH$ complex using VUV-ionization-detected IR predissociation (VUV-ID-IRPD) spectroscopy.[7-8] 25 cm^{-1} red-shift in S-H stretching frequency has been observed, whereas the same study finds a 56 cm^{-1} red-shift in O-H stretching frequency in H_2O dimer. Study of H_2S dimer using different matrix isolation spectroscopy has been studied.[160-161] However, Das and co-workers found a significant red-shift in S-H stretching frequency in the S-H⋯S hydrogen bonding study in the 2-Chlorothiophenol and Me_2S complex.[162]

1.6 Aim of the Thesis

Characterization of the strength and nature of the C-H⋯X hydrogen bonding has been well explored. It is found that being less electronegative elements, C-H⋯O, C-H⋯N, etc are very weak hydrogen bonding. Significant red-shift is also not always observed in such hydrogen bonding. In the periodic table, the electronegativity of the carbon and sulfur are almost similar. However, few sulfur-centered hydrogen bondings with sulfur as a hydrogen bond donor have been studied by spectroscopy and computationally. The nature of such hydrogen bonding, especially S-H⋯O hydrogen bonding, has not been prospected well. Aliphatic S-H was found to form S-H⋯O hydrogen bonding in a study of 2-phenyl ethanethiol and Et_2O complex. However, no such report is available for aromatic S-H, which has been studied in the light of spectroscopic signature.

We investigated S-H⋯O hydrogen bonding in aromatic molecules containing S-H groups through mass-selected gas-phase electronic and infrared spectroscopy, coupled with quantum chemical calculations. We have chosen 2-fluorothiophenol as the hydrogen bond donor and water as the hydrogen bond acceptor, which makes a competition of forming O-H⋯S or S-H⋯O hydrogen bonding. Additionally, we conducted a comparative analysis of the strength and characteristics of S-H⋯O hydrogen bonding in contrast to conventionally reported O-H⋯O hydrogen bonding, employing quantum calculations. To gain insights into the nature of hydrogen bonding, we explored the decomposition of the total interaction energy within this context.

As we discussed in section 1.4.4, in conventional hydrogen bonding, modulation of the hydrogen bonding can be achieved by modulating the proton affinity of the donor and the acidity(pKa) of the acceptor part. We have explored the modulation of the S-H⋯O hydrogen bonding strength by changing the proton affinity of the acceptor molecules by moving water to MeOH and EtOH as hydrogen bond acceptors.

Increasing the proton affinity by adding a methyl group around the oxygen atom in the hydrogen bond acceptor also increases the steric hindrance. Using mass-selected gas-phase spectroscopy, We studied the Et_2O complex with the 2-Flurothiophenol. Additionally, using quantum calculation, we have studied the change in nature and strength of the hydrogen bonding with the higher analog of the ethers.

Chapter 2

Experimental and Computational Methods

In this chapter, we have described the methodologies used for experimentation, including various spectroscopic techniques as well as theoretical calculations. We have also provided a comprehensive overview of the experimental set-up used for our experiments.

2.1 Experimental method

2.1.1 Supersonic Jet Expansion

The core of the experiments detailed in this thesis lies in the utilization of the supersonic jet expansion technique.[163-165] This method primarily focuses on conducting high-resolution spectroscopic (electronic, vibrational, and rotational) investigations of isolated molecules and non-covalently bonded molecular complexes. More importantly, this specialized approach enables the formation of weakly bound molecular complexes of various sizes and the interrogation of their high-resolution mass-selected spectroscopy using high-resolution lasers. The supersonic jet expansion method generates a cold molecular beam in an isolated gas-phase, ensuring that molecules exist in the lowest energy state (rotational and vibrational) without experiencing any collision. This is the fundamental objective of the high-resolution spectroscopy technique, which looks for well-defined quantum states to understand the light-matter interaction very precisely.

In 1951, Kantrowitz and Gray introduced the supersonic jet technique as a high-intensity molecular beam source for effective velocity monochromatization.[166] Before this development, velocity monochromatization relied on other methods, such as rotating sectors or magnetic selection, which significantly reduced the intensity of the molecular beam despite achieving the desired velocity.[167] In contrast, the supersonic jet beam reaches the velocity monochromatization without compromising the intensity. Experimental realization of the molecular beam experiment was achieved by

Kistiakowsky & Slichter and Becker & Bier.[167-168] Subsequently, Levy and co-workers developed the spectroscopic technique based on the supersonic jet for the first time.[163-164] Significant technical details of the supersonic jet expansion technique and molecular spectroscopy based on this are described in many excellent reviews.[163-165, 169-176] A brief description of this technique has been provided here.[163-165, 169-170]

The formation of the supersonic molecular beam involves seeding vapor of the desired sample in a monoatomic inert carrier gas, typically helium (He), argon (Ar), or a mixture of helium and neon (He-Ne), at a pressure of a few atmospheres. A mixture of the sample vapor and carrier gas is expanded into a high vacuum chamber (~5.00 × 10^{-7} mbar) through a small orifice of 500-800 microns diameter. The resulting molecular beam could be either effusive or supersonic, depending on the mean free path (λ_0) of the expanding gas in comparison to the orifice diameter (D). In the scenario where the orifice diameter is significantly smaller compared to the mean free path of the atoms/molecules (i,e; $D \ll \lambda_0$), they exit the nozzle with a few collisions and form an effusive beam.[177] Velocity distribution and internal degrees of freedom do not alter in such cases. The atoms/molecules in an effusive beam exhibit a Maxwellian velocity distribution ($f(v)$), which can be determined using the following equation.

$$f(v) = 4\pi \left(\frac{M}{4\pi RT}\right)^{3/2} v^2 \, exp\left(-\frac{Mv^2}{2RT}\right) \tag{2.1}$$

Where M and v are the molecular mass and speed of the atoms/molecules, respectively, R is the universal gas constant, and T is the temperature (K).

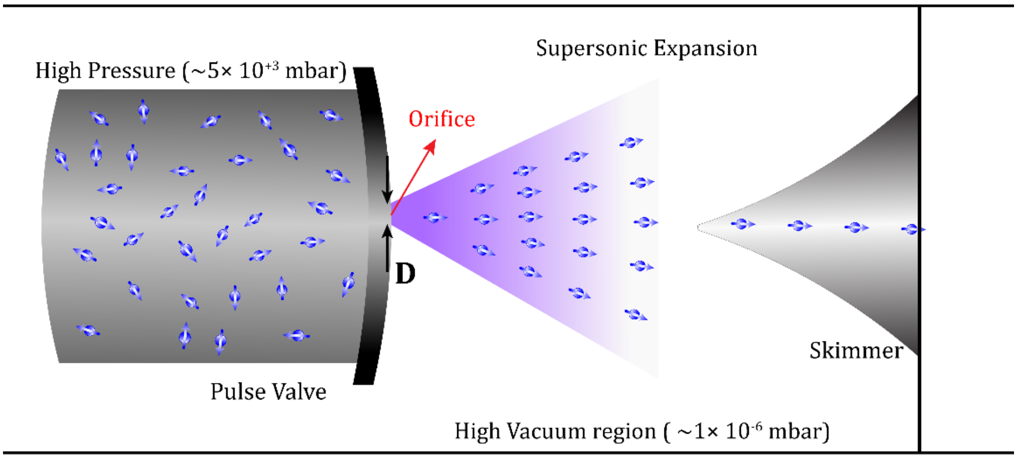
High Pressure (~5× 10^{+3} mbar)
Supersonic Expansion
Orifice
D
Skimmer
Pulse Valve
High Vacuum region (~1× 10^{-6} mbar)

Figure 2. 1. A schematic diagram of the supersonic expansion.

On the other hand, in the case of the supersonic beam, atoms/molecules undergo enormous collisions during the expansion through the orifice as D>> λ_0. The maximum number of collisions takes place in the post-expansion zone a few mm downstream from the orifice. When there are no other external forces, such as viscous forces, heat conduction, and shock waves, these enormous collisions convert the enthalpy associated with the random motion of expanding atoms/molecules into mass flow in the direction of the beam axis. Consequently, the mass flow velocity increases, leading to a narrowing down of the velocity-weighted Maxwell-Boltzmann distribution. A comparison of the velocity distribution curves of the effusive and supersonic beams is given in Figure 2.2. As a significant part of the thermal energy linked to the molecules is transformed into kinetic energy, the temperature of the molecules significantly cools down very rapidly. Velocity distribution becomes narrower, and molecules move faster because of such a reduction in translation temperature. The speed of the sound (a) and the translational temperature (T) are connected by the formula $a = (\gamma KT/m)^{1/2}$ where γ is the heat capacity ratio (Cp/Cv), K and m are the Boltzmann constant, and the mass of the gas molecules, respectively. The Mach number (M) represents the ratio of the velocity of an object to the speed of sound (a). In this case, the object is molecules in the beam. When the velocity of the molecules increases, or the speed of sound decreases, the Mach number also increases. The flow becomes supersonic when it achieves M>1. The translation temperature of the supersonic molecular beam is very low, around ~0.1K. The cold translational temperature of the buffer gas acts as a bath to cool down the rotational and vibrational degrees of freedom of the sample molecules. Because of the fast equilibrium between the translational-rotational energies, the rotational temperature of the molecule cools down to a few kelvins, but slower translational-vibrational equilibrium cannot reduce the vibrational temperature efficiently.[178] The vibrational temperature in the molecular beam remains in the range of 20-50 K. The molecular density in the beam also gets lower as the expansion continues towards downstream. So, the cooling of the rotational and vibrational energies stops as there are no more collisions in the low molecular density.

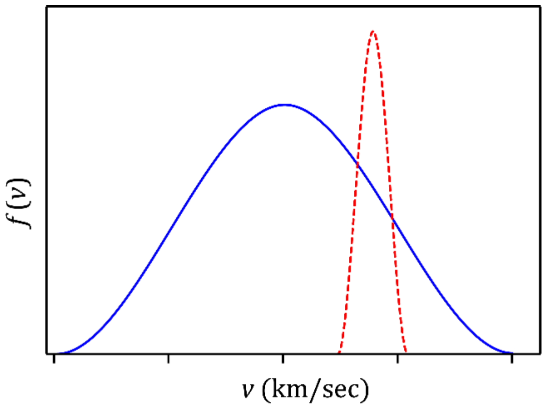

Figure 2.2. Comparison of the velocity distribution curve of effusive (blue-solid) and supersonic beam (red-dotted).

Supersonic expansion is an isentropic as well as adiabatic reversible process. Consequently, the ensuing equation can be employed to characterize the temperature, pressure and density within the molecular beam:[163-165]

$$\frac{T}{T_0} = \left(\frac{P}{P_0}\right)^{(\gamma-1)/\gamma} = \left(\frac{\rho}{\rho_0}\right)^{\gamma-1} = \frac{1}{1+\frac{1}{2}(\gamma-1)M^2} \qquad (2.2)$$

Where T_0, P_0, and ρ_0 represent the temperature, pressure, and density of the molecules in the pre-expansion high-pressure reservoir, respectively, while the corresponding quantities in the supersonic beam are denoted as T, P, and ρ. The heat capacity ratio (γ), is defined as Cp/Cv, and M represents the Mach number. When treating the molecular beam as continuous, the relationship of the Mach number with the orifice diameter (D) and the distance from the orifice (X) can be expressed in the following manner:[178]

$$\boldsymbol{M = A\left(\frac{X}{D}\right)^{\gamma-1}} \tag{2.3}$$

A is a constant term in this equation based on the heat capacity ratio. This equitation (2.3) clearly represents that the Mach number rises with increasing the distance downstream from the orifice. However, the equation cannot hold true at a very long distance from the orifice (X>>D). A model proposed by Anderson and Fenn, where the particles are thought of as classical hard spheres.[179] According to their conclusions, the amount of collisions that might occur between two hard spheres is finite. As a result, Mach number and temperature reduction can reach a critical value within the flow. This critical value of Mach number is termed terminal Mach number (M_T). M_T can be computed using the following equation.[164]

$$\boldsymbol{M_T = 2.05\,\epsilon^{-\frac{1-\gamma}{\gamma}}(\lambda_0/D)^{\frac{1-\gamma}{\gamma}}} \tag{2.4}$$

Here, $\boldsymbol{\epsilon}$ represents the collision effectiveness constant. For argon (Ar) gas, M_T is equal to 133 $(P_0D)^{0.4}$. This suggests that the M_T is directly proportional to both the pressure in the pre-expansion region as well as the diameter of the orifice. However, elevating $\boldsymbol{P_0}$ and $\boldsymbol{D}$ to increase the effective cooling makes a prerequisite of a significantly robust pumping system to sustain the desired vacuum for the expansion of the gas. Employing a vacuum pump with exceptionally high pumping speed can be impractical. Conversely, a pulse valve operating at a repetition rate of 10/20 Hz can effectively manage the excess pressure of the gas introduced into the vacuum chamber.

In summary, the supersonic jet expansion technique lets molecules cool down below their melting point without inducing condensation, allowing them to remain in the isolated gas-phase. This cooling of internal degrees of freedom contributes to the acquisition of highly resolved and simplified molecular spectra. The application of the supersonic expansion technique leads to a discernible decrease in both homogeneous and inhomogeneous broadening within the spectral band. Bandwidth represents the lifetime of the molecule in the excited state. This level of spectral resolution is not attainable in studies conducted in the solution phase.

2.1.2 Resonantly enhanced multiphoton ionization (REMPI) spectroscopy and Time of Flight (TOF) mass spectrometry

High-resolution spectroscopy of the Jet-cooled molecules or non-covalently bonded weak complexes can be achieved using tunable UV lasers and the REMPI spectroscopy technique. Time-of-flight (TOF) mass spectrometry is utilized to measure the mass-selected electronic spectra of molecules or complexes with different sizes. The fundamental principles of both the REMPI and TOF mass spectrometry are elaborated here.

2.1.2.1 REMPI

A schematic overview of the core concept behind REMPI is presented in Figure 2.3. The electronic ground state, first excited state, and ionic ground state of the molecules are symbolized by S_0, S_1, and D_0 in the diagram, respectively. In order to ionize the molecules from their S_0 state, REMPI requires the absorption of multiple photons. The most prevalent form of ionization is resonant two-photon ionization (R2PI), which uses two photons for the purpose. One-color resonant two-photon ionization (1C-R2PI) method (shown in Figure 2.3a) and two-color resonant two-photon ionization (2C-R2PI) technique (shown in Figure 2.3b) are the two types of R2PI techniques that are basically achievable in the experiment.[180-181] In the 1C-R2PI method, molecules first experience an electronic excitation to the vibronic levels of the S1 state using a UV photon of one color. Following this, another photon with equivalent energy is employed to ionize the molecules. Successful ionization requires that the cumulative energy absorbed by both photons exceeds the ionization potential (IP) of the molecules.

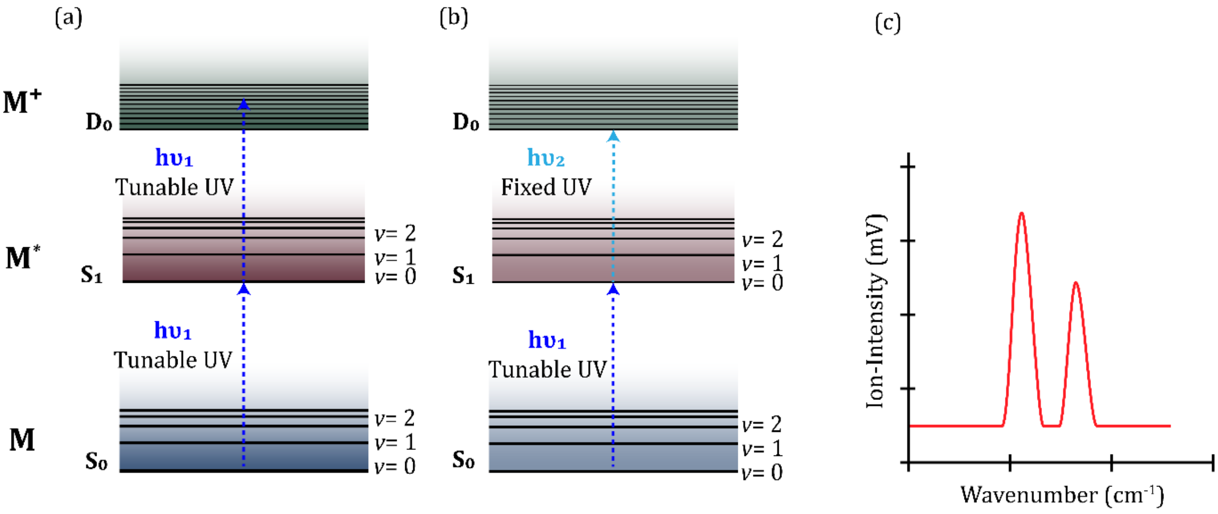
(a)
(b)
(c)
M^+
D_0
$h\upsilon_1$
Tunable UV
M^*
S_1
v= 2
v= 1
v= 0
$h\upsilon_1$
Tunable UV
M
S_0
v= 2
v= 1
v= 0
D_0
$h\upsilon_2$
Fixed UV
S_1
v= 2
v= 1
v= 0
$h\upsilon_1$
Tunable UV
S_0
v= 2
v= 1
v= 0
Ion-Intensity (mV)
Wavenumber (cm^{-1})

Figure 2. 3. Schematic diagram of (a) one-color resonant two-photon ionisation (1C- R2PI) spectroscopy (b) two-color resonant two-photon ionisation (2-C R2PI) spectroscopy (c) a representative REMPI spectrum.

In the 2C-R2PI technique, the second photon, serving as the ionization photon, differs in wavelength and originates from a distinct laser source. This technique proves valuable when the combined energy of two photons of the same wavelength falls short of surpassing the ionization potential of the molecule. For the weakly bound complexes, ionic states are shallow; thus, surplus energy available in the 1C-R2PI spectroscopy might lead to the dissociation of the molecular clusters. The 2C-R2PI method offers more advantages in this regard.

2.1.2.2 Time of Flight (TOF) mass spectrometry

Time-of-flight mass spectrometry separates the ions with distinct masses based on their varying times of flight. Ions generated by the REMPI process are accelerated by a known electric field created by applying a predetermined voltage difference. This process converts the potential energy of the charged particles into kinetic energy. Potential energy (U) of a charged particle of q charge in an electric field of V potential difference is related as follows:

$$\mathrm{U} = \mathrm{qV} \tag{2.5}$$

The kinetic energy of the particle is:

$$KE = \frac{1}{2}mv^2 \tag{2.6}$$

Here, m and v are the mass and velocity of the particle, respectively. As the potential energy transforms into kinetic energy, we can infer from equation 2.5 and 2.6 that,

$$\mathrm{qV} = \frac{1}{2}mv^2 \tag{2.7}$$

When a charged particle covers a distance d, which represents the path of the field-free region, with a time t before reaching the detector, the velocity (v) is expressed as $\frac{d}{t}$. With this, equation 2.7 can be rearranged like this:

$$t = \left[m\left(\frac{d^2}{2\mathrm{qV}}\right)\right]^{1/2} \tag{2.8}$$

Therefore, t is proportional to $\sqrt{m}$, denoted as $t = k(m)^{1/2}$, here $k = \left[\frac{d^2}{2\mathrm{qV}}\right]^{1/2}$ is a constant as all the ions bear the same charge and traverse an identical distance to reach the detector. Also, all the ions experience the same electric field. Hence, it is easy to understand that the time required to cover the distance to the detector is directly correlated with the mass of the ions. In other words, ions with a greater mass will have a higher flight time than those with a lighter mass.

This study employs a time-of-flight (TOF) mass spectrometer featuring a Wiley-McLaren three-electrode design to enhance the mass resolution of both molecules and clusters.[182] The TOF mass spectrometer's schematic diagram is presented in Figure 2.4, illustrating three electrode plates, a field-free TOF tube for the mass-based ion separation, and a microchannel plate (MCP) detector positioned at the top of the TOF for the detection of the ions. The first two electrode plates are the repeller plate and the extraction grid, where the repeller plate carries a higher positive voltage compared to the extraction grid. The separation distance between them is denoted as ***s*** in Figure 2.4. The third plate, the accelerating grid, is connected to the ground. Utilizing the R2PI technique, positively charged ions are generated in the middle of the ionization region formed by the repeller plate and the extraction grid. The repeller plate propels the molecular ions towards the extraction grid, given its higher positive voltage. The ions, formed inside the ionization region experience an electric field $\boldsymbol{E_s}$ between the repeller plate and the extraction grid, which causes them to drive in the direction of the accelerating grid. The accelerating grid is placed at a distance ***d*** from the extraction grid, as shown in Figure 2.4. The electric field

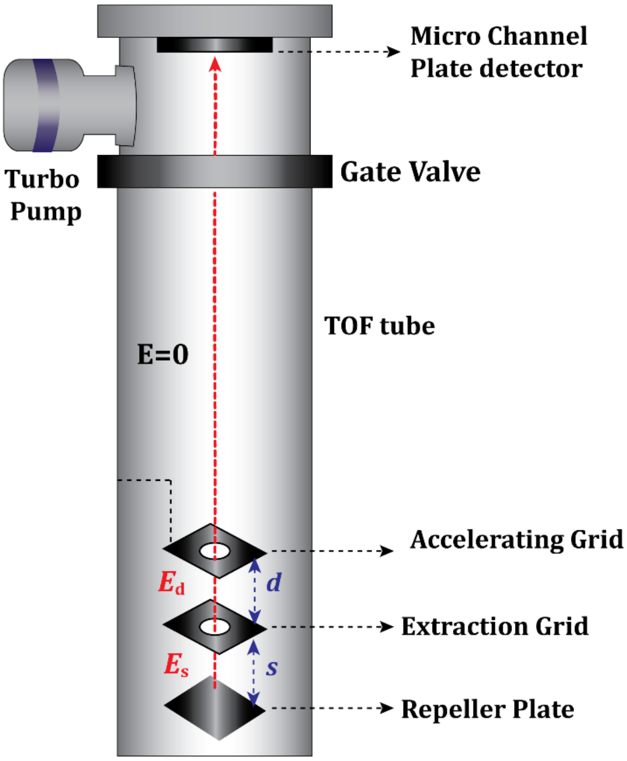

Figure 2.4. Schematic diagram of time of flight mass spectroscopy

developed between the accelerating and extraction grid is denoted as $\boldsymbol{E_d}$. Because of $\boldsymbol{E_d} > \boldsymbol{E_s}$, ions in the region undergo a greater acceleration to travel into the TOF tube.

Upon ionization of the molecular beam by a pulsed laser, a packet of ions, distributed across different positions in space, is generated, constituting the initial spatial distribution. As these ions undergo acceleration, those in proximity to the repeller plate exhibit swifter movement compared to those nearer to the extraction grid. This discrepancy in velocity is termed the initial velocity distribution, which is also called the kinetic energy distribution. The resolution of the time-of-flight (TOF) spectra diminishes because of the initial spatial and energy distributions of the ions. That can be resolved by adjusting the dual–source field. This process is known as energy focusing or space focusing, which enhances the resolution of the TOF mass spectrometer by diminishing the temporal spread among the ions with identical masses.

In our experimental configuration, the TOF mass spectrometer (manufactured by Jordon TOF Products Inc.) is positioned perpendicularly with respect to both the molecular and laser beam axes. The extraction grid and repeller plate are placed one centimeter apart, and here is where the molecular beam is injected. At the Sametime, a UV laser beam is introduced perpendicular to the molecular beam, leading to the ionization of the molecule. Maintaining a voltage of +3060 V for the repeller plate and ground at the accelerating grid, molecular ions are accelerated into a 1m long TOF tube with an optimum adjustment in extraction grid voltage between 2750 -2850V. At the top end, 18mm dual chevron-type microchannel plate (MCP) detector is positioned to detect the ions. MCP detector operates at a negative voltage (typically in a range of -3000 V to -3200 V). An ion emits an electron from the channel wall as it enters a microchannel. The applied voltage on either side of the microchannel plate creates an electric field that accelerates this secondary electron. The electrical signal produced by the detector in response to ion bombardment is observed in the oscilloscope. Different masses of ions generate signals at distinct times on the oscilloscope.

2.1.3 Laser systems used for the experiments

We employed tunable dye lasers pumped by solid-state Nd:YAG lasers to explore mass-selected electronic as well as infrared spectra of molecules and non-covalently bonded complexes in a supersonic jet. Below is a brief explanation of each laser's basic working principles.

2.1.3.1 Dye Laser

The dye laser belongs to the liquid laser category. The active medium is made with the organic dye solution made with a liquid solvent like methanol.[183-185] Generally, dye molecules need to have strong electronic absorption, a large quantum yield, and outstanding photochemical stability. Additionally, negligible intersystem crossing is crucial for the laser to operate effectively. The optical paths of the dye laser are schematically depicted in Figure 2.5, along with a brief description of the working principle of the dye laser.

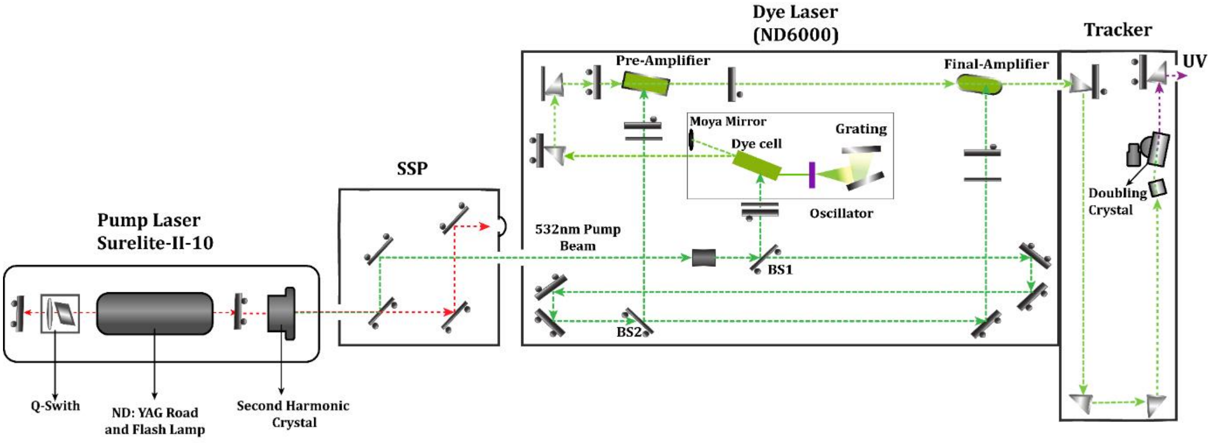
Dye Laser
(ND6000)
Tracker
Pre-Amplifier
Final-Amplifier
UV
Moya Mirror
Dye cell
Grating
Oscillator
SSP
532nm Pump
Beam
BS1
BS2
Doubling
Crystal
Pump Laser
Surelite-II-10
Q-Swith
ND: YAG Road
and Flash Lamp
Second Harmonic
Crystal

Figure 2.5. Schematic diagram of the Nd:YAG laser pumped dye laser

We have utilized the frequency-double ultraviolet (UV) output of a tunable dye laser (ND6000, Continuum, linewidth 0.08 cm^{-1}) to conduct R2PI spectroscopy on molecules or complexes in a supersonic jet. The dye laser, specifically designed for versatility, covers the entire UV-visible range by employing various dyes and frequency-doubling crystals. In the context of this thesis, electronic spectra of different molecular systems were measured using a range of dyes, including Rhodamine 590 (Rhodamine 6G), Rhodamine 610 (Rhodamine B), and Rhodamine 590-Rhodamine 610 mixture.

In this experiment, we employed the ND6000 continuum dye laser, which is pumped by the second harmonic output (532 nm) of an ND:YAG laser (Continuum, Surelite II-10, 10Hz, 10 ns). Two amplifier cells and a single oscillator make up the dye laser. The oscillator and preamplifier (1st amplifier) have a rectangular shape, whereas the final amplifier is constructed in a capillary form. The vertically polarized (532 nm) light from the YAG laser encounters beam splitter NS1, which reflects 5% of the total laser pulse energy toward the oscillator dye cell. The remainder travels through a series of dichroic mirrors and strikes beam splitter BS2. Reflecting 10% of the laser pulse energy toward the preamplifier cell, the rest of the laser pulse energy is transferred to the final amplifier dye cell. The dye laser cavity includes a beam expander, two gratings with 2400 line/mm grooving, a front mirror (referred to as the Moya mirror), and an oscillator dye cell. When light from the beam splitter BS1 enters the oscillator dye cell, it is first magnified using a telescopic lens. Upon interaction with the 532 nm light, the the dye molecule in the oscillator cell experiences excitation, resulting in stimulated emission. The oscillator dye cell emits a laser beam that undergoes expansion through the beam expander before reaching the grating. This process aids in selecting specific wavelengths from the wide output of the dye. The final UV output is generated using a KDP doubling crystal with a compensating crystal housed in the UV tracker (UVT).

The oscillator dye cell emits a laser beam that undergoes expansion through the beam expander before reaching the grating. This process aids in selecting specific wavelengths from the wide output of the dye. The ultimate UV output is produced by utilizing a KDP doubling crystal, accompanied by a compensating crystal housed in the UV tracker (UVT).

2.1.3.2 IR Optical Parametric Oscillator (OPO)/Optical Parametric Amplifier (OPA) System

The IR OPO/OPA system, developed by Laser Vision, produces an infrared laser beam with a wavelength range of 1.35 to 5 microns. This system is pumped by the 1064 nm output of an unseeded Nd:YAG laser (Continuum, Surelite II-10, 10Hz, 10 ns) with a typical pulse energy of 480 ±10 mJ. The schematic diagram of the optical arrangement for OPO/OPA system, which uses non-linear optical processes at several stages, is shown in Figure 2.6. In the OPO stage, a KTP crystal (Potassium Titanyl Phosphate, $KTiOPO_4$) serves as the non-linear crystal, while the OPA stage incorporates four KTA crystals (Potassium Titanyl Arsenate, $KTiOAsO_4$). Here is a quick explanation of the working concept of the IR OPO/OPA system.

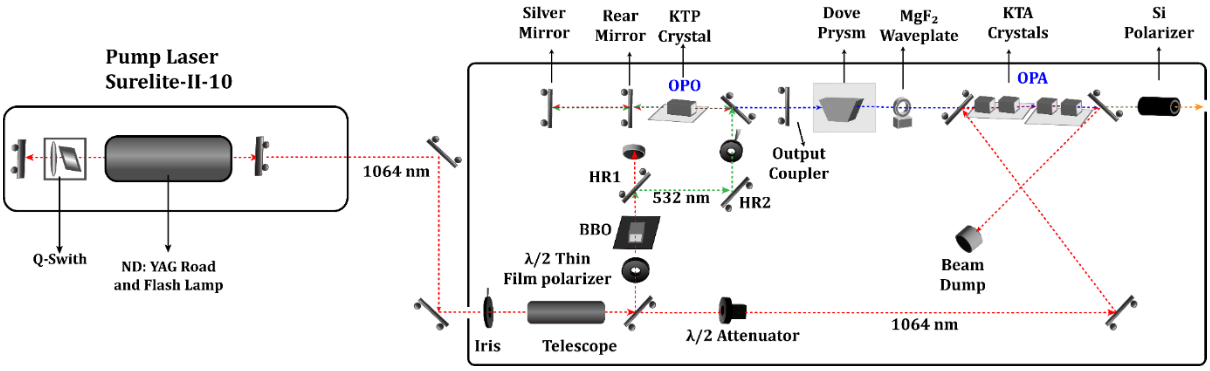
Silver Mirror
Rear Mirror
KTP Crystal
Dove Prysm
MgF_2 Waveplate
KTA Crystals
Si Polarizer
Pump Laser Surelite-II-10
OPO
OPA
1064 nm
Output Coupler
HR1
532 nm
HR2
BBO
Q-Swith
ND: YAG Road and Flash Lamp
λ/2 Thin Film polarizer
Beam Dump
1064 nm
Iris
Telescope
λ/2 Attenuator

Figure 2.6. Schematic diagram of Nd:YAG pumped OPO-OPA system IR laser (Laser Vison)

The 1064 nm pump beam from the unseeded Nd:YAG laser is focused employing a telescope and directed onto a beam splitter, which separates the horizontally polarized pump beam into two distinct beams. One beam, made of one-third of the total pump power, after frequency doubling through BBO (β-Barium borate) crystal, is guided towards the OPO stage, while the remaining part of the 1064 pump beam is mixed further with the idler output, which is generated at the OPO stage. In order to control the efficiency of the conversion from 1046 nm to 532 nm, one rotatable half-waveplate (attenuator) is positioned in front of the BBO crystal. During the OPO step, the KTP crystal is exposed to a frequency-doubled pump beam (532 nm). This causes the incoming photon to undergo optical parametric oscillation (OPO), splitting into two distinct photons that have different energies: the signal ($\boldsymbol{\omega_s}$) and idler ($\boldsymbol{\omega_i}$). The relation between the signal and idler beams is given by the energy conversion relationship and phase matching requirement, which gives $\boldsymbol{\omega_p = \omega_i + \omega_s}$, where ωp is the OPO pump frequency. It may be written as follows in terms of wavelength: $\frac{\mathbf{1}}{\boldsymbol{\lambda_p}} = \frac{\mathbf{1}}{\boldsymbol{\lambda_i}} + \frac{\mathbf{1}}{\boldsymbol{\lambda_s}}$. λp is 532 nm in this instance. The KTP crystal is positioned between two highly reflective mirrors in an optical resonator. To reflect back the idler beam that seeped through the rear mirror, a second silver (Ag) mirror is positioned just behind the first one. At the OPO step, tunable infrared light with a wavelength between 740 and 850 nm is produced by varying the angle of the KTP crystal with respect to the incident beam. The polarization of the idler beam is changed using a MgF2 waveplate before the OPA stage, which enables the OPA crystals to be adjusted horizontally.

For the purpose of rotating polarization from horizontal to vertical and adjusting the 1064 nm pump energy delivered to the OPA stage, a λ/2 wave plate and adjustable attenuator are placed into the 1064 nm beam path. The 1064 nm beam and the idler light from the OPO stage combine to form a combined beam that is directed toward the OPA stage. OPA systems are made with 4 KTP crystals, and the angles of these crystals are optimized for the maximum IR output. In the OPA stage, difference-frequency generation occurs, which can be represented as $\frac{1}{\lambda_i} - \frac{1}{1064} = \frac{1}{\lambda_I}$ (difference frequency mixing). Here, λ_I is the idler wavelength generated in the OPA stage. Similarly, the signal photon is also generated in the OPA stage, which can be represented as $\frac{1}{\lambda_S} = \frac{1}{1064} - \frac{1}{\lambda_I}$. Idler and signal photons, generated after the OPA stage, have different polarisations; the idler is vertically polarized, whereas the signal is horizontally polarized. These polarized lights are isolated from these combined outputs using a silicon (Si) polarizer. For the IR-UV double resonance spectroscopy described in the thesis, vertically polarized idler photons are used. In our experiment, the unseeded IR laser used has a typical resolution of approximately 2-3 cm^{-1}.

2.1.4 Experimental Set-Up

We conducted the experiments using a customized home-built jet-cooled REMPI-TOF mass spectrometer. The configuration comprises two vacuum chambers; one is bigger, and another is smaller, and they are interconnected by a skimmer of 2 mm diameter and 1-inch length (Beam Dynamics Inc.). A pulse valve (Parker, General valve, series 9) with 0.5 mm orifice driven by a pulse driver (Parker, IOTA ONE), is employed in the larger vacuum chamber. Two chambers are pumped with two separate diffstack diffusion pumps, further supported by two roughing pumps. The bigger chamber is connected with a 10-inch diffstak diffusion pump (OD250 Hind Hivac), which has the capacity to pump 3000L/s, and the supported roughing pump (FD-60, Hind Hivac) has a speed of 17L/s. On the other hand, a smaller chamber is pumped by a 4.5 inch diffstack diffusion pump (OD114, Hind Hivac) with a pumping speed 280L/s and the backing roughing pump (ED-21 , Hind Hivac) with a pumping speed 6L/s. Circulating water from a chiller (Refricon Hvac System) maintains the cooling of the upper side wall of the diffusion pump at a temperature of 18°C. The gate valve separates the vacuum chambers from the diffusion pumps, and a liquid nitrogen trap is strategically placed between them to eliminate contamination from the vapor of the diffusion pump oil. Cold cathode ionization gauges are utilized to measure the high vacuum in different chambers. Figure 2.7 provides a visual representation of the set-up.

In the ionization chamber, a two-stage ion source (Wiley-MacLaren design)[182] with a 1m long linear time-of-flight (TOF) tube (Jordan TOF Products) is positioned perpendicular to the molecular beam axis. At the top end of the tube, there is an 18 mm diameter dual Micro Channel Plate (MCP) detector (Jordon TOF products) enclosed in a small chamber, pumped by a 70L/s turbo molecular pump (Varian, Turbo -V81). This turbo is backed by a dry scroll pump (Varian, SH-110) having a speed of 1.5L/s. A TOF power supply (D-603, Jordon TOF Products) is utilized to apply high voltage to the detector, the repeller plate, and the extraction grid. A preamplifier (SRS, SR445A)

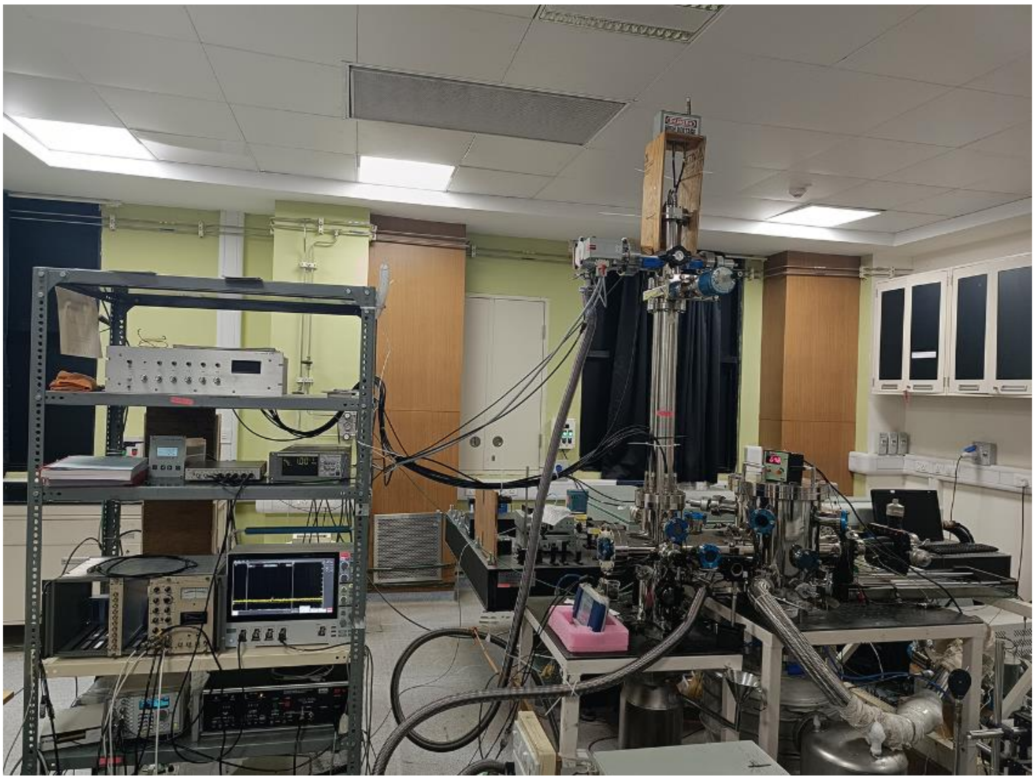

Figure 2.7. Photograph of the laboratory of home-built jet-cooled REMPI Time of Flight(TOF) mass spectrometry

amplifies the ion signal from the detector and sends it to a digital oscilloscope (Tektronix, DPO 4034, 350 MHz), which connects to a PC through a USB port. During scans, data acquisition and laser wavelength control are executed with a home-build LabView program (National Instrument, version 9.0). Temporal synchronization among the pulse valve and the lasers is achieved using a digital delay generator (BNC, Model-575).

2.1.5 Experimental Scheme

A schematic diagram of the experimental set-up is presented in Figure 2.8. In the experiment, two different sample holders made of stainless steel were used. Samples with lower vapor pressure are kept inside that sample holder, situated behind the pulse valve in the molecular beam chamber. Here, the sample was heated at 60-80°C with a heating coil. Conversely, the samples with very high vapor pressure are placed in the sample

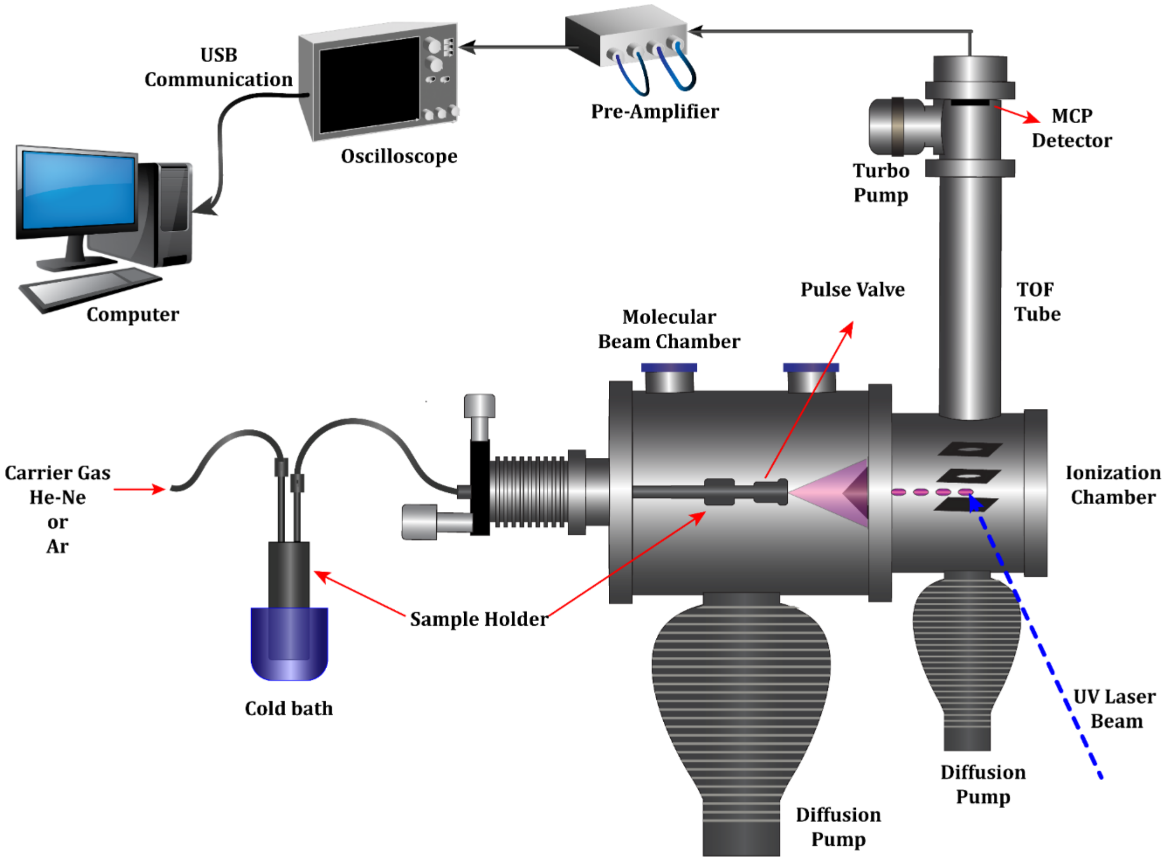
USB
Communication
Oscilloscope
Pre-Amplifier
MCP
Detector
Turbo
Pump
Computer
Pulse Valve
TOF
Tube
Molecular
Beam Chamber
Carrier Gas
He-Ne
or
Ar
Ionization
Chamber
Sample Holder
Cold bath
UV Laser
Beam
Diffusion
Pump
Diffusion
Pump

Figure 2.8. A schematic diagram of the experimental set-up

holder, which is kept outside the chamber. This sample holder is further cooled in a suitable freezing bath to control the vapor flow. The vapor generated from the sample holder is seeded in Ar or He-Ne carrier gas at 50-60 psig and undergoes expansion into a vacuum through the pulsed nozzle. Typical operating pressure in the molecular beam chamber and ionization chamber are 5×10^{-6} and 5×10^{-7} mbar, respectively. The pulse valve operates at 10 or 20Hz with a typical pulse duration of 180-200 µs. The resulting pulsed molecular beam, collimated through a skimmer, intersects perpendicularly with the pulse UV laser beam in the ionization chamber. In order to synchronize the laser beam with the molecular beam temporally, the digital delay generator initiates the pulse valve first, followed by firing the laser with a delay of a few hundred microseconds.

REMPI technique is employed to ionize the molecules with a tunable UV laser beam. The ions generated are then extracted and accelerated by applying voltages of +3060 V and +2800 V at the repeller plate (VA1) and extraction grid (VA2), respectively. The accelerating plate is maintained at ground potential. As the ions of different masses traverse the field-free TOF tube, they undergo separation and are subsequently detected by the MCP detector. The ion signal from the detector is amplified, usually by a factor of 125, using the preamplifier and transmitted to the oscilloscope. Data acquisition is done with a USB port from the oscilloscope to the PC.

A data acquisition program, which has been developed in the laboratory using LabVIEW, is utilized to acquire data from the oscilloscope and perform laser wavelength scanning. The time of flight for various ions can be determined through the equation:

$$t_2 = t_1 \times \sqrt{\frac{m_1}{m_2}} \tag{2.9}$$

Where t_1 and m1 represent the time of flight and mass of a reference molecule (whose values are known), respectively, while t2 and m2 are the time of flight and mass of the unknown sample, respectively. An oscilloscope visually represents ions of different masses in relation to their time of flight. The home-build LabVIEW program selects a specific time of flight of an ion and measures the signal amount at that particular wavelength. In the next step, this program changes the wavelength automatically, measures the signal amount at the selected region, and continues. At the same time, the program also captures the laser power with a piezoelectric sensor and power meter. Unwanted laser power fluctuations are removed by the normalization of the signal with respect to the laser power.

2.1.6 Spectroscopic Techniques

Using the supersonic jet approach, we investigated the structure of molecules or molecular complexes using a variety of spectroscopic techniques. We have observed mass-selected electronic spectroscopy of both single molecules and complexes using 1C-R2PI spectroscopy. UV-UV and IR-UV hole-burning spectroscopy were used to identify many conformers in the experiment. Additionally, high-resolution IR spectra were recorded utilizing the resonant ion dip infrared spectroscopy (RIDIRS) technique. We have integrated quantum chemical calculations with our experiments to discern the structures of the conformers of molecules or molecular clusters observed in the experiment. Various gas-phase spectroscopic techniques used in the experiment are briefly described below.

2.1.6.1 One color resonant two-photon ionization (1C-R2PI)

This technique has already been described in section 2.1.2.1.

2.1.6.2 UV-UV hole-burning spectroscopy

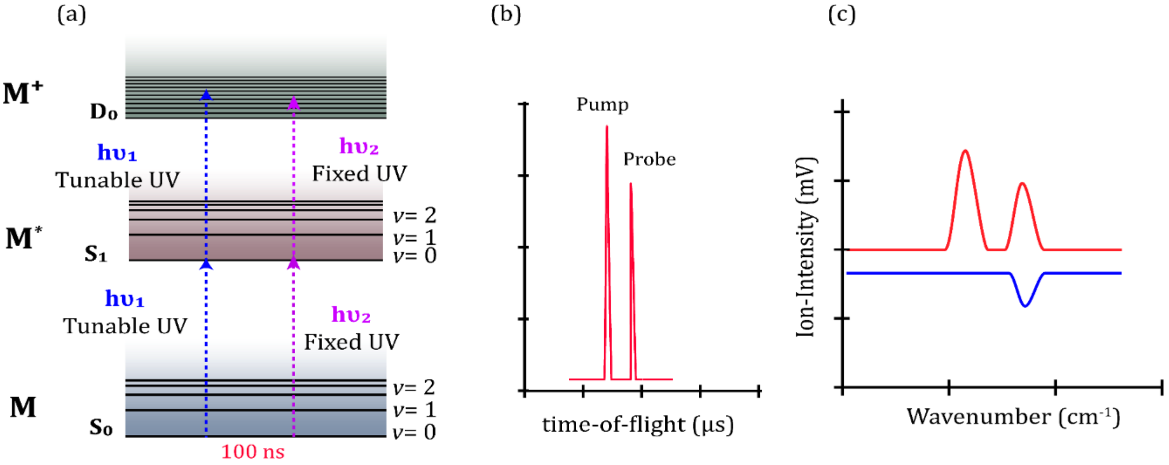

Figure 2.9. (a) Schematic diagram of UV-UV hole burning spectroscopy. (b) Mass spectra of a molecule due to pump and probe UV lasers. (c) UV-UV hole burning spectrum (Blue color) correspond to the R2PI spectra (Red color)

Experiments employing the UV-UV hole-burning spectroscopic techniques were conducted to distinguish the transitions in the high-resolution electronic spectra associated with different conformers.[186] Figure 2.9a illustrates a schematic diagram of this technique. In this process, two UV lasers are used, which propagate in opposite directions to each other. Both of them spatially overlap and intersect the molecular beam in a mutually perpendicular manner. UV laser beam of higher power (10Hz, pulse energy 0.5-0.6 mJ) , a pump laser, is systematically scanned in the wavelength range corresponding to the R2PI or electronic spectra of molecules or complexes. Another UV laser having relatively lower power (10Hz, pulse energy 0.2-0.3 mJ), termed as probe laser, is kept fixed at a particular transition of the electronic spectra. This probe laser is fired 100-120 ns later to the pump laser. All the vibronic transitions that originated from the same ground state exhibit depletion in the ion signal, as shown in the schematic UV-UV hole-burning spectra provided in Figure 2.9c.

2.1.6.3 Resonant ion-dip infrared spectroscopy (RIDIRS)

Figure 2.10a illustrates a schematic diagram of the RIDIRS technique. In this method, IR and UV laser beams are employed, and these counter-propagating beams spatially overlap and intersect the molecular beam in a mutually perpendicular fashion. The IR beam is focused with a CaF2 lens of 100cm focal length. The IR beam is fired 100-120 ns before the UV laser, and the digital delay generator controls the delay between these two lasers. While the UV wavelength is fixed on a specific transition in the electronic spectra of the molecule or complex, the IR laser is scanned. While the IR laser frequency resonates with a particular vibrational transition of the molecules/complexes in the ground electronic state, there is a depletion of the UV ion signal.

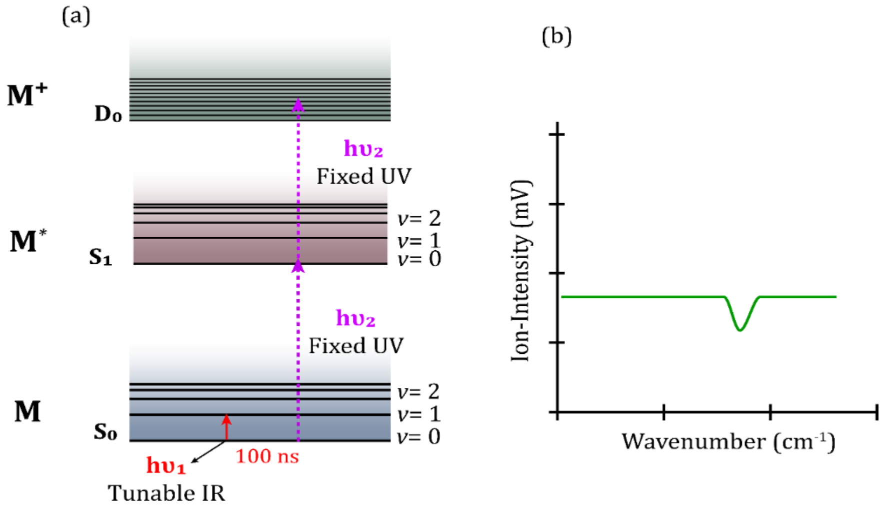

Figure 2.10. (a) Schematic diagrams of the RIDIRS technique and (b) an IR spectrum as a depletion of ion signal.

As a result, an IR spectrum is obtained as a depletion of the ion signal corresponding to a fixed electronic band belonging to a particular conformer. Figure 2.10b shows an arbitrary example of IR spectra recorded with the RIDIRS technique.

2.1.6.4 IR-UV hole-burning spectroscopy

This method furnishes analogous information to that obtained through UV-UV hole-burning spectroscopy. Illustrated in 2.11a is a schematic representation of this methodology. Compared to the RIDIRS technique, the key distinction lies here in the scanning source. In this case, the UV laser is scanned instead of the IR laser.[187-188] The IR

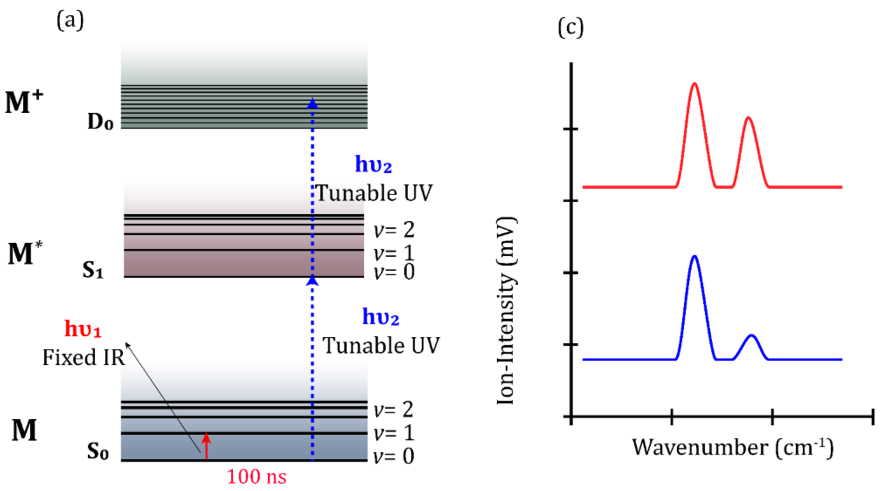

Figure 2.11. (a) Schematic diagrams of IR-UV hole burning spectroscopy and (b) IR UV hole-burning spectrum (blue) correspond to the R2PI spectra (red).

laser is kept at a specific vibrational frequency of a conformer of the molecule or complex. The UV laser is fired 80-120 ns after the IR laser. Through vibrational excitation induced by the IR laser, the population of a particular conformer is selectively burned, resulting in a reduced intensity in the UV transition for the selective bands of that particular conformer. Meanwhile, the intensity of the electronic band corresponded to other conformers are remained unaffected. Figure 2.11b shows a schematic of an IR-UV hole-burning spectrum.

2.2. Computational Methods

Spectra of molecules and complexes derived from the laser spectroscopy experiments conducted in the isolated gas-phase and the results obtained from quantum chemistry calculations complement each other. Quantum chemistry calculations prove invaluable in determining the structures of the molecules or complexes observed in the experiments. Frequently, experimental data from gas-phase spectroscopy are employed to validate the precision of the outcomes obtained from quantum calculations. In our investigation, we have used various quantum chemical calculation methods using program packages like Gaussian 09, Gamess 14, Orca 4.1, MultiWFN, NBO6 etc.[189-193]

2.2.1. Geometry optimization and frequency calculation

We performed ground state geometry optimization and harmonic vibrational frequency calculations for molecules and complexes using various levels of Density Functional Theory (DFT) as well as wave function theory using Gaussian 09 program package. We have employed several dispersion-corrected DFT functionals (M06-2X, B3LYP-D3, ωB97-XD)[194-197] and 2nd order Moller-Plesset Perturbation (MP2)[198-200] theory with Pople-type and Dunnings correlation-consistent basis-sets. Initial geometries of different conformers of the molecules or complexes are either chosen based on chemical intuition or generated using the Molclus program package.[201] We have restricted the optimization calculation using the "ULTRAFINE" numerical integration grid and "TIGHT" convergence criteria. Binding energies of various conformers of the weakly bound dimer complexes are corrected for the Basis Set Superposition Error (BSSE) and Zero-Point Vibrational Energy (ZPE). The BSSE correction was implemented using the counterpoise method developed by Boys and Bernardi.[202] The binding energies of the complexes are calculated as follows.

$$\Delta \mathrm{E_{BE}(AB)} = \mathrm{E_{AB}^{AB}(AB)} - \mathrm{E_{A}^{A}(A)} - \mathrm{E_{B}^{B}(B)} \qquad (2.10)$$

Where A and B are monomers when they are infinitely separated from each other. AB is the molecular complex made with A and B. $\Delta \mathrm{E_{BE}(AB)}$ is the energy of the complex AB calculated using a dimer basis set. $\mathrm{E_{A}^{A}(A)}$ and $\mathrm{E_{B}^{B}(B)}$ are the energy of the monomer calculated using their own basis set. As the monomers come together during complex formation, each monomer partially utilizes the basis functions of the other, resulting into additional stability to the molecular complex. This additional stabilization is referred to the BSSE. The BSSE corrected binding energy is calculated as:

$$\Delta E_{BE}^{CP}(\mathrm{AB}) = \mathrm{E}_{\mathrm{AB}}^{\mathrm{AB}}(\mathrm{AB}) - \mathrm{E}_{\mathrm{A}}^{\mathrm{AB}}(\mathrm{A}) - \mathrm{E}_{\mathrm{B}}^{\mathrm{AB}}(\mathrm{B}) \qquad (2.11)$$

Here, $\Delta E_{BE}^{CP}(\mathrm{AB})$ represents the counterpoise corrected binding energy of the molecular complex. $\mathrm{E}_{\mathrm{A}}^{\mathrm{AB}}(\mathrm{A})$ and $\mathrm{E}_{\mathrm{B}}^{\mathrm{AB}}(\mathrm{B})$ stand for the energies of A and B monomers using dimer basis sets, respectively.

Additional correction for the zero-point energy (ZPE) in the binding energy of the complexes is carried out using the following equation.

$$\Delta E^{ZPE}(\mathrm{AB}) = E^{ZPE}(\mathrm{AB}) - E^{ZPE}(\mathrm{A}) - E^{ZPE}(\mathrm{B}) \qquad (2.12)$$

We compared the experimentally measured IR frequencies with the theoretically predicted IR frequencies of likely low-energy conformers of the molecules or complexes to ascertain the structures of the complexes found in the experiment. Harmonic vibrational frequencies of the complexes studied here, obtained from quantum calculations using the Gaussian program, were scaled by a factor derived from the ratio of the experimental and calculated SH or OH stretching vibrational frequencies of the monomer.

2.2.2. Natural Bond Orbital (NBO) analysis

Nature and strength of various weak non-covalent interactions were analyzed qualitatively using NBO 6.0 program available within the Gaussian 09 program package. The NBO program was developed by Weinhold and co-workers. NBO program transforms the delocalized molecular orbitals into localized Natural Bond Orbitals (NBOs).[203] NBOs can be localized in one center, two centers or three centers. The mathematical algorithm of this program converts the input of atomic orbital basis functions into Natural Atomic Orbitals (NAOs). These NAOs generate Natural Hybrid Orbitals (NHOs) through linear combination, which are further combined linearly to make Natural Bond Orbitals (NBOs).

NBOs are two types: bonding NBO (Lewis type) and an antibonding NBO (Non-Lewis type). The bonding NBOs are electron occupied while antibonding NBOs are not. Weak non-covalent interactions, according to NBO formalism, involves the delocalization of electron density from the filled Lewis-type orbitals to vacant non-Lewis type orbitals. The strength of the hydrogen bonding interaction is evaluated by the second-order perturbation energy, given as:

$$E^{(2)}_{i\to j*} = q_i \frac{F(i,j)^2}{\varepsilon_j - \varepsilon_i} \tag{2.13}$$

Here, i and j* represent the donor and acceptor orbitals, respectively. *F(i,j)* is the off-diagonal NBO Fock matrix element.

2.2.3. Energy Decomposition Analysis

Binding energies of the non-covalently bonded complexes studied here were decomposed into different physically meaningful components utilizing the Localised Molecular Orbital-Energy Decomposition Analysis (LMO-EDA) method introduced by Su and Li and implemented in Gamess.[204] This approach employs a straightforward yet resilient basis set-insensitive method for the decomposition analysis of the interaction energies of the complexes. This LMO-EDA method dissects the total Khon-Sham interaction energy of the molecular complexes into electrostatic, exchange, repulsion, polarization, and dispersion components. The Hayes and Stone approach is used to separate the electrostatic, exchange, and repulsion components of the interaction energy.[34] The difference in exchange and correlation functions from the complex state to the monomer state is used to calculate the exchange and dispersion components of the interaction energy.

2.2.4. Quantum Theory of Atoms in Molecules (QTAIM) calculation

QTAIM is a very useful theoretical framework that provides a detailed and insightful understanding on bonding in molecular systems, especially for the molecular complexes formed by weak non-covalent interactions. It was developed by Richard F.W. Bader.[205-206] This theory was built upon the concept of the electron density distribution within a molecule. QTAIM utilizes the topology of the electron density to identify atoms within a molecule and characterize the interaction. The key concept in QTAIM is the idea of bond paths that connect the maximum electron density points called bond critical points (BCP). These BCPs characterize various features of the molecular structure, such as the position of the atoms and the nature of the chemical bond. This QTAIM calculation provides the possibility of the BCP in a non-covalent interaction path. Electron density on that BCP gives a qualitative idea of the strength of the non-covalent interactions.

Chapter 3

S−H⋯O Hydrogen Bond Can Win over O−H⋯S Hydrogen Bond: Gas-Phase Spectroscopy of 2-Fluorothiophenol⋯H_2O Complex

(Adapted with permission from "Metya S. and Das A., *J. Phys. Chem. A* **2022**, 126, 49, 9178–9189." Copyright© 2022 American Chemical Society.)

3.1. Introduction

In Chapter 1, we have discussed that hydrogen bonding is an indispensable component in the realm of biomolecules and materials [55, 57-59, 72, 76, 207-208] In recent times, the scope of research on hydrogen bonding has extended to unconventional hydrogen bonding involving carbon (C), sulfur (S), selenium (Se), phosphorous (P), halogens, etc.[1-2, 9, 68, 72, 130-131, 142, 162, 209-219] Such unconventional hydrogen bonding interactions play a significant role in the supramolecular assembly, drug design, material chemistry, and crystal engineering.[55, 207] Among all, sulfur-centered hydrogen bonding (SCHB) has gained much attention due to its unprecedented significance in biology and functional materials.[6, 154, 220-222] Sulfur-containing amino acids cysteine (Cys) and methionine (Met) emerge as key players in stabilizing secondary protein structures wherein sulfur functions as both hydrogen bond donor and acceptor.[141, 223] Sulfur is also abundant in drugs, vitamins, and antioxidants.[224-225] Sulfur-containing drugs and amino acids often interact with proteins, DNA, etc., through SCHB interactions.[216, 226-227] Various studies have found that S-H⋯O hydrogen bonding interactions between the S-H group of cysteine and the carbonyl oxygen of the backbone in proteins is more prevalent than any other type of hydrogen bonding interaction involving the S-H group present there.[6, 154] Very recently, Das and co-workers performed a comprehensive analysis of 156947 protein data bank (PDB) structures and found the presence of ~750 S−H⋯S hydrogen-bond interactions between the cysteine and methionine residues.[162] From Cambridge structural database (CSD) analysis, Allen et al. reported that S is more dominant as a hydrogen-bond donor than as an acceptor in organic crystals.[228] X-Ray crystallographic studies indicate the presence of various hydrogen bonding in biomolecules and materials, while IR and microwave spectroscopy techniques can demonstrate the inherent existence and strength of these non-covalent interactions. Due to the importance and significant abundance of the SCHB interactions, a growing number of studies are recently been reported in the literature to understand this interaction from gas-phase IR and microwave spectroscopy. However, most of these studies on the SCHB were focused on X−H⋯S, where sulfur acts as a hydrogen-bond acceptor and hydrogen bond donor atoms are conventional electronegative atoms i.e., X = O and N.[2, 5, 130-131, 141, 215-217] Interestingly, it has been found recently that the O−H⋯S and N−H⋯S hydrogen bonds are of similar strength as any conventional hydrogen bonds, i.e., O−H···N, O−H···O, N−H···O, etc.[2-4, 131, 229]

Surprisingly, spectroscopic investigation on the SCHBs with sulfur as a hydrogen-bond donor is sparse in the literature, although crystallographic studies reveal the dominance of the hydrogen-bond donor ability of sulfur over that as an acceptor. Nevertheless, there were a few very early as well as recent solution phase FTIR spectroscopy studies reporting the observation of the S−H···O, S−H···N, and S−H···S hydrogen bonds in several complexes of organic molecules with various solvents.[230-233] On the other hand, gas-phase studies on the SCHBs with sulfur as a hydrogen-bond donor are further limited in the literature. Wategaonkar and co-workers studied the S−H···S hydrogen bond in H_2S dimer and the S−H···O hydrogen bond in H_2S···CH_3OH, H_2S···Et_2O, H_2S···Bu_2O, and H_2S···dioxane complexes using VUV ionization detected IR-predissociation spectroscopy.[7-8] Lobo et al. reported the observation of the S−H···O hydrogen bond in 2-phenyl-ethanethiol···Et_2O complex using IR/UV double resonance spectroscopy.[9] The S−H···O hydrogen bond in a dipeptide Ac-Phe-Cys-NH_2 was reported by Rijs and co-workers employing various gas-phase spectroscopic techniques.[223] Recently, Das and co-workers probed the S−H···S hydrogen bond in 2-cholorothiophenol···Me_2S complex using UV/UV and IR/UV double resonance spectroscopy techniques.[162] There are reports of very few microwave spectroscopy studies on the SCHB involving sulfur as a hydrogen-bond donor.[234-236]

In this chapter, we have investigated the S−H···O hydrogen bond in the 2-FTP (2-fluorothiophenol)···H_2O complex using resonant 2-photon ionization (R2PI), UV−UV hole-burning spectroscopy, and resonant ion-dip infrared (RIDIR) spectroscopy combined with quantum chemistry calculations. Here, we have studied the complex of 2-FTP instead of thiophenol as the ultrashort S1 state lifetime (50 fs) of thiophenol prohibits the measurement of the R2PI spectra.[237] *Ortho* substitution of the fluorine atom on thiophenol significantly increases the S1 state lifetime of 2-FTP to 12.3 ps and favors the measurement of the R2PI (electronic) spectrum of 2-FTP.[238] The present spectroscopic investigation on the 2- FTP···H_2O complex is quite intriguing as it allows us to study the competition between the S−H···O and O−H···S hydrogen bonds due to the dual nature of H_2O as hydrogen-bond donor and acceptor. Quantum chemical calculations such as natural bond orbital (NBO), non-covalent interaction index (NCI), atoms in molecules (AIM), and energy decomposition analysis (EDA) are performed to probe the nature of various interactions present in the complex.

3.2. Result and Discussion

3.2.1. Conformational Landscape of 2-FTP···H_2O complex

Probable conformers of 1:1 complex of 2-FTP and H_2O are predicted from wave function theory as well as DFT calculations. The 2-FTP monomer has two distinct conformers, i.e., is and trans, in terms of the orientation of the S−H group toward the F atom and away from the F atom, respectively. Figure 3.1(a) shows the cis and trans conformers of the 2-FTP monomer optimized at the MP2/6-311++G (d, p) level of theory. cis-2-FTP has been found to be more stable than trans-2-FTP by 4.76 kJ mol^{-1} at the MP2 level of calculation.

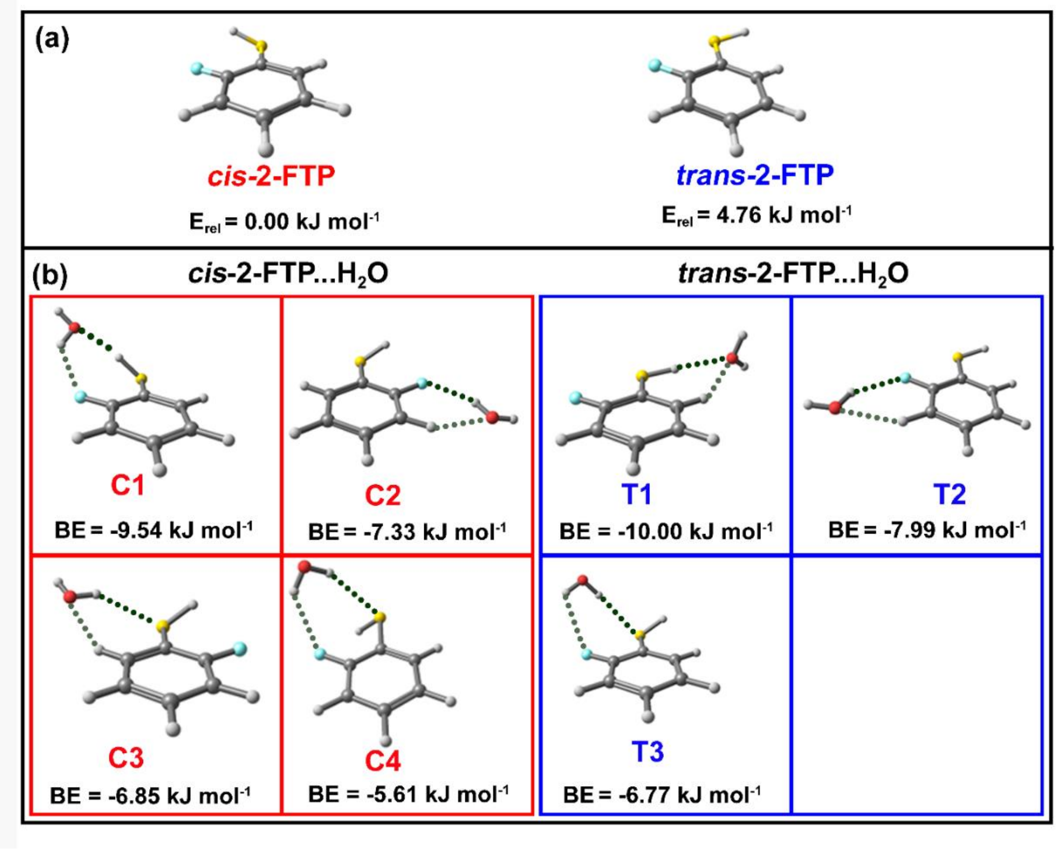
(a)
cis-2-FTP
E_{rel} = 0.00 kJ mol^{-1}
trans-2-FTP
E_{rel} = 4.76 kJ mol^{-1}
(b)
cis-2-FTP...H_2O
trans-2-FTP...H_2O
C1
BE = -9.54 kJ mol^{-1}
C2
BE = -7.33 kJ mol^{-1}
T1
BE = -10.00 kJ mol^{-1}
T2
BE = -7.99 kJ mol^{-1}
C3
BE = -6.85 kJ mol^{-1}
C4
BE = -5.61 kJ mol^{-1}
T3
BE = -6.77 kJ mol^{-1}

Figure 3.1. Various low energy conformers of the (a) 2-FTP monomer and (b) 2-FTP···H2O complex optimized at the MP2/6-311++G(d,p) and cp-MP2/6-311++G(d,p) levels of theory, respectively. E_{rel} stands for the relative electronic energy of the monomer while BE denotes the binding energy of the complex. Both E_{rel} and BE are zero-point energy corrected while BE is additionally counterpoise (cp) corrected at every step during the geometry optimization.

A few low-energy conformers of the 2-FTP···H_2O complex optimized at the cp-MP2/6-311++G (d,p) level of theory are provided in Figure 3.1(b). Four cis conformers of the complex obtained from the calculation are named C1, C2, C3, and C4, while three trans conformers of the complex are termed T1, T2, and T3. The T1 conformer is the global minimum, although the binding energies of the C1 and T1 are quite close to each other. The primary interaction presents in both C1 and T1 is S–H···O hydrogen bond, while O–H···F and C–H···O hydrogen bonds constitute weak secondary interactions in C1 and T1, respectively. Both the C2 and T2 conformers are stabilized by the O–H···F and C–H···O hydrogen bonds. It could be noted that the O–H···S hydrogen-bonded conformers (C3, C4, and T3) are less stable than the S–H···O hydrogen-bonded structures (C1 and T1). Both the C4 and T3 structures are additionally stabilized by a weak O–H···F hydrogen bond, while the secondary interaction in C3 is a C– H···O hydrogen bond.

Table 3.1. Zero-point energy (ZPE) and BSSE corrected binding energy (BE) calculated at different levels of theory for all the conformers of 2FTP···H_2O complex

		BE (kJ.mol^{-1})						
Level of theory		**C1**	**C2**	**C3**	**C4**	**T1**	**T2**	**T3**
6-311++G(d, p)	cp-MP2	-9.54	-7.33	-6.85	-5.61	-10.00	-7.99	-6.77
	cp-M062X	-12.24	-11.34	-11.08	-8.00	-12.75	-11.29	-9.05
	cp-B3LYP-D3	-12.86	-11.94	-10.20	-8.87	-14.76	-12.82	-10.65
	MP2	-7.28	-5.05	-5.53	-4.23	-8.29	-6.60	-4.06
	B3LYP-D3	-10.48	-10.20	-8.17	-2.64	-11.39	-11.15	-7.52
aug-cc-pVTZ	cp-M062X	-10.35	-8.97	-10.00	-8.48	-11.40	-9.44	-9.65
	cp-B3LYP-D3	-11.12	-10.42	-9.62	-9.11	-12.27	-11.19	-10.28
cc-PVTZ	cp-MP2	-7.63	-7.20	-6.79	-4.80	-11.02	-7.95	-6.38
	CCSD(T)*	-12.16				-14.71		

* BE calculated at CCSD(T) using the single point energy calculation with the optimized geometry at cp-MP2/6-311++G(d,p) level of theory. This BE is not ZPE corrected.

Although fluorine is known to be a poor hydrogen-bond acceptor,[239] it is noteworthy that the fluorine hydrogen bonding is quite important in the stability and structural preferences of microhydrated complexes of fluorinated compounds. It was reported that the O–H···π hydrogen bonding motif in a nonplanar benzene···H_2O complex switched to a cyclic O−H··· F and C−H···O hydrogen bonding network forming planar structures in 1:1 complexes of H_2O and fluorobenzenes except hexafluorobenzene.[240-243] Observation of a cooperative O−H···O−H···F−C hydrogen-bonded structure was reported for the o-fluorophenol···H_2O complex by Chakraborty and co-workers.[244] A similar cyclic hydrogen-bonded network consisting of the O−H···O and O−H···F hydrogen bonds were observed in the complexes of fluorinated ethanols with H_2O.[234] A combination of the O−H···F and C−H···O hydrogen bonds was reported in the complexes of p-fluoroacetylene and p-fluorostyrene.[245-246] Robertson and co-workers reported the observation of O−H···X (X = F, Cl, Br) hydrogen bonds in hydrated clusters of halolethylbenzenes ($PhCH_2CH_2X$).[247] Observation of the O−H···F hydrogen bond in difluoromethane···H_2O complex was reported by Caminati *et al.*[304]

The binding energies of all the conformers of the 2-FTP···H_2O complex calculated at the cp-MP2 and MP2 levels as well as various DFT levels with and without cp corrected surface, are provided in Table 3.1. It has been found from all the levels of calculation that T1 is the global minimum. Single point energy calculation at the CCSD(T)/cc-pVTZ level on the cp-MP2/6-311++G (d,p) optimized geometries of the two major conformers C1 and T1 also shows that T1 is more stable than C1 by 1.55 kJ mol^{-1} (Table 3.1). The basic trend of the binding energies of all the conformers at various levels of the calculation is mostly similar.

A few important geometrical parameters of the 2-FTP monomer and the two significant conformers C1 and T1 of the 2-FTP···H_2O complex calculated at the cp-MP2/6-311++G (d,p) level of theory are listed in Table 3.2. It is noteworthy that the S−H group in cis-2-FTP and trans-2-FTP is out of the plane by 33° and 15°, respectively, considering the ∠C−C−S− H dihedral angle (Table 3.2). The nonplanarity of the S−H group in the C1 conformer increases to 46° while the same in the T1 conformer decreases to 7°. cis-2-FTP has a very weak intramolecular S−H···F hydrogen bonding interaction, which is missing in the trans-2-FTP monomer. Apart from the very poor hydrogen-bond acceptor property of fluorine, the ∠S−H···F of 102° and S−H···F hydrogen-bond distance of 245 pm indicate the very weak nature of the S−H···F hydrogen bond present in cis-2-FTP (Table 3.2).[239] The S−H···O hydrogen bond distance and ∠S−H···O in the C1 and T1 conformers of 2-FTP···H_2O fall in the regular domain of the hydrogen bond (Table 3.2). The O−H···F hydrogen bond in C1 and C−H···O hydrogen bond in T1 are identified as weak hydrogen

Table 3.2. Detailed geometrical parameters for the most stable conformers of the monomers and complexes calculated in cp-MP2/6-311++G (d,p) level of theory.

Geometrical Parameters	**2-FTP**		**2-FTP···H2O**	
	cis	trans	C1	T1
$r_{S[7]-H[8]}$ (pm)	133.57	133.60	133.88	133.82
$\Delta r_{S[7]-H[8]}$ (pm)	-	-	0.31	0.22
$r_{S[7]-C[6]}$ (pm)	176.86	176.89	177.03	176.72
$l_{O[10]-H[11]}$ (pm)	-	-	95.93	96.02
$l'_{O[10]-H[12]}$ (pm)	-	-	96.08	96.03
$d_{S[7]-H[8]\cdots O[10]}$ (pm)	-	-	223.24	231.48
$d_{S[7]\cdots O[10]}$ (pm)	-	-	355.10	364.99
$d_{O[10]-H[12]\cdots F[9]}$ (pm)	-	-	227.79	-
$d_{S[7]\cdots F[9]}$ (pm)	302.05	291.31	304.06	291.66
$d_{S[7]-H[8]\cdots F[9]}$ (pm)	245.48	-	265.41	-
$d_{C[5]-H[14]\cdots O[10]}$ (pm)	-	-	-	267.82
$\angle S[7]-H[8]\cdots O[10]$ (°)	-	-	167.4	175.1
$\angle \mathrm{C}[6]-S[7]-H[8]$ (°)	96.1	94.5	96.5	94.6
$\angle \mathrm{H}[11]-O[10]-H[12]$ (°)	-	-	104.6	103.8
$\angle \mathrm{S}[7]-H[8]\cdots F[9]$ (°)	101.6	-	93.3	-
$\angle \mathrm{O}[10]-H[12]\cdots F[9]$ (°)	-	-	127.5	-
$\angle \mathrm{C}[5]-H[14]\cdots O[10]$ (°)	-		-	148.9
$\angle \mathrm{C}[1]-C[6]-S[7]-H[8]$ (°)	33.3	165.2	46.2	172.6
$\angle \mathrm{C}[1]-C[6]-S[7]\cdots O[10]$ (°)	-	-	41.6	172.8

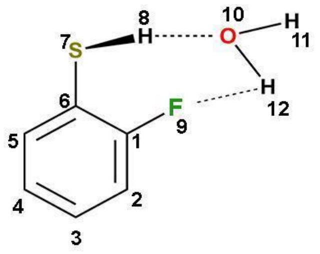

cis-2-FTP...H2O

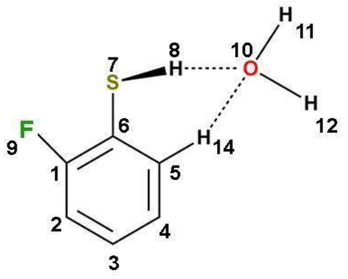

trans-2-FTP...H2O

3.2.2. Electronic Spectra of the 2-FTP monomer and 2- FTP⋯H_2O complex

The time of flight (TOF) mass spectrum of mixed vapor of 2-FTP and H_2O measured at 35221 cm^{-1} employing 1C-R2PI spectroscopy is shown in Figure 3.2. The mass spectrum shows the peaks for only the 2-FTP monomer and 2-FTP⋯H_2O dimer. The vapor pressure of both 2-FTP and H_2O was controlled to minimize the formation of higher-order clusters. Mass-selected electronic spectra of the 2-FTP monomer and 2-FTP⋯H_2O complex measured in argon (Ar) carrier gas using the 1C-R2PI technique are given in Figure 3.3 panels a and b, respectively. The electronic spectrum of the 2-FTP monomer was reported earlier, and only the electronic origin band of the monomer (35555 cm^{-1}) has been shown here. It was reported by Kim and co-workers that the electronic band presented here in Figure 3.3(a) was due to the cis-2-FTP monomer.[237] They assigned the S1 vibronic bands observed in the R2PI spectrum to the cis conformer of the 2-FTP monomer using detailed Franck–Condon analysis based on the DFT calculations. We have also determined the cis–trans isomerization barrier in 2-FTP at the MP2 as well as several DFT level calculations and found that the barrier height was in the range of 180–260 cm^{-1} (Table 3.3). Such a low isomerization barrier could be

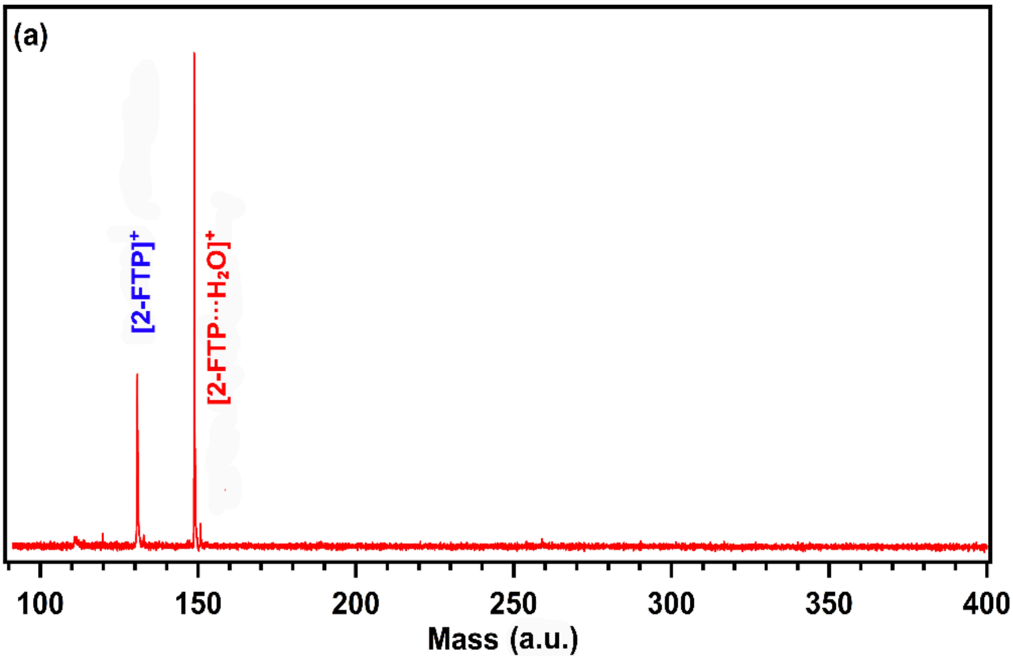

Figure 3.2. TOF Mass spectrum of mixed vapor of 2-FTP and H_2O measured at 35221 cm^{-1} (origin band of the 2-FTP⋯H_2O complex) employing 1C-R2PI spectroscopy.

responsible for the complete collisional relaxation of trans-2-FTP to cis-2-FTP.[248]

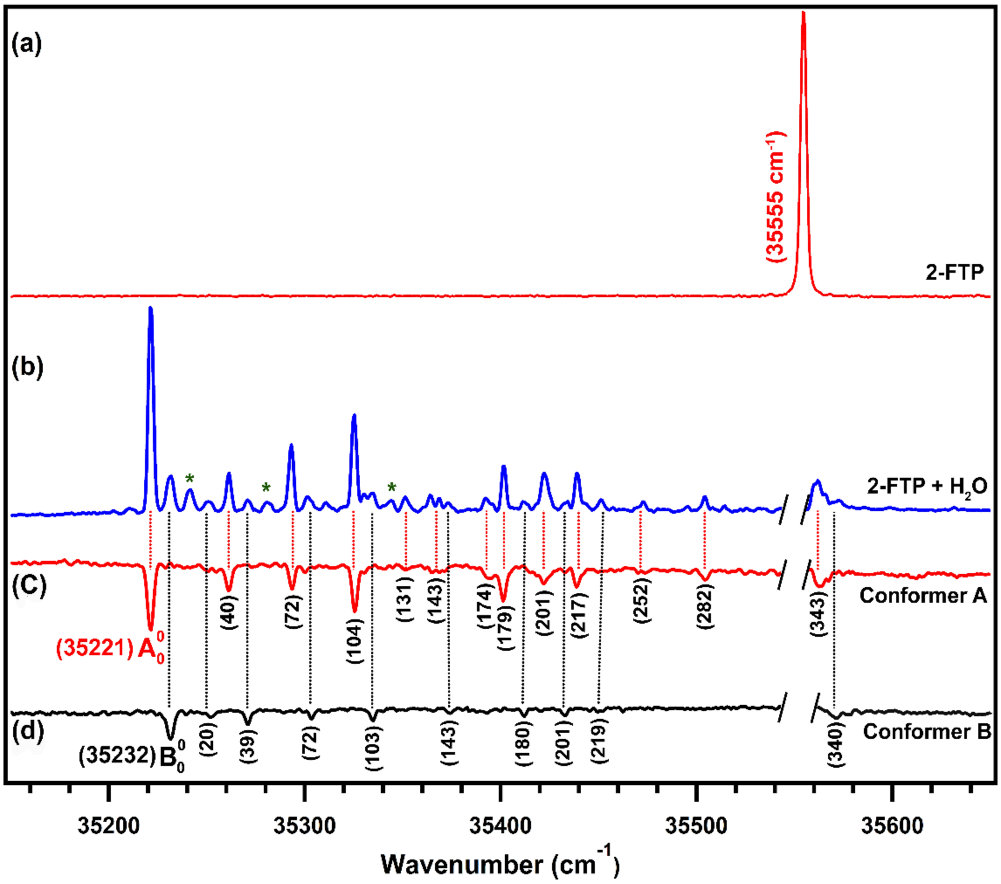

Figure 3.3. Mass-selected electronic spectra of the (a) cis-2-FTP monomer showing the origin band and (b) 2-FTP···H_2O complex measured by 1C-R2PI technique. (c,d) UV–UV hole-burning spectra of the conformers A and B of the 2-FTP···H_2O complex measured by probing the 35221 (A_0^0) and 35232 (B_0^0) cm^{-1} bands, respectively, in the electronic spectrum. The number in the parentheses below each band of the hole-burning spectra in parts c and d denotes the intermolecular vibrational frequency of the complex in cm^{-1}. A tentative assignment of the low frequency intermolecular vibration is provided in Table 3.4. Assignment of the bands marked with asterisks in Figure 3.3(b) could not be done through UV–UV hole-burning due to their weak intensity

Table 3.3. Energy barrier between the cis and trans conformers of the 2-FTP monomer

Level of theory	Energy barrier (cm-1)
MP2/6-311 ++ G (d,p)	267
M06-2X/6-311++ G (d,p)	191
ωB97X-D/6-311 + G (d,p)	183

The origin band for the S1 ← S0 transition of the 2-FTP⋯H_2O complex (35221 cm^{-1}) displayed in Figure 3.3(b) is red-shifted from that of the 2-FTP monomer by 334 cm^{-1}. The red-shift in the origin band transition of the complex with respect to that of the monomer signifies that the stability of the complex with respect to the monomer in the S1 state is more than that in the S0 state. Multiple low-frequency bands (Figure 3.3 (b)) observed in the higher energy side of the origin band of the complex are assigned by the

Table 3.4. Observed and calculated low-frequency intermolecular vibrations of the T1 and C1 conformers of the 2-FTP⋯H_2O complex. Excited state (S1) vibrational frequencies are calculated at the CIS/6-311++G(d,p) level of theory using the optimized geometry obtained at the cp-MP2/6-311++G(d,p) level of theory

Low-frequency intermolecular vibrations (cm^{-1})					
Conformer A			**Conformer B**		
Observed	Calculated (T1)	Assignment	Observed	Calculated (C1)	Assignment
35221		A_0^0	35232		B_0^0
	24	α	20	27	α'
40	39	β	39	41	β'
72	85	γ	72	82	γ'
104	98	δ	103	89	δ'
	122	ε		107	ε'
131		(β+γ)	143		2γ'
143		2γ	180		(γ'+δ')
174		(γ+δ)		188	ζ
179	179	ζ	201		2δ'
201		2δ	219		3γ'
217		3γ	340		(2γ'+2δ')
252		(β+2δ)			
282		4γ			

UV–UV hole-burning spectra are presented in Figure 3.3(c,d). Figure 3.3(c) exhibits the UV–UV hole-burning spectrum of conformer A of 2-FTP···H2O by probing the origin band (A_0^0) at 35221 cm^{-1}. The low-frequency vibronic bands in the spectrum shown in Figure 3.3(c) are tentatively assigned as several intermolecular modes of the complex and their overtones, as well as combination bands. Figure 3.3(d) shows the UV–UV hole-burning spectrum of the conformer B of 2-FTP···H2O by probing the origin band (B_0^0) at 35232 cm^{-1}. Interestingly, the low-frequency intermolecular vibrations riding on B0 0 are quite similar to those observed for the conformer A. Assignment of the low-frequency intermolecular vibrations of the conformers A and B provided in Figure 3.3(c) and 3.3(d), respectively, is done with the help of the S1 state vibrational frequency calculation of the T1 and C1 conformers performed at the CIS/6-311++G(d,p) level of theory. A comparison

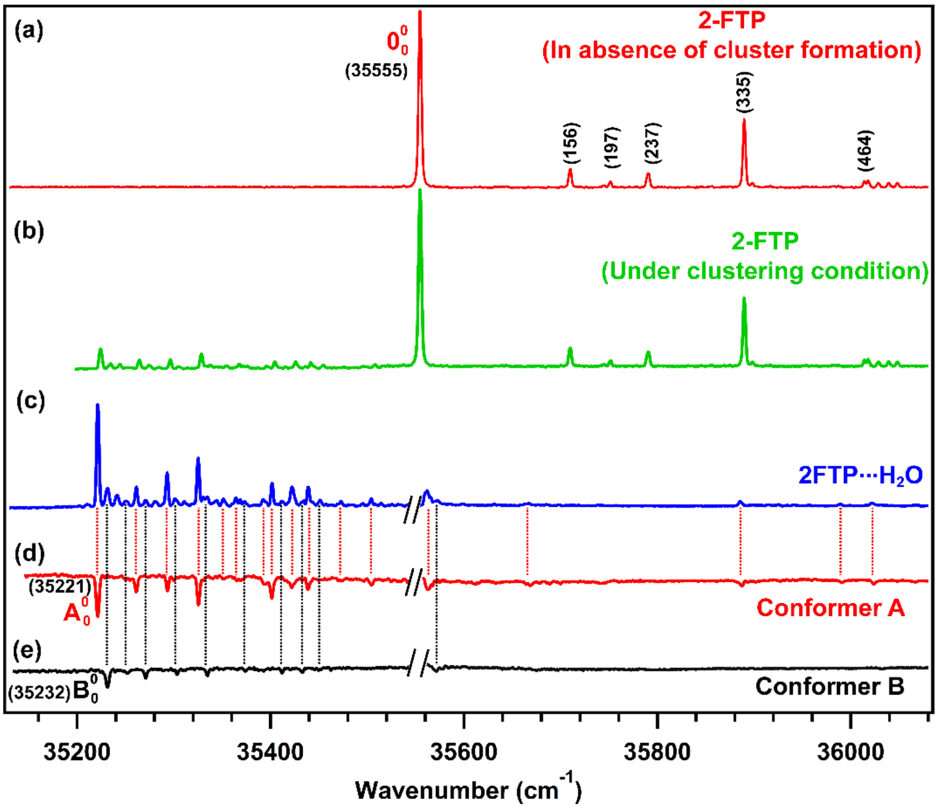

Figure 3.4. Electronic spectra measured at the (a) 2-FTP monomer mass channel (in the absence of cluster formation with H2O), (b) 2-FTP monomer mass channel (under the clustering condition), and (c) 2-FTP···H2O mass channel. (d) and (e) are the UV-UV hole-burning spectra of the 2-FTP···H2O complex.

of the observed low-frequency vibrations of the conformers A and B with the predicted S1 state intermolecular vibrations of the T1 and C1 conformers of 2- FTP···H2O is provided in Table 3.4.

It could be noted that a few very weak bands, marked by asterisks, present in the R2PI spectrum in Figure 3.3(b) did not give any depletion in the hole-burning spectrum of either conformer A or conformer B. Thus, these weak bands belong to a different species other than conformers A and B. However, it was found difficult to obtain any hole-burning spectrum by probing any one of these weak bands, and hence, we did not make any assignment for these bands. We have also measured the electronic spectrum of 2-FTP···H_2O further in the blue side (~500 cm^{-1}) of the origin band of the 2-FTP monomer to search for any other conformer of the complex. Figure 3.4(c) shows the complete electronic spectrum of 2-FTP···H_2O covering the extended blue region. A few very weak bands observed in the blue side of the 2-FTP monomer origin band were assigned to conformer A of 2-FTP···H_2O through UV– UV hole-burning spectroscopy (Figure 3.4(d)).

To check for the fragmentation of the 2-FTP···H_2O dimer and its higher order clusters upon ionization, we have also measured the electronic spectrum in the 2-FTP monomer mass channel under the clustering conditions. A comparison of the electronic spectra measured in the 2-FTP···H_2O, 2-FTP monomer (under clustering conditions), and pure 2-FTP monomer (while cluster is not forming) mass channels has been displayed in Figure 3.4(c) 3.4(b), and 3.4(a), respectively. It is obvious from the comparison that the bands, which are on the red side of the 2-FTP monomer origin and appear in the 2-FTP···H_2O mass channel, are also present in the electronic spectrum obtained in the 2-FTP monomer mass channel under clustering conditions (Figure 3.4(b,c)). The bands,

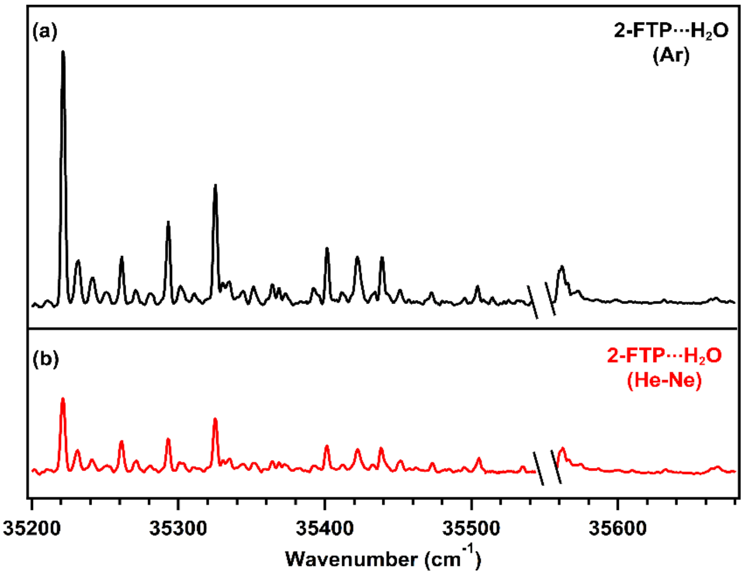

Figure 3.5. Comparison of the electronic spectra of the 2-FTP···H_2O complex recorded by 1C R2PI technique using (a) argon (Ar) and (b) He-Ne (70%-30%) carrier gases.

which are in the blue side of the 2-FTP monomer origin and appearing in the 2-FTP···H_2O mass channel, are so weak that they are not even present in the 2-FTP monomer mass channel under clustering conditions. Thus, there is an efficient fragmentation of the 2-FTP···H_2O dimer into the 2-FTP monomer upon ionization of the dimer. It is unlikely, considering the overall results, that there is fragmentation of any higher order clusters, which appear in the 2-FTP monomer mass channel.

We have further measured the electronic spectrum of the 2- FTP···H_2O complex using 30%He-70%Ne carrier gas and compared the spectrum with that measured using Ar carrier gas. It is found from the comparison provided in Figure 3.5 that the two electronic spectra measured using different carrier gases are mostly identical. Thus, there was no conformation relaxation of the 2-FTP···H_2O complex due to the use of Ar as a carrier gas.

3.2.3. IR Spectra of the 2-FTP Monomer and 2-FTP··· H_2O Complex

IR spectrum of the cis-2-FTP monomer is measured in the S−H stretching frequency region, while the IR spectra of the 2-FTP···H_2O complex are measured in both the S−H and O−H stretching frequency regions using RIDIR spectroscopy. Figure 3.6(a) shows the IR spectrum of the cis-2- FTP monomer by probing the 0_0^0 band (35555 cm^{-1}) of the monomer in the electronic spectrum. The S−H stretching frequency of the cis-2-FTP monomer is observed at 2625 cm^{-1}. It should be noted that the intensity of the S−H stretching transition is very weak. The theoretical intensity of the S−H transition in the 2-FTP monomer is found ~1 km/mol at the MP2/6-311++G(d,p) level of theory. To detect this low-intensity transition in the IR spectrum, we have averaged 15 individual S−H scans, each of which is already averaged over 256 laser shots. Robertson and co-workers reported the observation of the weak S−H transition of 2-phenylethanethiol at 2590 cm^{-1} in the gas-phase using IR/UV double resonance spectroscopy.[9]

Figure 3.6(c,e) displays the IR spectra of the 2-FTP···H_2O complex measured in the S−H and O−H stretching regions by probing the A_0^0 (35221 cm^{-1}) and B_0^0 (35232 cm^{-1}) bands in the electronic spectrum. Theoretical IR spectra of the T1 and C1 conformers of 2-FTP···H_2O calculated at the cp-MP2/6- 311++G(d,p) level of theory are provided in Figure 3.6 panels (d) and (f), respectively. The S−H frequency in the complex

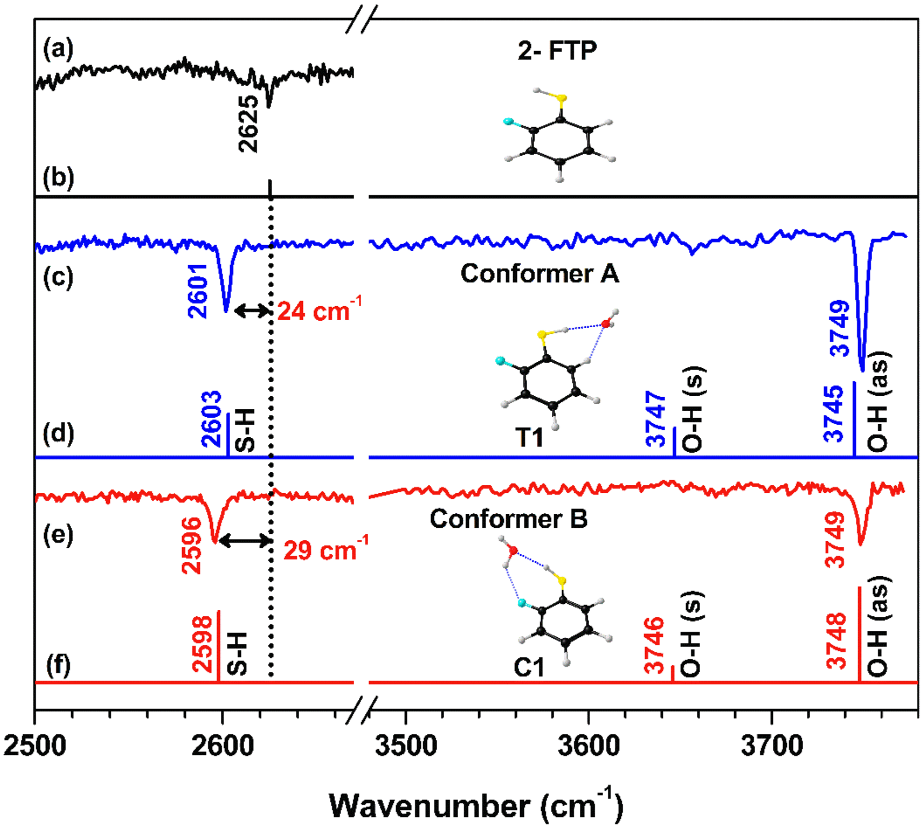

Figure 3.6. IR spectra of the (a) 2-FTP monomer, (c) conformer A of 2-FTP···H_2O, and (e) conformer B of 2-FTP···H_2O measured by RIDIR spectroscopy. (b,d,f) Theoretical scaled IR stick spectra of the 2-FTP monomer, T1, and C1 conformers of the 2-FTP···H_2O complex, respectively, calculated at the cp-MP2/6-311++G(d,p) level of theory. O−H (s) and O−H (as) in parts (d) and (f) denote symmetric and asymmetric O−H stretching frequencies, respectively. The scaling factors for the harmonic S−H and O−H frequencies are discussed in the text.

obtained from the harmonic calculation is scaled by a factor of 0.9375 derived from the ratio of the experimental (2625 cm^{-1}) and MP2/6- 311++G(d,p) level calculated (2800 cm^{-1}) S−H stretching frequency of the 2-FTP monomer. Similarly, the theoretical O−H frequencies in the complex obtained from the harmonic frequency calculations are multiplied by a scaling factor of 0.9378 derived from the ratio of the experimental asymmetric O−H stretching frequency (3756 cm^{-1}) of free H_2O reported in the literature and that obtained from the MP2/6-311++G(d,p) level of calculation.[249-250] There is a nice agreement between the experimental and theoretical IR spectra of the two conformers of the complex. The theoretical scaled IR spectrum of the 2-FTP monomer is also provided in Figure 3.6(b). It has been shown recently that the cp-MP2 level of theory reproduces well the experimental IR frequencies of the sulfur-centered hydrogen-bonded complexes.[7, 251-252]

The 2601 cm^{-1} band in the IR spectrum of the conformer A provided in Figure 3.6(c) is assigned to the transition of the S−H group, which is hydrogen bonded with the oxygen atom of the H_2O molecule in the T1 conformer of 2-FTP⋯H_2O. The IR band of the conformer B of 2-FTP⋯H_2O appearing at 2596 cm^{-1} arises due to the hydrogen bonded (S−H⋯O) S−H group present in the C1 conformer [Figure 3.6(e)]. The hydrogen-bonded S−H frequency values in the T1 and C1 conformers are red-shifted by 24 and 29 cm^{-1} , respectively, from the frequency of the free S−H group in the 2-FTP monomer.

The 3749 cm^{-1} band observed in the IR spectra of both the conformers A and B provided in Figure 3.6 panels (c) and (e), respectively, is assigned to the asymmetric (as) O−H stretch of H_2O in 2-FTP⋯H_2O. The symmetric (s) O−H stretching vibration of H_2O in 2-FTP⋯H_2O, which is not observed in either of the IR spectra of the conformers A and B due to its weak intensity, appears weakly at 3647/3646 cm^{-1} in the theoretical IR spectra provided in Figure 3.6(d,f). The absence of the weak symmetric O−H stretching vibration was also reported earlier in the gas-phase IR spectrum of the phenol⋯H_2O complex.[249] The asymmetric and symmetric O−H stretching vibrations in the gas-phase IR spectrum of free H_2O appear at 3756 and 3658 cm^{-1} , respectively.[249-250] It should be noted that both phenol and 2-FTP act as hydrogen-bond donor while H_2O acts as a hydrogen-bond acceptor in phenol⋯H_2O as well as 2-FTP⋯H_2O complexes. Both the O−H groups of H_2O in the T1 and C1 conformers are mostly free, although one of the O−H groups in C1 makes a very weak O−H⋯F hydrogen bond suggested by the corresponding hydrogen-bond parameters provided in Table 3.2

A comparison of the experimental IR spectra of the two observed conformers of 2-FTP⋯H_2O with the theoretical IR spectra of the seven low-energy conformers of the complex calculated at the cp-MP2/6- 311++G(d,p) level of theory has been provided in Figure 3.7. It is apparent from the comparison that the two observed conformers of 2-FTP⋯H_2O are T1 and C1 only. The S−H group in all the conformers of 2-FTP⋯H_2O except T1 and C1, as seen in Figure 3.7(c) and 3.7(e), are free, and hence, the IR intensity of the free S−H vibration of those conformers is extremely weak. The intensity of the IR band of the free S−H group of these conformers is multiplied by a factor of 100 to make it visible in the IR spectra provided in Figure 3.7. The IR frequency of the free S−H group in the conformers (C2, C3, C4, T2, and T3) of 2-FTP⋯H_2O appears at the position similar to that in the 2-FTP monomer (2625 cm^{-1}). Here, the S–H IR band rather than the O–H band acts as a clear diagnostic marker for the assignment of the two observed conformers of 2-FTP···H_2O.

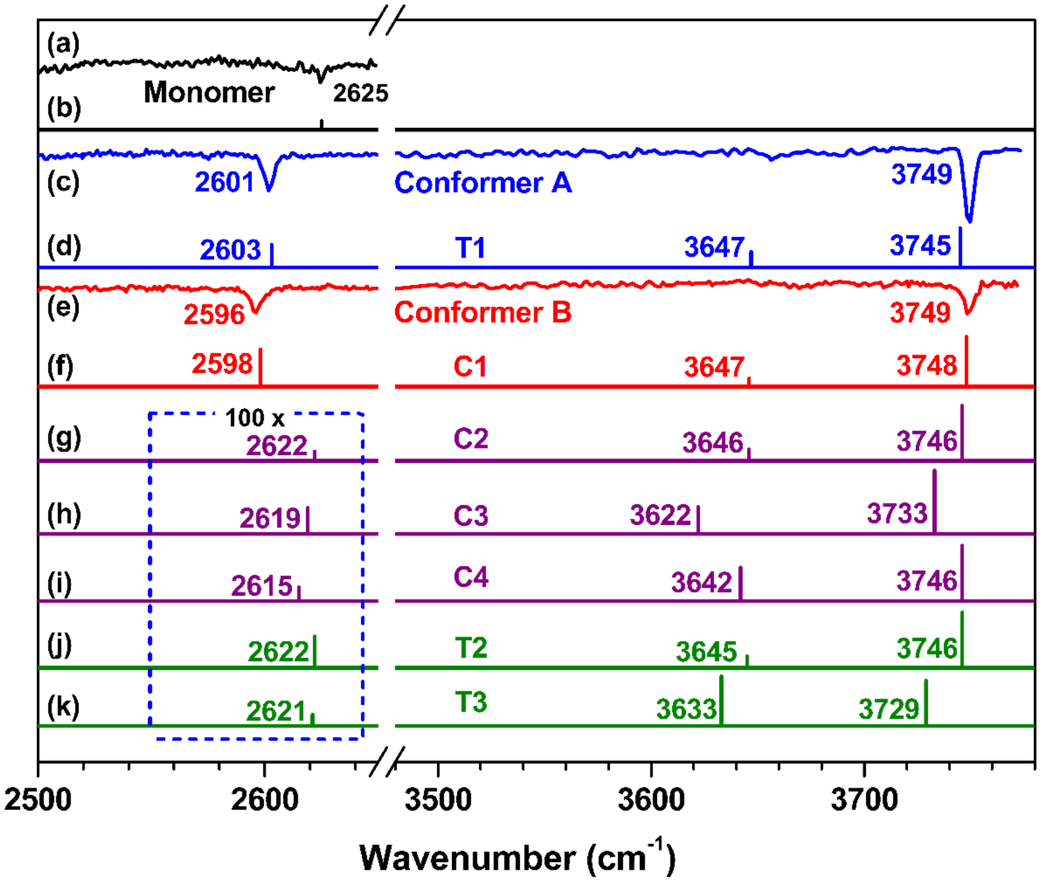

Figure 3.7. Experimental and Calculated S-H and O-H Stretching frequencies of all the conformers of 2-FTP···H_2O complex. Frequencies are calculated at the cp-MP2/6-311++G (d,p) level of theory. S-H stretching frequencies are scaled with a factor of 0.9375, derived from the ratio of experimental and calculated S-H stretching frequency of the 2-FTP monomer. Similarly, O-H frequencies are scaled by a factor of 0.9378 obtained from the observed and calculated antisymmetric O-H frequencies of free water

The amount of the IR red-shift (25–30 cm^{-1}) observed in the S–H frequency in 2-FTP···H_2O indicates that the S–H···O hydrogen bond is quite weak in comparison to its counterpart, i.e., O–H···O hydrogen in the phenol···H_2O complex reported in the literature.[249] The IR red-shift in the O–H stretching frequency for the O–H···O hydrogen in the phenol···H_2O complex observed by Mikami and co-workers is 133 cm^{-1}.[249] Interestingly, Robertson and co-workers could not observe the S–H···O bound conformer in their gas-phase spectroscopic study of the 2-phenylethanethiol···H_2O complex.[9]

However, they found the conformer of 2-phenylethanethiol···H_2O complex with the O−H···S hydrogen bond having a red-shift of 117 cm^{-1} in the O−H stretching frequency. Here, 2- phenylethanethiol acts as a strong hydrogen-bond acceptor while H_2O performs as a good hydrogen-bond donor, unlike the case of the 2-FTP···H_2O complex where the thiol and H_2O play opposite roles for the hydrogen-bond interaction. Thus, the role of the hydrogen-bond donor or acceptor in a given set of hydrogen bonding partners depends on their combined proton affinity and pKa values apart from the electronegativity values of the hydrogen-bond donor and acceptor atoms.[8, 252] The pKa value of 2-FTP is much less than that of 2- phenylethanethiol as aromatic thiols are more acidic than aliphatic thiols. Hence, the hydrogen-bond donor ability of 2- FTP is more than that of 2-phenylethanethiol. Although the pKa values of 2-FTP and 2-phenylethanethiol are not found in the literature, those values for similar compounds such as thiophenol (6.52) and phenylmethanethiol (9.43) are reported in the literature.[253] Furthermore, the pKa values of phenol (9.99) and 2-fluorophenol (8.73) are reported in the literature.[254-255]

In the case of the 2-phenylethanethiol···Et_2O complex reported in the literature, the S−H···O hydrogen-bonded conformer observed in the experiment as 2-phenylethanethiol is the only choice as a hydrogen-bond donor in the complex. The IR red-shift of 24 cm^{-1} in the S−H frequency for the S− H···O hydrogen bond in 2-phenylethanethiol···Et_2O has been reported by Robertson and co-workers.[9] Bhattacharjee et al. observed S−H···O hydrogen bond with an IR red-shift of 44 cm^{-1} in the S−H frequency in the H_2S···MeOH complex.[8] Here, MeOH is favored over H_2S as a hydrogen-bond acceptor in terms of their proton affinity values, while H_2S is preferred over MeOH as a hydrogen-bond donor in terms of their pKa values. The proton affinity values of MeOH and H_2S are 754 and 705 kJ mol^{-1}, respectively, while their pKa values are 15.5 and 7.0, respectively.[256-258] 100−103 Later, they reported the observation of the S−H···O hydrogen bond in H_2S···Et_2O, H_2S···Bu_2O and H_2S···1,4-dioxane with IR red-shift values of 46, 63, and 49 cm^{-1}, respectively.[8] Thus, the overall results on the S−H···O hydrogen bond reveal that this interaction, although weak, can be modulated by a suitable choice of the hydrogen-bond donor and acceptor molecules.

3.2.4. Analysis of the Non-covalent Interactions in the 2-FTP···H_2O complex

The non-covalent interactions present in the observed conformers of the 2-FTP···H_2O complex, i.e., C1 and T1 are analyzed by QTAIM, NCI, NBO, and EDA calculations. These quantum mechanical analyses are extremely important to have a qualitative understanding of the physical nature and strength of the hydrogen bond or any other non-covalent interaction observed in the molecular systems from the experiment. Although only the major non-covalent interactions, i.e., S–H···O and O–H···O hydrogen bonds in the complex, have been probed through the IR experiment, the

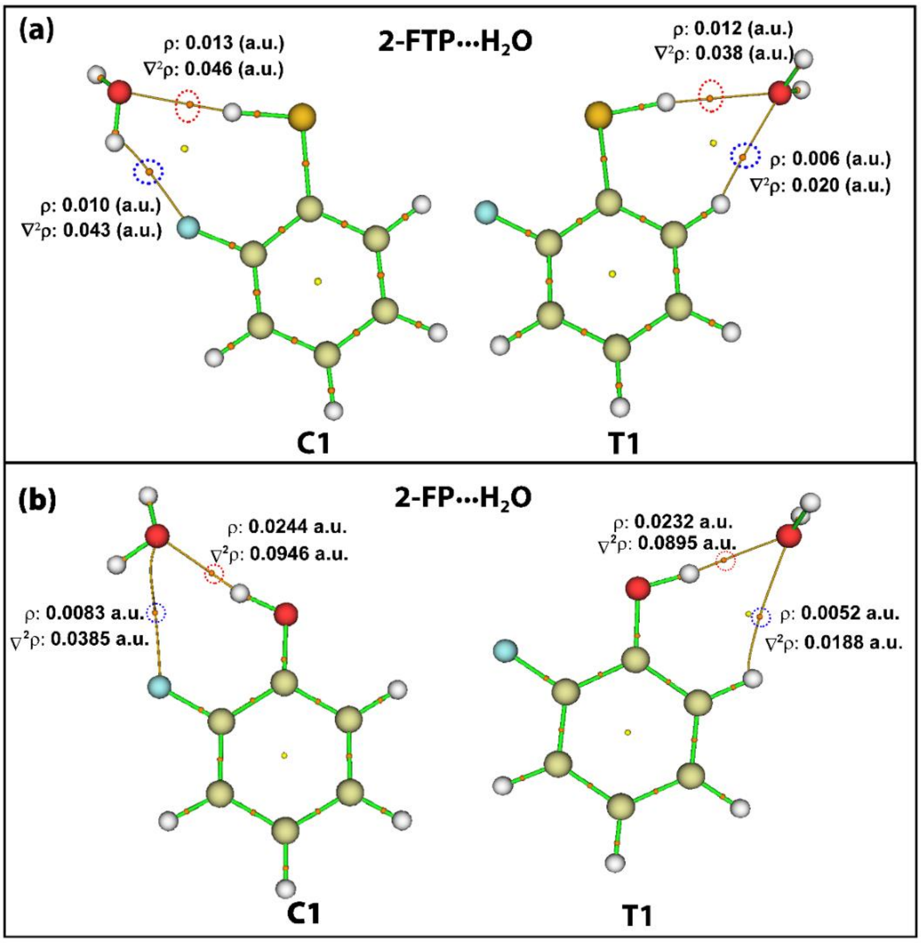
(a)
2-FTP···H_2O
ρ: 0.013 (a.u.)
$\nabla^2\rho$: 0.046 (a.u.)
ρ: 0.010 (a.u.)
$\nabla^2\rho$: 0.043 (a.u.)
ρ: 0.012 (a.u.)
$\nabla^2\rho$: 0.038 (a.u.)
ρ: 0.006 (a.u.)
$\nabla^2\rho$: 0.020 (a.u.)
C1
T1
(b)
2-FP···H_2O
ρ: 0.0244 a.u.
$\nabla^2\rho$: 0.0946 a.u.
ρ: 0.0083 a.u.
$\nabla^2\rho$: 0.0385 a.u.
ρ: 0.0232 a.u.
$\nabla^2\rho$: 0.0895 a.u.
ρ: 0.0052 a.u.
$\nabla^2\rho$: 0.0188 a.u.
C1
T1

Figure 3.8. Molecular graphs of the C1 and T1 conformers of the (a) 2-FTP···H_2O and (b) 2 FP···H_2O complex obtained from QTAIM calculation performed on the cp-MP2/6-311++G(d,p) level optimized geometries. Electron density (ρ) and its Laplacian (∇2 ρ) values at the bond critical points (BCPs) of the hydrogen bonds present in the two conformers are provided with the figure. (b)

weak/secondary interactions (O−H···F and C−H···O) in combination with the primary interactions are addressed through the QTAIM, NCI, and NBO analyses.

Electron density maps in the two conformers are generated by QTAIM analysis using the wave functions calculated from the structures optimized at the cp-MP2/6-311++G(d,p) level of theory. The molecular graphs representing the bond critical points (BCPs) and bond paths for the C1 and T1 conformers of the 2-FTP···H_2O complex are shown in Figure 3.8 panels (a). The most important AIM parameters, i.e., electron density (ρ) and its Laplacian ($\nabla^2\rho$) at the BCPs of the hydrogen bonds in the C1 and T1 conformers, are provided with the figure. The AIM molecular graphs indicate the presence of the S−H···O and O−H···F hydrogen bonds in C1 and the S−H···O and C−H···O

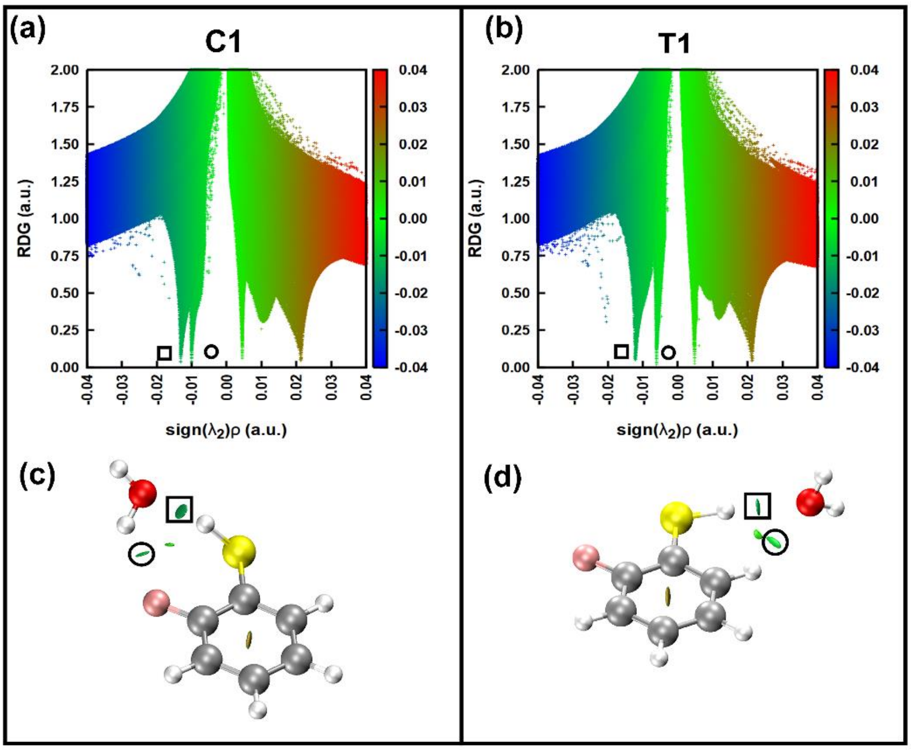

Figure 3.9. (a,b) NCI plot of reduced density gradient (RDG, a.u.) as a function of the electron density multiplied with the sign of the second eigenvalue of the electron density Hessian matrix [sign $(\lambda_2)\rho$, (a.u.)] for the C1 and T1 conformers of 2-FTP···H_2O. (c,d) NCI isosurface plots showing the non-covalent interactions present in the C1 and T1 conformers. Gradient isosurface follows a blue-green-red color scheme over the range of $-0.04 < \mathrm{sign}(\lambda_2)\rho < 0.04$, where blue, green, and red colors denote very strong attraction, weak attraction, and strong repulsion, respectively. RDG minima and corresponding non-covalent interactions represented by NCI isosurfaces are marked by squares and circles. The NCI calculations are performed on the cp-MP2/6-311++G(d,p) level geometries.

hydrogen bonds in T1. It could be noted that the weak nature of the O–H···F hydrogen bond is not reproduced well from the AIM analysis.

Figure 3.9 shows the reduced density gradient (RDG) plot and NCI isosurface for the two experimentally observed conformers C1 and T1 of 2-FTP···H_2O obtained from NCI analysis. The RDG is plotted against the sign(λ_2)ρ, where λ_2 is the second eigenvalue of the electron density Hessian matrix. A negative value of λ_2 represents an attractive interaction, while a positive value illustrates a repulsive interaction. The RDG and density (ρ) cutoff values are set at 2.0 and 0.1 au, respectively, while the NCI isosurface value is fixed at 0.3 a.u. The S–H···O hydrogen bonding, which is a primary interaction in both C1 and T1 conformers, is highlighted with a square in both the RDG plot and NCI isosurface. Similarly, the secondary interactions, i.e., O–H···F and C–H···O hydrogen bonds present in the C1 and T1 conformers, respectively, are marked with circles in the RDG and NCI

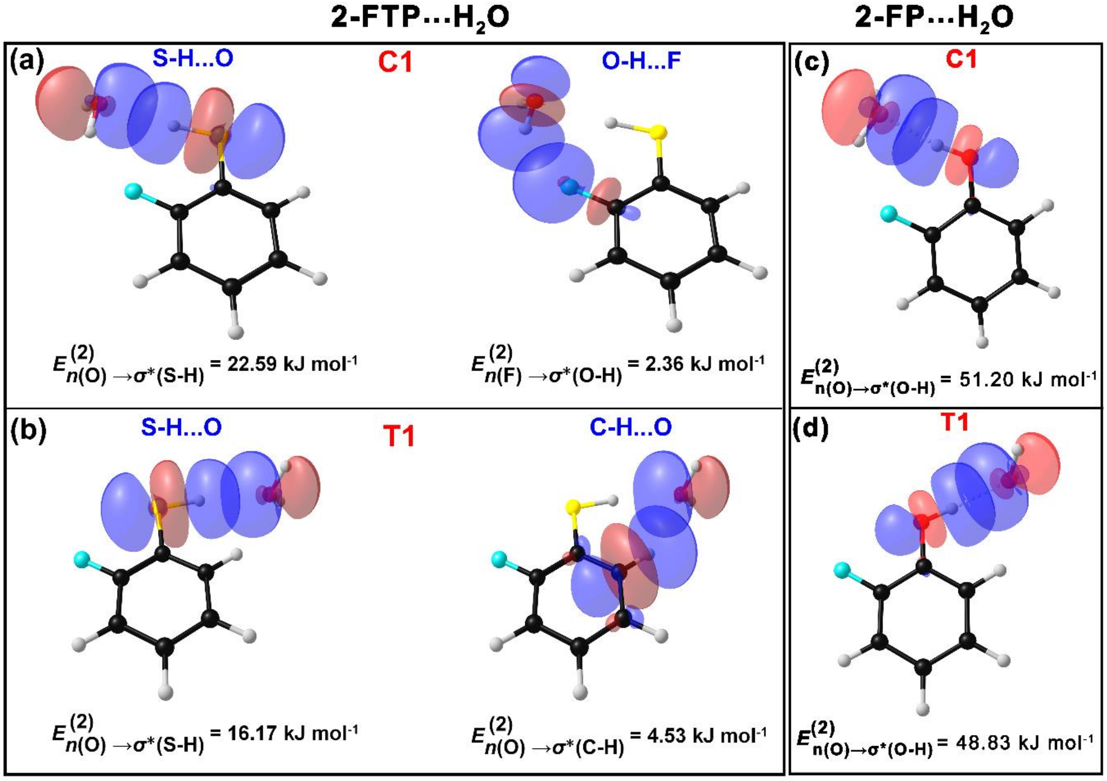
2-FTP···H_2O
2-FP···H_2O
(a)
S-H...O
C1
O-H...F
$E^{(2)}_{n(O)\rightarrow\sigma^*(S-H)}$ = 22.59 kJ mol^{-1}
$E^{(2)}_{n(F)\rightarrow\sigma^*(O-H)}$ = 2.36 kJ mol^{-1}
(c)
C1
$E^{(2)}_{n(O)\rightarrow\sigma^*(O-H)}$ = 51.20 kJ mol^{-1}
(b)
S-H...O
T1
C-H...O
$E^{(2)}_{n(O)\rightarrow\sigma^*(S-H)}$ = 16.17 kJ mol^{-1}
$E^{(2)}_{n(O)\rightarrow\sigma^*(C-H)}$ = 4.53 kJ mol^{-1}
(d)
T1
$E^{(2)}_{n(O)\rightarrow\sigma^*(O-H)}$ = 48.83 kJ mol^{-1}

Figure 3.10. NBO overlap for the (a) S–H···O and O–H···F hydrogen bonds in the C1 conformer of 2-FTP···H_2O, (b) S–H···O and C– H···O hydrogen bonds in the T1 conformer of 2-FTP···H_2O (c,d) are conventional O-H···O hydrogen bonds in the C1 and T1 conformers of 2- FP (2-fluorophenol)···H_2O complexes, respectively. NBO 2nd order perturbation energy value for individual non-covalent interaction is provided with the NBO plot. NBO calculations are performed on the MP2/6-311++G(d,p) level optimized geometries.

isosurface plots. The RDG plots clearly show that the S−H⋯O hydrogen bond present in both the conformers is stronger than the O−H⋯F or C−H⋯O hydrogen bonds present there.

NBO analysis further corroborates the presence of multiple hydrogen-bond interactions in the C1 and T1 conformers of 2- FTP⋯H_2O. According to the NBO theory, the lone pair electrons in the donor NBO (i) get delocalized into the antibonding acceptor NBO (j*) when hydrogen bond or some other non-covalent interaction is present in a molecule or complex. The strength of the non-covalent interaction is represented by NBO second-order perturbation energy ($E^{(2)}_{i\rightarrow j^*}$). Figure 3.10 (a, b) depicts the NBO overlap and Ei→j (2) values for the S− H⋯O and O−H⋯F hydrogen bonds in the C1 conformer and S−H⋯O and C−H⋯O hydrogen bonds in the T1 conformer of 2-FTP⋯H_2O. The NBO results indicate that the S−H⋯O hydrogen bond present in the C1 conformer (22.59 kJ mol^{-1}) is relatively stronger than that in the T1 conformer (16.17 kJ mol^{-1}). In the case of the S−H⋯O hydrogen bond present in both the conformers, the p-type lone pair of the oxygen atom of H_2O has a major contribution to the NBO overlap, while the contribution of the s-type lone pair is insignificant. The NBO interaction energy obtained for the S−H⋯O hydrogen bond in the T1 (16.17 kJ mol^{-1}) and C1 (22.59 kJ mol^{-1}) conformers qualitatively agree with the IR red-shift of 24 and 29 cm^{-1} , respectively, observed for the two conformers in the experiment. The small amount of red-shift (~25−30 cm^{-1}) in the S−H frequency of the C1 and T1 conformers observed from IR spectroscopy indicate that the unconventional S−H⋯O hydrogen bond is weak in nature and the NBO interaction energy of 16−22 kJ mol^{-1} for the S−H⋯O hydrogen bond obtained for the two conformers corroborate this. Generally, NBO interaction energy for any conventional hydrogen bond such as O−H⋯O is much higher than that obtained here for the S−H⋯O hydrogen bond. We have calculated the NBO interaction energy for the O−H⋯O hydrogen bond in the C1 conformer of 2-fluorophenol (2-FP)⋯H2O and found that the interaction energy is 51 kJ mol^{-1} (Figure 3.10 c, d). It has been reported from IR spectroscopy experiments that the IR red-shift in the OH stretching frequency for the strong O−H⋯O hydrogen bond in 2-FP⋯H2O is 242 cm^{-1}.[244] Thus, the NBO results obtained for the unconventional S–H⋯O and conventional O–H⋯O hydrogen bonds corroborate the IR spectroscopy results.

Although the S–H⋯O hydrogen bond present in the C1 conformer is stronger than that in the T1 conformer, the binding energy of the latter one is slightly higher than the former one. However, the binding energies of the complexes are not only due to the hydrogen-bond interactions present there. The binding energies are due to the overall contribution of the electrostatics, exchange, repulsion, polarization, and dispersion interactions present in the complex, which are calculated from energy decomposition analysis (EDA) and displayed in Figure 3.11. The EDA results discussed in the following section will be able to shed light on the correlation between the binding energy values and S–H⋯O hydrogen-bond strength of the C1 and T1 conformers of the complex.

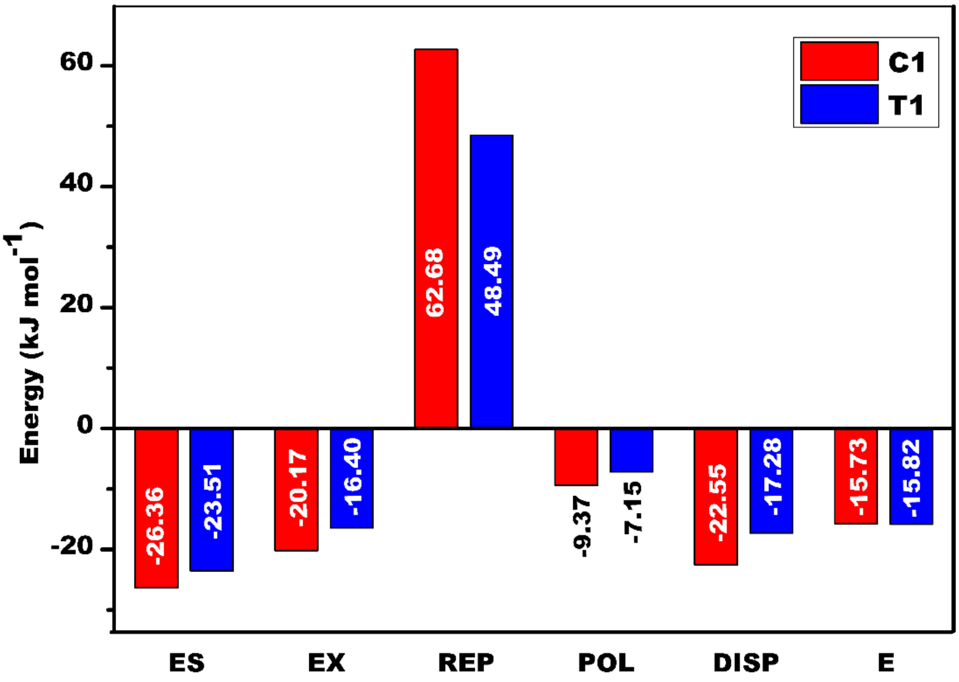

Figure 3.11. Decomposition of the total interaction energies of the C1 and T1 conformers of 2-FTP⋯H_2O at the M06-2X/aug-cc-pVTZ level of theory on the cp-MP2/6-311++G(d,p) optimized geometries using the LMO-EDA method. The total interaction energy (E) of the complex is decomposed into electrostatics (ES), exchange (EX), repulsion (REP), and polarization (POL) components.

The NBO calculation also shows that the secondary interactions, i.e., O–H⋯F and C–H⋯O hydrogen bonds in C1 and T1, respectively, are much weaker than the S–H⋯O hydrogen bond. Furthermore, the O–H⋯F hydrogen bond is found to be weaker than the

C–H⋯O hydrogen bond. The O–H⋯F hydrogen bond interaction is inherently weak in nature as fluorine is a very poor hydrogen-bond acceptor.[239]

In order to get a qualitative idea of the origin of the stability of the C1 and T1 conformers of 2-FTP⋯H_2O, total interaction energies are decomposed into different components using the localized molecular orbital energy decomposition analysis (LMO-EDA) method. In the EDA method, total interaction energy (E) is decomposed into electrostatics (E_{ES}), exchange (E_{EX}), repulsion (E_{REP}), polarization (E_{POL}), and dispersion (E_{DISP}) components. Figure 3.11 shows the different components of the interaction energy for the C1 and T1 conformers obtained from the EDA calculation performed at the M06-2X/ aug-cc-pVTZ level of theory. It is noteworthy that both the conformers are stabilized by a significant amount of electrostatics as well as dispersion interactions. However, the repulsion energy in the C1 conformer (62.68 kJ mol^{-1}) is much higher than that in the T1 conformer (48.49 kJ mol^{-1}), although the electrostatics, exchange, and dispersion energies in the former are higher than those in the latter. Thus, the binding energy of the T1 conformer eventually becomes a little higher than that of the C1 conformer.

The weak nature of the unconventional S–H⋯O hydrogen bond in 2-FTP⋯H_2O revealed from the NBO, AIM, analyses can be compared with the strong conventional O–H⋯O hydrogen bond in 2-fluorophenol (2-FP)⋯H_2O determined from similar quantum mechanical analyses. A comparison between the NBO, AIM, and NCI parameters for the S–H⋯O hydrogen bond in 2-FTP⋯H_2O and O–H⋯O hydrogen bond in 2-FP⋯H_2O is provided in Figures 3.10 (c, d), 3.8 (b), respectively. It is obvious from the comparison that the NBO, AIM, and NCI values are much higher for the O–H⋯O hydrogen bond than for the S–H⋯O hydrogen bond.

3.3. Conclusions

We have studied a 1:1 complex of 2-FTP and H_2O in the gas-phase using R2PI and IR-UV double resonance spectroscopy combined with quantum chemistry calculations. Two conformers of the complex observed in the experiment are assigned as monohydrated clusters of the cis and trans-2-FTP monomers denoted as C1 and T1, respectively. It is found that both the observed conformers, C1 and T1, are formed by S–H⋯O hydrogen bonding as a primary interaction. Theoretical calculations predict that C1 and T1 are almost isoenergetic. Interestingly, the O–H⋯S hydrogen-bonded conformers of 2- FTP⋯H_2O, which are higher in energy, are not observed in the experiment. The S–H⋯O hydrogen-bonded conformers dominate over the O–H⋯S hydrogen-bonded conformers as 2-FTP is a much better hydrogen-bond donor than H_2O. However, the red-shift observed in the S–H stretching frequency for the S–H⋯O hydrogen bond in 2-FTP⋯H_2O is small (25–30 cm^{-1}), and hence, this interaction is found to be weak in nature. NBO, NCI, and AIM analyses support the observation of the S–H⋯O hydrogen bond in the experiment.

Chapter 4

Modulation of the strength of weak S-H···O hydrogen-bond: Spectroscopic study of the complexes of 2-Flurothiophenol with methanol and ethanol

4.1. Introduction

We have discussed in Chapter 1 that the concept of hydrogen bonding holds significant importance in diverse fields, including biology, material science, supramolecular chemistry, and medicinal study.[55, 57, 59, 68, 76, 207-208, 210, 212, 259-261] Since the redefinition of the hydrogen bond in 2011, there have been tremendous efforts among researchers to understand the physical nature and strength of the non-covalent interactions, involving various weakly electronegative elements (S, Se, P, C, halogens, etc.) in the periodic table.[1-2, 5, 129, 141-142, 162, 211, 213-218, 262-263] Sulfur-centered hydrogen bonding (SCHB) is the one of the most recognized unconventional hydrogen bonding interactions due to its essential role in the structures and functions of proteins, supramolecular assemblies, and synthesis of novel material for optoelectronic purposes.[2-5, 141, 215, 217, 264]

It has been found from the literature studies that sulfur can act as a hydrogen bond donor as well as an acceptor, and the dual roles of sulfur are important for the structures and functions of biomolecules and materials.[215] In the previous chapter, we have discussed that the study of the SCHBs in the literature is mostly focused on the hydrogen-bonded systems where sulfur is a hydrogen bond acceptor.[2-5, 141, 215-217, 229, 265] There are only handful studies of SCHBs in the literature involving sulfur as a hydrogen bond donor.[7, 9, 223, 230-233, 252, 266] Solution phase FTIR spectroscopy studies of a few thiophenol complexes reported many decades ago demonstrated the formation of S–H···O, S–H···N, and S–H···π hydrogen bonds.[230-232] A few gas-phase spectroscopic evidence of S-H···S and S-H···O hydrogen bonding where sulfur serves as a hydrogen bond donor in the non-covalently bound complexes are reported using IR-UV double resonance spectroscopy, microwave spectroscopy.[7-8, 223, 266]

In the previous chapter, we have reported the strength of the S-H⋯O hydrogen bond in 2-fluorothiophenol⋯H_2O (2-FTP⋯H_2O) complex, which has been found to be weaker in terms of the red-shift in the S-H frequency (~30 cm^{-1}). Interestingly, a preference of the S-H⋯O over the O-H⋯S hydrogen bond was observed in the 2-FTP⋯H_2O complex, which demonstrated that the inherent choice of the hydrogen bond donor or acceptor in a hydrogen-bonded complex was governed by the pKa and proton affinities of the hydrogen bonding partners present there. In this chapter, we have further explored the modulation of the strength of weak S-H⋯O hydrogen bond by studying the 1:1 complexes of 2-FTP with MeOH and EtOH using resonant 2-photon ionization (R2PI), resonant ion-dip infrared (RIDIR), and UV-UV hole-burning spectroscopy in combination with quantum chemistry calculations.

4.2. Results and discussion

4.2.1. Electronic spectra of 2-FTP⋯MeOH and 2-FTP⋯ETOH complexes

Time of flight mass spectra of mixed vapor of 2-FTP and MeOH as well as 2-FTP and EtOH measured separately using 1C-R2PI spectroscopy are shown in Figures 4.1(a) and 4.1(b), respectively. Vapor pressure of 2-FTP as well as MeOH and EtOH was controlled to restrict the cluster formation to 1:1 2-FTP⋯MeOH and 2-FTP⋯EtOH dimeric complexes in the experiment. Figure 4.2(b) shows the electronic spectrum measured in the mass channel of the 2-FTP⋯MeOH complex (1:1) employing 1C-R2PI spectroscopy. The electronic spectrum of the 2-FTP monomer shown in Figure 4.2(a) displaying only its electronic origin band (35555 cm^{-1}) was reported earlier.[237] UV-UV hole-burning spectroscopy was used to determine the presence of different conformers of the complex

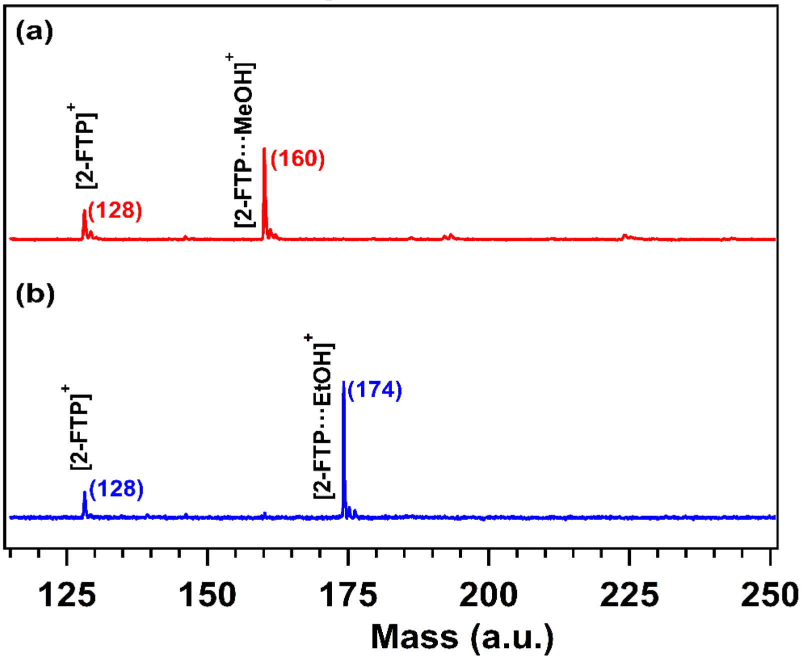

Figure 4.1. TOF mass spectra of (a) 2-FTP···MeOH complex recorded at 35277 cm^{-1} and (b) 2-FTP···EtOH complex recorded at 35307 cm^{-1}.

in the experiment. Figure 4.2(c-e) shows UV-UV hole-burning spectra of the 2-FTP···MeOH complex by probing the electronic bands marked with asterisks in Figure 4.2(b). The presence of three distinct conformers of the 2-FTP···MeOH complex marked as conformers A, B, and C are observed in the experiment. The origin bands for the $S_1 \leftarrow S_0$ transitions of the conformers A, B, and C appear at 35232, 35208, and 35202 cm^{-1}, respectively. Both of the conformers A and B exhibit a Franck-Condon progression of a low-frequency intermolecular vibrational mode of 14 cm^{-1}, although the progression is much longer for the conformer A than that for B. On the other hand, the conformer C shows a single electronic band (origin transition) without any low-frequency intermolecular modes of appreciable intensity. The electronic spectra of the three conformers signify that the geometry change after electronic excitation of the conformer A along the 14 cm^{-1} mode is maximum while the same for the conformer C is negligible.

Figure 4.3(b) shows the electronic spectrum measured in the mass channel of 2-FTP···EtOH (1:1) using 1-C R2PI spectroscopy. Figure 4.2(c-d) shows UV-UV hole-burning spectra of the 2-FTP···EtOH complex by probing the electronic bands marked by asterisks in Figure 4.3 (b). The hole-burning spectroscopy confirms the presence of two conformers of the 2-FTP···EtOH complex, marked as conformers A and B, in the

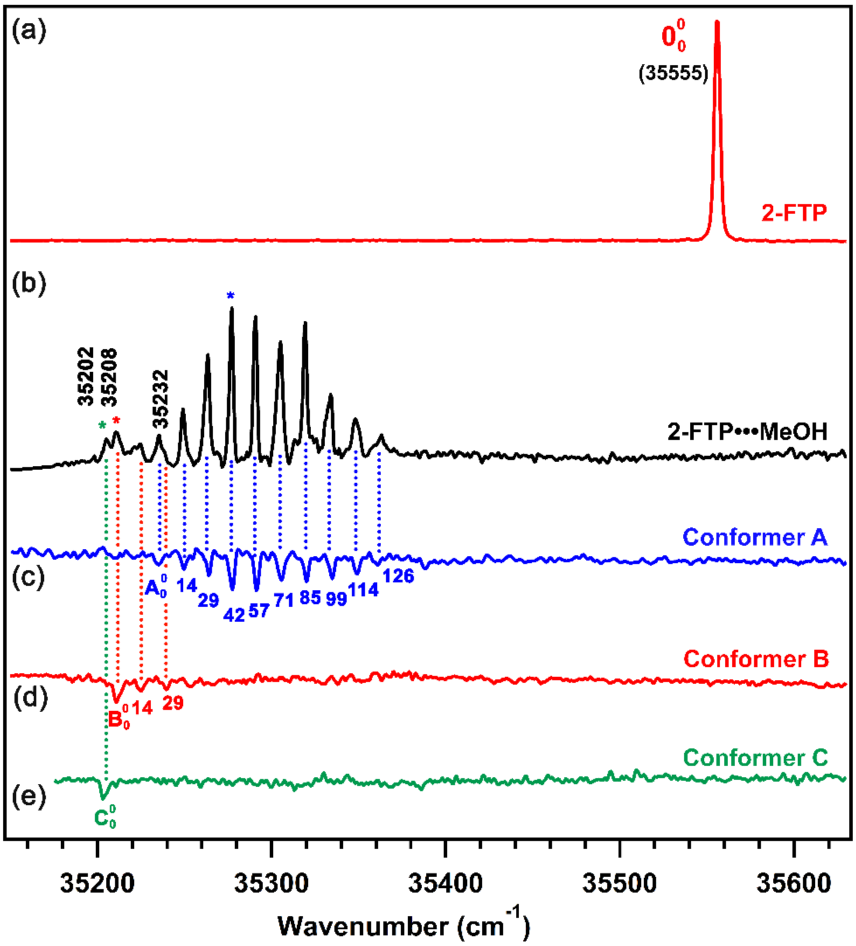

Figure 4.2. Electronic spectra measured in the mass channels of the (a) *cis*-2-FTP monomer and (b) 2-FTP···MeOH dimeric complex using 1C-R2PI technique. UV-UV hole-burning spectra corresponding to the three conformers of 2-FTP···MeOH, named A, B, and C, are shown in the panels (c), (d), and (e), respectively. Hole-burning spectra were measured by probing the bands marked with asterisks (*) in the electronic spectrum presented in Figure 4.2 (b). The origin bands for the conformers A, B, and C of the complex appear at 35232 cm^{-1}, 35208 cm^{-1}, and 35202 cm^{-1}, respectively. Intermolecular vibrational frequencies (in cm^{-1}) of the conformers of the complex are marked underneath each of the vibronic bands in the spectra depicted in the panels c, d, and e.

experiment, with their electronic origin bands appearing at 35269 and 35251 cm^{-1}, respectively. Both of the conformers show a long progression of a low-frequency

intermolecular mode of ~12 cm^{-1}. Interestingly, the frequency of the intermolecular mode observed for the 2-FTP···EtOH complex is similar to that found for the 2-FTP···MeOH complex. This has been discussed further (vide infra) in the light of the quantum chemistry calculations of these two complexes.

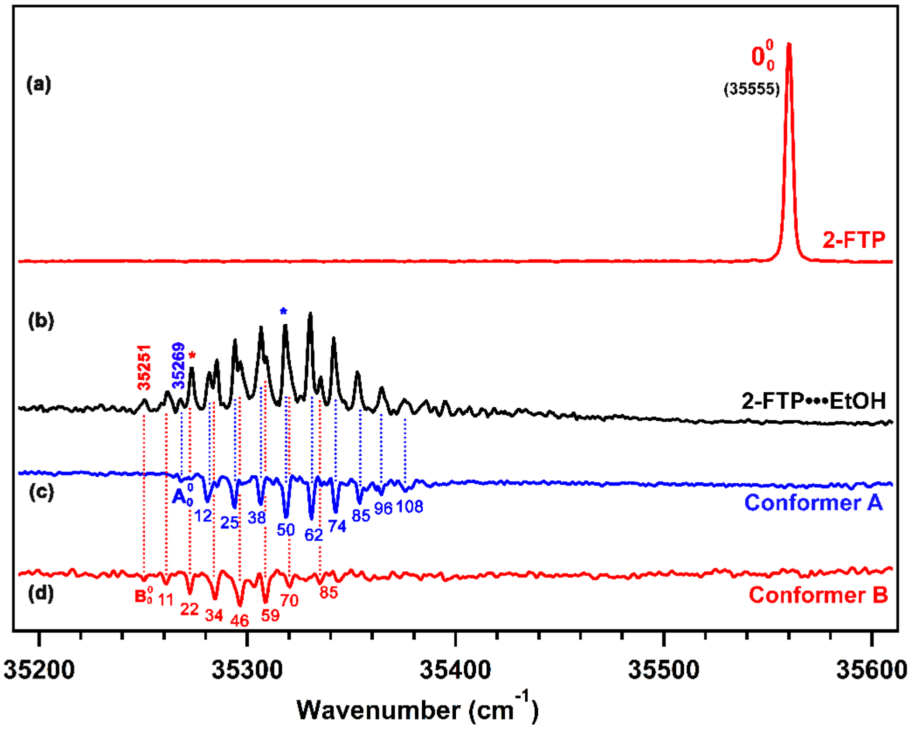

Figure 4.3. Electronic spectra measured in the mass channels of the (a) *cis*-2-FTP monomer and (b) 2-FTP···EtOH dimeric complex using 1C-R2PI technique. UV-UV hole burning spectra of the two conformers of the 2-FTP···EtOH complex designated as A (0^0_0 band at 35269 cm^{-1}) and B (0^0_0 band at 35251 cm^{-1}) are presented in panels c and d, respectively. Hole-burning spectra were obtained by probing the bands marked with asterisks in the electronic spectra presented in Figure 4.3(b). Intermolecular vibrational frequencies (in cm^{-1}) of the conformers of the complex are marked underneath each of the vibronic bands in the spectra depicted in the panels c and d.

It is worth comparing the electronic origin bands for the $S_1 \leftarrow S_0$ transitions of the 2-FTP···MeOH, 2-FTP···EtOH, and 2-FTP···H_2O complexes. The origin bands for the two conformers of the 2-FTP···H_2O complex were reported at 35221 and 35232 cm^{-1}.[267] It is apparent from the comparison that the red-shift in the electronic band origin of the three complexes of 2-FTP with respect to the origin band of the 2-FTP monomer (35555 cm^{-1}) is similar i.e., in the range of 300-350 cm^{-1}. A similar amount of red-shift in the band origin of these three complexes indicates that their stabilization energies with respect to the monomer in the S_1 state are larger by a similar amount than that in the S_0 state.

We have also recorded the electronic spectra in the mass channel of the 2-FTP monomer under the clustering condition to verify whether there is any fragmentation of 1:1 2-FTP···MeOH or 2-FTP···EtOH and their higher order clusters upon one-color 2-photon ionization. Figures 4.4 and 4.5 show a comparison of the electronic spectra measured in the mass channels of the pure 2-FTP monomer (while cluster is not forming), 2-FTP monomer (under clustering conditions), 2-FTP···MeOH, and 2-FTP···EtOH. The comparison clearly shows that there is no appreciable fragmentation of the dimeric complexes of 2-FTP with MeOH or EtOH and their higher-order clusters into the 2-FTP monomer mass channel.

The structures, bonding, and stability of the observed conformers of the 2-FTP···MeOH and 2-FTP···EtOH complexes are determined through a combination of quantum chemistry calculations and conformation-specific gas-phase IR spectroscopy described below.

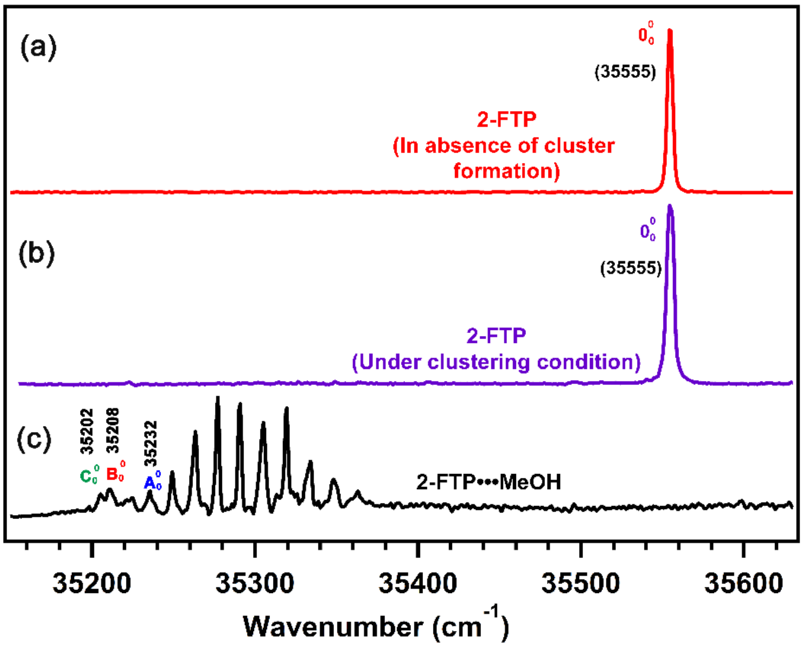

Figure 4.4. Mass-selected electronic spectra of (a) 2-FTP monomer in the absence of any complexing partner (b) 2-FTP monomer recorded at the fragmented monomer mass channel in cluster formation condition with methanol (c) 2-FTP···MeOH complex observed at the complex mass channel. A_0^0, B_0^0, *and* C_0^0 are the origin band for the $S_1 \leftarrow S_0$ transition for the three conformers of the 2-FTP···MeOH complex.

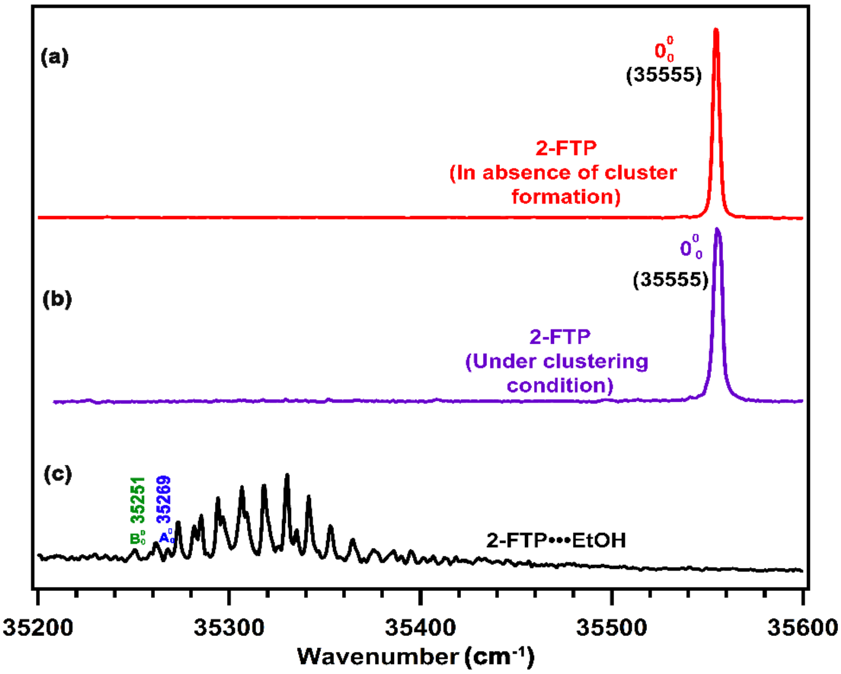

Figure 4.5. Mass-selected electronic spectra of (a) 2-FTP monomer in the absence of EtOH, (b) 2-FTP in the presence of EtOH and recorded in the monomer mass channel, and (c) 2-FTP···EtOH complex measured at the complex mass channel. A_0^0, *and* B_0^0 are the origin bands of the corresponding A and B conformers of the 2-FTP···EtOH complex.

4.2.2 Quantum chemistry calculations of the 2-FTP···MeOH and 2-FTP···ETOH complexes

4.2.2.1 Low-energy conformations of the 2-FTP···MeOH and 2-FTP···EtOH complexes.

As reported earlier, 2-FTP monomer exists as two conformers i.e., *cis* and *trans*, while the *cis* conformer is more stable than the *trans* by 4.2 kJ/mol at the MP2/6-311++G(d,p) level of theory.[267] Thus, probable conformers of the 1:1 complexes of MeOH and EtOH have been considered with both *cis*-2-FTP and *trans*-2-FTP. Geometry optimization of various conformers of 2-FTP···MeOH and 2-FTP···EtOH was performed at the MP2 as well as various DFT levels. Figure 4.6. shows the structures of six low-energy conformers of the

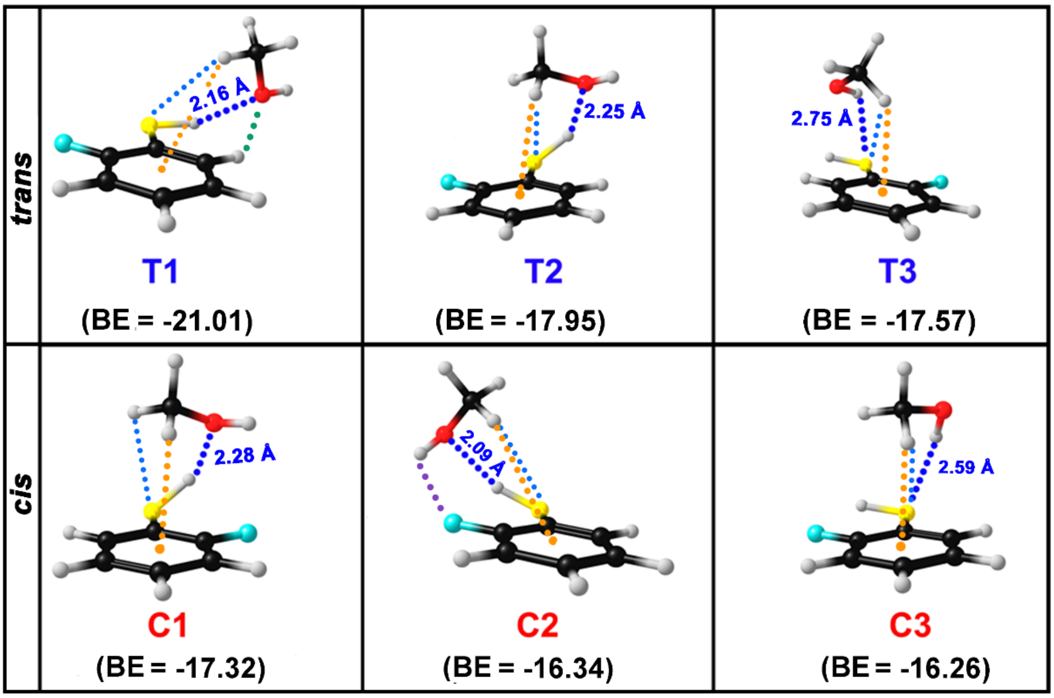

Figure 4.6. Structures of six low energy conformers of 2-FTP···MeOH complex optimized at the M06-2X/6-311++G(d,p) level of theory. BE stands for the BSSE and ZPE corrected binding energy in kJ/mol. Different colored dotted lines in the structures represent different non-covalent interactions present there. Distance (in Å) between two atoms involved only in the primary S-H···O hydrogen bonding interaction is provided with the structures. Geometrical parameters for the all interactions are given in Table 4.1.

2-FTP···MeOH complex optimized at the M06-2X/6-311++G(d,p) level of theory. The conformers of 2-FTP···MeOH are classified into two main categories i.e., *trans* and *cis* complexes of 2-FTP. The conformers belonging to *trans*-2-FTP are named T1, T2, and T3 while those belonging to *cis*-2-FTP are termed C1, C2, and C3. BSSE and ZPE corrected binding energies (BE) of the conformers calculated at the M06-2X/6-311++G(d,p) level are also provided in Figure 4.6. It is interesting to note that the *trans* complexes (T1, T2, T3) of 2-FTP are more stable than the *cis* complexes (C1, C2, C3) of 2-FTP, although the stability order of the *cis* and *trans* conformer in the 2-FTP monomer is opposite.

Important geometrical parameters of the conformers of the 2-FTP monomer and 2-FTP···MeOH complex are listed in Table 4.1. The global minimum conformer of the complex, T1, is primarily bound by a S-H···O hydrogen bonding interaction along with secondary weak C-H···O, C-H···S, and C-H···π interactions. The S-H···O hydrogen bond present in T2 is slightly weaker than that in T1, and the weakening of this primary hydrogen bond in T2 is due to a subtle balance between the S-H···O hydrogen bond and stacking interaction between the methyl group of MeOH and phenyl group of 2-FTP. The secondary interactions C-H···S and C-H···π are also present in T2. The interactions present in C1 are similar to those in T2, while C2 resembles T1 in terms of the interactions present there. However, C2 has additional weak O-H···F interaction in place of the C-H···O interaction present in T1. The C3 and T3 structures are stabilized primarily by O-H···S interaction apart from the C-H···π/stacking interaction present there.

Table 4.1. Geometrical parameter of different conformers of 2-FTP···MeOH complex calculated at M062X/6-311++G(d,p) level of theory. Distances are given in Å unit and angles, and dihedral angles are reported in (∘) unit

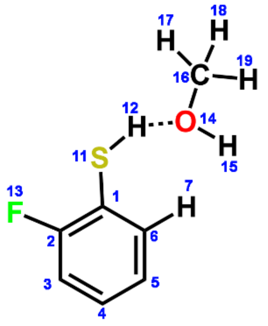

t-2-FTP···MeOH

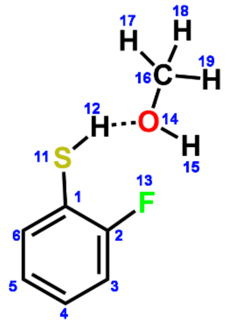

c-2-FTP···MeOH

Interaction	*c*-2-FTP	*t*-2-FTP	MeOH	C1	C2	C3	T1	T2	T3
In 2-FTP part									
$d_{S[11]-H[12]}$	1.34	1.34	-	1.35	1.35	1.34	1.35	1.35	1.34
⍰$C_{[1]}-S_{[11]}-H_{[12]}$	96.3	94.9	-	94.9	93.9	94.0	94.7	97.3	96.4
$d_{C[1]-S[11]}$	1.77	1.77	-	1.77	1.77	1.77	1.77	1.77	1.77
⍰ $C_{[2]}-C_{[1]}-S_{[11]}-H_{[12]}$	8.6	3	-	8.6	3.0	-4.7	-37.1	7.2	-41.7
$d_{S[11]}$⍰$_{F[13]}$	3.01	2.87	-	3.00	3.03	3.01	2.89	2.94	2.88
$d_{S[11]-H[12]}$⍰$_{F[13]}$	2.29	-	-	2.54	2.43	2.29	-	-	-
⍰$S_{[11]}-H_{[12]}$⍰$F_{[13]}$	109.6	-	-	95.8	102.9	109.4	-	-	-
In MeOH part									
$d_{O[14]-H[15]}$	-	-	0.96	0.96	0.96	0.96	0.96	0.96	0.96
⍰$C_{[16]}-O_{[14]}-H_{[15]}$	-	-	108.9	109.4	108.4	108.6	108.8	108.4	109.5
Primary S-H···O interaction									
$d_{S[11]-H[12]\cdots O[14]}$	-	-	-	2.28	2.09	-	2.16	2.25	-
$\angle S_{[11]}-H_{[12]}\cdots O_{[14]}$	-	-	-	129.0	159.4	-	148.3	132.7	-
⍰ $C_{[2]}-C_{[1]}-S_{[11]}\cdots O_{[14]}$	-	-	-	-61.8	36.5	-	-21.7	-58.1	-
$d_{S[11]}$⍰$_{O[14]}$	-	-	-	3.29	3.38	3.51	3.38	3.32	3.34
Secondary interactions									
$d_{C[16]-H[18]}$⍰$_{\pi}$	-	-	-	2.91	2.87	2.85	2.93	2.93	2.84
$d_{C[2]-H[7]}$⍰$_{O[14]}$	-	-	-	-	-	-	2.39	-	-

$d_{O[14]-H[15]\cdots S[11]}$	-	-	-	-	-	2.59	-	-	2.84
$d_{O[14]-H[15]\cdots F[13]}$	-	-	-	-	2.27	-	-	-	-
$d_{C[2]-H[7]\cdots O[14]}$				3.27	3.28	-	3.1	3.05	-
$d_{C[16]-C[1]}$				3.57	3.86	3.84	2.95	2.76	3.83
$d_{C[16]-C[2]}$				3.08	3.34	-	3.69	3.64	-
$d_{C[16]-C[3]}$				3.66	-	-	-	-	-
$d_{C[16]-C[5]}$				-	-	-	-	3.79	-
$d_{C[16]-C[6]}$				-	-	3.38	3.32	2.98	3.51

The six low-energy structures of 2-FTP⋯MeOH are also optimized at the MP2 and various other DFT levels of theory. Energy landscape of these six conformers of 2-FTP⋯MeOH calculated at different levels of theory are provided in Figure 4.7. The

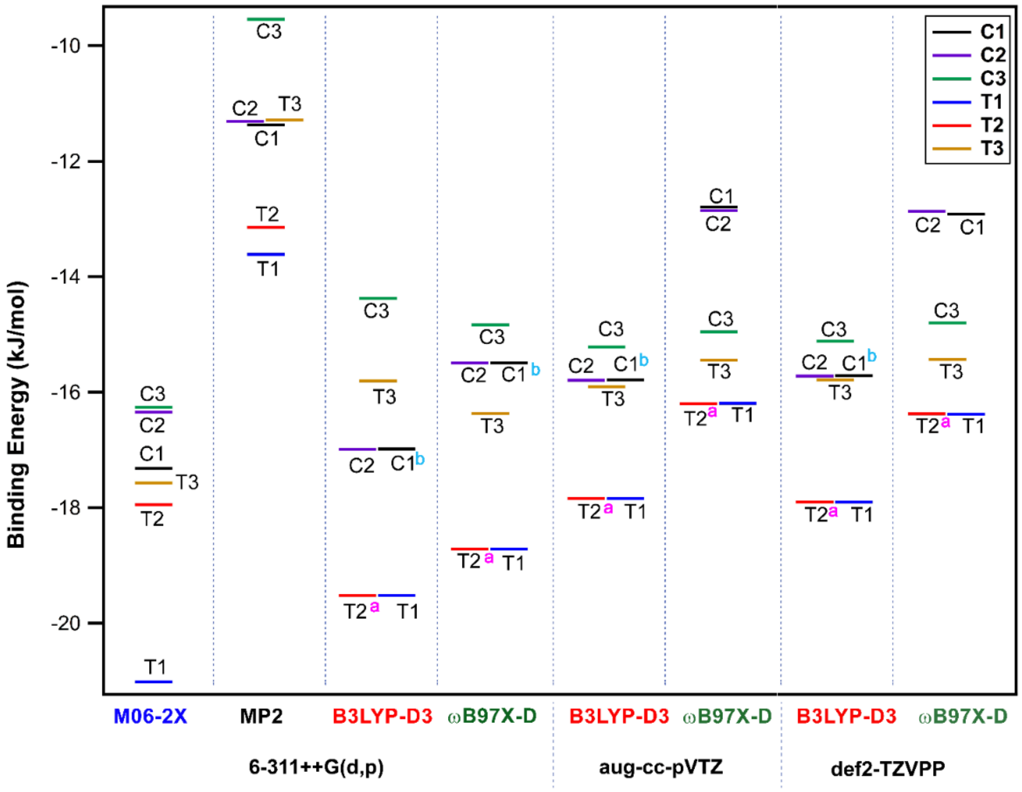

Figure 4.7. Graphical representation of the Binding energies of the conformers of the 2-FTP⋯MeOH complexes at different level of theory.

energetic trend of the T1 and T2 conformers at the MP2 level is similar to that obtained at the M06-2X/6-311++G(d,p) level of theory. However, the C2 conformer converges to C1 at the MP2 level of theory, and this convergence could be due to the overestimation of the dispersion interaction at this level of theory. Other DFT levels of theory, such as B3LYP-D3 and ωB97X-D converge the T2 structure to T1 and the C1 structure to C2. Hence, these two DFT functionals seem to underestimate the dispersion interactions present in both T2 and C1 conformers of 2-FTP···MeOH containing both C-H···π and stacking interactions. The performance of the M06-2X/6-311++G(d,p) level of theory appears to be satisfactory in terms of maintaining a subtle balance between the electrostatic and dispersion interactions present in various conformers of the 2-FTP···MeOH complex.

It is worthwhile to have a comparison of the structures of the conformers of the 2-FTP···MeOH complex with those of the 2-FTP···H_2O complex reported in the literature.[267] In the case of the 2-FTP···H_2O complex, only the T1 and C2 versions of the S-H···O hydrogen bonded conformers of the 2-FTP···MeOH complex are present. Thus, the existence of the additional T2 and C1 conformers of the 2-FTP···MeOH complex bound by secondary methyl/phenyl stacking interaction is quite anticipated. The conformational landscape of 2-FTP···EtOH complex gets further complicated due to the presence of ethyl group in the place of one of the hydrogen atoms in H_2O.

In the case of the 2-FTP···EtOH complex, the conformational population arises due to the combination of *cis*-2-FTP (C) and *trans*-2-FTP (T) with the gauche$^+$ (g^+), gauche$^-$ (g^-), and anti (a) conformers of EtOH. The g^+, g^- conformers of EtOH are a type of orientation with OH torsional angle of about +60° and -60°, respectively, while the OH torsional angle in the a conformer is +180°. Thus, the probable basic conformers for 2-FTP···EtOH are

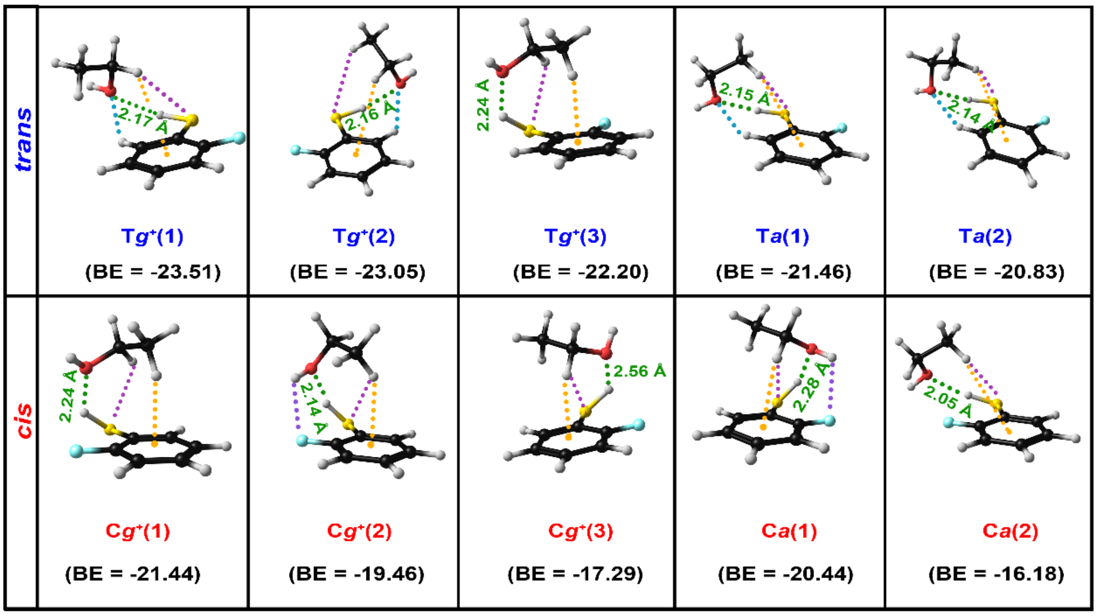
trans
2.17 Å
Tg^+(1)
(BE = -23.51)
2.16 Å
Tg^+(2)
(BE = -23.05)
2.24 Å
Tg^+(3)
(BE = -22.20)
2.15 Å
Ta(1)
(BE = -21.46)
2.14 Å
Ta(2)
(BE = -20.83)
cis
2.24 Å
Cg^+(1)
(BE = -21.44)
2.14 Å
Cg^+(2)
(BE = -19.46)
2.56 Å
Cg^+(3)
(BE = -17.29)
2.28 Å
Ca(1)
(BE = -20.44)
2.05 Å
Ca(2)
(BE = -16.18)

Figure 4.8. Structures of ten low energy conformers of 2-FTP···EtOH complex optimized at the M06-2X/6-311++G(d,p) level of theory. BE stands for the BSSE and ZPE corrected binding energy in kJ/mol. Different colored dotted lines in the structures represent different non-covalent interactions present there. Distance (in Å) between two atoms involved only in the primary S-H···O hydrogen bonding interaction is provided with the structures. Geometrical parameters corresponding to all the interactions are presented in Table 4.2. The structures of Tg^- and Cg^- are mirror images of those of Tg^+ and Cg^+, respectively. Thus, the Tg^- and Cg^- are identical in structure and energy to the Tg^+ and Cg^+, respectively. The Tg^- and Cg^- structures, corresponding to the Tg^+ and Cg^+ structures presented in this figure, are provided in Figure 4.9.

Tg^+, Tg^-, Ta, Cg^+, Cg^-, and Ca. Figure 4.8 shows the structures of a few low-energy conformers of the 2-FTP···EtOH complex optimized at the M06-2X/6-311++G(d,p) level of theory. The structures and energetics of the g+ and g^- versions of the conformers of the complex are very much similar. Hence, the Tg^+ and Cg^+ conformers are provided in Figure 4, while the corresponding Tg^- and Cg^- conformers are given in Figure 4.9. In the case of Tg^+, there are three closely lying structures Tg^+(1), Tg^+(2), and Tg^+(3), due to different orientations of the EtOH moiety with respect to 2-FTP in the complex and the corresponding g^-versions are Tg^-(1), Tg^-(2) and Tg^-(3). Similarly, in the case of Cg^+, there are three closely lying conformers named as Cg^+(1), Cg^+(2), and Cg^+(3) and the corresponding Cg^{-} structures are named as Cg^{-}(1) Cg^{-}(2), and Cg^{-} (3). On the other hand, two low-energy conformers are present in each case of T*a* and C*a* and these conformers are termed T*a*(1), T*a*(2), C*a*(1), and C*a*(2).

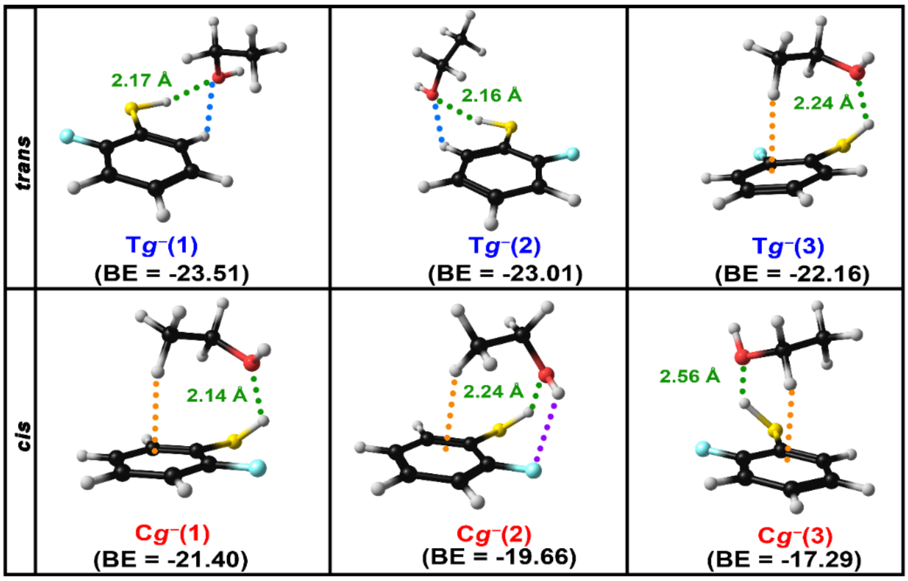

Figure 4.9. Structure of the g^{-}version of the conformers of 2-FTP···EtOH complexes, calculated at M06-2X/6-311++G(d,p) level of theory. BE represents the BSSE and ZPE corrected binding energy in KJ/mol.

All the low-energy conformers of the 2-FTP···EtOH complex are primarily bound by S-H···O hydrogen bond interaction. The conformers of 2-FTP···EtOH bound by O-H···S or O-H···π hydrogen bonds are generally less stable than those bound by O-H···S hydrogen bonds as EtOH is more favorable as a hydrogen bond acceptor in terms of the proton affinity/pKa values of the two hydrogen bonding partners in the complex as reported earlier.[253-254, 268] In the case of the phenol···MeOH/EtOH or *p*-cresol···MeOH/EtOH complexes, the most stable conformers observed in the experiment are those with MeOH/EtOH acting as hydrogen bond acceptors.[4, 106, 269-270]

Table 4.2 presents several crucial geometric parameters of the 2-FTP···EtOH complex, computed at the M06-2X/6-311++G(d,p) level of theory. It can be noticed from Figure 4.8 that Tg^{+}(1) is the global minimum structure of the 2-FTP···EtOH complex, while

Tg^+(2) and Tg^+(3) are slightly higher in energy than Tg^+(1). The Tg^+(1) and Tg^+(2) conformers are primarily stabilized by S-H···O hydrogen bond along with several secondary interactions such as C-H···O, C-H···π, and C-H···S. In Tg^+(3), the S-H···O hydrogen bond gets relatively weaker in order to accommodate more pronounced C-H···π/stacking interaction between the ethyl group of EtOH and phenyl group of 2-FTP. The C-H···O hydrogen bond is absent in Tg^+(3) but other secondary interaction C-H···S hydrogen bond is present there. The T*a* conformers [T*a*(1) and T*a*(2)] are mostly stabilized by S-H···O and C-H···O hydrogen bond interactions apart from very weak C-H···π, and C-H···S interactions. The Cg^+ conformers [Cg^+(1), Cg^+(2), and Cg^+(3)] are stabilized by S-H···O hydrogen bond as well as stacking/C-H···π interaction between the EtOH and 2-FTP moieties. The structure of the C*a*(1) conformer is due to a subtle balance among the S-H···O, O-H···F, and stacking/C-H···π interactions while the stabilization of the C*a*(2) conformer is dominated by S-H···O hydrogen bond apart from very weak C-H···S and C-H···π interactions. It is noteworthy that the torsional angles of the three conformers of the ethanol monomer and ∠C-C-S-H angle of the 2-FTP monomer are significantly altered in all the conformers of the 2-FTP···EtOH complex (Table 4.2).

Table 4.2. Geometrical parameter of different conformers of 2-FTP···EtOH complex calculated at M062X/6-311++G(d,p) level of theory. Distances are given in Å unit and angles, and dihedral angles are reported in (∘) unit

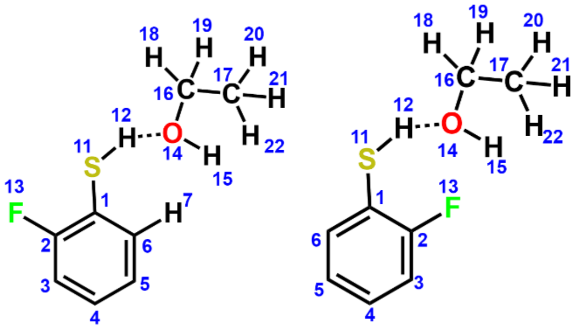

t-2-FTP···EtOH *c*-2-FTP···EtOH

In 2-FTP part	*t*-2-FTP	*c*-2-FTP	*Tg*(1)	*Tg*(2)	*Tg*(3)	*Ta*(1)	*Ta*(2)	*Cg*(1)	*Cg*(2)	*Cg*(3)	*Ca*(1)	*Ca*(2)
$d_{S[11]-H[12]}$	1.34	1.34	1.35	1.35	1.35	1.35	1.35	1.35	1.35	1.34	1.35	1.35
$d_{[S_{11}⋯F_{13}]}$	2.87	3.01	2.89	2.89	2.94	2.89	2.89	2.99	3.00	3.44	3.36	3.39
$∠C_{[1]}-S_{[11]}-H_{[12]}$	94.9	96.3	94.9	94.8	94.0	94.4	94.9	95.0	94.8	94.7	94.5	97.3
$d_{[C_1-S_{11}]}$	1.77	1.77	1.77	1.77	1.78	1.77	1.77	1.77	1.77	1.77	1.77	1.77
$d_{S[11]-H[12]⋯F_{13}}$	-	2.29	-	-	-	-	-	2.51	2.59	2.50	2.66	2.38
$∠S_{[11]}-H_{[12]}⋯F_{13}$	-	109.6	-	-	-	-	-	97.4	94.0	97.2	90.6	104.7
□ $C_{[2]}-C_{[1]}-S_{[11]}-H_{[12]}$	3	8.6	8.4	-4.7	37.5	3.9	7.8	39.6	44.9	-39.6	-50.7	20.7

In EtOH part	*g*+ EtOH	*g*- EtOH	*a*- EtOH	*Tg*+(1)	*Tg*+(2)	*Tg*+(3)	*Tg*-(1)	*Tg*- (2)	*Tg*- (3)	*Ta*(1)	*Ta*(2)
$d_{O[14]-H_{15}]}$	0.96	0.96	0.96	0.96	0.96	0.96	0.96	0.96	0.96	0.96	0.96
$∠ C_{[16]}-O_{[14]}-H_{[15]}$	108.5	108.5	109.2	109.2	109.0	108.6	109.1	109.0	108.6	109.4	109.6
□ $C_{[17]}-C_{[16]}-O_{[14]}-H_{[15]}$	58.9	-58.8	180	63.5	60.4	56.3	-63.5	-64.4	-56.3	170	-170.8
$O_{[14]}-H_{[15]}\cdots C_{[1]}$	2.60	2.61	-	2.65	2.63	2.59	2.65	2.63	2.59	-	-

	g+ EtOH	*g*- EtOH	*a*- EtOH	*Cg*+(1)	*Cg*+(2)	*Cg*+(3)	*Cg*-(1)	*Cg*- (2)	*Cg*- (3)	*Ca*(1)	*Ca*(2)
$d_{S[11]-H_{12}]}$	0.96	0.96	0.96	0.96	0.96	0.96	0.96	0.96	0.96	0.96	0.96
$∠ C_{[16]}-O_{[14]}-H_{[15]}$	108.5	108.5	109.2	109.2	109.5	108.4	109.2	109.6	108.4	109.5	109.2
□ $C_{[19]}-C_{[16]}-O_{[14]}-H_{[15]}$	58.9	-58.8	180	53.1	54.7	67.3	-53.3	-54.7	-67.3	-177.4	171
$O_{[14]}-H_{[15]}\cdots C_{[19]}$	2.60	2.61	-	2.58	2.60	2.67	2.57	2.59	2.67	-	-

Interaction between *trans*-2-FTP···EtOH

S-H···O interaction	T*g*+(1)	T*g*+(2)	T*g*+(3)	T*g*⁻(1)	T*g*⁻ (2)	T*g*⁻ (3)	T*a*(1)	T*a*(2)
$\mathbf{d}_{S[11]\text{-}H[12]⍰O[14]}$	2.17	2.16	2.24	2.17	2.16	2.24	2.15	2.14
∠ $S_{[12]}$-$H_{[13]}$···$O_{[14]}$	147.8	148.2	130.7	147.7	148.5	130.7	161.1	163.6
⍰ $C_{[2]}$-$C_{[1]}$-$S_{[12]}$···$O_{[14]}$	25.2	-22.0	61.3	-25.3	21.9	-61.2	13.7	15.0
⍰ $C_{[2]}$-$S_{[11]}$-$H_{[12]}$···$O_{[14]}$	57.2	-61.3	48.4	-57.3	63.1	-48.5	56.3	45.8
$S_{[12]}$···$O_{[14]}$	3.38	3.38	3.28	3.38	3.38	3.28	3.45	3.45
C-H···O interaction								
$\mathbf{d}_{C[2]\text{-}H[7]\cdots O[14]}$	2.41	2.40	3.02	2.41	2.40	3.01	2.43	2.44
⍰$C_{[2]}$-$H_{[7]}$···$O_{[14]}$	131.5	135.3	90.4	131.5	135.4	90.4	144.5	143.2
C-H···π interaction								
$\mathbf{d}_{C[16]\text{-}H[18]\cdots C[1]}$	2.92	2.96	2.92	2.92	2.96	2.92	-	-
$\mathbf{d}_{C[16]\text{-}H[18]\cdots C[2]}$	2.86	2.80	3.61	2.86	2.80	3.61	-	-
$\mathbf{d}_{C[16]\text{-}H[18]\cdots C[3]}$	3.77	3.71	-	3.77	3.71	-	-	-
$\mathbf{d}_{C[16]\text{-}H[18]\cdots C[6]}$	3.87	-	3.26	3.87	-	3.27	-	-
$\mathbf{d}_{C[17]\text{-}H[22]\cdots C[1]}$	-	-	2.94	-	-	2.94	2.87	2.97
$\mathbf{d}_{C[17]\text{-}H[22]\cdots C[2]}$	3.03	-	2.83	3.03	-	2.83	2.95	2.80
$\mathbf{d}_{C[17]\text{-}H[22]\cdots C[3]}$	3.22	-	2.81	3.23	-	2.81	-	3.64
$\mathbf{d}_{C[17]\text{-}H[22]\cdots C[4]}$	-	-	2.90	-	-	2.90	-	-
$\mathbf{d}_{C[17]\text{-}H[22]\cdots C[5]}$	-	-	3.00	-	-	3.00	-	-
$\mathbf{d}_{C[17]\text{-}H[22]\cdots C[6]}$	-	-	3.00	-	-	3.00	-	-
C···C interaction								
$d_{C[16]\cdots C[1]}$	3.75	3.81	3.42	3.75	3.81	3.42	-	-
$d_{C[16]\cdots C[2]}$	3.40	3.54	3.71	3.40	3.54	3.71	-	-

$d_{C_{[16]}\cdots C_{[6]}}$	-	-	3.89	-	-	3.89	-	-
$d_{C_{[17]}\cdots C_{[1]}}$	-	-	3.65	-	-	3.65	3.87	3.89
$d_{C_{[17]}\cdots C_{[2]}}$	-	-	3.68	-	-	3.68	3.51	3.70
$d_{C_{[17]}\cdots C_{[3]}}$	-	-	3.84	-	-	3.85	-	-
$d_{C_{[17]}\cdots C_{[4]}}$	-	-	3.89	-	-	3.89	-	-
$d_{C_{[17]}\cdots C_{[6]}}$	3.70		3.77	3.70	-	3.78	-	-
Interaction between *cis*-2-FTP···EtOH								
S-H···O interaction	$Cg+(1)$	$Cg+(2)$	$Cg+(3)$	$Cg^{-}(1)$	Cg^{-} (2)	Cg^{-} (3)	$Ca(1)$	$Ca(2)$
$d_{S_{[11]}-H_{[12]}\cdots O_{[14]}}$	2.24	2.14	2.56	2.24	2.14	2.56	2.28	2.05
$\angle S_{[12]} - H_{[13]}\cdots O_{[14]}$	127.1	142.7	120.7	127.2	142.7	120.7	134.8	170.2
⍰ $C_{[2]}$-$C_{[1]}$-$S_{[12]}\cdots O_{[14]}$	63.4	55.8	-65.1	-63.4	55.8	65.1	-63.2	25.6
⍰ $C_{[2]}$-$S_{[11]}$-$H_{[12]}\cdots O_{[14]}$	43.6	27.7	-37.2	-43.5	27.7	37.1	-24.3	126.3
$S_{[12]}\cdots O_{[14]}$	3.24	3.31	3.45	3.23	3.31	3.45	3.36	3.39
O-H···F interaction								
$d_{O_{[14]}-H_{[15]}\cdots F_{[13]}}$	3.16	2.40	-	3.16	2.40	-	2.54	3.16
$\angle O_{[14]} - H_{[15]}\cdots F_{[13]}$	70.6	107.9	-	70.4	107.9	-	106.2	68.9
C-H···π interaction								
$d_{C_{[16]}-H_{[18]}\cdots C_{[1]}}$	2.96	-	2.81	2.96	-	2.81	2.86	-
$d_{C_{[16]}-H_{[18]}\cdots C_{[2]}}$	3.65	-	2.79	3.65	-	2.79	3.49	-
$d_{C_{[16]}-H_{[18]}\cdots C_{[3]}}$	-	-	2.85	-	-	2.85	2.91	-
$d_{C_{[16]}-H_{[18]}\cdots C_{[4]}}$	-	-	2.92	-	-	2.92	3.08	-
$d_{C_{[16]}-H_{[18]}\cdots C_{[5]}}$	-	-	2.93	-	-	2.93	3.14	-
$d_{C_{[16]}-H_{[18]}\cdots C_{[6]}}$	3.25	-	2.86	3.25	-	2.86	3.03	-
$d_{C_{[17]}-H_{[22]}\cdots C_{[1]}}$	2.96	2.82	2.99	2.96	2.82	2.99	2.98	2.93

$d_{C_{[17]}-H_{[22]}\cdots C_{[2]}}$	2.89	2.90	-	2.89	2.90	-	-	2.80
$d_{C_{[17]}-H_{[22]}\cdots C_{[3]}}$	2.85	3.06	-	2.85	3.06	-	-	3.65
$d_{C_{[17]}-H_{[22]}\cdots C_{[4]}}$	2.85	3.13	-	2.85	3.13	-	-	-
$d_{C_{[17]}-H_{[22]}\cdots C_{[5]}}$	2.90	3.05	-	2.90	3.05	-	-	-
$d_{C_{[17]}-H_{[22]}\cdots C_{[6]}}$	2.94	2.88	2.99	2.94	2.88	2.99	3.03	-
C···C interaction								
$d_{C_{[16]}\cdots C_{[1]}}$	3.40	3.90	3.31	3.40	3.90	3.31	3.35	-
$d_{C_{[16]}\cdots C_{[2]}}$	3.70	3.88	3.57	3.70	3.88	3.57	3.39	3.95
$d_{C_{[16]}\cdots C_{[3]}}$	-	-	3.90	-	-	3.90	3.80	-
$d_{C_{[16]}\cdots C_{[4]}}$	-	-	3.98	-	-	3.98	-	-
$d_{C_{[16]}\cdots C_{[5]}}$	-	-	3.74	-	-	3.74	-	-
$d_{C_{[16]}\cdots C_{[6]}}$	3.84	-	3.40	3.84	-	3.40	3.71	-
$d_{C_{[17]}\cdots C_{[1]}}$	3.66	3.68	3.64	3.66	3.68	3.65	3.66	3.95
$d_{C_{[22]}\cdots C_{[2]}}$	3.70	3.52	-	3.70	3.52	-	3.74	3.75
$d_{C_{[17]}\cdots C_{[3]}}$	3.85	3.66	-	3.85	3.66	-	-	-
$d_{C_{[17]}\cdots C_{[4]}}$	3.94	3.94	-	3.94	3.94	-	-	-
$d_{C_{[17]}\cdots C_{[5]}}$	3.89	-	-	3.89	-	-	-	-
$d_{C_{[17]}\cdots C_{[6]}}$	3.74	3.94	3.63	3.74	3.94	3.74	-	-

The structures and energetics of the low-energy conformers of 2-FTP···EtOH are also calculated at other DFT levels such as B3LYP-D3 as well as MP2 level of theory using 6-311++G(d,p) basis set and energy landscape of these conformers obtained from different calculation levels are provided in Figure 4.10. Although there are some changes in the energetic trend of the conformers calculated at different levels of theory, it is found that the Tg^+ class of conformer is the global minimum. It is intriguing to note in Figure 4.10 that MP2 theory converges the Tg^+(1), Cg^+(2), and Ca(2) structures to dispersion dominated Tg^+(3), Cg^+(1), and Ca(1) structures, respectively. On the other hand, B3LYP-

D3 theory converges the dispersion dominated T*g*⁺(3), C*g*⁺(1), and C*a*(1) structures to

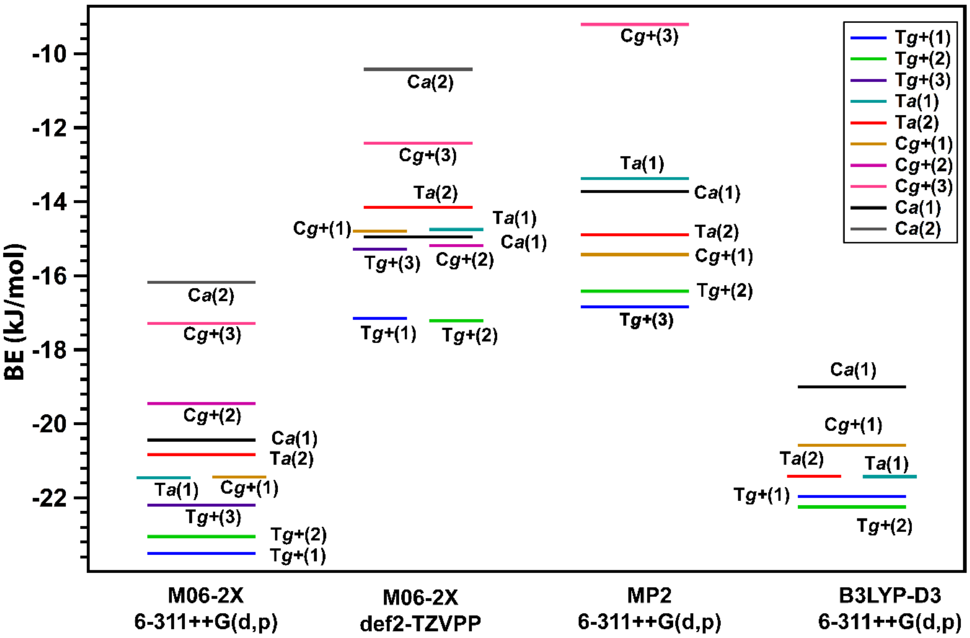

Figure 4.10. Graphical representation of the Binding energies of the conformers of the 2-FTP···EtOH complexes at different levels of theory.

T*g*⁺(1), C*g*⁺(2), and C*a*(2) structures, respectively, having relatively less dispersion interactions. Similar performance of the MP2 and B3LYP-D3 theories on the calculations of the structures of the low-energy conformers of the 2-FTP···MeOH complex has also been noted in this study (vide supra). Hence, the M06-2X/6-311++G(d,p) level of theory seems to be more appropriate for the exploration of the conformational landscape of both 2-FTP···MeOH and 2-FTP···EtOH complexes.

Furthermore, excited state (S_1) calculations of the low-energy conformers of the 2-FTP···MeOH and 2-FTP···EtOH complexes performed at the CIS/6-311++G(d,p) level predict that the low-frequency (12-14 cm^{-1}) intermolecular mode observed in the electronic spectra (Figures 4.2 and 4.3) is due to out of plane bending vibration of the S-H···O hydrogen bond (Table 4.3a-b and 4.4a-b).

Table 4.3.a. Six intermolecular vibrational modes in the excited electronic state (S_1) of

Modes	T1		T2[a]		C1	
	Frequency (cm^{-1})	Vibration[b]	Frequency (cm^{-1})	Vibration[b]	Frequency (cm^{-1})	Vibration[b]
1	17	β_1	17	β_1	16	β_1
2	25	β_2	25	β_2	35	β'_1
3	43	β'_2	43	β'_2	45	β_2
4	64	σ	64	σ	77	σ
5	69	τ_1	69	τ_1	85	τ_1
6	91	τ_2	91	τ_2	98	τ_2

the T1, T2, and C1 conformers of the 2-FTP···MeOH complex calculated at the CIS/6-311++G(d,p) level of theory

[a] In the excited state calculation, the T2 conformer converged to the exited state geometry of the T1 conformer.

[b] β_1 and β'_1 denote out-of-plane bending of the intermolecular S-H···O hydrogen bond, whereas β_2 and β'_2 are in-plane bending for the intermolecular S-H···O hydrogen bond respectively, σ represents intermolecular stretching vibration of the S-H···O hydrogen bond and $\tau1$, $\tau2$ are mixed vibrations due to ring twist and methyl rotation.

Table 4.3.b. Tentative assignment of the low-frequency intermolecular vibrations (cm^{-1}) observed in the electronic spectra (Figure 4.2) of the three conformers of the 2-FTP···MeOH complex

Conformer A	T1	Conformer B	T2	Conformer C	C1
35232	A_0^0	35208	B_0^0	35202	C_0^0
+14	β_1	+14	β_1		
+29	$2\beta_1$	+29	$2\beta_1$		
+42	$3\beta_1$				
+57	$4\beta_1$				
+71	$5\beta_1$				
+85	$6\beta_1$				
+99	$7\beta_1$				
+114	$8\beta_1$				
+126	$9\beta_1$				

Table 4.4.a. Six intermolecular vibrational modes in the excited electronic state (S_1) of the T1, T2, and C1 conformers of the 2-FTP···EtOH complex calculated at the CIS/6-311++G(d,p) level of theory

	Tg^+(2)		**Tg^+(1)**		**Tg^+(3)[a]**		**Ta(2)**		**Ta(1)**	
Modes	Frequency (cm^{-1})	Vibration[b]	Frequency (cm^{-1})	Vibration[b]	Frequency (cm^{-1})	Vibration[b]	Frequency (cm^{-1})	Vibration[b]	Frequency (cm^{-1})	Vibration[b]
1	12	β_1	11	β_1	11	β_1	16	β_1	14	β_1
2	18	τ_1	21	τ_1	21	τ_1	22	τ_1	20	β_1'
3	30	β_2	28	τ_2	28	τ_2	30	$\beta2$	30	τ_1
4	35	β_2'	43	β_2	43	β_2	46	β_2'	45	$\beta2$
5	63	β_1'	66	β_1'	66	β_1'	63	β_1'	52	β_2'
6	88	σ	92	σ	92	σ	91	σ	87	σ

[a] In the excited state calculation, the Tg^+(3) conformer converged to the exited state geometry of the Tg^+(1) conformer.

[b] β_1 and β_1' denote out-of-plane bending of the intermolecular S-H···O hydrogen bond, whereas β_2 and β_2' are in-plane bending for the intermolecular S-H···O hydrogen bond, σ represents intermolecular stretching vibration of the S-H···O hydrogen bond, and $\tau1$, $\tau2$ are mixed vibrations due to ring twist and methyl rotation.

Table 4.4.b. Tentative assignment of the low-frequency intermolecular vibrations (cm^{-1}) observed in the electronic spectra (Figure 4.3) of the three conformers of the 2-FTP···EtOH complex

Conformer A	**T1**	**Conformer B**	**T2**
35232	A_0^0	35208	B_0^0
+12	β_1	+11	β_1
+25	$2\beta_1$	+22	$2\beta_1$
+38	$3\beta_1$	+34	$3\beta_1$
+50	$4\beta_1$	+46	$4\beta_1$
+62	$5\beta_1$	+59	$5\beta_1$
+74	$6\beta_1$	+70	$6\beta_1$
+85	$7\beta_1$	+85	$7\beta_1$
+96	$8\beta_1$		
+108	$9\beta_1$		

4.2.3 IR spectra of the 2-FTP···MeOH and 2-FTP···ETOH complexes and assignment of the observed conformers

4.2.3.1 2-FTP···MeOH complex

Figure 4.11 shows conformation-specific IR spectra of the 2-FTP monomer and 2-FTP···MeOH complex measured using RIDIR spectroscopy. The IR spectrum of the *cis*-2-FTP monomer with the S-H stretching frequency at 2625 cm^{-1}, shown in Figure 4.11(a) ,iwas[267] Theoretical S-H stretching frequency of *cis*-2-FTP calculated at the M06-2X/6-311++G(d,p) level of theory is scaled with respect to the experimental S-H frequency of the monomer and provided in Figure 4.11(b). The corresponding scaling factor (0.954) has been used to correct the calculated harmonic S-H frequencies of different conformers of 2-FTP···MeOH. Figure 4.11(c, e-f) shows IR spectra of 2-FTP···MeOH measured in the S-H and O-H stretching frequency regions by probing the $A_0^0 + 42$ (35274 cm^{-1}), B_0^0 (35208 cm^{-1}), and C_0^0 (35202 cm^{-1}) bands in the electronic spectra of the conformers A, B, and C, respectively, presented in Figure 4.2. Theoretical IR spectra of the six low-energy conformers of 2-FTP···MeOH i.e., T1, T2, C1, C2, T3, C3 (see Figure 4.6 for the structures) exhibiting the S-H and O-H frequencies calculated at the M06-2X/6-311++G(d,p) level of theory are provided in Figure 4.11(d, g-k) respectively. The calculated harmonic O-H frequency of the complex is scaled with respect to the experimental O-H frequency (3686 cm^{-1}) of the MeOH monomer reported in the literature.[271]

A red-shift of ~70-75 cm^{-1} in the experimental S-H frequency of the three conformers of 2-FTP···MeOH with respect to that of the 2-FTP monomer clearly indicates

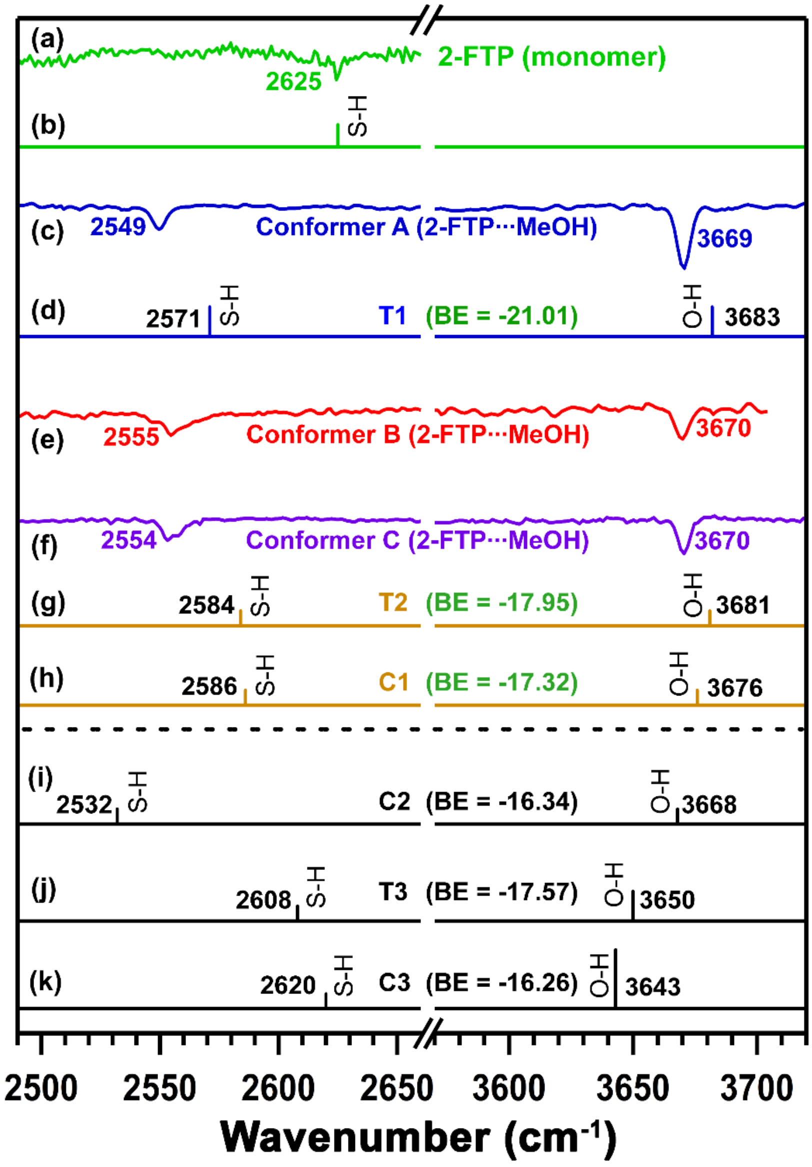

Figure 4.11. Experimental IR spectra of the (a) 2-FTP monomer, (c,e,f) conformers A, B, and C of the 2-FTP···MeOH complex, respectively, measured in the S-H and O-H stretching regions by RIDIR spectroscopy. (b,d,g-k) Theoretical scaled IR spectra of the 2-FTP monomer and T1, T2, C1, C2, T3, and C3 conformers of the 2-FTP···MeOH complex, respectively, calculated at the M06-2X/6-311++G(d,p) level of theory. The scaling of the calculated harmonic S-H frequencies in the complex is done with respect to the experimental S-H frequency of the 2-FTP monomer[267] [Figure 4.11(a)], while the calculated harmonic O-H frequencies in the complex are scaled with reference to the O-H frequency of bare MeOH[271] in the gas-phase.

that all the three conformers of the complex are S-H···O hydrogen bonded. On the other hand, observation of the O-H frequency of the three conformers of 2-FTP···MeOH at ~3670 cm^{-1} with respect to that of the MeOH monomer at 3686 cm^{-1} further confirms that the methanolic O-H group in the complex is free. A small reduction (~16 cm^{-1}) in the dangling O-H frequency is due to the interaction of the methanolic O-H group with the S-H group through S-H···O-H interaction. In the case of phenol···MeOH complex, the frequency of the free O-H group of MeOH was reported at 3680 cm^{-1} while the O-H···O hydrogen bonded phenolic O-H group present there was found to be red-shifted by 199 cm^{-1} with respect to the O-H group of the phenol monomer.[272] Similar amount of red-shift (191 cm^{-1}) in the stretching frequency of phenolic O-H group (O-H···O hydrogen bonded) was observed in p-cresol···MeOH complex while the dangling free O-H frequency of the MeOH moiety present in the complex was found at 3681 cm^{-1}.[4] Indeed, the S-H···O hydrogen bond is turned out to be much weaker than the O-H···O although O-H···S hydrogen bond is reported to be similar in strength to the O-H···O hydrogen bond.[4]

The structures of the three observed conformers of the 2-FTP···MeOH complex can be determined from a careful comparison of their experimental IR spectra with the theoretical IR spectra of the six low-energy conformers of the complex presented in Figure 4.11. The theoretical IR spectra of the O-H···S hydrogen bonded T3 and C3 conformers [Figure 4.11(j, k)] indeed show that the O-H frequency is reasonably red-shifted than that in the other conformers while the perturbation of the S-H frequency with respect to that in the 2-FTP monomer is insignificant. Hence, the T3 and C3 conformers can be excluded easily from the assignment of the observed S-H···O bound conformers. Out of the four remaining conformers, the theoretical IR spectra of T1, T2, and C1 match reasonably well with the experimental IR spectra of the conformers A, B, and C.

The harmonic S-H and O-H frequencies obtained from the M06-2X/6-311++G(d,p) level of calculations are also corrected using the scaling factor of 0.944 deduced at the same level of theory employing the reduced scale factor optimization model as described in the database.[273] A comparison of the experimental IR spectra of the 2-FTP monomer as well as the three observed conformers of the 2-FTP···MeOH complex with the theoretical IR spectra of the six low-energy conformers obtained using database frequency scaling factors are provided in Figure 4.12.A. Interestingly, the matching of the theoretical S-H frequencies derived from the database scaling for the assigned T1, T2, and C1 conformers with their experimental S-H frequencies is excellent, although the same is not satisfactory for the O-H frequencies. We have further calculated the anharmonic vibrational frequencies at the DLPNO-CCSD(T)-F12/aug-cc-pVTZ level on the M06-2X/6-311++G(d,p) level optimized geometries of the 2-FTP monomer, as well as the low-energy conformers of the 2-FTP···MeOH complex using single mode discrete variable representation (DVR) method and the corresponding IR spectra are provided in Figure 4.12.B. Although the experimental S-H frequency of the 2-FTP monomer is well reproduced by the anharmonic calculations, the anharmonic S-H, as well as O-H frequencies of the three assigned conformers (T1, T2, and C1) of 2-FTP···MeOH does not corroborate well with the corresponding frequencies of the observed conformers. However, the anharmonic frequencies of the assigned conformers follow the trend of the experimental frequencies of the three observed conformers of the complex.

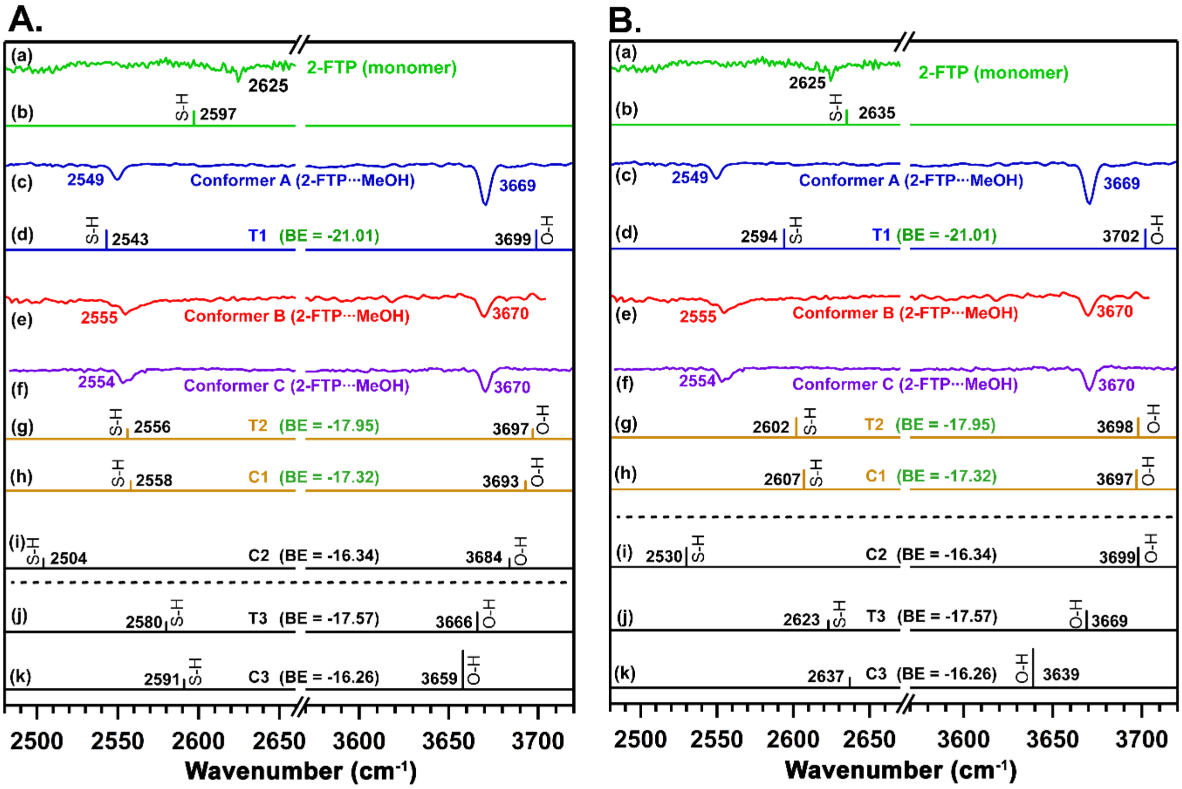

Figure 4.12. Gas-phase IR spectra of (a) 2-FTP and (c, e, f) three experimentally observed conformers of 2-FTP···MeOH complex. (b, d, g-k) are theoretically calculated [**A.**] IR spectra at M06-2X /6-311++G(d,p) level of theory with a scaling factor of 0.944 taken from the database for this specific level of theory.[273] [**B.**] anharmonic vibrational stretching frequencies at S-H and O-H region using the DVR method at DLPNO-CCSD(T)/aug-cc-pVTZ-F12 level of theory using the optimized structure at M06-2X /6-311++G(d,p) level of theory.

4.2.3.2 2-FTP···EtOH complex

IR spectra of the 2-FTP monomer in the S-H stretching frequency region and the conformers A and B of the 2-FTP···EtOH complex in the S-H and O-H frequency regions measured by RIDIR spectroscopy are provided in Figure 4.13(a-b, d) respectively. It is quite clear from the experiment itself that both the observed conformers of the complex are S-H···O hydrogen bonded like those of the 2-FTP···MeOH complex as the S-H frequency is red-shifted by 83-88 cm^{-1} with respect to that in the 2-FTP monomer. On the other hand, the observed O-H stretching frequencies of the conformer A (3648 cm^{-1}) and

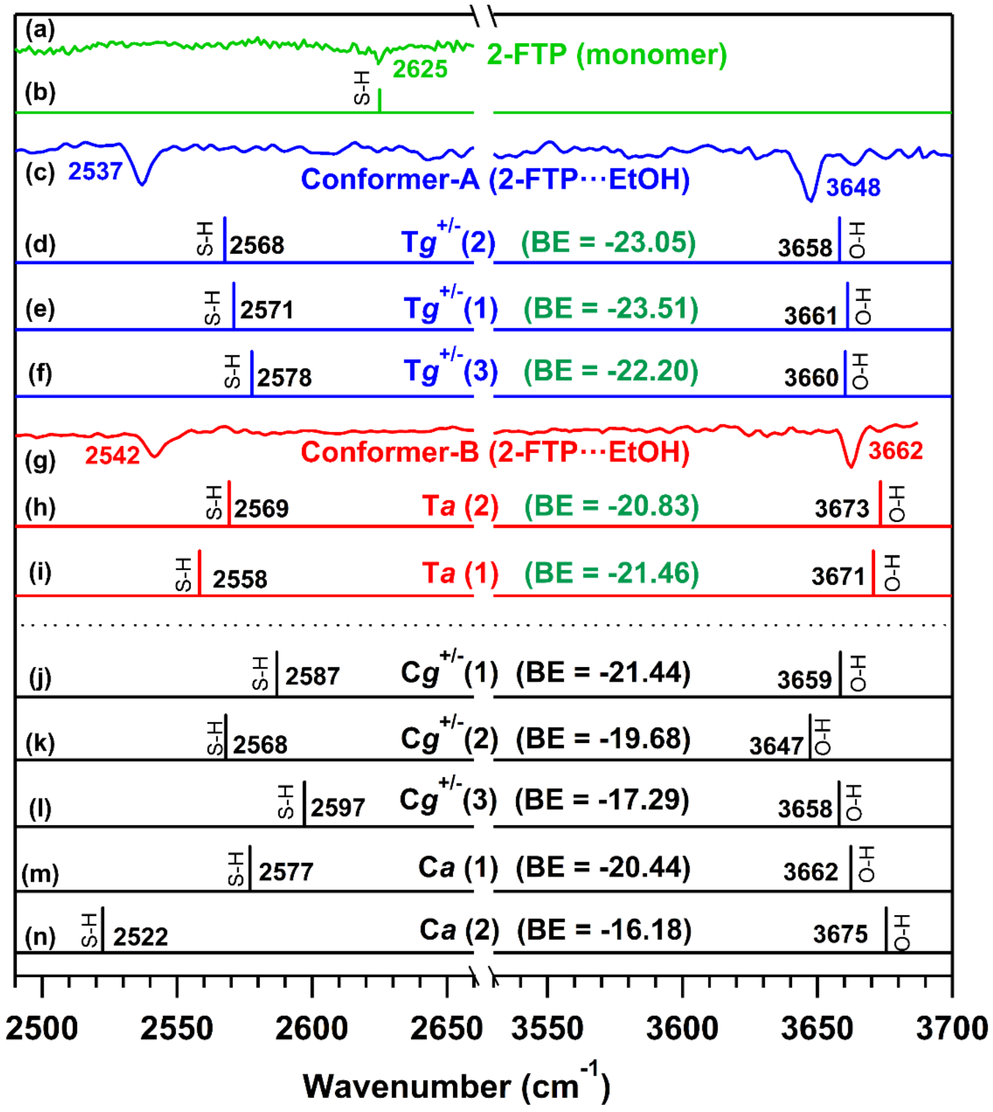

Figure 4.13. Experimental IR spectra of the (a) 2-FTP monomer, (c,g) conformers A and B of the 2-FTP···EtOH complex, respectively, measured in the S-H and O-H stretching regions by RIDIR spectroscopy. (b,d-f,h-n) Theoretical scaled IR spectra of the 2-FTP monomer and T*g*$^{+/-}$(2), Tg$^{+/-}$(1), Tg$^{+/-}$(3), Ta(2), Ta(1), Cg$^{+/-}$(1), Cg$^{+/-}$(2), Cg$^{+/-}$(3), C*a*(1), and C*a*(2) conformers of the 2-FTP···EtOH complex, respectively, calculated at the M06-2X/6-311++G(d,p) level of theory. The scaling of the calculated harmonic S-H frequencies in the complex is done with respect to the experimental S-H frequency of the 2-FTP monomer[267] [Figure 4.13(a)], while the calculated harmonic O-H frequencies in the complex is scaled with reference to the O-H frequency of bare EtOH[274] in the gas-phase.

conformer B (3662 cm^{-1}) of the 2-FTP···EtOH complex are very close to those of the *gauche* (3660 cm^{-1}) and *anti* (3678 cm^{-1}) conformers, respectively, of bare EtOH reported from gas-phase spectroscopy experiments.[274] The O-H stretching frequency of the *anti*-

conformer of the bare EtOH is blue-shifted by 18 cm^{-1} with respect to that of the *gauche* conformer. It should be mentioned here that the ethanolic O-H stretching frequencies of the observed *gauche* and *anti*-conformers of the phenol⋯EtOH complex were reported at 3653 and 3667 cm^{-1}, respectively.[107] In the case of the *p*-cresol⋯EtOH complex reported in the literature, the ethanolic O-H frequencies of the observed *gauche* and *anti*-conformers were found at 3654 and 3669 cm^{-1}, respectively.[4] With regard to both the complexes of phenol and *p*-cresol with EtOH, the O-H group of phenol/*p*-cresol was found to be O-H⋯O hydrogen bonded while the ethanolic O-H was free. A similar difference (14 cm^{-1}) in the O-H stretching frequencies of the *anti* and *gauche* conformers is maintained with the ethanolic moiety bonded with 2-FTP through S-H⋯O hydrogen bond. Hence, the conformers B and A of the 2-FTP⋯EtOH complex observed in the experiment can be assigned easily as the *anti* and *gauche* conformers, respectively, where the ethanolic O-H is free, and the 2-FTP moiety is S-H⋯O hydrogen bonded.

Further detailed assignment of the two observed conformers of the 2-FTP⋯EtOH complex has been done by comparing their IR spectra obtained from the experiment with those of the probable low-energy conformers of the complex derived from the M06-2X/6-311++G(d,p) level of calculations as shown in Figure 4.13. The calculated harmonic S-H and O-H frequencies are scaled with respect to the experimentally recorded S-H frequency of the 2-FTP monomer and the experimental O-H frequency of bare ethanol, respectively.[267, 274] Although a large number of possible conformers are found from the calculations, the experimental IR spectra of the complex presented in Figure 4.13(c, g) indeed simplify the assignment to a good extent, as discussed above. Thus, all the low-energy conformers that are considered for the assignment are S-H⋯O hydrogen bonded, while T$g^{+/-}$(1) is the global minimum. It is worthwhile to mention that the g^{+} and g^{-} conformers of the complex cannot be differentiated, as their structures, energetics, and vibrational frequencies are similar. Hence, both g^+ and g^- conformers are used together to assign the observed conformers through the IR spectra shown in Figure 4.13.

Primarily, the O-H bands of the two observed conformers in the IR spectra of the 2-FTP···EtOH complex dictate the conformational assignment with one of the conformers as *gauche* and the other one as *anti*. It should also be noted that the S-H frequencies (2537 and 2541 cm^{-1}) of the two observed conformers of the complex are very close to each other. Thus, the overall assignment of the observed conformers is done based on the theoretical S-H frequencies of the two conformers, which are close to each other, and their O-H frequencies are separated by 10-15 cm^{-1}. The conformer A could be assigned as one of the T$g^{+/-}$ structures, i.e., T$g^{+/-}$(1), T$g^{+/-}$(2), and T$g^{+/-}$(3) as they are energetically closer and their O-H as well as S-H frequencies are similar as provided in Figure 4.13(d-f) respectively. In that case, the ethanolic O-H group of the conformer B must have *anti*-orientation, and its O-H frequency will be blue-shifted by ~15 cm^{-1}. Hence, one of the Ta conformers [Ta(1) with O-H frequency at 3671 cm^{-1} and Ta(2) with O-H frequency at 3673 cm^{-1}] presented in Figure 4.13 (h, i) could be the most possible choices for the conformer B. The C$g^{+/-}$ and Ca conformers could be excluded from the assignment of the two observed conformers considering the overall energetics of the theoretically calculated conformers of 2-FTP···EtOH, the possibility of the observation of the global minimum conformer T$g^{+/-}$ and the trend of the S-H and OH frequencies of the two conformers observed in the experiment. Interestingly, the two observed conformers of phenol···EtOH as well as *p*-cresol···EtOH reported in the literature are similarly *gauche* and *anti* only.[4, 107]

Additionally, the harmonic S-H and O-H frequencies of various conformers of the 2-FTP···EtOH complex calculated at the M06-2X/6-311++G(d,p) level of theory are corrected with a scaling factor of 0.944 obtained from the database.[273] A comparison of the experimental IR spectra of the two observed conformers with the theoretical IR spectra of the low-energy conformers scaled from the database is shown in Figure 4.14.A. Again, the database scaling of the harmonic frequencies demonstrates an excellent matching of the experimental S-H frequencies of the complex with the theoretical S-H frequencies of the assigned conformers although the agreement between the experimental and theoretical O-H frequencies is inadequate. Furthermore, anharmonic S-H and O-H frequencies of the assigned conformers of 2-FTP···EtOH calculated at the DLPNO-CCSD(T)-F12/aug-cc-pVTZ level on the M06-2X/6-311++G(d,p) level optimized

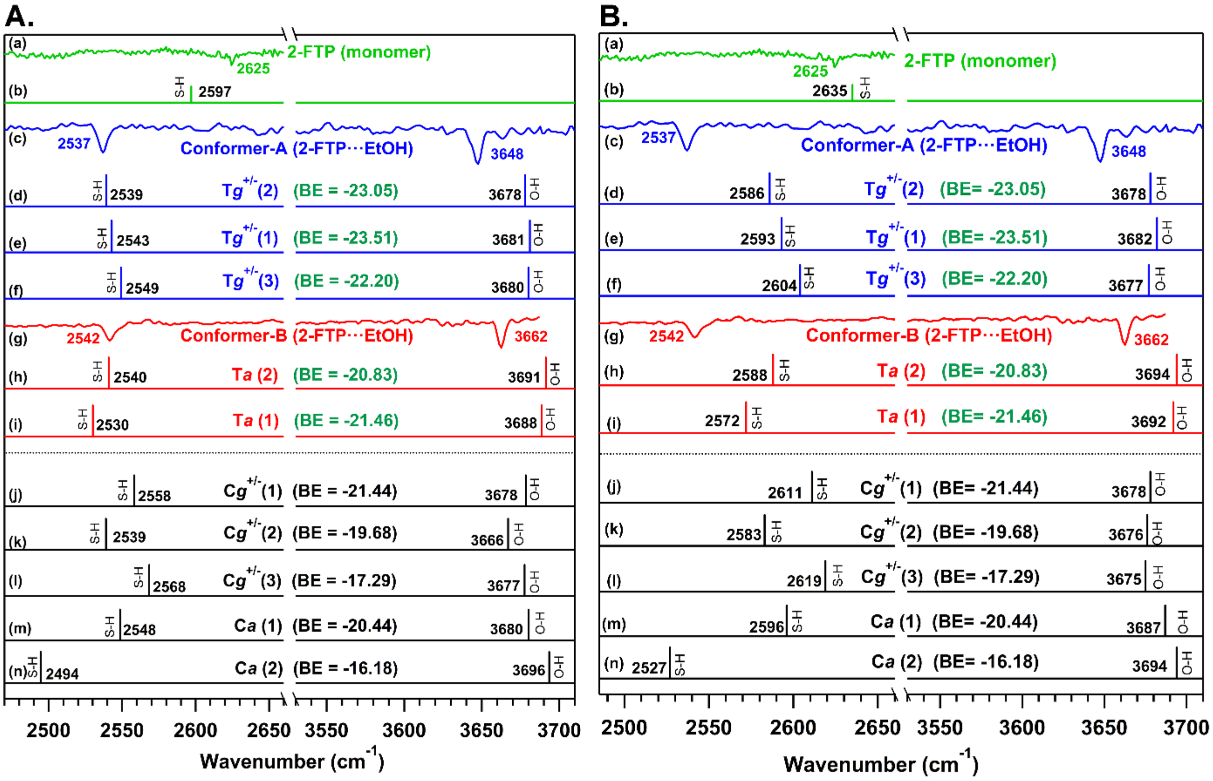

Figure 4.14. Gas-phase IR spectra of (a) 2-FTP and (c,g) two experimentally observed conformers of 2-FTP···EtOH complex. (b, d-f, h-n) are theoretically calculated [**A.**] IR spectra at M06-2X /6-311++G(d,p) level of theory with a scaling factor of 0.944 taken from the database for this specific level of theory.[273] [**B.**] anharmonic vibrational stretching frequencies at S-H and O-H region using the DVR method at DLPNO-CCSD(T)/aug-cc-pVTZ-F12 level of theory using the optimized structure at M06-2X /6-311++G(d,p) level of theory

geometries (Figure 4.14.B) follow the trend of the experimental frequencies of the two observed conformers although the quantitative agreement between the experimental and theoretical frequencies is not good.

Finally, a comparison of the observed IR red-shift in the S-H stretching frequency ($\Delta\upsilon_{S\text{-}H}$) in 2-FTP···EtOH (88 cm^{-1}), and 2-FTP···MeOH (76 cm^{-1}) with that in 2-FTP···H_2O (30 cm^{-1}),[267] reveals that the strength of the S-H···O hydrogen bond increases systematically by changing the hydrogen bond acceptor from H_2O to MeOH to EtOH. A plot of $\Delta\upsilon_{S\text{-}H}$ as a function of the proton affinity of these three hydrogen bond acceptors exhibited in Figure 4.15 shows a linear correlation between the $\Delta\upsilon_{S\text{-}H}$ i.e., strength of the S-H···O hydrogen bond and proton affinity of H_2O (697 kJ/mol), MeOH (761 kJ/mol), and EtOH (788 kJ/mol).[275] Wategaonkar and coworkers reported $\Delta\upsilon_{S\text{-}H}$ of 44, 46, and 49 cm^{-1} in S-H···O hydrogen bonded H_2S···MeOH, H_2S···Et_2O, and H_2S···dioxane complexes, respectively.[7] On the other hand, $\Delta\upsilon_{S\text{-}H}$ of only 30 cm^{-1} was observed in the S-H···O hydrogen bonded 2-phenylethanethiol···Et_2O complex studied by Robertson and

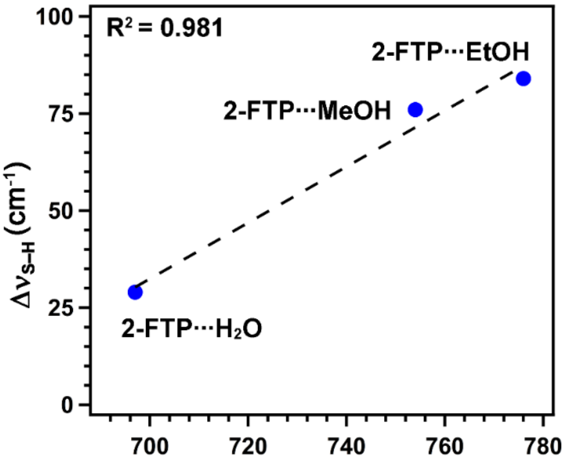

Figure 4.15. Correlation between the red-shift in the experimental stretching frequency corresponding to the S-H bond and proton-affinity (PA) of the acceptor part.

coworkers.[9] Hence, the present work demonstrates that the S-H⋯O hydrogen bond, although weak, can be strengthened by a proper choice of the hydrogen bond donor and acceptor in terms of their pKa and proton affinity, respectively.

4.2.4 Theoretical evaluation of the non-covalent interactions present in the observed conformers of the 2-FTP⋯MeOH and 2-FTP⋯EtOH complexes.

The nature and strength of various non-covalent interactions, including weak secondary interactions present in the observed conformers of the 2-FTP⋯MeOH and 2-FTP⋯EtOH complexes, are evaluated through NBO, QTAIM, and LMO-EDA calculations. Figure 4.16 shows the NBO overlap and 2nd order perturbation energy [$E^{(2)}$] for different non-covalent interactions present in the T1, T2, and C1 conformers of 2-FTP⋯MeOH calculated at the M06-2X/6-311++G(d,p) level of theory. It could be noted from Figure 7 that the total $E^{(2)}$ value for the S-H⋯O hydrogen bond in T1 is 17.99 kJ/mol (7.45+10.54 kJ/mol), and the $E^{(2)}$ values for the secondary C-H⋯O, C-H⋯π, and C-H⋯S interactions present there are 5.52, 1.30, and 0.88 kJ/mol, respectively. The $E^{(2)}$ value for the S-H⋯O hydrogen bond in T2 is 11.05 kJ/mol (3.81+7.24 kJ/mol), while the values for the weak secondary n(O)→π*(C=C), C-H⋯π, and C-H⋯S interactions are 3.14, 0.92, and 1.26 kJ/mol, respectively. The $E^{(2)}$ value presented for the S-H⋯O hydrogen bond in C1 is 10.46 kJ/mol (4.35+6.11 kJ/mol), and the $E^{(2)}$ values for the secondary weak n(O)→π*(C=C), C-H⋯π, and C-H⋯S interactions are 4.23, 1.79 and 0.54 kJ/mol, respectively.

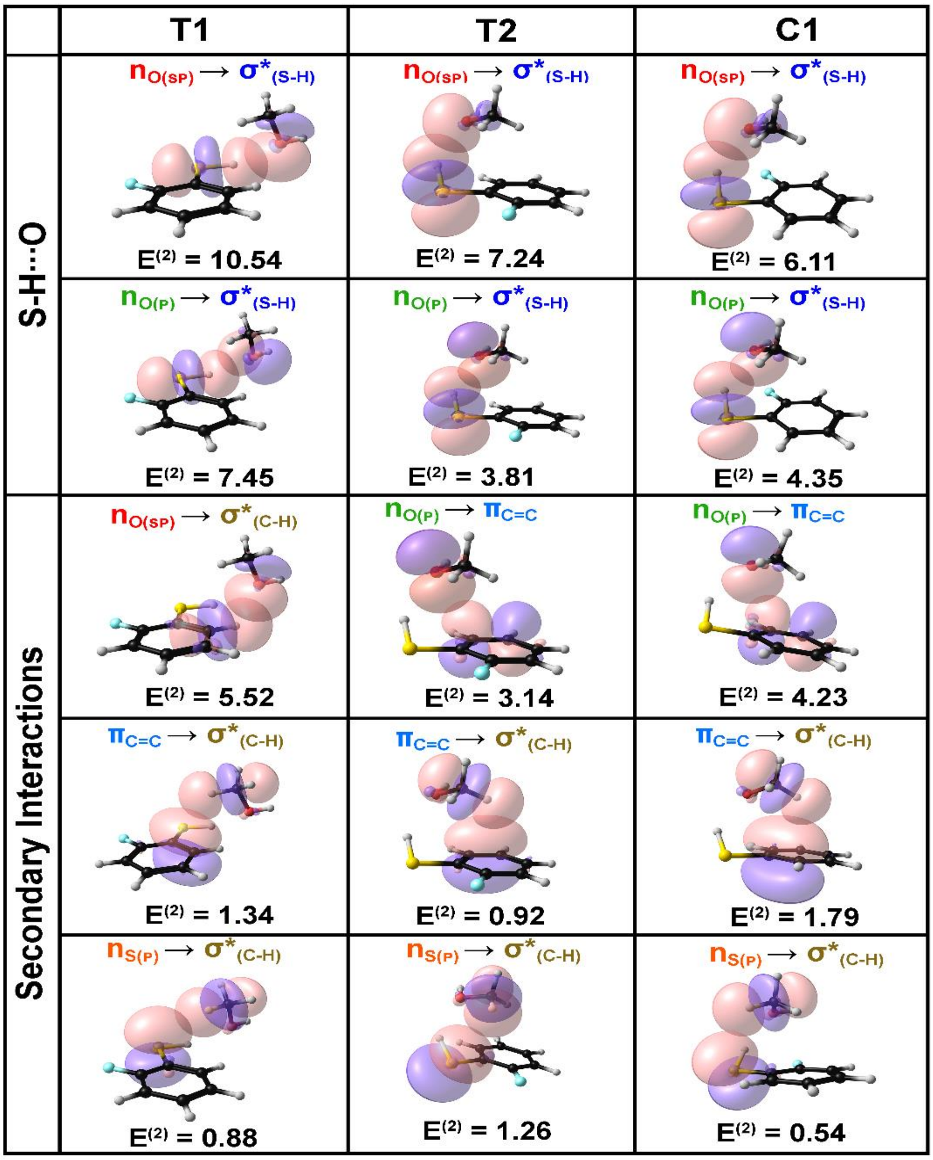
T1
T2
C1
S-H···O
$n_{O(SP)} \rightarrow \sigma^*_{(S-H)}$
E(2) = 10.54
$n_{O(SP)} \rightarrow \sigma^*_{(S-H)}$
E(2) = 7.24
$n_{O(SP)} \rightarrow \sigma^*_{(S-H)}$
E(2) = 6.11
$n_{O(P)} \rightarrow \sigma^*_{(S-H)}$
E(2) = 7.45
$n_{O(P)} \rightarrow \sigma^*_{(S-H)}$
E(2) = 3.81
$n_{O(P)} \rightarrow \sigma^*_{(S-H)}$
E(2) = 4.35
Secondary Interactions
$n_{O(SP)} \rightarrow \sigma^*_{(C-H)}$
E(2) = 5.52
$n_{O(P)} \rightarrow \pi_{C=C}$
E(2) = 3.14
$n_{O(P)} \rightarrow \pi_{C=C}$
E(2) = 4.23
$\pi_{C=C} \rightarrow \sigma^*_{(C-H)}$
E(2) = 1.34
$\pi_{C=C} \rightarrow \sigma^*_{(C-H)}$
E(2) = 0.92
$\pi_{C=C} \rightarrow \sigma^*_{(C-H)}$
E(2) = 1.79
$n_{S(P)} \rightarrow \sigma^*_{(C-H)}$
E(2) = 0.88
$n_{S(P)} \rightarrow \sigma^*_{(C-H)}$
E(2) = 1.26
$n_{S(P)} \rightarrow \sigma^*_{(C-H)}$
E(2) = 0.54

Figure 4.16. NBO overlap for different non-covalent interactions present in the observed T1, T2, and C1 conformers of the 2-FTP···MeOH complex calculated at the M06-2X/6-311++G(d,p) level of theory. NBO second-order perturbation energy [$E^{(2)}$] values in kJ/mol are also provided with each of the interactions shown in the figure.

The NBO interaction energy for the primary non-covalent interaction, i.e., S-H···O hydrogen bond present in T1, T2, and C1, can be compared with the relative strength of this hydrogen bond revealed from the IR spectra in terms of the red-shift in the S-H stretching frequency ($\Delta\upsilon_{S\text{-}H}$). It is found from Figure 4.16 that the NBO interaction energy for the S-H···O hydrogen bond in T1 (17.99 kJ/mol) is higher than that in T2 (11.05 kJ/mol) and C1 (10.46 kJ/mol). This finding correlates qualitatively with the observed

$\Delta\upsilon_{S\text{-}H}$ values in T1 (76 cm^{-1}), T2 (70 cm^{-1}), and C1 (71 cm^{-1}) i.e., the strength of the S-H···O hydrogen bond. The geometrical parameters for the S-H···O hydrogen bond of these three conformers provided in Figure 4.7 and Table 4.1 also corroborate the findings from the IR spectroscopy and NBO results.

Figure 4.17 shows the NBO overlap and E$^{(2)}$ values for different non-covalent interactions present in the observed Tg^+ and Ta conformers of the 2-FTP···EtOH complex obtained from the M06-2X/6-311++G(d,p) level of calculation. The total E$^{(2)}$ values for the S-H···O hydrogen bond present in the Tg^+(1), Tg^+(2), and Tg^+(3) conformers are 16.02 kJ/mol (12.80+3.22 kJ/mol), 19.67 kJ/mol (7.41+12.26 kJ/mol), 9.46 kJ/mol, respectively (Figure 4.17). In the case of the Ta(1) and Ta(2) conformers, the total E$^{(2)}$ values for the S-H···O hydrogen bond are 24.52 kJ/mol (5.90+18.62 kJ/mol) and 20.21 kJ/mol, respectively. The conformers Tg^+(1), Tg^+(2), Ta(1) and Ta(2) are stabilized by additional secondary interactions namely C-H···O, C-H···π, and C-H···S. The Tg^+(3) conformer has C-H···π, and C-H···S secondary interactions while the C-H···O interaction is replaced there by n(O)→π^*(C=C) interaction. As the $\Delta\upsilon_{S\text{-}H}$ values of the two observed conformers A (88 cm^{-1}) and B (83 cm^{-1}) of 2-FTP···EtOH are very close to each other, the Tg^+(2) [19.67 kJ/mol] and Ta(2) [20.20 kJ/mol] with similar NBO E$^{(2)}$ values for the S-H···O hydrogen bond can tentatively better represent the two assigned conformers. However, it is more

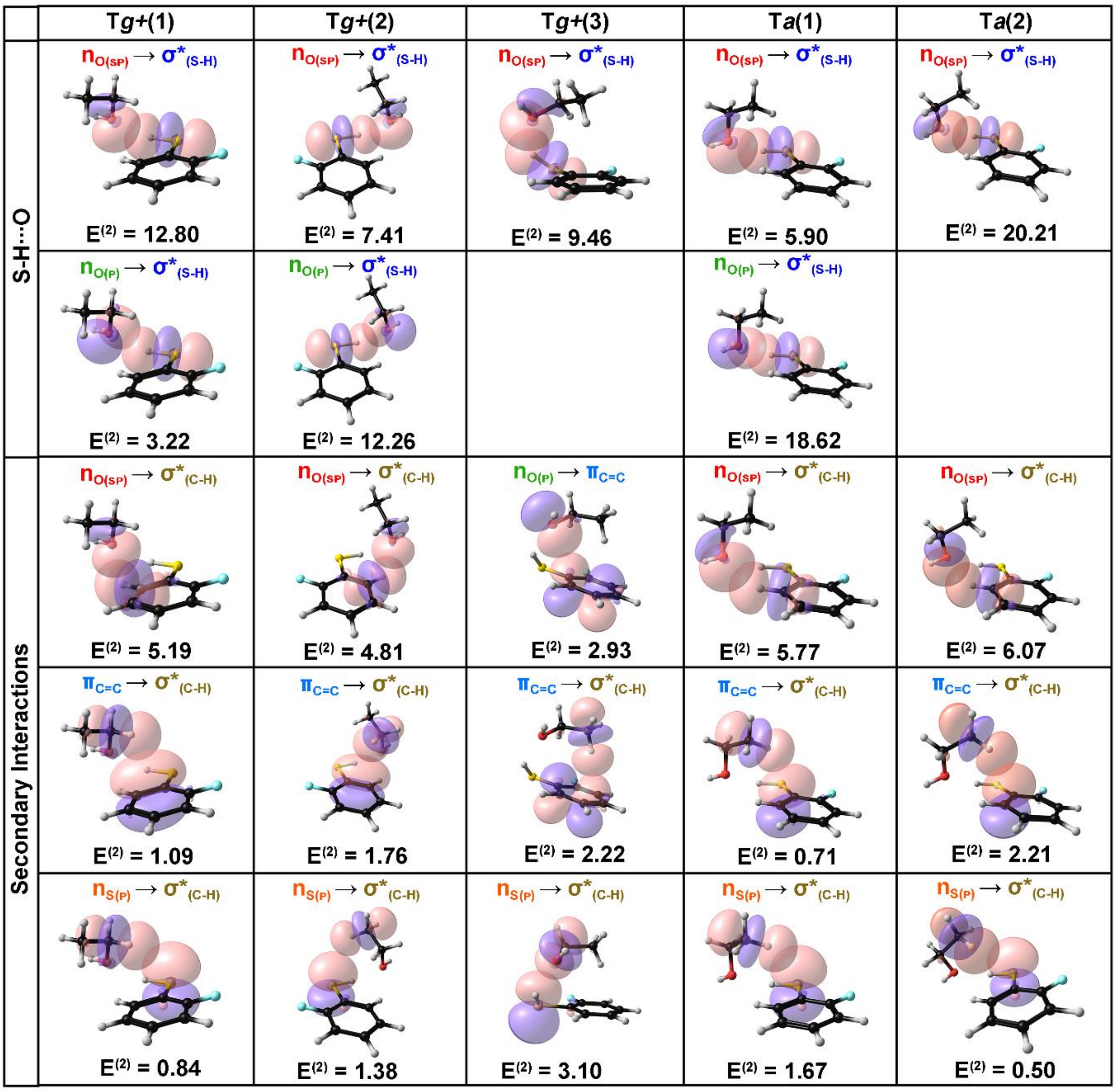

T*g*+(1)
T*g*+(2)
T*g*+(3)
T*a*(1)
T*a*(2)
S-H···O
$n_{O(SP)} \rightarrow \sigma^*_{(S-H)}$
$E^{(2)} = 12.80$
$n_{O(SP)} \rightarrow \sigma^*_{(S-H)}$
$E^{(2)} = 7.41$
$n_{O(SP)} \rightarrow \sigma^*_{(S-H)}$
$E^{(2)} = 9.46$
$n_{O(SP)} \rightarrow \sigma^*_{(S-H)}$
$E^{(2)} = 5.90$
$n_{O(SP)} \rightarrow \sigma^*_{(S-H)}$
$E^{(2)} = 20.21$
$n_{O(P)} \rightarrow \sigma^*_{(S-H)}$
$E^{(2)} = 3.22$
$n_{O(P)} \rightarrow \sigma^*_{(S-H)}$
$E^{(2)} = 12.26$
$n_{O(P)} \rightarrow \sigma^*_{(S-H)}$
$E^{(2)} = 18.62$
Secondary Interactions
$n_{O(SP)} \rightarrow \sigma^*_{(C-H)}$
$E^{(2)} = 5.19$
$n_{O(SP)} \rightarrow \sigma^*_{(C-H)}$
$E^{(2)} = 4.81$
$n_{O(P)} \rightarrow \pi_{C=C}$
$E^{(2)} = 2.93$
$n_{O(SP)} \rightarrow \sigma^*_{(C-H)}$
$E^{(2)} = 5.77$
$n_{O(SP)} \rightarrow \sigma^*_{(C-H)}$
$E^{(2)} = 6.07$
$\pi_{C=C} \rightarrow \sigma^*_{(C-H)}$
$E^{(2)} = 1.09$
$\pi_{C=C} \rightarrow \sigma^*_{(C-H)}$
$E^{(2)} = 1.76$
$\pi_{C=C} \rightarrow \sigma^*_{(C-H)}$
$E^{(2)} = 2.22$
$\pi_{C=C} \rightarrow \sigma^*_{(C-H)}$
$E^{(2)} = 0.71$
$\pi_{C=C} \rightarrow \sigma^*_{(C-H)}$
$E^{(2)} = 2.21$
$n_{S(P)} \rightarrow \sigma^*_{(C-H)}$
$E^{(2)} = 0.84$
$n_{S(P)} \rightarrow \sigma^*_{(C-H)}$
$E^{(2)} = 1.38$
$n_{S(P)} \rightarrow \sigma^*_{(C-H)}$
$E^{(2)} = 3.10$
$n_{S(P)} \rightarrow \sigma^*_{(C-H)}$
$E^{(2)} = 1.67$
$n_{S(P)} \rightarrow \sigma^*_{(C-H)}$
$E^{(2)} = 0.50$

Figure 4.17. NBO overlap for different non-covalent interactions present in the observed Tg^+ and Ta conformers of the 2-FTP···EtOH complex calculated at the M06-2X/6-311++G(d,p) level of theory. NBO second-order perturbation energy [$E^{(2)}$] values in kJ/mol are also provided with each of the interactions shown in the figure.

appropriate to conclude that one of the three T$g^{+/-}$ conformers and one of the two Ta conformers can be the preferred candidates for the observed conformers A and B, respectively, of the 2-FTP···EtOH complex.

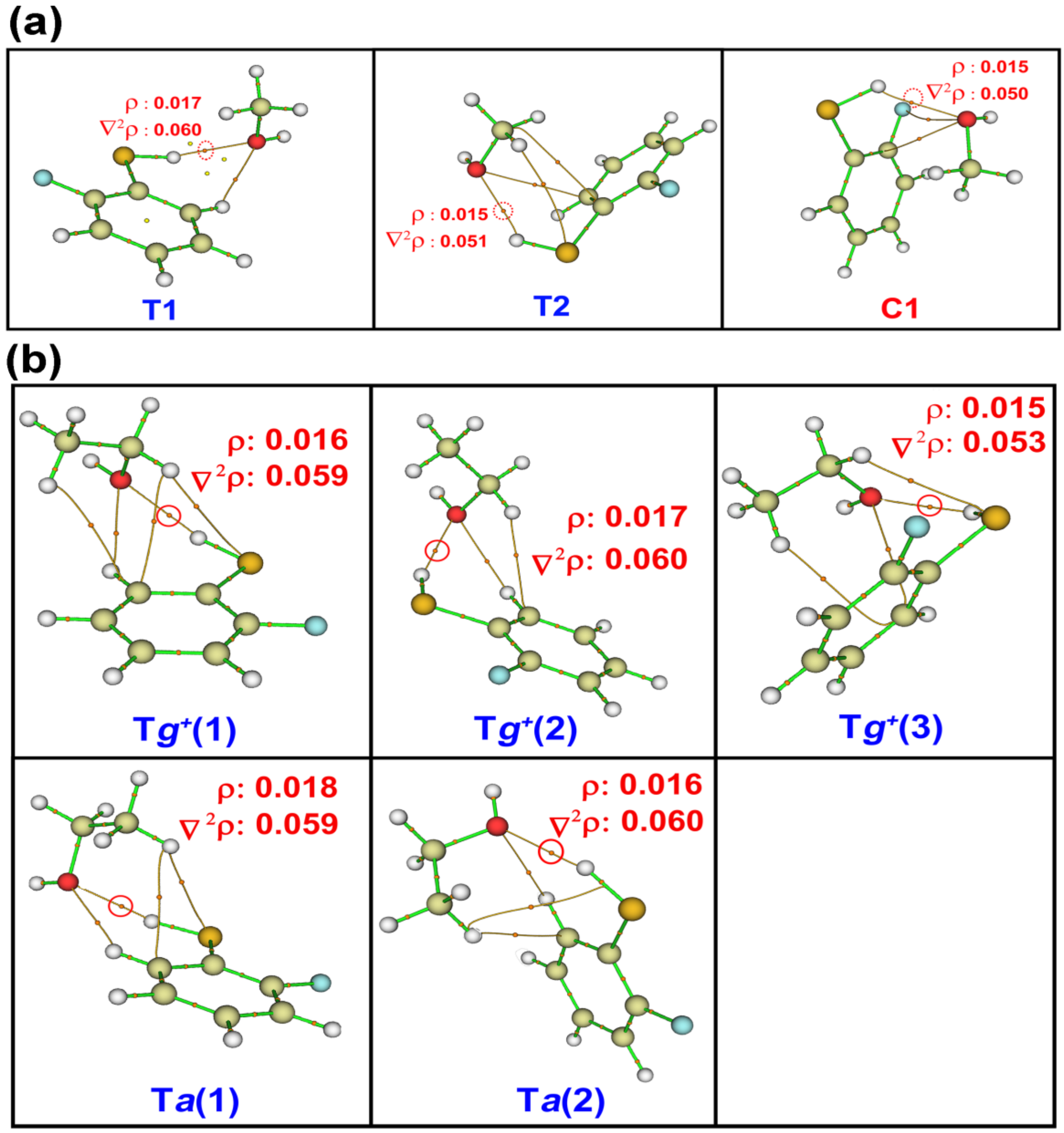
(a)
ρ : 0.017
∇²ρ : 0.060
T1
ρ : 0.015
∇²ρ : 0.051
T2
ρ : 0.015
∇²ρ : 0.050
C1
(b)
ρ: 0.016
∇²ρ: 0.059
Tg⁺(1)
ρ: 0.017
∇²ρ: 0.060
Tg⁺(2)
ρ: 0.015
∇²ρ: 0.053
Tg⁺(3)
ρ: 0.018
∇²ρ: 0.059
Ta(1)
ρ: 0.016
∇²ρ: 0.060
Ta(2)

Figure 4.18. Topology of the electron density of the (a) T1, T2, and C1 conformers of the 2-FTP···MeOH (b) $Tg^+(1)$, $Tg^+(2)$, $Tg^+(3)$, Ta(1), and Ta(2) conformers of the 2-FTP···EtOH complexes obtained from QTAIM calculations performed on the M06-2X/6-311++G(d,p) level optimized structures. The electron density (ρ) and its Laplacian ($\nabla^2\rho$) at the BCPs of only the primary non-covalent interaction i.e., S-H···O hydrogen bond for all the conformers of the two complexes are provided with the molecular graphs.

The presence of multiple non-covalent interactions in the T1, T2, and C1 conformers of 2-FTP···MeOH as well as in the Tg^+ and T*a* conformers of 2-FTP···EtOH are further confirmed from QTAIM calculations. The molecular graphs containing the bond critical points (BCPs) and bond paths for all the three observed conformers of 2-

FTP···MeOH and the two observed conformers of 2-FTP···EtOH obtained from the M06-2X/6-311++G(d,p) level of calculation are presented in Figure 4.18 (a and b), respectively. The BCPs for the S-H···O hydrogen bond as well as other weak secondary interactions for each of the conformers of 2-FTP···MeOH and 2-FTP···EtOH shown in Figure 4.18 corroborate with the NBO results presented in Figures 4.16 and 4.17. The electron density (ρ) and its Laplacian ($\nabla^2\rho$) at the BCPs of only the primary non-covalent interaction, i.e., S-H···O hydrogen bond for all the conformers of the two complexes are provided with the molecular graphs presented in Figure 4.18. Furthermore, plots of the experimental $\Delta\upsilon_{S\text{-}H}$ (IR red-shift) values as a function of ρ at the BCPs as well as $E^{(2)}$ (NBO interaction energies) values for the S-H···O hydrogen bond of the most stable conformer of the 2-FTP···H_2O, 2-FTP···MeOH, and 2-FTP···EtOH presented in Figures 4.19(a) and 4.19(b) exhibit a linear correlation. Hence, the overall correlation between the strength of the S-H···O hydrogen bond revealed from the experimental IR red-shift and the theoretically evaluated corresponding QTAIM and NBO parameters of the complexes is

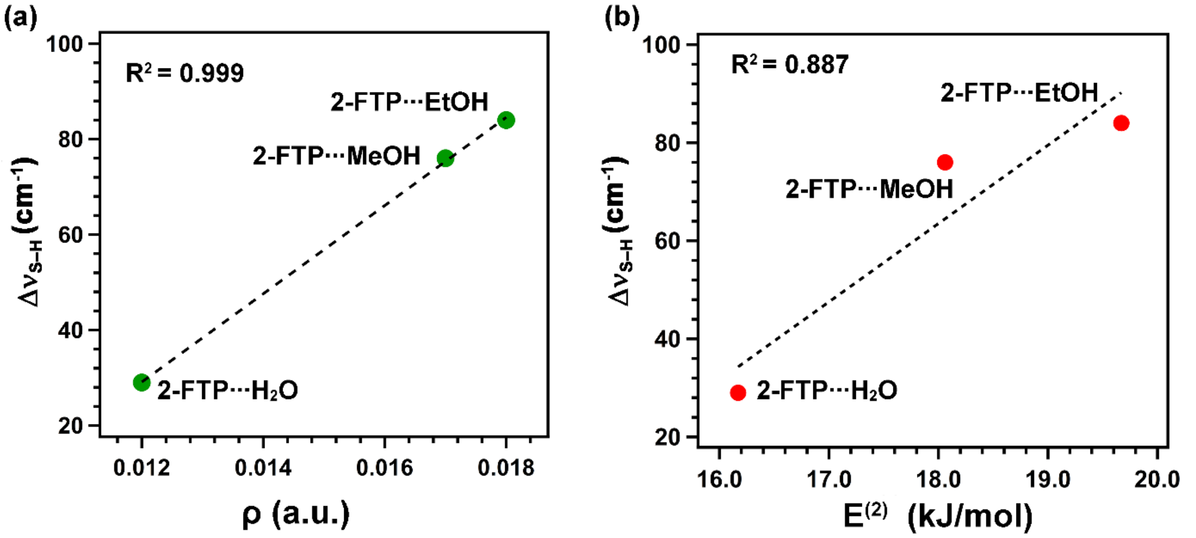

Figure 4.19. Correlation between the red-shift in experimental S-H stretching frequency and (a) NBO second order perturbation energy ($E^{(2)}$) and (b) electron density (ρ) at the bond critical point S-H···O contacts. NBO perturbation energy and the electron density are calculated at M06-2X/6-311++G(d,p) level of theory.

noteworthy.

Furthermore, we have decomposed the total interaction energies of the three observed conformers of 2-FTP···MeOH and the two observed conformers of 2-FTP···EtOH using the LMO-EDA method in order to determine the relative contribution of their different components to the stability of the complexes. The LMO-EDA method decomposes the total interaction energy (E_{TOTAL}) of a complex into electrostatics (E_{ES}), exchange (E_{EX}), repulsion (E_{REP}), polarization (E_{POL}) and dispersion (E_{DISP}). Different components of the total interaction energies of the T1, T2, and C1 conformers of 2-FTP···MeOH and Tg^+(1), Tg^+(2), Tg^+(3), Ta(1), and Ta(2) conformers of 2-FTP···EtOH are presented in Figures 4.20 and 4.21, respectively. It is intriguing to note that both electrostatics and dispersion play a significant role in the stabilization of all the observed conformers of 2-FTP···MeOH and 2-FTP···EtOH although the dispersion is the dominating

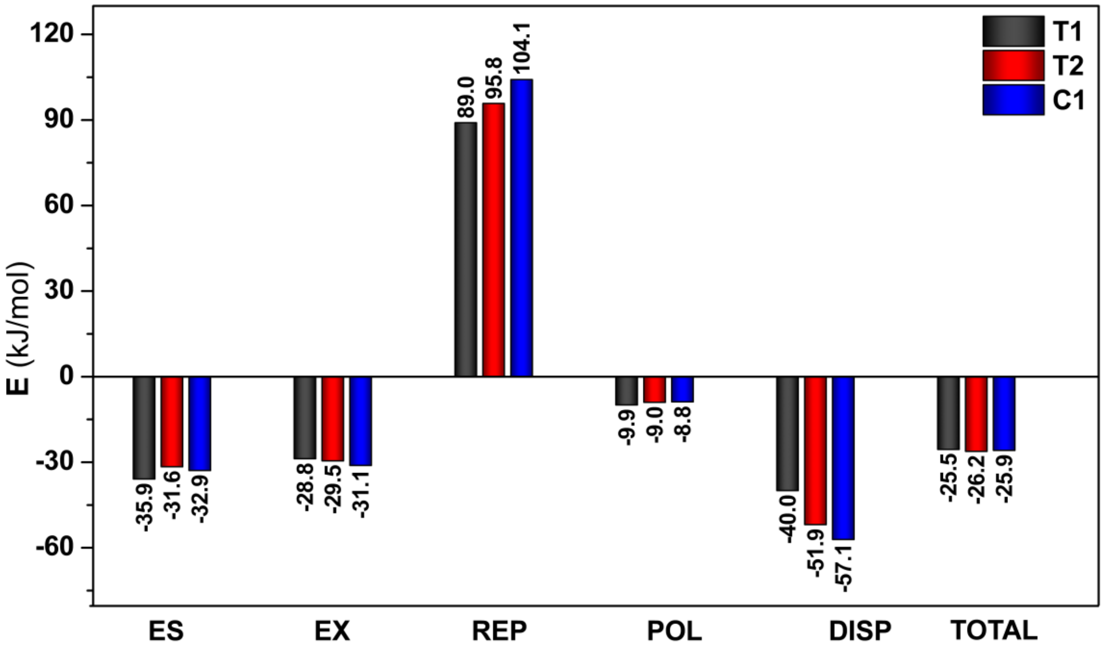

Figure 4.20. Decomposition of the total interaction energies of the T1, T2, and C1 conformers of the 2-FTP···MeOH complex using LMO-EDA method at the M06-2X/6-311++G(d,p) level of theory. The total interaction energy (TOTAL) is decomposed into electrostatics (ES), exchange (EX), repulsion (REP), polarization (POL), and dispersion (DISP).

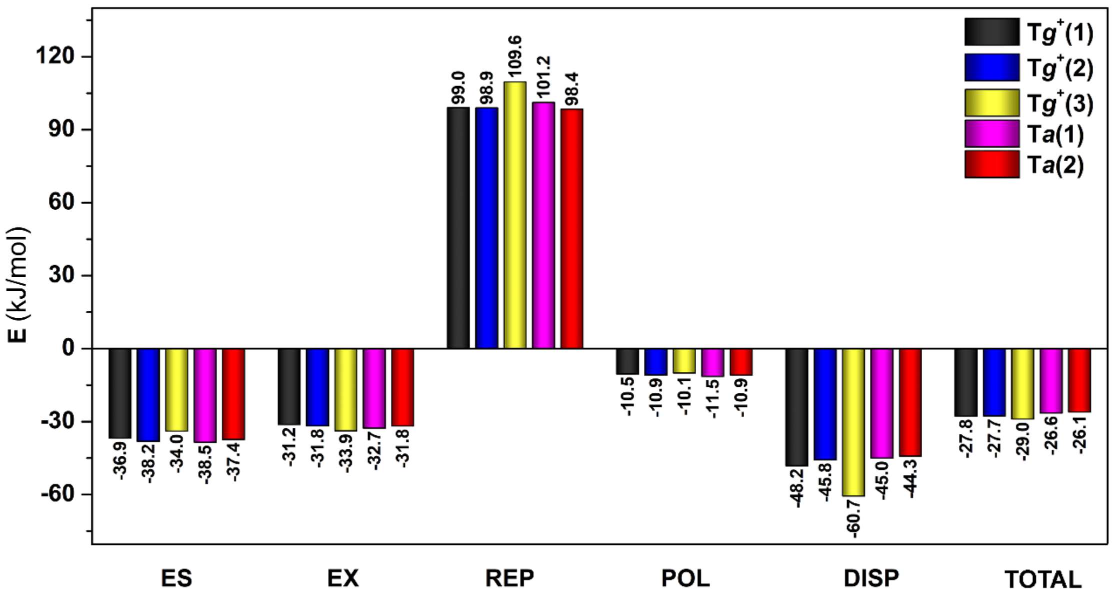

Figure 4.21. Decomposition of the total interaction energies of the T*g*+(1), T*g*+(2), T*g*+(3), T*a*(1), and T*a*(2) conformers of the 2-FTP···EtOH complex using LMO-EDA method at the M06-2X/6-311++G(d,p) level of theory. The total interaction energy is decomposed into electrostatics (ES), exchange (EX), repulsion (REP), polarization (POL), and dispersion (DISP).

interaction for all the observed conformers of the two complexes. It is also remarkable that the dispersion component in the stacked structures (T2 and C1) of 2-FTP···MeOH is significantly larger than that in the non-stacked structure (T1). Similarly, the dispersion interaction presents in the stacked structure [T*g*+(3)] of 2-FTP···EtOH is found to be larger than that in the non-stacked structures [T*g*+(1), T*g*+(2), T*a*(1), and T*a*(2)]. It is also noteworthy that the repulsion component of the interaction energy is larger for the stacked structures [T2, C1, and T*g*+(3)] having pronounced dispersion interaction than that for the non-stacked structures [T1, T*g*+(1), T*g*+(2), T*a*(1) and T*a*(2)] of the two complexes. Hence, the components of the interaction energies revealed from the EDA calculations correlate qualitatively with the structures and geometrical parameters of the observed conformers of the 2-FTP···MeOH and 2-FTP···EtOH complexes provided in Figures 4.6, 4.8, and Tables 4.1, 4.2.

4.3 Conclusions

In summary, we have studied 1:1 complexes of 2-FTP with MeOH as well as EtOH by measuring mass-selected conformation-specific electronic and IR spectra using 1C-R2PI, UV-UV hole-burning and IR-UV double resonance spectroscopy combined with quantum chemistry calculations. Three conformers of 2-FTP···MeOH and two conformers of 2-FTP···EtOH are observed in the experiment. Quantum chemistry calculations predict that the observed conformers of these two complexes are stabilized primarily by S-H···O hydrogen bonding along with various weak secondary interactions such as C-H···O, C-H···π, C-H···S, and stacking interactions. Conformation-specific IR spectra show that the red-shift values in the S-H stretching frequency in the 2-FTP···MeOH and 2-FTP···EtOH complexes are 76 and 88 cm^{-1}, respectively. A comparison of the IR red-shift in the S-H stretching frequency in 2-FTP···H_2O (30 cm^{-1}) with respect to that in 2-FTP···MeOH and 2-FTP···EtOH points out that the strength of the S-H···O hydrogen bond, although weak, can be modulated systematically by varying the proton affinities of the hydrogen bond acceptors. The presence of the S-H···O hydrogen bond and other weak secondary interactions in the experimentally observed conformers is also verified by NBO and QTAIM calculations. Various components of the interaction energies in 2-FTP···MeOH and 2-FTP···EtOH determined from the LMO-EDA calculations correlate well with the structures of the complexes observed in the experiment.

Chapter 5

Interplay between proton affinity and steric repulsion on S-H···O hydrogen bond: Spectroscopic study and quantum chemical calculations

5.1 Introduction

In preceding chapters, we have detailed how the strength of the sulfur-centered hydrogen bonding (SCHB) interaction (S-H···O) relies on the interplay of the proton affinity (PA) of the hydrogen bond acceptor atom or group of atoms and the acidity (pKa) of the hydrogen bond donor part. We have observed a linear correlation between the red-shift in the stretching frequency of the S-H bond and the proton affinity of the complexing partner. Notably, a linear increment in binding energy was identified as we moved from water to methanol to ethanol. In Chapter 1, we have discussed the importance of sulfur-center hydrogen bonding in biological and materials studies. Because of its strength and directionality nature, SCHB can also act like a glue between the molecules in the non-covalent assembly. In addition, the modulation of such hydrogen bonding is equally important for the development of supramolecular materials, drug design, and crystal engineering. Conventional hydrogen bonding has already been established for these purposes.[276-278] The forefront of current interest lies in the exploration of unconventional hydrogen bonding for the development of valuable drugs and other materials [64, 147-148, 216, 279-282] Exploring the modulation of weak unconventional hydrogen bonds has become an exceptionally intriguing area of study. There are several ways to modulate the strength of the hydrogen bonding.[120-123, 283] The most common method is tweaking the pKa of the donor and PA of the acceptor part, as the strength of the hydrogen bonding depends on the pKa of the hydrogen bond donor and the PA of the hydrogen bond acceptor. Wategaonkar and co-workers reported a linear correlation of the red-shift in the phenolic O-H and pKa of the hydrogen bond donor in the study of the complexes of a series of phenol derivatives with Me_2O and Me_2S.[284] In their report, it was observed that the correlation between pKa and $\Delta\nu_{\mathrm{O-H}}$ in conventional O-H···O and unconventional O-H···S hydrogen bonding where sulfur is a hydrogen bond acceptor are almost similar. It was also established that the strength of the O-H···S hydrogen bonding is similar to conventional O-H···O hydrogen bonding.[3-4, 130, 229, 285-286] However, the study of S-H···O hydrogen bonding, where sulfur acts as a hydrogen bond donor, is scarce in the literature.[7-9, 162, 267] It was also found that such unconventional hydrogen bonding interactions are relatively weaker in nature.[267]

In the previous chapter, we have demonstrated the modulation of the strength of the weak S-H···O hydrogen bond present in 2-FTP···H_2O by changing the hydrogen bond acceptor H_2O to MeOH and EtOH, which are better acceptors than the former as the proton affinity of MeOH and EtOH is higher than that of H_2O. It has been found that the strength of the S-H···O hydrogen bond, i.e., the IR red-shift in the S-H stretching frequency, increases dramatically (from 30 to 76 cm^{-1}) by substituting one H atom in H_2O by a methyl group. On the other hand, the substitution of one H atom in H_2O by an ethyl group instead of methyl increases the red-shift to 88 cm^{-1}, which is similar to that obtained in the case of methyl substitution. In this chapter, we have studied 2-FTP···Et_2O complex to explore the strength of the S-H···O hydrogen bond by substituting both the hydrogens in H_2O by ethyl group. Here, Et_2O can act as solely hydrogen bond acceptor while all the three previously studied complexing partners of 2-FTP i.e., H_2O, MeOH, and EtOH, had both hydrogen bond donor and acceptor properties. Additionally, the proton affinity of Et_2O (828 kJ/mol)[287] is higher than that of MeOH (761 kJ/mol), and EtOH (788 kJ/mol)[287] although the steric effect of Et_2O is also larger than that of MeOH and EtOH that can significantly affect the optimized geometry of the S-H···O hydrogen bond in the complex. At the same time, dispersion interaction in the complex containing Et_2O is much larger than that in the complexes containing MeOH and EtOH. Hence, the dispersion interaction in the case of Et_2O can also reduce the strength of the S-H···O hydrogen bond compared to that in the case of MeOH and EtOH. Overall, the strength of the S-H···O hydrogen bond in the 2-FTP···Et_2O complex will rely on a fine interplay among the proton affinity of the hydrogen bond acceptor, steric crowding, and dispersion interaction.

We have addressed here the subtle balance among multiple interactions to shape the structure of the 2-FTP···Et_2O complex using mass-selected conformer-specific electronic and IR spectroscopy utilizing 1C-R2PI, UV-UV hole-burning, and IR-UV double resonance spectroscopic techniques accompanying with quantum chemical calculations. To obtain a broader perspective on the interplay of multiple interactions, we have further explored theoretically the S-H···O hydrogen bonding in 2-FTP complexes with a series of cyclic and acyclic ethers.

5.2 Result and Discussion

5.2.1 Conformational landscape of 2-FTP···Et_2O complex

Diethyl ether (Et_2O) itself exhibits multiple conformers, denoted as *trans-trans* (*tt*), *trans-gauche* ($tg^{\pm}$), and *gauche-gauche* ($g^{\pm}g^{\pm}$), based on the dihedral angles ϕ_1 and ϕ_2, as depicted in Figure 5.1(a). The nomenclature $g^{\pm}$ indicates that each gauche geometry has two distinct orientations, i.e., *gauche*$^{+}$ (g^{+}) and *gauche*$^{-}$ (g^{-}), corresponding to the dihedral angle of approximately ±60°. On the other hand, the *t* term in the nomenclature specifies the orientation of the dihedral angles ϕ_1 and ϕ_2 at 180°. The relative electronic energies (ΔE_{rel}) of these conformers, calculated at the M06-2X/6-311++G(d,p) level of theory, follow the order $tt > tg^{\pm} > g^{\pm}g^{\pm}$. Optimized geometries of the Et_2O conformers at the same level of theory are illustrated in Figure 5.1 (b-d). Notably, these results align

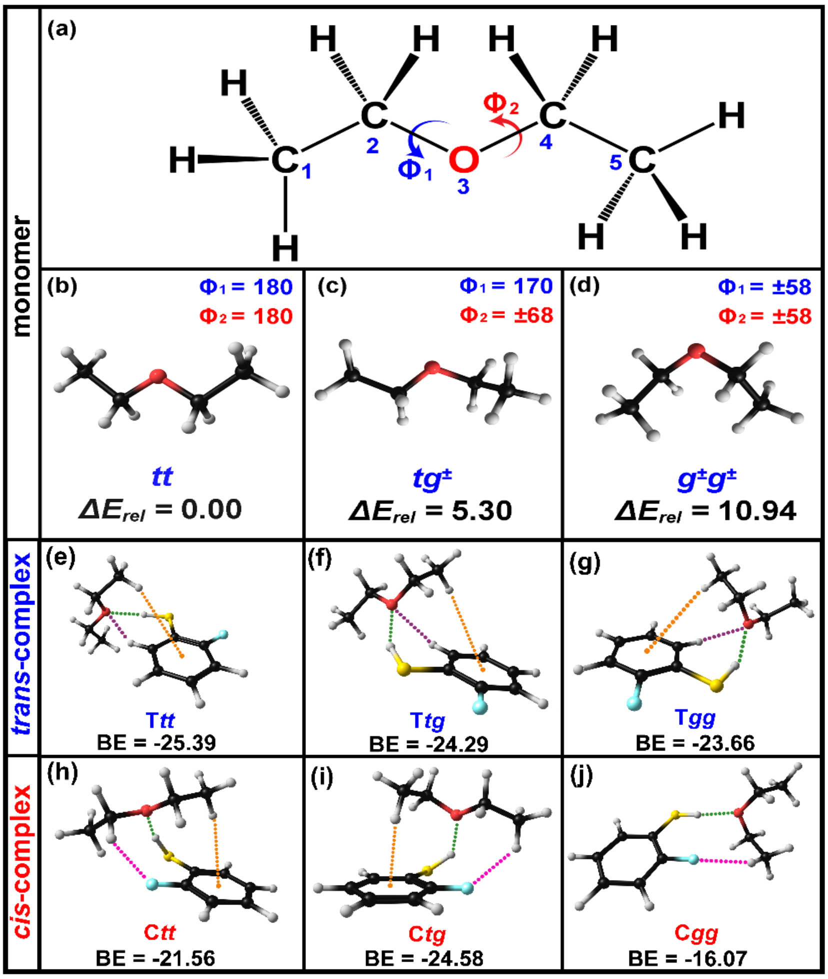
(a)
monomer
H
H
H
H
H
H
C
1
C
2
Φ2
C
4
O
3
Φ1
5
C
H
H
H
(b)
Φ1 = 180
Φ2 = 180
tt
ΔErel = 0.00
(c)
Φ1 = 170
Φ2 = ±68
tg±
ΔErel = 5.30
(d)
Φ1 = ±58
Φ2 = ±58
g±g±
ΔErel = 10.94
trans-complex
(e)
Ttt
BE = -25.39
(f)
Ttg
BE = -24.29
(g)
Tgg
BE = -23.66
cis-complex
(h)
Ctt
BE = -21.56
(i)
Ctg
BE = -24.58
(j)
Cgg
BE = -16.07

Figure 5. 1. (a) 3D representation of diethylether (Et_2O) that shows the two dihedral angles $\phi_1 = C_1 - C_2 - O_3 - C_4$ and $\phi_2 = C_2 - O_3 - C_4 - C_5$ along which conformers are generated. (b-d) three conformers of Et_2O opimised at the M06-2X/6-311++G(d,p) level. Relative electronic energies are provided in kJ/mol unit. (e-j) optimized geometries of the complexes of 2-FTP and Et_2O at the M06-2X/6-311++G(d,p) level of theory. Geometries (e-g) belong to the *trans* complex category according to the complexation with *trans*-2-FTP and (h-j) belong to the *cis* complex category according to the complexation with *cis*-2-FTP. Colored Dotted lines on the 2-FTP···Et_2O complexes are represnting the non-covalent interactions. Geomerical parameters for the various non-covalent interaction are provided in Table 5.1.

with previous research on Et_2O reported in the literature.[288-298] The abundance of these three classes of the conformers of Et_2O is also drastically different, and this has a correlation with their relative electronic energies. Sundararajan and co-workers reported population percentages of 78%, 21%, and 1% for *tt*, $tg^{\pm}$, and $g^{\pm}g^{\pm}$ conformers, respectively.[299] However, the matrix isolation studies in N_2 and Ar matrices showed the existence of the only *tt* and *tg*$^{\pm}$ conformers, which was much anticipated.[299] Similarly, several past studies on Et_2O also suggested the presence of only two conformers, *tt* and *tg*$^{\pm}$, under experimental conditions.[289, 300] We have not considered identical or degenerate conformers of Et_2O in our analysis. Instead, we have focused on summarizing the three unique conformers of Et_2O: *trans-trans* (*tt*), *trans-gauche* (*tg*), and *gauche-gauche* (*gg*). We have predicted the complexes of these three conformers of Et_2O with 2-FTP at the M06-2X/6-311++G(d,p) level of theory. 2-FTP has two conformers, *cis* and *trans*. In previous chapters, we have shown that *cis*-2-FTP is more stable than *trans*-2-FTP by 4.77 kJ/mol at the M06-2X/6-311++G(d,p) level of theory. The combination of the three conformers of the Et_2O and two conformers of 2-FTP generates a large number of conformers of the 2-FTP···Et_2O complex. However, six low-energy predicted conformers of the 2-FTP···Et_2O complex are shown in Figure 5.1 (e-j). The conformers of the complexes are termed T*tt*, T*tg*, and T*gg* for the *trans* category as the complexes are formed with *trans*-2-FTP, and similarly, C*tt*, C*tg*, and C*gg* are named for the *cis* complex category as those are formed with *cis*-2-FTP. As the oxygen atom in Et_2O has no option to act like a hydrogen bond donor, all the conformers of Et_2O can only be hydrogen bond acceptors, while 2-FTP can act as a hydrogen bond donor. Additionally, the pKa and proton affinity (PA) values of 2-FTP and Et_2O are favorable for the formation of such complexes. Similar results have been reported from the previous studies on the *p*-cresol···Et_2O complex and 2-Phenylehanethiol···Et_2O complex.[9] Out of the six predicted geometries, T*tt* is the global minimum in terms of the zero-point energy and BSSE-corrected binding energy. The least stable conformer of the complex in terms of binding energy is the C*gg* conformer. Important geometrical parameters of 2-FTP, and Et_2O monomers as well as the conformers of the 2-FTP···Et_2O complex, are listed in Table 5.1.

Table 5.1. Geometrical parameters of the various conformers of both of the 2-FTP and Et_2O monomers along with the 2-FTP···Et_2O complex calculated at the M062X/6-311++G(d,p) level of theory

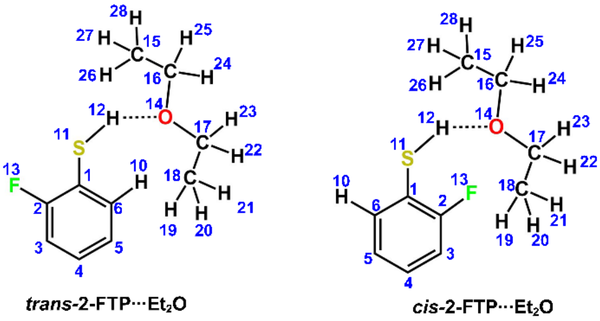

trans-2-FTP···Et_2O *cis*-2-FTP···Et_2O

Within 2-FTP	**2-FTP**		***trans*-complex**			***cis*-complex**		
	trans	***cis***	**T*tt***	**T*tg***	**T*gg***	**C*tt***	**C*tg***	**C*gg***
$d_{S[11]-H[12]}$ (Å)	1.34	1.34	1.35	1.35	1.35	1.35	1.35	1.35
$\angle C_{[1]}-S_{[11]}-H_{[12]}$ (°)	94.9	96.3	94.9	94.8	94.8	94.5	94.7	97.9
$d_{C[1]-S[11]}$ (Å)	1.77	1.77	1.77	1.77	1.77	1.77	1.77	1.77
$\angle C_{[2]}-C_{[1]}-S_{[11]}-H_{[12]}$(°)	3	8.6	6.4	-8.6	8.4	48.9	-38.7	-20.1
$d_{S[11]\cdots F[13]}$ (Å)	2.87	3.01	2.89	2.90	2.90	3.00	2.99	3.01
$d_{S[11]-H[12]\cdots F[13]}$ (Å)	-	2.29	-	-	-	2.66	2.52	2.39
$\angle S_{[11]}-H_{[12]}\cdots F_{[13]}$ (°)	-	109.6	-	-	-	90.8	96.7	103.6

Within Et_2O	**Et_2O**			***trans*-complex**			***cis*-complex**		
	tt	***tg***	***gg***	**T*tt***	**T*tg***	**T*gg***	**C*tt***	**C*tg***	**C*gg***
$\angle C_{[16]}-O_{[14]}-C_{[17]}$ (°)	112.9	114.3	115.8	113.6	114.9	116.2	112.6	114.7	116.4
$\Phi1_{\angle C[15]-C[16]-O[14]-C[17]}$(°)	180	170	58	177.6	170.9	58.3	174.4	160.1	56.6
$\Phi2_{\angle C[16]-O[14]-C[17]-C[18]}$(°)	180	68	58	176.7	70.4	59.4	176.6	59.2	59.2

	***trans*-complex**			***cis*-complex**		
S-H···O	**T*tt***	**T*tg***	**T*gg***	**C*tt***	**C*tg***	**C*gg***

$d_{S[11]-H[12]\cdots O[14]}$ (Å)	2.10	2.12	2.12	2.10	2.20	1.99
$\angle S_{[11]}-H_{[12]}\cdots O_{[14]}$ (°)	166.0	151.7	151.8	155.4	130.8	161.0
$d_{S[11]\cdots O[14]}$ (Å)	3.42	3.36	3.37	3.37	3.24	3.30
$\angle C_{[2]}-C_{[1]}-S_{[11]}\cdots O_{[14]}$(°)	10.5	-23.1	23.1	50.4	-59.3	-14.6
$\angle C_{[1]}-S_{[11]}-H_{[12]}\cdots O_{[14]}$(°)	28.7	-56.5	57.7	5.6	-40.6	152.0
C-H···O						
$d_{C[6]-H[10]\cdots O_{14}}$ (Å)	2.36	2.40	2.42	-	-	-
$\angle C_{[6]}-H_{[10]}\cdots O_{[14]}$ (°)	146.00	133.7	133.80	-	-	-
C-H···S						
$d_{C[15]-H[26]\cdots S[11]}$ (Å)	3.18	3.06	3.02	3.31	3.07	-
C-H···π						
$d_{C[15]-H[26]\cdots C[1]}$ (Å)	-	-	3.31	-	2.87	-
$d_{C[15]-H[26]\cdots C[2]}$ (Å)	-	3.05	3.07	3.04	2.89	-
$d_{C[15]-H[26]\cdots C[3]}$ (Å)	3.08	3.29	-	2.67	2.89	-
$d_{C[15]-H[26]\cdots C[4]}$ (Å)	2.94	-	-	2.91	2.83	-
$d_{C[15]-H[26]\cdots C[5]}$ (Å)	-	-	-	-	2.81	-
$d_{C[15]-H[26]\cdots C[6]}$ (Å)	-	-	-	-	2.83	-
$d_{C[16]-H[24]\cdots C[1]}$ (Å)	-	2.98	-	3.15	-	-
$d_{C[16]-H[24]\cdots C[2]}$ (Å)	-	2.88	2.94	2.92	-	-
$d_{C[16]-H[24]\cdots C[3]}$ (Å)	-	-	2.85	-	-	-
C···C						
$d_{C[15]\cdots C[1]}$ (Å)	-	-	4.17	4.17	3.88	-
$d_{C[15]\cdots C[2]}$ (Å)	-	-	3.71	3.73	3.73	-
$d_{C[15]\cdots C[3]}$ (Å)	4.02	-	-	3.61	3.63	-
$d_{C[15]\cdots C[4]}$ (Å)	3.77	-	-	3.98	3.66	-
$d_{C[15]\cdots C[5]}$ (Å)	-	4.17	-	-	3.80	-

$d_{C[15]\cdots C[6]}$ (Å)	-	3.72	-	-	3.91	-
$d_{C[16]\cdots C[1]}$ (Å)	-	3.80	-	3.96	-	-
$d_{C[16]\cdots C[2]}$ (Å)	-	3.42	3.41	3.45	-	-
$d_{C[16]\cdots C[3]}$ (Å)	-	-	3.78	3.79	-	-
C-H···F						
$d_{C[16]-H[24]\cdots F[13]}$ (Å)	-	-	-	2.86	-	-
$d_{C[17]-H[22]\cdots F[13]}$ (Å)	-	-	-	2.50	2.99	2.63
$d_{C[18]-H[29]\cdots F[13]}$ (Å)	-	-	-	2.63	2.44	2.49

The main binding force for all the conformers of the 2-FTP···Et_2O complex is S-H···O hydrogen bonding. However, a variety of other non-covalent interactions is present in each of the conformers of the complex. All the conformers except the C*gg* conformer are stabilized by secondary C-H···π and C-H···S interactions with a varied amount of stacking interaction. The *trans*-complexes have additional C-H···O hydrogen bonding, which is absent in the *cis*-complexes. Similarly, *cis*-complexes have additional C-H···F interaction. In terms of the distances between the atoms involved in the interactions, S-H···O interaction is stronger in the T*tt* conformer among the *trans*-complexes. On the other hand, S-H···O interaction was found to be stronger in the C*gg* conformer in the cis-complex category. However, the binding energy of the C*gg* conformer is least due to the absence of weak C-H···π/stacking and C-H···S interactions. C-H···π/stacking interaction is found to be more in T*tg*, T*gg*, and C*tg* conformers. There are changes in the ϕ_1 and ϕ_2 angles in Et_2O due to the formation of the complex, and these changes are more significant in the case of the *cis*-complex category. There are also noticeable changes in the $\angle C_{[2]}-C_{[1]}-S_{[11]}-H_{[12]}$(°) dihedral angle due to complex formation in the cis-complex category.

Intermolecular vibrations for all the conformers of the complex at the ground electronic state are given in Table 5.2.

Table 5.2. Six intermolecular vibrational modes in the ground electronic state (S_0) of the conformers of the 2-FTP···Et$_2$O complex calculated at the M06-2X/6-311++G(d,p) level of theory

	***trans*-complex**						***cis*-complex**					
Mode	**T*tt***		**T*tg***		**T*gg***		**C*tt***		**C*tg***		**C*gg***	
	ν	Vib*	ν	Vib*	ν	Vib*	ν	Vib*	ν	Vib*	ν	Vib*
1	10	β_1	27	β_1	27	β_1	25	β_1	35	τ_1	13	β_1
2	31	β_1'	47	τ_1	32	τ_1	34	β_1'	53	β_1	26	τ_1
3	39	τ_1	56	β_2	45	β_1'	71	β_2	64	β_1'	48	β_1'
4	56	τ_2	61	τ_2	71	β_2	82	σ	81	β_2	55	τ_2
5	73	β_2	83	τ_3	82	σ	106	τ_1	105	σ	63	β_2
6	85	σ	102	σ	95	τ_2	115	τ_2	112	τ_2	93	σ

* β_1 and β_1' denote the out-of-plane bending vibration of the S-H···O hydrogen bonding whereas β_2 represents the in-plane bending for the same. σ represents the stretching vibration along the S-H···O hydrogen bonding. τ_1, τ_2, and τ_3 represent mixed vibration, including ethyl group rotation and ring twist.

Geometries of all the conformers of 2-FTP···Et$_2$O are also optimized at MP2 as well as other different DFT levels using various basis sets. A graphical representation of the energy landscape of the low-energy conformers of the complex is given in Figure 5.2. Calculations performed at all three DFT levels show that the T*tt* conformer is the global minimum, while the stability order of other low-energy conformers is almost similar. However, the trend in the binding energies of the conformers derived at the MP2/6-311++G(d,p) level of theory is a bit different from that obtained at the DFT, mostly due to the overestimation of the dispersion interaction at the former level. The T*tg* conformer is the global minimum at the MP2/6-311++G(d,p) level of theory.

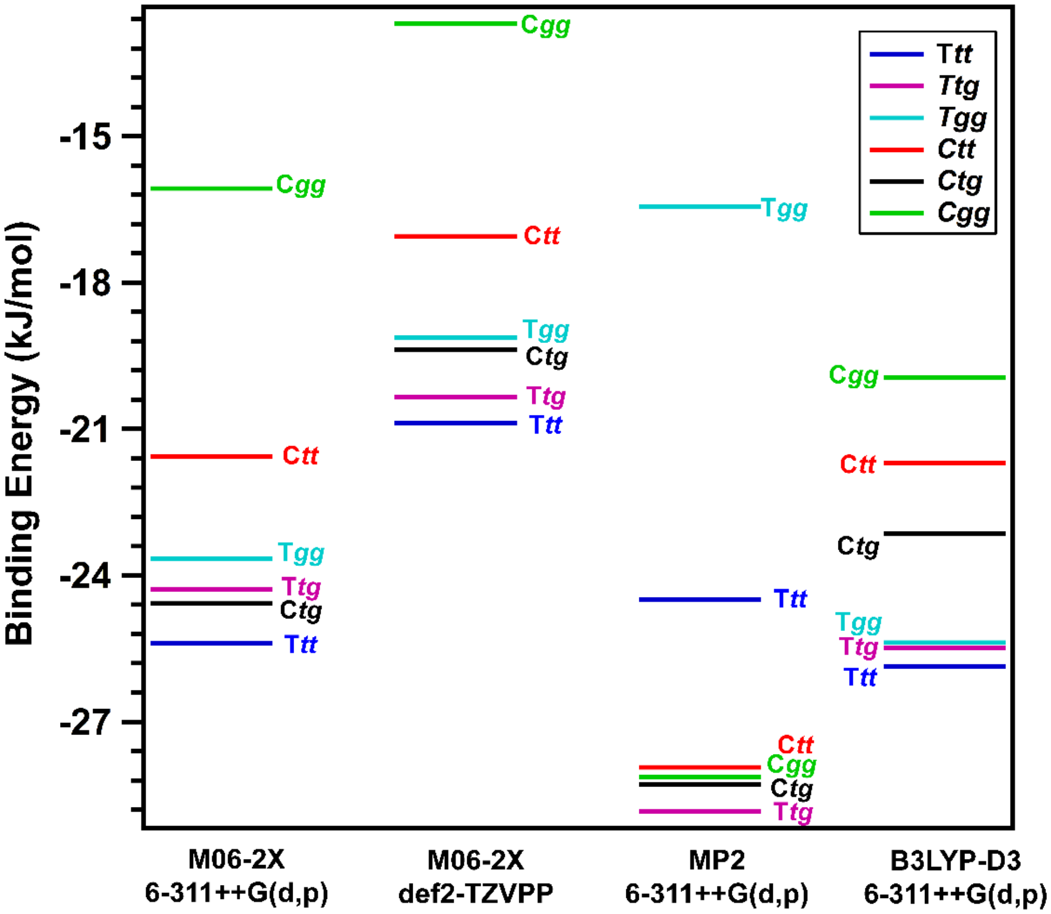

Figure 5.2. Graphical representation of the binding energies of the conformers of the 2-FTP···Et_2O complexes calculated at different levels of theory.

5.2.2 Mass-selected Electronic Spectra of the 2-FTP···Et_2O complex

Time of flight (TOF) mass spectrum of the 2-FTP···Et_2O complex measured utilizing the 1C-R2PI spectroscopic technique is shown in Figure 5.3. To avoid the formation of higher order cluster of 2-FTP···Et_2O complex, vapor pressure of highly volatile Et_2O was controlled by keeping it in a -100 °C cold bath. Heating of 2-FTP was also restricted at ~55 °C to maximize the selective formation of 1:1 cluster of 2-FTP···Et_2O complex. Figure 5.4(b) shows the mass-selected electronic spectrum of the 2-FTP···Et_2O

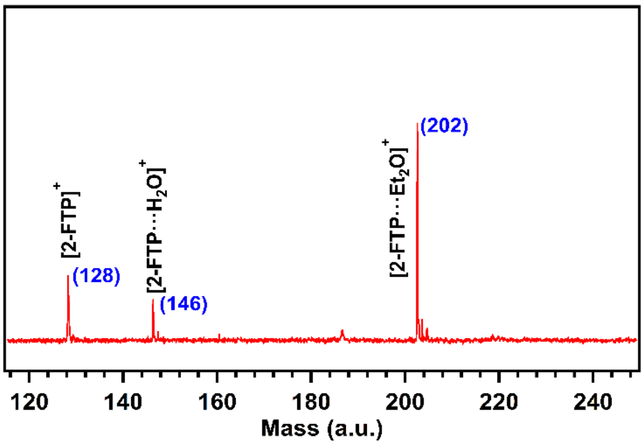

Figure 5.3. TOF Mass spectrum of mixed vapor of 2-FTP and Et_2O measured at 35240 cm^{-1} (most intense electronic band of the 2-FTP···Et_2O complex) employing 1C-R2PI spectroscopy.

complex (1:1) recorded using the 1C-R2PI technique. The origin band of the *cis* conformer of the 2-FTP monomer observed at 35555 cm^{-1} is shown in Figure 5.4(a), and this is in good agreement with the reported spectrum of the monomer by Kim and co-workers.[237] In Chapter 3, we have shown that the very low *cis-trans* isomerization barrier for 2-FTP allows the collisional relaxation of *trans*-2-FTP to *cis*-2-FTP.

Multiple low-frequency bands are observed in the electronic spectrum of the 2-FTP···Et_2O complex. To understand whether the bands observed in the electronic spectrum belong to the same conformer or not, UV-UV hole-burning spectroscopy experiment has been performed. Figure 5.4(c) and (d) display the UV-UV hole-burning spectra corresponding to the two conformers, A and B, existing in the gas-phase spectroscopic experiment. UV-UV hole-burning spectra were recorded by fixing the electronic band marked by asterisks in Figure 5.4(b). The origin bands due to the $S_1 \leftarrow S_0$ transitions of the conformers A and B were observed at 35230 cm^{-1} and 35066 cm^{-1}, respectively. Conformer A manifests several low-frequency intermolecular vibrations, which are tentatively assigned in Table 5.3. Conversely, conformer B lacks any low-frequency vibrational mode, but it does showcase an intramolecular fundamental (6a) band corresponding to the in-plane ring deformation of the 2-FTP monomer.

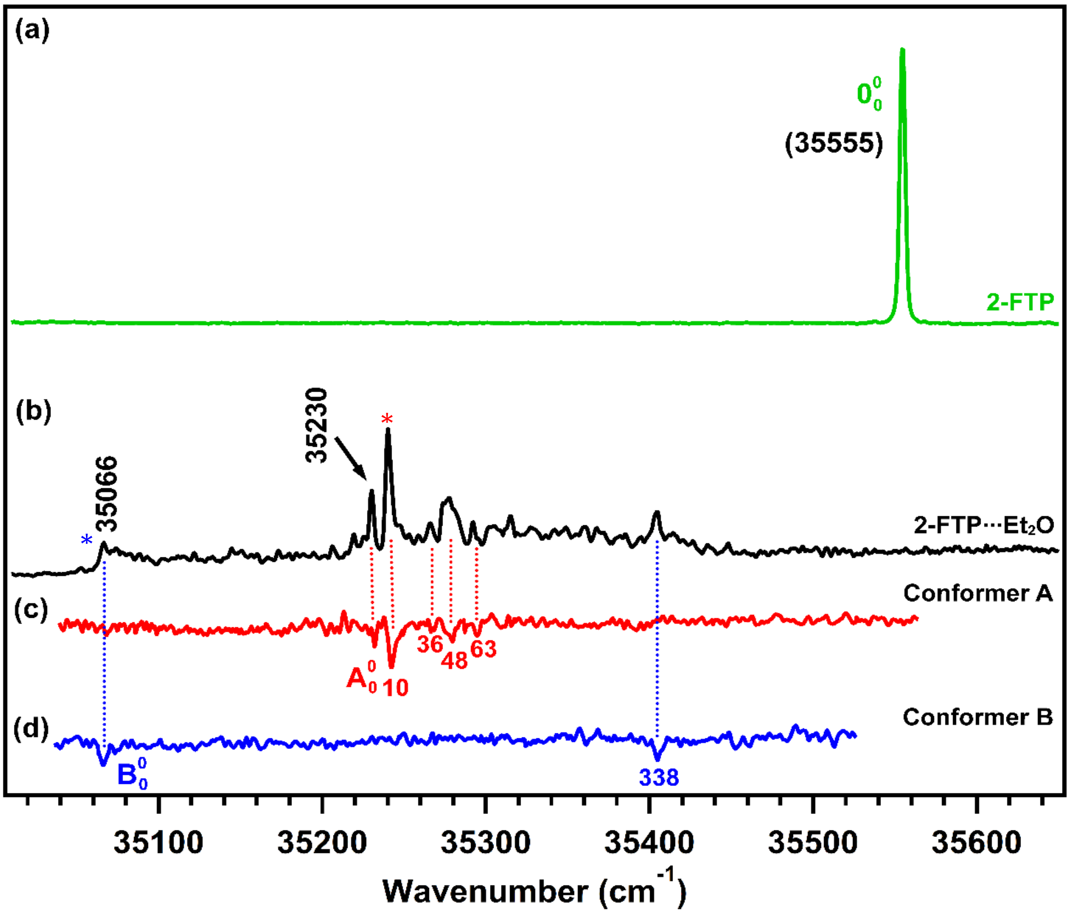

Figure 5.4. Mass selected electronic spectra of the (a) 2-FTP monomer and (b) 2-FTP···Et$_2$O complex recorded utilizing 1C-R2PI spectroscopic technique with He-Ne carrier gas. (c, d) UV-UV hole-burning spectra for the conformers A and B of the 2-FTP···Et$_2$O complex recorded by fixing the probe energy correspond to $A_0^0 + 10$ (35240 cm^{-1}) and B_0^0 (35066 cm^{-1}) bands. Numbers are given in (c) correspond to the bands represent the intermolecular vibration of the conformer A. Band at +338 cm^{-1} in (d) is the 6a intramolecular vibration of 2-FTP.

Table 5.3. Tentative assignment of the low-frequency intermolecular vibrations (cm^{-1}) observed in the electronic spectra (Figure 5.4) of the two conformers of 2-FTP···Et$_2$O complex

Conformer A	T*tt**	Conformer B	C*tt*
35230	A_0^0	35066	B_0^0
+10	β_1		
+36	β_1'		
+48	$\tau_1 /\beta_1 + \beta_1'$		
+63	τ_2		

* β_1 and β_1' denote the out-of-plane bending vibration of the S-H···O hydrogen bonding where as τ_1, and τ_2 represent mixed vibration, including ethyl group rotation and ring twist.

The electronic origin bands of the conformers A and B of the 2-FTP···Et_2O complex experience red-shifts of 325 cm^{-1} and 489 cm^{-1}, respectively, with respect to that of the 2-FTP monomer. The red-shift in the electronic origin band of the conformer A of 2-FTP···Et_2O is similar to that obtained for the 2-FTP···H_2O, 2-FTP···MeOH, and 2-FTP···EtOH complexes. This result suggests that the stabilization of the S_1 state of all the complexes except the conformer B of the 2-FTP···Et_2O compared to the S_0 state with respect to that of the monomer is similar.

5.2.3 IR spectra of 2-FTP···Et_2O and assignment of the conformers

Conformer-specific IR spectra of the 2-FTP monomer and 2-FTP···Et_2O complex in the region of the S-H stretching frequency, measured using RIDIR spectroscopy, are shown in Figure 5.5. The S-H stretching frequency of the 2-FTP monomer (Figure 5.3a) observed at 2625 cm^{-1} was reported earlier.[267] Scaled theoretical S-H stretching vibration for the *cis*-2-FTP with respect to the experimental value, calculated at M06-2X/6-311++G(d,p) level of theory, is provided in Figure 5.3b. To scale the harmonic stretching frequencies of different conformers of the 2-FTP···Et_2O complex, the scaling factor is derived from the ratio of the experimental (2625 cm^{-1})[267] and the calculated S-H stretching frequency (2751 cm^{-1}) at the M06-2X/6-311++G(d,p) level of theory. Figure 5.4(c) and (h) show the IR spectra of the conformers A and B of the 2-FTP···Et_2O complex, respectively. The spectra were obtained by probing the $A_0^0 + 10$ (35240 cm^{-1}) band for the conformer A and B_0^0 (35066 cm^{-1}) for the conformer B. Theoretically scaled IR spectra in the S-H stretching frequency region of the six low-energy conformers of the 2-FTP···Et_2O complex are provided in Figure 5.4(d-g, i-j).

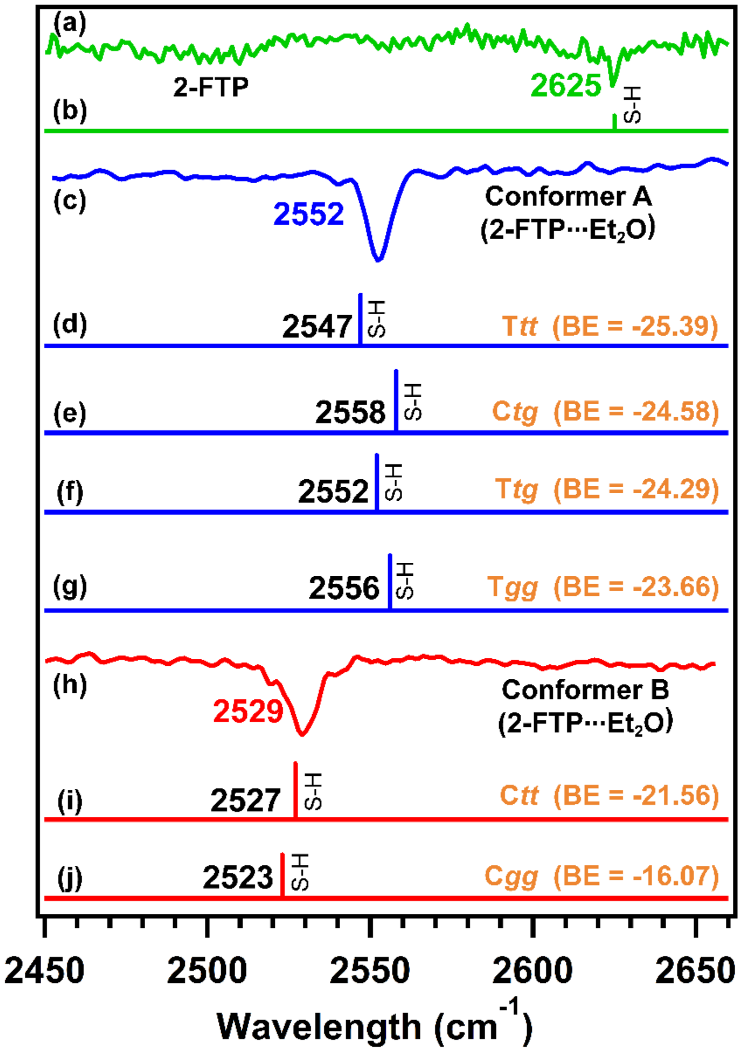

Figure 5.5. Experimental IR spectra of the (a) 2-FTP monomer, (c, h) conformers A and B of the 2-FTP···Et$_2$O complex, respectively measured in the S-H regions by RIDIR spectroscopy. (b, d-g, i-j) Theoretical scaled IR spectra of the 2-FTP monomer and T*tt*, C*tg*, T*tg*, T*gg*, C*tt*, and C*gg* conformer of 2-FTP···Et$_2$O complex, respectively, calculated at M06-2X/6-311++G(d,p) level of theory. Scaling of the S-H frequencies are done with respect to the experimentally observed S-H frequency of the 2-FTP monomer.[267]

Experimental IR spectrum of the conformer A of the 2-FTP···Et$_2$O complex shows a red-shift of 73 cm^{-1} in the S-H stretching frequency with respect to the S-H stretching frequency of the 2-FTP monomer, whereas the red-shift observed for the conformer B is 98 cm^{-1}. This result clearly indicates that both of the two conformers of the 2-FTP···Et$_2$O complex have S-H···O hydrogen bonding interaction of reasonable strength. In the case of the *p*-cresol···Et_2O complex, the red-shift observed in the O-H···O hydrogen-bonded O-H stretching frequency with respect to the p-cresol monomer was 280 cm^{-1}.[285] Interestingly, similar amount of red-shift (275-290 cm^{-1}) in the O-H stretching frequency for the O-H···S hydrogen bonding (Sulfur-centered hydrogen bond) in *p*-cresol···Et_2O complex was reported in the literature.[285] The red-shift (290 cm^{-1}) reported in the O-H stretching frequency in the phenol···Et_2O complex was also similar.[301] In the *o*-cyanophenol···Et_2O complex, further larger red-shift (430 cm^{-1}) was observed in the O-H stretching frequency for the O-H···O hydrogen bond present there. This comparison shows that the S-H···O hydrogen bonding interaction is much weaker compared to both conventional O-H···O and unconventional O-H···S hydrogen bonding.

Assignment of the observed conformers of 2-FTP···Et_2O has been done by comparing their experimental IR spectra with the theoretical IR spectra of the low-energy conformers of the complex. The experimental S-H stretching frequencies of the conformers A and B appear at 2552 and 2529 cm^{-1}, respectively. There is a distinct difference of 23 cm^{-1} in the S-H stretching frequencies of the two observed conformers. It can be noticed from the theoretical scaled IR spectra presented in Figure 5.5 that there are mostly two groups of conformers in terms of the S-H stretching frequency. The one group of the conformers is with the *trans*-2-FTP moiety, i.e., T*tt*, T*tg,* and T*gg,* having the S-H frequency in the range of 2547-2556 cm^{-1}. Another group of the conformers is with the *cis*-2-FTP moiety, i.e., C*tt* and C*gg,* having the S-H frequency in the range of 2523-2527 cm^{-1}, although the C*tg* conformer with the S-H frequency of 2558 cm^{-1} is the exception as it falls in the category with the *trans*-2-FTP moiety.

It is noteworthy from Figure 5.5 that the S-H stretching frequencies of the conformers T*tt*, C*tg*, T*tg,* and T*gg* are very close to each other and corroborate well with the experimental

S-H frequency of the observed conformer A (2552 cm^{-1}). T*tt* conformer, being the global minimum at all the three DFT levels of theory, can be assigned to conformer A. However, the binding energies of the T*tt*, C*tg*, T*tg,* and T*gg* conformers are also very close to each other and hence, the observed conformer A can be tentatively represented by any one of these four conformers. On the other hand, the S-H stretching frequencies of the conformers C*tt* and C*gg* are quite close to each other and match well with the experimental S-H stretching frequency of the observed conformer B (2529 cm^{-1}). However, the C*gg* conformer is higher in energy than the C*tt* conformer by ~5 kJ/mol and thus, C*tt* is the favorable choice for conformer B. Based on the stretching frequencies as well as binding energies of the predicted low-energy conformers, T*tt* and C*tt* can be assigned to the observed conformers A and B, respectively. It is worth mentioning that the literature on the $H_2S\cdots Et_2O$ complex indicates the observation of a single conformer corresponding to the *tt* conformer of Et_2O with a red-shift of 46 cm^{-1} in the S-H stretching frequency.[7] Similarly, observation of a single conformer of 2-phenlyethanethiol$\cdots Et_2O$ complex with only the *tt* orientation of Et_2O is reported by Robertson and coworkers.[9]

Table 5.4. Scaled harmonic stretching frequencies (in cm^{-1} unit) of the conformers of 2-FTP$\cdots Et_2O$ complex calculated at various levels of theory

2-FTP$\cdots Et_2O$ Conformers	**M06-2X 6-311++G(d,p)**	**M06-2X def2-TZVPP**	**MP2 6-311++G(d,p)**	**B3LYP-D3 6-311++G(d,p)**
T*tt*	2547	2560	2566	2541
T*tg*	2552	2566	2569	2530
T*gg*	2556	2569	2561	2523
C*tt*	2529	2549	2548	2464
C*tg*	2558	2583	2571	2455
C*gg*	2523	2554	2566	2460

In the previous chapters, we explored the S-H···O hydrogen bonding by studying 2-FTP···H2O, 2-FTP···MeOH, and 2-FTP···EtOH complexes.[267] The red-shifts obtained in the S-H stretching frequency due to the complex formation were 30, 76, and 80 cm^{-1} for 2-FTP···H2O, 2-FTP···MeOH, and 2-FTP···EtOH complexes, respectively. A comparison can be made between the strength of the S-H···O hydrogen bonding and the increasing proton affinity of the hydrogen bond acceptors, including H2O, MeOH, EtOH, and Et2O. Figure 5.5 shows a linear correlation between the experimentally observed red-shift in the S-H stretching frequency and the proton affinity of the hydrogen bond acceptors. It is worth mentioning that the correlation between the O-H stretching frequency and proton affinities of the acceptors involving conventional O-H···O hydrogen bonding in PhOH···H2O, PhOH···MeOH, PhOH···Et2O shows much steeper linear plot (Figure 5.6).[272,

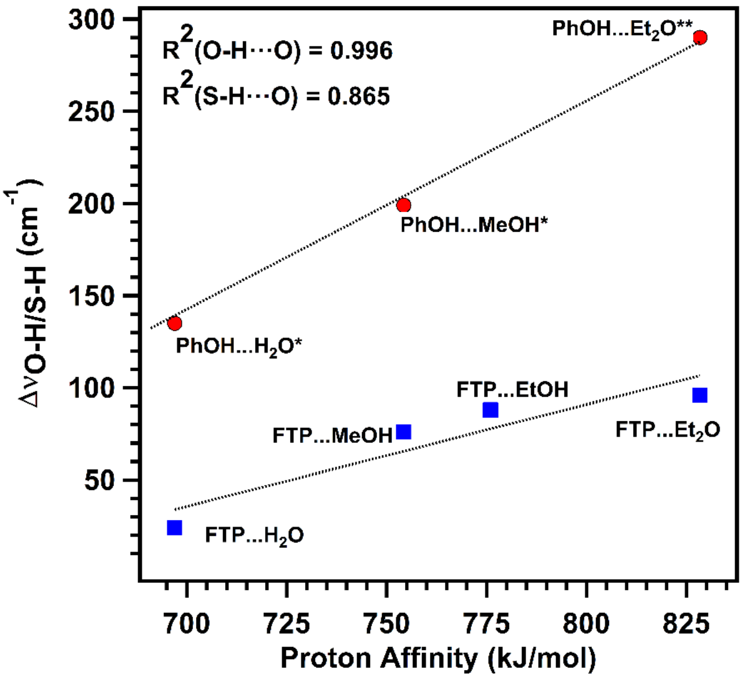

Figure 5.6. Fitted line through the blue square points represents the correlation between the strength of the S-H···O hydrogen bonding interaction in terms of the red-shift with the proton affinity of the hydrogen bond acceptor. Fitted line along the red circle represents the correlation between strength of the O-H···O hydrogen bonding with the proton affinity of the hydrogen bond acceptors. Asterisks are given for the value taken form the references (249, 301).

[301] This finding reveals that the change of the electron density on the O atom of the hydrogen bond acceptors by changing their proton affinities does not influence the strength of the unconventional hydrogen bonding in the similar way it does the conventional hydrogen bonding. The result also reflects that the nature of the unconventional hydrogen bonding, unlike the conventional hydrogen bonding, is not majorly dependent on the electrostatic interaction. Thus, the electrostatic component of the interaction energy, which has a major contribution to the IR red-shift, is significantly less for the sulfur-centered hydrogen bonds.

5.2.4 Analysis of the non-covalent interactions in 2-FTP···Et$_2$O

The strength and the nature of the non-covalent interactions present in the 2-FTP···Et$_2$O complex are analyzed utilizing NBO and QTAIM calculations. Figure 5.7 depicts the NBO overlap and corresponding 2nd order perturbation energy [$E^{(2)}$] for the different non-covalent interactions present in the six low-energy conformers of the 2-FTP···Et$_2$O complex calculated at the M06-2X/6-311++G(d,p) level of theory. Total $E^{(2)}$ for the S-H···O hydrogen bonding in the T*tt* conformer is 24.86 kJ/mol, which is contributed by 20.38 kJ/mol due to the delocalization of the electron density from sp-type lone pair atomic orbitals (AOs) to the σ^* antibonding orbital of the S-H bond [$n_{O(sp)} \rightarrow \sigma^*$(S-H)] and 4.48 kJ/mol for the delocalization of electron density from the p-type lone pair AOs to the σ^* of S-H bond [$n_{O(p)} \rightarrow \sigma^*$(S-H)]. The $E^{(2)}$ value for the C*tt* conformer is 25.48 kJ/mol [16.82 kJ/mol for $n_{O(sp)} \rightarrow \sigma^*$(S-H) and 8.66 for $n_{O(p)} \rightarrow \sigma^*$(S-H)]. It has been observed that the red-shift in the S-H stretching frequency in the case of the C*tt* conformer is more compared to that for the T*tt* conformer, and this is qualitatively reflected in the $E^{(2)}$ values. The $E^{(2)}$ values for the secondary interactions, including C-H···O, C-H···π, and C-H···S in the T*tt*

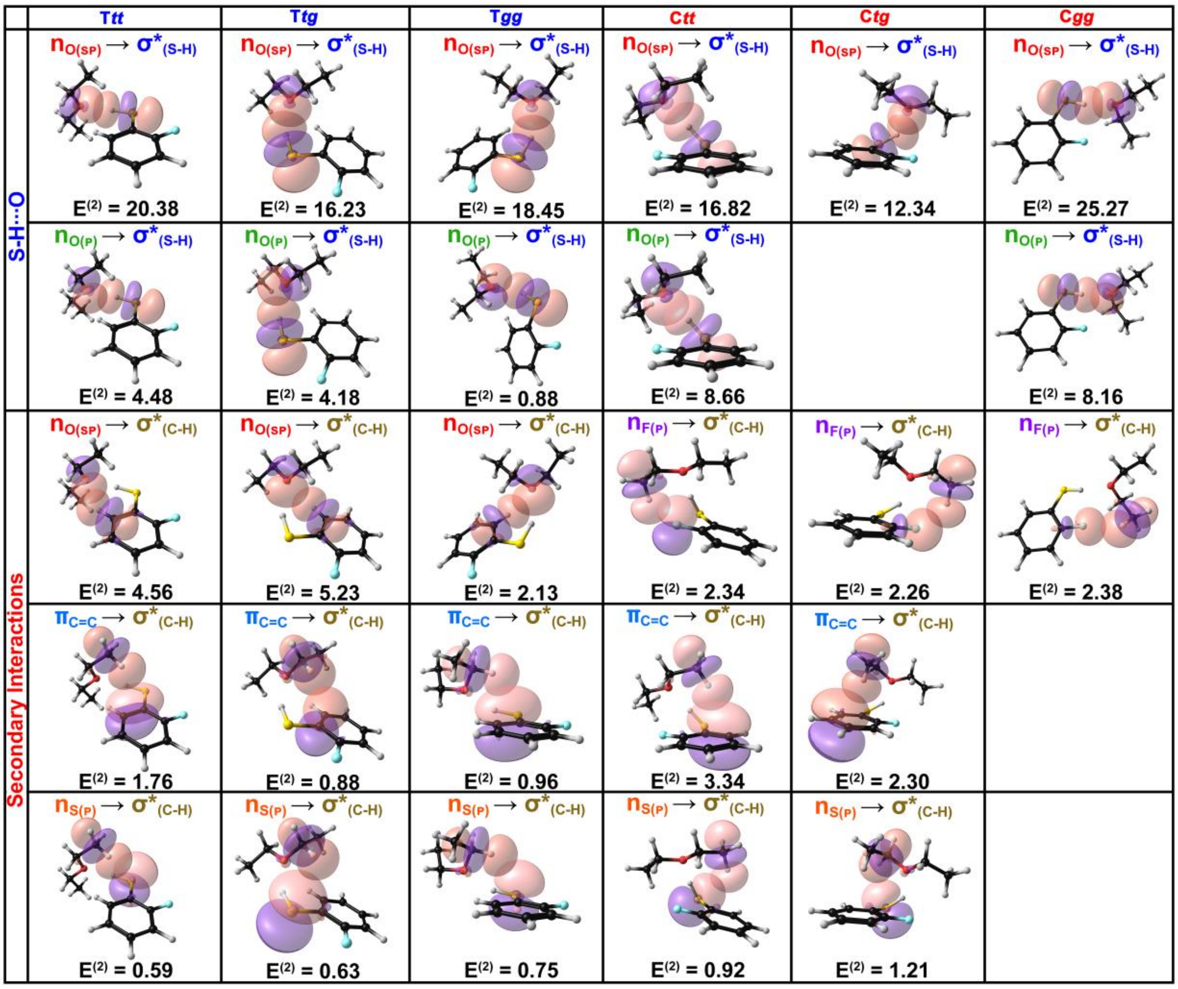
Ttt
Ttg
Tgg
Ctt
Ctg
Cgg
S-H···O
n_O(SP) → σ*(S-H)
E(2) = 20.38
E(2) = 16.23
E(2) = 18.45
E(2) = 16.82
E(2) = 12.34
E(2) = 25.27
n_O(P) → σ*(S-H)
E(2) = 4.48
E(2) = 4.18
E(2) = 0.88
E(2) = 8.66
E(2) = 8.16
Secondary Interactions
n_O(SP) → σ*(C-H)
E(2) = 4.56
E(2) = 5.23
E(2) = 2.13
n_F(P) → σ*(C-H)
E(2) = 2.34
E(2) = 2.26
E(2) = 2.38
π_C=C → σ*(C-H)
E(2) = 1.76
E(2) = 0.88
E(2) = 0.96
E(2) = 3.34
E(2) = 2.30
n_S(P) → σ*(C-H)
E(2) = 0.59
E(2) = 0.63
E(2) = 0.75
E(2) = 0.92
E(2) = 1.21

Figure 5.7. NBO overlap for the various non-covalent interactions including S-H···O hydrogen bonding interactions and other secondary interactions present in the conformers of the 2-FTP···Et$_2$O complex calculated at the M06-2X/6-311++G(d,p) level of theory.

conformer are 4.48 kJ/mol, 1.76 kJ/mol, and 0.59 kJ/mol, respectively. On the other hand, the E$^{(2)}$ values for the secondary interactions C-H···F, C-H···π, and C-H···S in the C*tt* conformer are 2.34 kJ/mol. 3.34 kJ/mol and 0.92 kJ/mol, respectively. The T*tg*, T*gg,* and C*tg* conformers exhibit fewer E$^{(2)}$ values for the S-H···O interaction compared to those for the T*tt* and C*tt* conformers. The C*gg* conformer has a large value of E$^{(2)}$ corresponding to the S-H···O interaction. However, other secondary interactions, including C-H···π and C-H···S interaction, are missing in C*gg*. Although the E$^{(2)}$ values are not sufficient to describe the total binding energies of the complexes, they justify a qualitative correlation between the red-shift in the S-H stretching frequency ($\Delta\nu_{S\text{-}H}$) and the E$^{(2)}$ values for the corresponding hydrogen bond interaction.

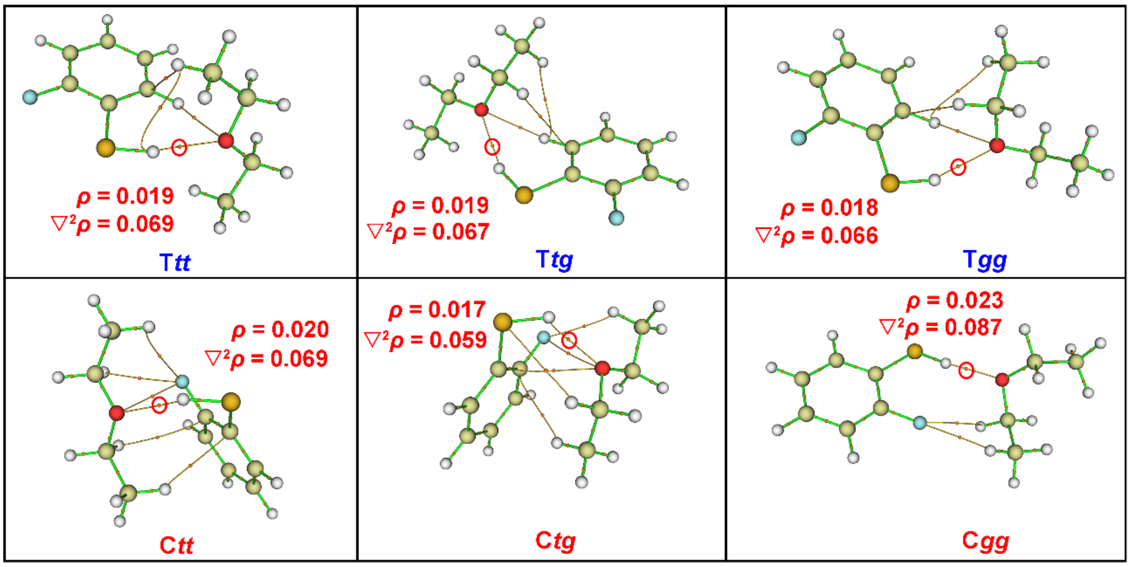

Figure 5.8. Topology of the electron density of the conformers of the 2-FTP···Et$_2$O complex calculated performing QTAIM calculation with the optimized geometries at M06-2X/6-311++G(d,p) level of theory. Red circle on each of the conformers are highlighting the bond critical point (BCP) correspond to S-H···O hydrogen bonding interactions. Total electron density (ρ) and the laplacian of the electron density ($\nabla^2\rho$) at the bond critical points are mentioned for to S-H···O hydrogen bonding interactions of each conformer.

Various non-covalent interactions present in the conformers of 2-FTP···Et$_2$O are further evaluated using QTAIM calculations with the optimized geometries of the conformers obtained at the M062-2X/6-311++G(d,p) level of theory. Figure 5.8 shows the molecular graphs displaying the bond critical point points (BCPs) and the bond path connecting the interacting atoms through non-covalent interactions in the conformers of the 2-FTP···Et$_2$O complex. Total electron density (ρ) and the Laplacian of the electron density ($\nabla^2\rho$) at the bond critical points for the primary interaction (S-H···O hydrogen bonding) of the corresponding conformer are also shown in Figure 5.8.

The theoretical evaluation of the S-H···O hydrogen bonding interaction utilizing NBO and the QTAIM result has an overall correlation with the experimental value of the red-shift in the S-H stretching frequency. At this point, it is worth comparing the NBO second-order perturbation energy [$E^{(2)}$] and the AIM parameters for the S-H···O hydrogen bonding interaction with those for the conventional O-H···O hydrogen bonding. The NBO and AIM analyses of the reported *p*-cresol···Et_2O complex were further performed at M06-2X/6-311++G(d,p) level of theory. To have a comparison between the S-H···O and O-H···O hydrogen bonding interactions, we have studied the oxygen analogs of 2-FTP, i.e., 2-Fluorophenol (2-FP) at the same level of theory. C1 and T1 are named to the *cis*-2-FP and *trans*-2-FP complexes, respectively, with the *tt* conformers of Et2O. Table 5.5 shows the comparison of the strength of the S-H···O and O-H···O hydrogen bonding interactions in terms of the IR red-shifts and NBO energies.

Table 5.5. Comparison of the NBO second-order perturbation energy and the AIM parameters calculated at M06-2X/6-311++G(d,p) level of theory with the red-shift in the experimentally observed S-H stretching frequency

	S-H···O		**O-H···O**		
	2-FTP···Et_2O		**p-CR···Et_2O**	**2-FP···Et_2O**	
	T*tt*	**C*tt***		**T1**	**C1**
$\Delta\nu_{S-H}$ (cm^{-1})	73	98	280*	-	-
$E^{(2)}$ (kJ/mol)	24.86	25.48	62.72	69.56	83.04
ρ (a.u.)	0.019	0.020	0.033	0.035	0.038
$\nabla^2\rho$ (a.u.)	0.069	0.069	0.128	0.133	0.136
$d_{S/O-H\cdots O}$ (Å)	2.10	2.10	1.80	1.78	1.75

* Experimental red-shift was taken from the reference (285)

5.2.5 Extension of theoretical studies on the nature and strength of the S-H···O hydrogen bonding

We have observed that the S-H···O hydrogen bonding interaction is quite weaker compared to the conventional hydrogen bonding interactions. However, it has been found from all the results obtained so far that this weak hydrogen bonding interaction has a direct correlation with the proton affinities of the hydrogen bond acceptors. Hence, the strength of the S-H···O hydrogen bond can be modulated by varying the proton affinities of the hydrogen bond acceptors. However, the increase in the proton affinities of the hydrogen bond acceptors is associated with the increase of alkyl groups in the acceptors. Hence, other competing factors, such as steric repulsion, dispersion, etc., come into the picture along with the electrostatic interaction. To have a further detailed understanding of the strength of the S-H···O hydrogen bond with the interplay between proton affinities of the acceptors and multiple interactions present in the complexes, we have extended the theoretical studies of the 2-FTP complexes with a series of ethers

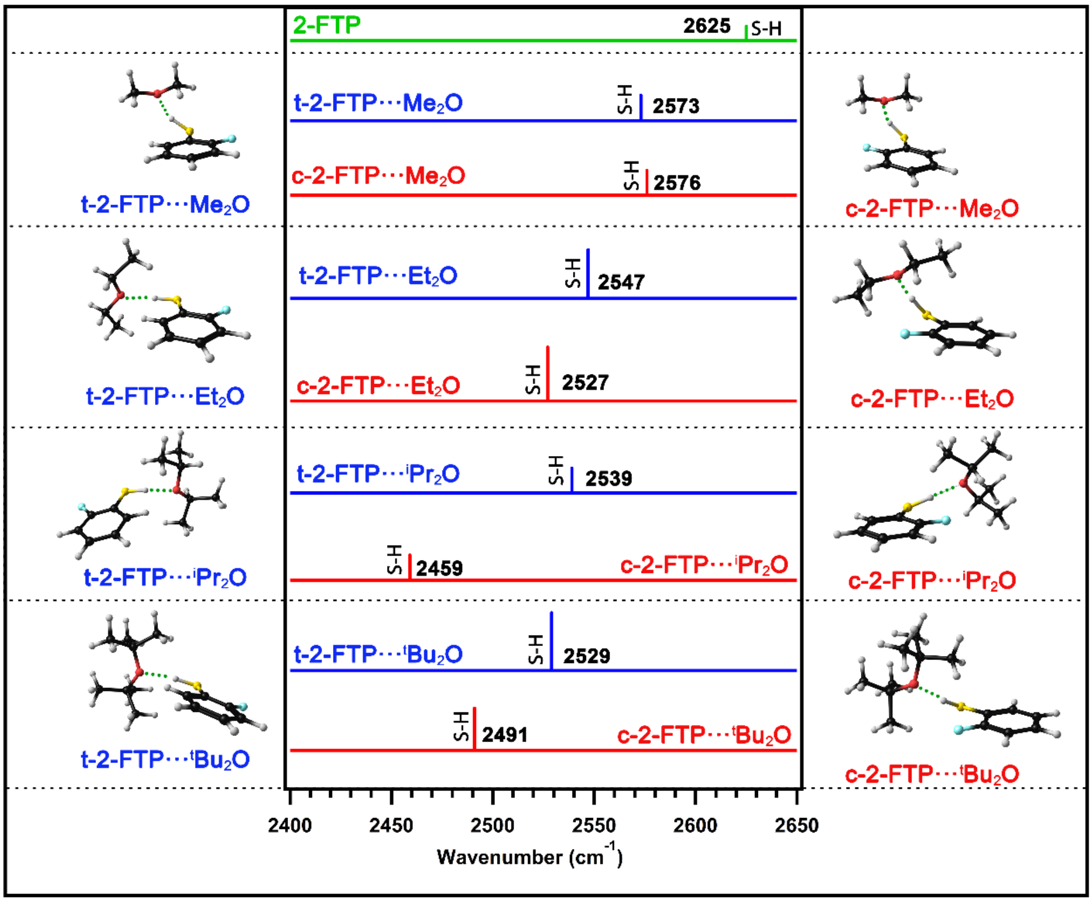

Figure 5.9. Scaled harmonic stretching frequencies in the S-H region of the most stable conformers of the complexes of 2-FTP with acyclic ethers optimized at the M06-2X/6-311++G(d,p) level of theory. Blue color stick spectra correspond to the *trans* conformers of the complex formed with *trans*-2-FTP while the red color stick spectra represent the *cis* conformer of the complexes formed with *cis*-2-FTP. Calculated stretcthing frequencies are scaled with respect to the experimental S-H stretching frequecy of the 2-FTP monomer.[267]

including cyclic and acyclic ones. However, the acyclic and cyclic ethers belong to different families, and hence, we have correlated them separately. Figure 5.9 shows the optimized geometries of the 2-FTP complexes with acyclic ethers. Red-shift in the S-H stretching frequencies scaled with respect to the experimentally observed S-H stretching frequency in the 2-FTP monomer. The theoretical IR spectra presented in Figure 5.8 show that the red-shift in the S-H stretching frequency increases with the increment in the proton affinities of the hydrogen bond acceptors [Me_2O (804 kJ/mol), Et_2O (828 kJ/mol)[287] and $^iPr_2O$ (856 kJ/mol)]. However, the trends in the increase of the IR red-shift with the increase of the proton affinity of the acceptor do not continue while we move from $^iPr_2O$ to $^tBu_2O$, although the proton affinity of $^tBu_2O$ (887) is larger than that of ^iPr2O. Rather, the red-shift observed in the case of $^tBu_2O$ is smaller than that for the $^iPr_2O$. A

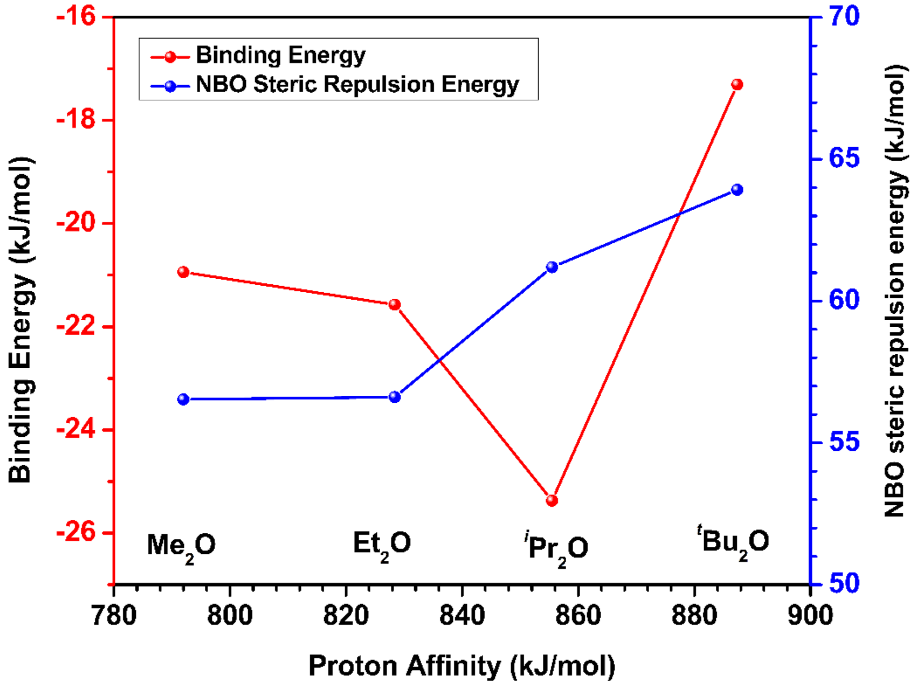

Figure 5.10. Correlation of the NBO steric repulsion energy and binding energy of the complexes with the proton affinity of the hydrogen bond acceptors calculated at M06-2X/6-311++G(d,p) level of theory. The lines through the points are not the fitted one but those are put to guide the eyes.

similar result in the conventional O-H···O hydrogen bonding with the study of the complexes between 4-fluorophenol and a series of ethers was reported by Berthelot and co-workers.[125] It is quite obvious that with the increment of the alkyl chain, proton affinity on the oxygen atom increases. However, at the same time, it increases the steric repulsion in the complexes as the size of the molecules increases. NBO steric calculation performed at the M06-2X/6-311++G(d,p) level of theory for the complexes, given in Figure 5.10, shows the change in the Pauli exchange antisymmetry contribution of the molecular potential energy value to the total interaction energies of the complexes.[302] Figure 5.10 shows correlations of the binding energies as well as NBO steric repulsion energies with the proton affinities of the hydrogen bond acceptors. While moving from the Me_2O to $^{t}Bu_2O$, NBO steric repulsion increases steadily aligned with the size of the acceptor, and the binding energy decreases. Hence, the binding energy follows a correlation with the combined effect of the proton affinity and steric repulsion of the hydrogen bond acceptor. This combined effect makes the 2-FTP···$^{i}Pr_2O$ complex as the strongest one among these. The strength of the S-H···O hydrogen bond and hence the IR red-shift gets affected accordingly.

Similarly in the case of the cyclic ethers, proton affinity increases with the increment of the ring size as it is found in oxirane (3-membered, PA = 793 kJ/mol)<oxetane (4-membered, PA = 796 kJ/mol), tetrahydrofuran (5-membered, PA = 824 kJ/mol) < tetrahydropyran (6-membered, PA = 825 kJ/mol).[303] Theoretical IR spectra of the most stable conformer of complexes formed between cyclic ethers and the 2-FTP are depicted in Figure 5.11. In the case of the complexes with the cyclic ethers, both the *cis* and *trans* conformers are observed to have a correlation between the red-shift in S-H stretching frequencies and the proton affinity of the ethers. However, the 2-FTP complex with the 6-membered cyclic ether (tetrahydropyran) has a lower red-shift due to the combined effect of the proton affinity and the steric repulsion.

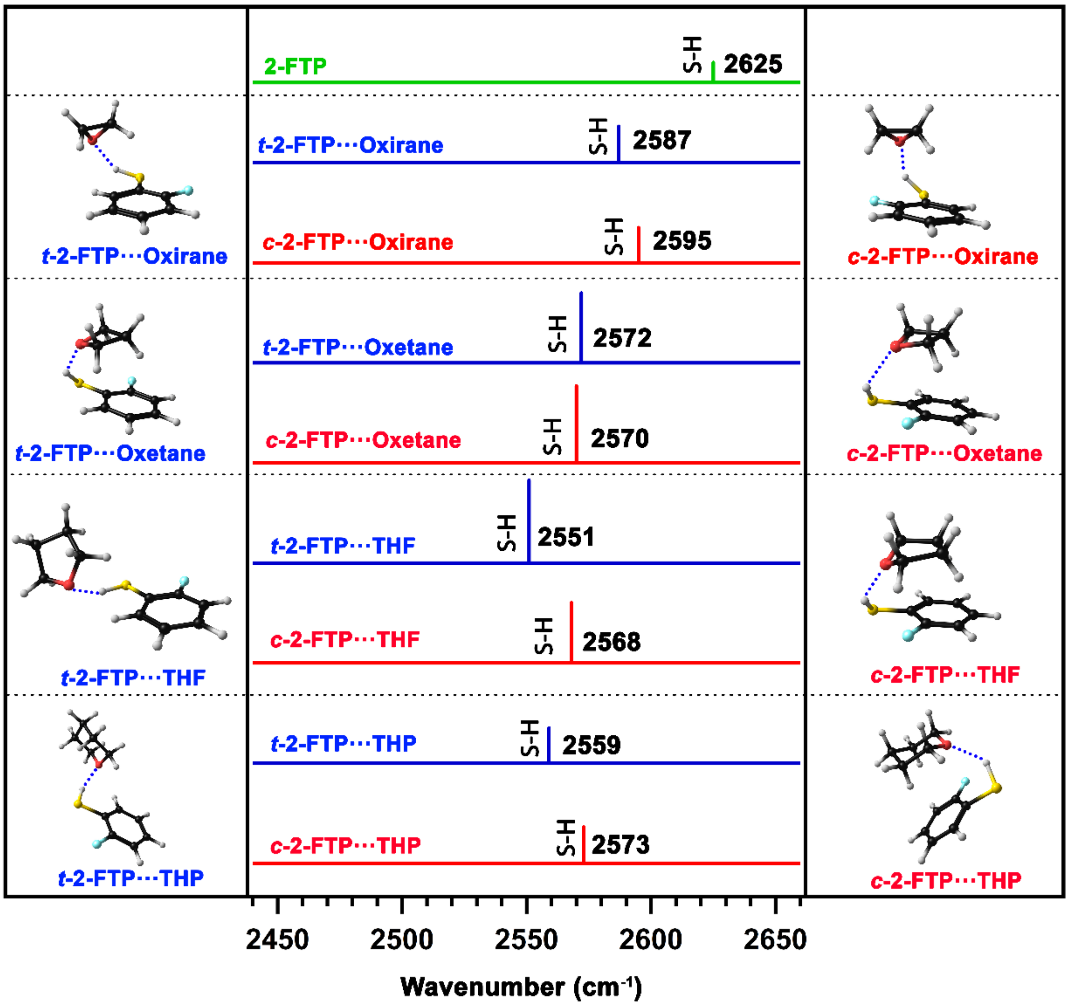

Figure 5.11. Scaled harmonic stretching frequencies in the S-H region of the most stable conformers of the complexes of 2-FTP with cyclic ethers optimized at the M06-2X/6-311++G(d,p) level of theory. Blue color stick spectra correspond to the *trans* conformers of the complex formed with *trans*-2-FTP while the red color stick spectra represent the *cis* conformer of the complexes formed with *cis*-2-FTP. Calculated stretcthing frequencies are scaled with respect to the experimental S-H stretching frequecy of the 2-FTP monomer.

The S-H···O hydrogen bonding interactions present in these complexes are further evaluated utilizing NBO and QTAIM calculations depicted in Figure 5.12. Correlation between the total electron density (ρ) at the bond critical points (BCP) of the S-H···O hydrogen bonding in both *cis* and *trans* complexes of 2-FTP with acyclic ethers and proton affinities of the hydrogen bond acceptors follow the trend in the IR red-shift in the S-H stretching frequencies. Similarly, NBO second-order perturbation energies [$E^{(2)}$] for these complexes hold the same correlation with the proton affinities. For the cyclic ether complexes, the correlation of the electron density as well as the NBO interaction energies with proton affinity follows the trend observed in the case of the red-shift in the S-H stretching frequencies in the complexes.

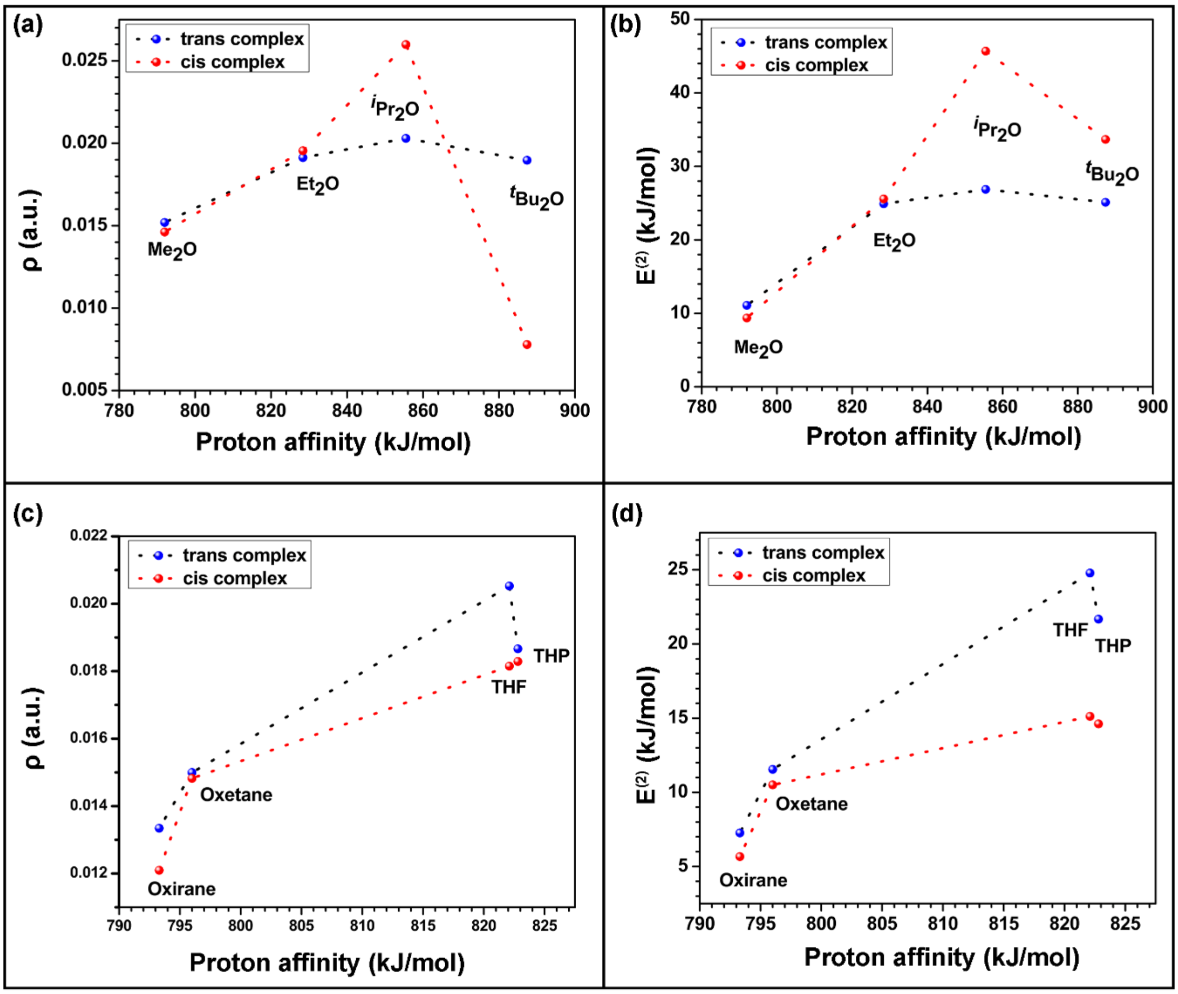

Figure 5.12. (a, b) correlation between the electron density and the NBO interaction energies with the proton affinity for the complexes of 2-FTP with acyclic ethers and (c, d) correlation between electron density and the NBO interaction energies with the proton affinity for the complexes of 2-FTP with cyclic ethers calculated at the M06-2X/6-311++G(d,p) level of theory. The lines through the points are not the fitted one but those are put to guide the eyes.

In the case of the acyclic ethers, the influence of the PA towards the increase of the strength of the S-H···O is maximum for the 2-FTP···^{i}Pr$_2$O complex, and the steric repulsion dominates and leads the interaction. Similarly, for the cyclic ethers, the dominance of the proton affinity on the strength of the S-H⋯O prevails up to the 5-membered cyclic ethers and steric repulsion takes over beyond that. From the theoretical point of view, the strength of the weak S-H⋯O hydrogen bonding can be modulated to some extent by varying the proton affinity of the hydrogen bond acceptor. However, there is always an interplay between the proton affinity, steric repulsion, and dispersion that controls the strength of the hydrogen bonding.

5.3 Conclusions

In this chapter, we have studied 1:1 complex of the 2-FTP with Et_2O in the gas-phase using mass-selected conformer-specific electronic and IR spectroscopy accompanied by quantum chemical calculations. Experimentally, two conformers of the complex are observed in the gas-phase. It has been confirmed from both experiments and calculations that both the observed conformers are stabilized by S-H⋯O hydrogen bonding interaction as a primary binding force. However, other weak secondary interactions, including C-H⋯O, C-H⋯F, C-H⋯π/stacking, and C-H⋯S interactions, also influence the overall stability and structures of the complexes. The S-H⋯O hydrogen bonding in the 2-FTP⋯Et_2O complex leads to the red-shift of 73 and 98 cm^{-1} in the stretching frequency of the S-H bond of the conformers A and B, respectively. This result also holds a linear correlation in the modulation of the hydrogen bonding strength with varying proton affinities of the hydrogen bond acceptors. However, the fitted line for the correlation between the strength of the S-H⋯O hydrogen bonding and the proton affinity of the hydrogen bonding acceptors is not steeper as it is observed in the case of the conventional O-H⋯O hydrogen bonding. It is also verified from the NBO and QTAIM calculations that the electron density and the NBO second-order perturbation energy due to the delocalization of electron density between the hydrogen bond donor and the acceptor are relatively smaller compared to those for the conventional hydrogen bonding. In this chapter, we have also extended further the understanding of the S-H···O hydrogen bonding interaction in terms of the theoretical study of the complexes of 2-FTP with several cyclic and acyclic ethers. It has been found that a subtle interplay between the proton affinity, steric repulsion, and dispersion interaction controls the strength of the S-H···O hydrogen bonding in the complexes. For acyclic ethers up to iPr_2O, the proton affinity factor dominates, and hence, the strength of the unconventional S-H···O hydrogen bonding increases from Me_2O to Et_2O and $^iPr_2O$. But in the case of $^tBu_2O$, steric repulsion dominates the overall structure of the complex, and hence, the S-H···O hydrogen bonding becomes weaker. Similarly, in the case of the complexes of 2-FTP with the cyclic ethers, the strength of the S-H···O hydrogen bonding is maximum for the 5-membered ether (Tetrahydrofuran), and it decreases thereafter.

Chapter 6

Summary and Future Directions

6.1. Conclusion

In conclusion, we have delved into the interaction of sulfur-centered hydrogen bonding (SCHB), focusing on the less investigated aspect where sulfur serves as a hydrogen bond donor. This exploration involved employing various gas-phase high-resolution spectroscopic techniques, including 1C-R2PI, UV-UV hole-burning, and IR-UV double resonance spectroscopy in conjunction with advanced quantum chemical calculations.

To comprehend the characteristics and the strength of S-H···O hydrogen bonding, an investigation was conducted on the 1:1 complex involving 2-FTP and H_2O. In this context, 2-FTP functions as an unconventional hydrogen bond donor, while H_2O acts as a conventional hydrogen bond acceptor. Conformer-specific electronic and IR spectra, obtained through mass-selected high-resolution spectroscopy, confirm the presence of two conformers in the complex formed with 2-FTP and H_2O. Employing quantum calculations, it was revealed that the formation of both complexes is driven primarily by S-H···O hydrogen bonding interaction. The absence of high-energy conformers of 2-FTP···H_2O based on O-H···S hydrogen bonding in the experiment concludes that the preference for S-H···O hydrogen bonding over O-H···S hydrogen bonding is influenced by the combined effect of the proton affinity of the hydrogen bond acceptor and the acidity (pKa) of the hydrogen bond donor. Nevertheless, both the experimental red-shift value (25-30 cm^{-1}) in the S-H stretching frequency and theoretical calculations suggest that the strength of S-H···O hydrogen bonding is much weaker than conventional O-H···O hydrogen bonding.

We have expanded our research to modulate the strength of S-H···O hydrogen bonding. In our gas-phase spectroscopic study, we investigated the complexes of 2-FTP with MeOH and EtOH. The observed conformers of the complex formed between 2-FTP and MeOH/EtOH are established through S-H···O hydrogen bonding. Experimental S-H···O hydrogen bonding strength in terms of the observed red-shift in S-H frequency increased as we moved from H2O to MeOH/EtOH, which is proportional to the proton affinity of the MeOH/EtOH. This study finds an interesting linear correlation between the strength of the S-H···O hydrogen bonding and the proton affinity.

Moreover, we examined the correlation between proton affinity and the strength of hydrogen bonding in both unconventional S-H···O and conventional O-H···O hydrogen bonding. Our observations revealed that the correlation curve is less steep for unconventional hydrogen bonding when compared to conventional hydrogen bonding. This investigation implies that the modulation of proton affinity in the hydrogen bond acceptor has a comparatively lesser influence on the electronic effect than in conventional hydrogen bonding. We conducted an additional investigation into the modulation of S-H···O hydrogen bonding across a range of cyclic and acyclic ethers. Ultimately, it became evident that steric repulsion plays a significant role, particularly when the size of the complexing partners is significantly larger. The strength of the hydrogen bonding is determined by the interplay between proton affinity and steric repulsion.

6.2 Future directions

It would be intriguing to explore unconventional S-H···N and S-H···S hydrogen bonding in the future through the application of diverse high-resolution gas-phase spectroscopic techniques. Both the sulfur and nitrogen are very much abundant in proteins and other biomolecules. We have already explored the S-H···O hydrogen bonding, which is quite weaker among the sulfur-centered hydrogen-bonding category.

It will also be interesting to compare the strength of the S-H···O and S-H···N/S unconventional hydrogen bonding in the future. Figure 6.1 shows Cambridge crystal database search results with a criterion of distance (2-3 Å) and angle (90°-180°). This outcome indicates the presence of a notable number of entries in the database that involve crystals exhibiting S-H···S or S-H···N interaction.

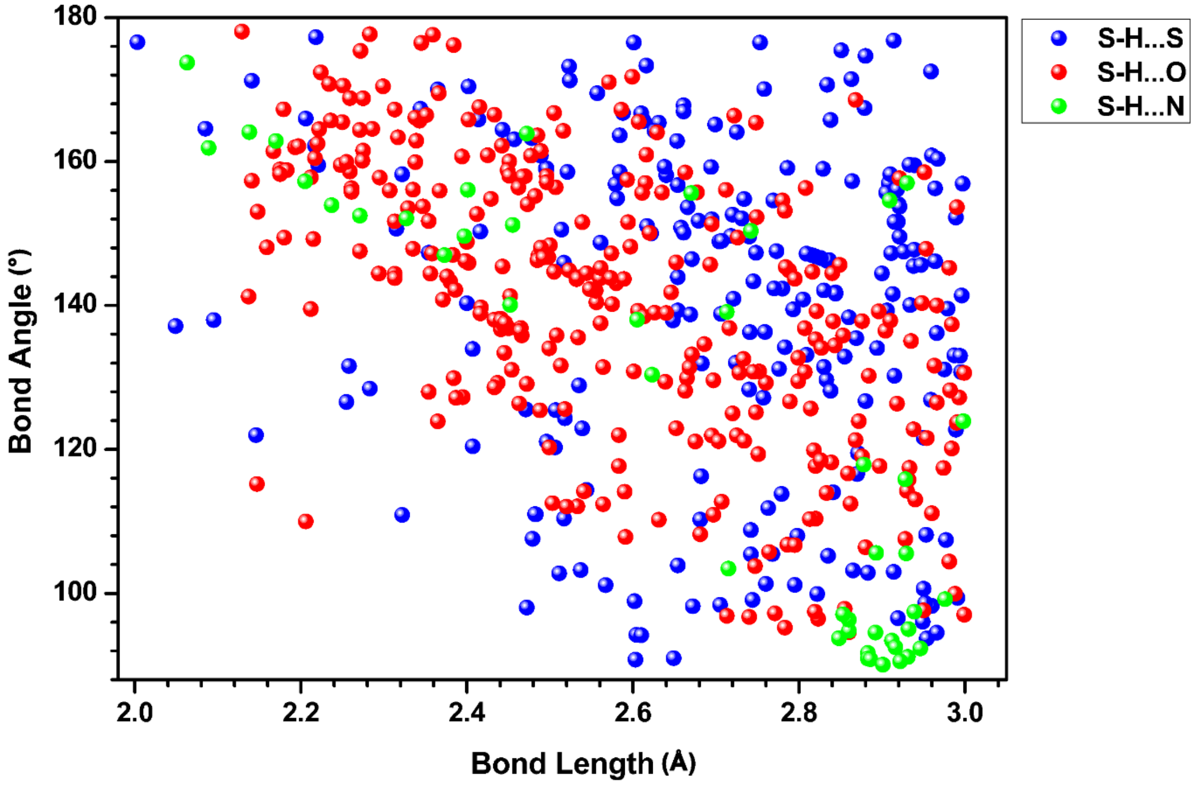

Figure 6.12. Representation of the entries in the Cambridge Crystal Database (CCDC 2022.2.0) within the search criteria of bond length (2-3Å) and angle (90°-180°).

We have primarily performed the computational calculation of S-H···N hydrogen bonding using a model of the complex in 2-FTP and pyridine and 4 -Methylpyridine has been performed at the level of M06-2X/6-311++G(d,p) level of theory. Figure 6.2 shows the optimized geometries of the complexes. Both the cis and trans conformers are analyzed in search of the S-H···N hydrogen bonding. *trans*-complexes are observed to make stronger hydrogen bonds in terms of red-shift value for both cases of pyridine (106 cm^{-1}) and 4-methyl pyridine complexes (116 cm^{-1}). However, due to the other non-covalent interactions, *cis* complexes are stabilized more.

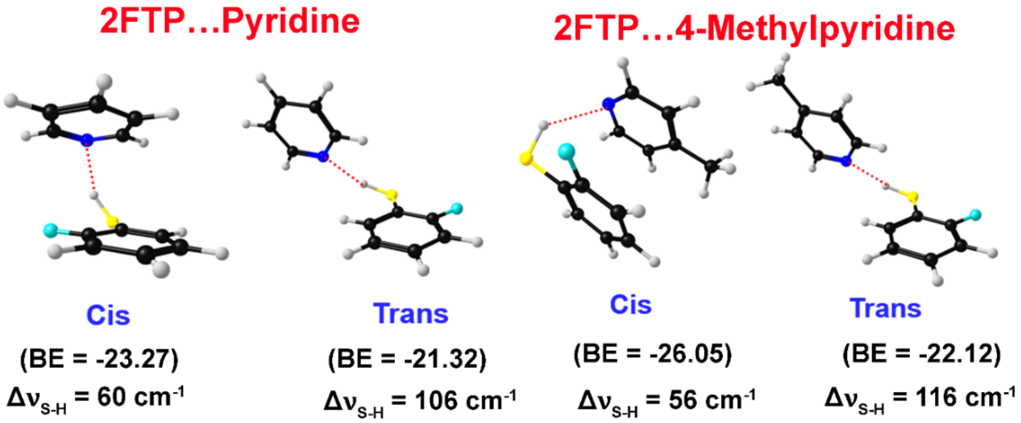
2FTP…Pyridine
2FTP…4-Methylpyridine
Cis
(BE = -23.27)
$\Delta\nu_{S\text{-}H}$ = 60 cm^{-1}
Trans
(BE = -21.32)
$\Delta\nu_{S\text{-}H}$ = 106 cm^{-1}
Cis
(BE = -26.05)
$\Delta\nu_{S\text{-}H}$ = 56 cm^{-1}
Trans
(BE = -22.12)
$\Delta\nu_{S\text{-}H}$ = 116 cm^{-1}

Figure 6.2. Optimised geometry of the 2-FTP complexes with pyridine and 4-methyl pyridine calculated at M06-2X/6-311++G(d,p) level of theory. In parenthesis Binding energies (BE) are given in kJ/mol. $\Delta\nu_{S\text{-}H}$ represent the red-shift in the scaled harmonic S-H stretching frequency.

S-H···S hydrogen belongs to the extremely unconventional category and is very interesting to the research community. A very few references exist in the literature where spectroscopically S-H···S hydrogen bond has been studied. Preliminary calculations of S-H···S hydrogen bonding in 2-FTP and Me_2S and Et_2S will be interesting. The ab initio

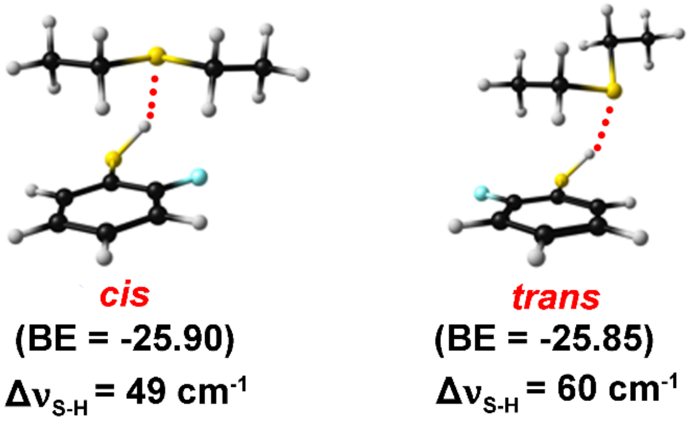
cis
(BE = -25.90)
$\Delta\nu_{S\text{-}H}$ = 49 cm^{-1}
trans
(BE = -25.85)
$\Delta\nu_{S\text{-}H}$ = 60 cm^{-1}

Figure 6.3. Optimised geometries of the *cis* and *trans* conformer of the 2-FTP…Et2S complex calculated at M06-2X/6-311++G(d,p) level of theory. In parenthesis Binding energys (BE) are given in kJ/mol. $\Delta\nu_{S\text{-}H}$ represent the red-shift in the scaled harmonic S-H stretching frequency.

calculation for the S-H···S hydrogen bonding is performed at M06-2X/6-311++G(d,p) level of theory. Optimized geometries are given in Figure 6.3.

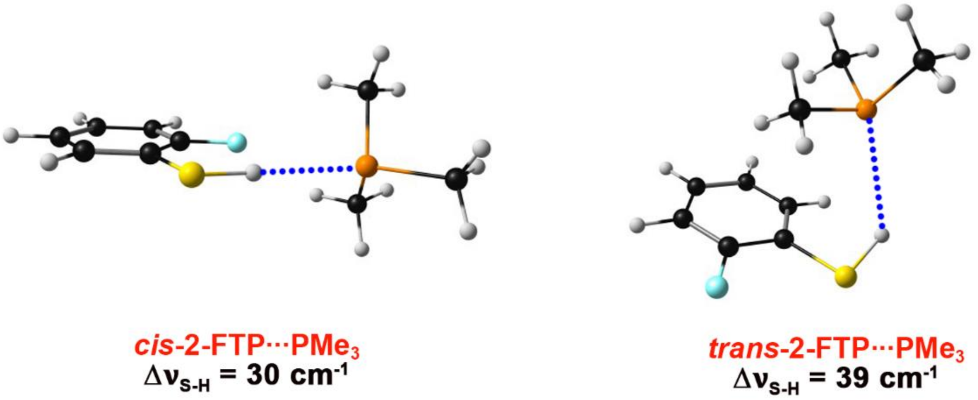
cis-2-FTP···PMe$_3$
$\Delta\nu_{S-H}$ = 30 cm^{-1}
trans-2-FTP···PMe$_3$
$\Delta\nu_{S-H}$ = 39 cm^{-1}

Figure 6.4. Optimized geometries of the *cis* and *trans* conformers of 2-FTP···Me$_3$P complex calculated at M06-2X/6-311++G(d,p) level of theory. $\Delta\nu_{S-H}$ represent the red-shift in the scaled harmonic S-H stretching frequency.

Phosphorous also has an important role in biological, pharmaceutical, and materials. The study of S-H···P hydrogen bonding could also be interesting as it falls in the extremely unconventional hydrogen bonding category. Figure 6.4 shows a preliminary calculation of the complex of 2-FTP and trimethyl phosphine (PMe3) at the M06-2X/6-311++G(d,p) level of theory. *cis* and *trans* complexes are observed to form with a S-H···P hydrogen bonding, and the corresponding red shift in S-H stretching frequency is 30 and 39 cm^{-1}.

References

1. Arunan, E., et al., Definition of the Hydrogen Bond (Iupac Recommendations 2011). *Pure Appl. Chem.* **2011**, *83*, 1637-1641.

2. Biswal, H. S.; Wategaonkar, S., Nature of the N–H···S Hydrogen Bond. *J. Phys. Chem. A* **2009**, *113*, 12763-12773.

3. Biswal, H. S.; Shirhatti, P. R.; Wategaonkar, S., O–H···O Versus O–H···S Hydrogen Bonding I: Experimental and Computational Studies on the P-Cresol·H2o and P-Cresol·H2s Complexes. *J. Phys. Chem. A* **2009**, *113*, 5633-5643.

4. Biswal, H. S.; Shirhatti, P. R.; Wategaonkar, S., O–H···O Versus O–H···S Hydrogen Bonding. 2. Alcohols and Thiols as Hydrogen Bond Acceptors. *J. Phys. Chem. A* **2010**, *114*, 6944-6955.

5. Andersen, C. L.; Jensen, C. S.; Mackeprang, K.; Du, L.; Jørgensen, S.; Kjaergaard, H. G., Similar Strength of the Nh···O and Nh···S Hydrogen Bonds in Binary Complexes. *J. Phys. Chem. A* **2014**, *118*, 11074.

6. Gregoret, L. M.; Rader, S. D.; Fletterick, R. J.; Cohen, F. E., Hydrogen Bonds Involving Sulfur Atoms in Proteins. *Proteins* **1991**, *9*, 99-107.

7. Bhattacherjee, A.; Matsuda, Y.; Fujii, A.; Wategaonkar, S., Acid–Base Formalism in Dispersion-Stabilized S–H···Y (Y = O, S) Hydrogen-Bonding Interactions. *J. Phys. Chem. A* **2015**, *119*, 1117-1126.

8. Bhattacherjee, A.; Matsuda, Y.; Fujii, A.; Wategaonkar, S., The Intermolecular S-H···Y (Y=S,O) Hydrogen Bond in the H_2s Dimer and the H_2s–Meoh Complex. *ChemPhysChem* **2013**, *14*, 905-914.

9. Lobo, I. A.; Robertson, P. A.; Villani, L.; Wilson, D. J.; Robertson, E. G., Thiols as Hydrogen Bond Acceptors and Donors: Spectroscopy of 2-Phenylethanethiol Complexes. *J. Phys. Chem. A* **2018**, *122*, 7171-7180.

10. Hobza, P.; Müller-Dethlefs, K., *Non-Covalent Interactions: Theory and Experiment*; Royal Society of Chemistry, 2010; Vol. 2.

11. Riley, K. E.; Hobza, P., Noncovalent Interactions in Biochemistry. *Wiley Interdisciplinary Reviews: Computational Molecular Science* **2011**, *1*, 3-17.

12. Chen, B.; Ivanov, I.; Klein, M. L.; Parrinello, M., Hydrogen Bonding in Water. *Phys. Rev. Lett.* **2003**, *91*, 215503.

13. Cerny, J.; Hobza, P., *Phys. Chem. Chem. Phys.* **2007**, *9*, 5291.

14. Šponer, J.; Leszczynski, J.; Hobza, P., Hydrogen Bonding and Stacking of DNA Bases: A Review of Quantum-Chemical Ab Initio Studies. *J. Biomol. Struct. Dyn.* **1996**, *14*, 117-135.

15. Kool, E. T., Hydrogen Bonding, Base Stacking, and Steric Effects in DNA Replication. *Annu. Rev. Biophys. Biomol. Struct.* **2001**, *30*, 1-22.

16. Fonseca Guerra, C.; Bickelhaupt, F. M.; Snijders, J. G.; Baerends, E. J., Hydrogen Bonding in DNA Base Pairs: Reconciliation of Theory and Experiment. *J. Am. Chem. Soc.* **2000**, *122*, 4117-4128.

17. Watson, J. D., *Molecular Biology of the Gene*; Pearson Education India, 2004.

18. Richmond, T. J.; Davey, C. A., The Structure of DNA in the Nucleosome Core. *Nature* **2003**, *423*, 145-150.

19. Watson, J. D.; Crick, F. H. In *The Structure of DNA*, Cold Spring Harbor symposia on quantitative biology, Cold Spring Harbor Laboratory Press: 1953; pp 123-131.

20. Persch, E.; Dumele, O.; Diederich, F., Molecular Recognition in Chemical and Biological Systems. *Angew. Chem. Int. Ed.* **2015**, *54*, 3290-3327.

21. von Hippel, P. H.; McGhee, J. D., DNA-Protein Interactions. *Annu. Rev. Biochem* **1972**, *41*, 231-300.

22. Mishra, R.; Kumar, A.; Chandra, R.; Kumar, D., A Review on Theoretical Studies of Various Types of Drug-DNA Interaction. *Int J Sci Technol Soc* **2017**, *3*, 11-27.

23. Bahadur, R. P.; Chakrabarti, P.; Janin, J., Protein–Protein Interaction and Quaternary Structure. *Quarterly Reviews of Biophysics* **2008**, *41*, 133-180.

24. Keskin, O.; Gursoy, A.; Ma, B.; Nussinov, R., Principles of Protein− Protein Interactions: What Are the Preferred Ways for Proteins to Interact? *Chem. Rev.* **2008**, *108*, 1225-1244.

25. Etter, M. C., Hydrogen Bonds as Design Elements in Organic Chemistry. *The Journal of Physical Chemistry* **1991**, *95*, 4601-4610.

26. Steiner, T.; Saenger, W., Lengthening of the Covalent O–H Bond in O–H··· O Hydrogen Bonds Re-Examined from Low-Temperature Neutron Diffraction Data of Organic Compounds. *Acta Crystallogr. Sect. B: Struct. Sci.* **1994**, *50*, 348-357.

27. Rablen, P. R.; Lockman, J. W.; Jorgensen, W. L., Ab Initio Study of Hydrogen-Bonded Complexes of Small Organic Molecules with Water. *J. Phys. Chem. A* **1998**, *102*, 3782-3797.

28. Kakiuchi, F.; Chatani, N., Catalytic Methods for C-H Bond Functionalization: Application in Organic Synthesis. *Adv. Synth. Catal.* **2003**, *345*, 1077-1101.

29. Nishio, M.; Umezawa, Y.; Honda, K.; Tsuboyama, S.; Suezawa, H., Ch/Π Hydrogen Bonds in Organic and Organometallic Chemistry. *CrystEngComm* **2009**, *11*, 1757-1788.

30. Takahashi, O.; Kohno, Y.; Nishio, M., Relevance of Weak Hydrogen Bonds in the Conformation of Organic Compounds and Bioconjugates: Evidence from Recent Experimental Data and High-Level Ab Initio Mo Calculations. *Chem. Rev.* **2010**, *110*, 6049-6076.

31. Novoa, J. J.; Mota, F.; D'Oria, E., The Nature of the C–H··· X Intermolecular Interactions in Molecular Crystals. A Theoretical Perspective. In *Hydrogen Bonding—New Insights*, Springer: 2006; pp 193-244.

32. Israelachvili, J. N., *Intermolecular and Surface Forces*; Academic Press Limited: London, 1991.

33. Stone, A., *The Theory of Intermolecular Forces*; oUP oxford, 2013.

34. Hayes, I.; Stone, A., An Intermolecular Perturbation Theory for the Region of Moderate Overlap. *Mol. Phys.* **1984**, *53*, 83-105.

35. Kitaura, K.; Morokuma, K., A New Energy Decomposition Scheme for Molecular Interactions within the Hartree-Fock Approximation. *Int. J. Quantum Chem* **1976**, *10*, 325-340.

36. Umeyama, H.; Morokuma, K., The Origin of Hydrogen Bonding. An Energy Decomposition Study. *J. Am. Chem. Soc.* **1977**, *99*, 1316-1332.

37. Viquez Rojas, C. I.; Fine, J.; Slipchenko, L. V., Exchange-Repulsion Energy in Qm/Efp. *J. Chem. Phys.* **2018**, *149*.

38. Domene, C.; Fowler, P.; Jemmer, P.; Madden, P., Dipole-Induced-Dipole Polarizabilities of Symmetric Clusters. *Mol. Phys.* **2000**, *98*, 1391-1407.

39. Steiner, T., The Hydrogen Bond in the Solid State. *Angew. Chem. Int. Ed.* **2002**, *41*, 48-76.

40. Becke, A. D.; Johnson, E. R., A Density-Functional Model of the Dispersion Interaction. *J. Chem. Phys.* **2005**, *123*.

41. Becke, A. D.; Johnson, E. R., Exchange-Hole Dipole Moment and the Dispersion Interaction. *J. Chem. Phys.* **2005**, *122*.

42. Pauling, L., The Nature of the Chemical Bond—1992. *J. Chem. Educ.* **1992**, *69*, 519.

43. Scheiner, S., The Hydrogen Bond: A Hundred Years and Counting. *J. Indian Inst. Sci.* **2020**, *100*, 61-76.

44. Dzyaloshinskii, I. E. e.; Lifshitz, E. M.; Pitaevskii, L. P., The General Theory of Van Der Waals Forces. *Advances in Physics* **1961**, *10*, 165-209.

45. Wagner, J. P.; Schreiner, P. R., London Dispersion in Molecular Chemistry—Reconsidering Steric Effects. *Angew. Chem. Int. Ed.* **2015**, *54*, 12274-12296.

46. Sinnokrot, M. O.; Sherrill, C. D., High-Accuracy Quantum Mechanical Studies of Π–Π Interactions in Benzene Dimers. *J. Phys. Chem. A* **2006**, *110*, 10656-10668.

47. Wheeler, S. E., Understanding Substituent Effects in Noncovalent Interactions Involving Aromatic Rings. *Acc. Chem. Res.* **2013**, *46*, 1029-1038.

48. Singh, S. K.; Das, A., The $N\rightarrow \Pi^*$ Interaction: A Rapidly Emerging Non-Covalent Interaction. *Phys. Chem. Chem. Phys.* **2015**, *17*, 9596-9612.

49. Singh, S. K.; Kumar, S.; Das, A., Competition between $N\rightarrow\Pi_{ar}^*$ and Conventional Hydrogen Bonding (N-H···N) Interactions: An Ab Initio Study of the Complexes of 7-Azaindole and Fluorosubstituted Pyridines. *Phys. Chem. Chem. Phys.* **2014**, *16*, 8819-8827.

50. Politzer, P.; Lane, P.; Concha, M. C.; Ma, Y.; Murray, J. S., An Overview of Halogen Bonding. *J. Mol. Model.* **2007**, *13*, 305-311.

51. Cavallo, G.; Metrangolo, P.; Milani, R.; Pilati, T.; Priimagi, A.; Resnati, G.; Terraneo, G., The Halogen Bond. *Chem. Rev.* **2016**, *116*, 2478-2601.

52. Vogel, L.; Wonner, P.; Huber, S. M., Chalcogen Bonding: An Overview. *Angew. Chem. Int. Ed.* **2019**, *58*, 1880-1891.

53. Pascoe, D. J.; Ling, K. B.; Cockroft, S. L., The Origin of Chalcogen-Bonding Interactions. *J. Am. Chem. Soc.* **2017**, *139*, 15160-15167.

54. Grabowski, S. J., Pnicogen and Tetrel Bonds—Tetrahedral Lewis Acid Centres. *Struct. Chem.* **2019**, *30*, 1141-1152.

55. Desiraju, G. R.; Steiner, T., *The Weak Hydrogen Bond in Structural Chemistry and Biology*; Oxford University Press, New York, 1999.

56. Pauling, L., The Nature of the Chemical Bond. Application of Results Obtained from the Quantum Mechanics and from a Theory of Paramagnetic Susceptibility to the Structure of Molecules. *J. Am. Chem. Soc.* **1931**, *53*, 1367-1400.

57. Lehn, J.-M., *Supramolecular Chemistry: Concepts and Perspectives*; John Wiley & Sons, New York, 1996.

58. Steed, J. W.; Atwood, J. L., *Supramolecular Chemistry: A Concise Introduction*; John Wiley & Sons Inc, New York, 2000.

59. Jeffrey, G. A.; Saenger, W., *Hydrogen Bonding in Biological Structures*; Springer: Berlin, 1991.

60. Perrin, C. L.; Nielson, J. B., “Strong” Hydrogen Bonds in Chemistry and Biology. *Annu. Rev. Phys. Chem.* **1997**, *48*, 511-544.

61. Aakeröy, C. B.; Seddon, K. R., The Hydrogen Bond and Crystal Engineering. *Chem. Soc. Rev.* **1993**, *22*, 397-407.

62. Subramanian, S.; Zaworotko, M. J., Exploitation of the Hydrogen Bond: Recent Developments in the Context of Crystal Engineering. *Coord. Chem. Rev.* **1994**, *137*, 357-401.

63. Kenny, P. W., Hydrogen-Bond Donors in Drug Design. *J. Med. Chem.* **2022**, *65*, 14261-14275.

64. Laurence, C.; Brameld, K. A.; Graton, J.; Le Questel, J.-Y.; Renault, E., The Pkbhx Database: Toward a Better Understanding of Hydrogen-Bond Basicity for Medicinal Chemists. *J. Med. Chem.* **2009**, *52*, 4073-4086.

65. Werner, A., Ueber Haupt-Und Nebenvalenzen Und Die Constitution Der Ammoniumverbindungen. *Justus Liebigs Annalen der Chemie* **1902**, *322*, 261-296.

66. Moore, T. S.; Winmill, T. F., Clxxvii.—the State of Amines in Aqueous Solution. *Journal of the Chemical Society, Transactions* **1912**, *101*, 1635-1676.

67. Pfeiffer, P.; Fischer, P.; Kuntner, J.; Monti, P.; Pros, Z., Zur Theorie Der Farblacke, Ii. *Justus Liebigs Annalen der Chemie* **1913**, *398*, 137-196.

68. Latimer, W. M.; Rodebush, W. H., Polarity and Ionization from the Standpoint of the Lewis Theory of Valence. *J. Am. Chem. Soc.* **1920**, *42*, 1419.

69. Lewis, G. N., *Valence and the Structure of Atoms and Molecules*; Chemical Catalog Company, Incorporated, 1923.

70. Pauling, L., *The Nature of the Chemical Bond*; Cornell University Press: Ithaca, NY, 1960.

71. Pimentel, G. C.; McClellan, A., Hydrogen Bonding. *Annu. Rev. Phys. Chem.* **1971**, *22*, 347-385.

72. Jeffrey, G. A., *An Introduction to Hydrogen Bonding*; Oxford University Press: New York, 1997.

73. Steiner, T.; Saenger, W., Role of Ch···O Hydrogen Bonds in the Coordination of Water Molecules. Analysis of Neutron Diffraction Data. *J. Am. Chem. Soc.* **1993**, *115*, 4540-4547.

74. Needham, P., Hydrogen Bonding: Homing in on a Tricky Chemical Concept. *Studies in History and Philosophy of Science Part A* **2013**, *44*, 51-65.

75. Parthasarathi, R.; Subramanian, V., Characterization of Hydrogen Bonding: From Van Der Waals Interactions to Covalency. *Hydrogen bonding—new insights* **2006**, 1-50.

76. Scheiner, S., *Hydrogen Bonding. A Theoretical Perspective*; Oxford University Press: Oxford, 1997.

77. Lu, J.; Scheiner, S., Effects of Halogen, Chalcogen, Pnicogen, and Tetrel Bonds on Ir and Nmr Spectra. *Molecules* **2019**, *24*, 2822.

78. Arnold, J.; Packard, M., Variations in Absolute Chemical Shift of Nuclear Induction Signals of Hydroxyl Groups of Methyl and Ethyl Alcohol. *J. Chem. Phys.* **1951**, *19*, 1608-1609.

79. Günther, H., *Nmr Spectroscopy: Basic Principles, Concepts and Applications in Chemistry*; John Wiley & Sons, 2013.

80. Pepinsky, R., Some New X-Ray and Neutron Studies of Hydrogen Bonding. *Reviews of Modern Physics* **1958**, *30*, 100.

81. Narten, A. H.; Habenschuss, A., Hydrogen Bonding in Liquid Methanol and Ethanol Determined by X-Ray Diffraction. *J. Chem. Phys.* **1984**, *80*, 3387-3391.

82. Taylor, R.; Kennard, O., Comparison of X-Ray and Neutron Diffraction Results for the Nh··· O= C Hydrogen Bond. *Acta Crystallogr. Sect. B: Struct. Sci.* **1983**, *39*, 133-138.

83. Dessent, C. E.; Müller-Dethlefs, K., Hydrogen-Bonding and Van Der Waals Complexes Studied by Zeke and Rempi Spectroscopy. *Chem. Rev.* **2000**, *100*, 3999-4022.

84. Gord, J. R.; Garrett, A. W.; Bandy, R. E.; Zwier, T. S., Rempi Fragmentation as a Probe of Hydrogen Bonding in Aromatic-X Clusters. *Chem. Phys. Lett.* **1990**, *171*, 443-450.

85. Goswami, M.; Arunan, E., Spectroscopic Determination of Hydrogen Bond Energies. *Spectroscopy and Computation of Hydrogen-Bonded Systems* **2023**, 293-343.

86. Helm, R. M.; Clara, M.; Grebner, T. L.; Neusser, H. J., Hydrogen Bonding in the Indole−Water Complex: A High Resolution Uv Study of the Hydrogen Donor Conformer. *J. Phys. Chem. A* **1998**, *102*, 3268-3272.

87. Giardini Guidoni, A.; Piccirillo, S.; Scuderi, D.; Satta, M.; Di Palma, T. M.; Speranza, M.; Filippi, A.; Paladini, A., R2pi Study of Intermolecular Hydrogen Bond in Solvent-Free Chiral Complexes. *Chirality* **2001**, *13*, 727-730.

88. Wu, R.; Vaupel, S.; Nachtigall, P.; Brutschy, B., Structure and Hydrogen Bonding of Different Isomers of 2-Aminopyridine⊙ Nh3 Studied by Ir/R2pi Spectroscopy. *J. Phys. Chem. A* **2004**, *108*, 3338-3343.

89. Janzen, C.; Spangenberg, D.; Roth, W.; Kleinermanns, K., Structure and Vibrations of Phenol(H2o)7,8 Studied by Infrared-Ultraviolet and Ultraviolet-Ultraviolet Double-Resonance Spectroscopy and Ab Initio Theory. *J. Chem. Phys.* **1999**, *110*, 9898-9907.

90. Inokuchi, Y.; Kobayashi, Y.; Ito, T.; Ebata, T., Conformation of L-Tyrosine Studied by Fluorescence-Detected Uv–Uv and Ir–Uv Double-Resonance Spectroscopy. *J. Phys. Chem. A* **2007**, *111*, 3209-3215.

91. Bondybey, V. E.; Smith, A. M.; Agreiter, J., New Developments in Matrix Isolation Spectroscopy. *Chem. Rev.* **1996**, *96*, 2113-2134.

92. Barnes, A.; Orville-Thomas, W.; Gaufrès, R.; Müller, A., *Matrix Isolation Spectroscopy*; Springer Science & Business Media, 2012; Vol. 76.

93. Davey, J.; Legon, A.; Waclawik, E., An Investigation of the Gas-Phase Complex of Water and Iodine Monochloride by Microwave Spectroscopy: Geometry, Binding Strength and Electron Redistribution. *Phys. Chem. Chem. Phys.* **2000**, *2*, 1659-1665.

94. Kinsey, J. L., Laser-Induced Fluorescence. *Annu. Rev. Phys. Chem.* **1977**, *28*, 349-372.

95. Huang, Z. S.; Miller, R. E., High-Resolution near-Infrared Spectroscopy of Water Dimer. *J. Chem. Phys.* **1989**, *91*, 6613-6631.

96. Szalewicz, K.; Cole, S. J.; Kol/os, W. o.; Bartlett, R. J., A Theoretical Study of the Water Dimer Interaction. *J. Chem. Phys.* **1988**, *89*, 3662-3673.

97. Del Bene, J.; Pople, J. A., Theory of Molecular Interactions. I. Molecular Orbital Studies of Water Polymers Using a Minimal Slater-Type Basis. *J. Chem. Phys.* **1970**, *52*, 4858-4866.

98. Popkie, H.; Kistenmacher, H.; Clementi, E., Study of the Structure of Molecular Complexes. Iv. The Hartree-Fock Potential for the Water Dimer and Its Application to the Liquid State. *J. Chem. Phys.* **1973**, *59*, 1325-1336.

99. Honegger, E.; Leutwyler, S., Intramolecular Vibrations of Small Water Clusters. *J. Chem. Phys.* **1988**, *88*, 2582-2595.

100. Coker, D.; Reimers, J.; Watts, R., The Infrared Absorption Spectrum of Water. *Australian Journal of Physics* **1982**, *35*, 623-638.

101. Coker, D.; Watts, R., Structure and Vibrational Spectroscopy of the Water Dimer Using Quantum Simulation. *J. Phys. Chem.* **1987**, *91*, 2513-2518.

102. Zhang, B.; Yu, Y.; Zhang, Z.; Zhang, Y.-Y.; Jiang, S.; Li, Q.; Yang, S.; Hu, H.-S.; Zhang, W.; Dai, D., Infrared Spectroscopy of Neutral Water Dimer Based on a Tunable Vacuum Ultraviolet Free Electron Laser. *J. Phys. Chem. Lett.* **2020**, *11*, 851-855.

103. Buck, U.; Huisken, F., Infrared Spectroscopy of Size-Selected Water and Methanol Clusters. *Chem. Rev.* **2000**, *100*, 3863-3890.

104. Dyczmons, V., Dimers of Ethanol. *J. Phys. Chem. A* **2004**, *108*, 2080-2086.

105. Weichert, A.; Riehn, C.; Brutschy, B., High-Resolution Rotational Coherence Spectroscopy of the Phenol Dimer. *J. Phys. Chem. A* **2001**, *105*, 5679-5691.

106. Wright, T. G.; Cordes, E.; Dopfer, O.; Müller-Dethlefs, K., Zero-Kinetic-Energy (Zeke) Photoelectron Spectroscopy of the Hydrogen-Bonded Phenol–Methanol Complex. *J. Chem. Soc., Faraday Trans.* **1993**, *89*, 1609-1621.

107. Spangenberg, D.; Imhof, P.; Roth, W.; Janzen, C.; Kleinermanns, K., Phenol−(Ethanol) 1 Isomers Studied by Double-Resonance Spectroscopy and Ab Initio Calculations. *J. Phys. Chem. A* **1999**, *103*, 5918-5924.

108. Bene, J. E. D., Theoretical Study of Open Chain Dimers and Trimers Containing Ch3oh and H2o. *J. Chem. Phys.* **2003**, *55*, 4633-4636.

109. Carney, J. R.; Hagemeister, F. C.; Zwier, T. S., The Hydrogen-Bonding Topologies of Indole--(Water)$_N$ Clusters from Resonant Ion-Dip Infrared Spectroscopy. *J. Chem. Phys.* **1998**, *108*, 3379-3382.

110. Gor, G. Y.; Tapio, S.; Domanskaya, A. V.; Räsänen, M.; Nemukhin, A. V.; Khriachtchev, L., Matrix-Isolation Study of the Phenol–Water Complex and Phenol Dimer. *Chem. Phys. Lett.* **2011**, *517*, 9-15.

111. Pittner, J.; Hobza, P., Ccsdt and Ccsd (T) Calculations on Model H-Bonded and Stacked Complexes. *Chem. Phys. Lett.* **2004**, *390*, 496-499.

112. Jurečka, P.; Hobza, P., On the Convergence of the (Δeccsd (T)− Δemp2) Term for Complexes with Multiple H-Bonds. *Chem. Phys. Lett.* **2002**, *365*, 89-94.

113. Halkier, A.; Jørgensen, P.; Gauss, J.; Helgaker, T., Ccsdt Calculations of Molecular Equilibrium Geometries. *Chem. Phys. Lett.* **1997**, *274*, 235-241.

114. Klopper, W.; Van Duijneveldt-Van De Rijdt, J.; Van Duijneveldt, F., Computational Determination of Equilibrium Geometry and Dissociation Energy of the Water Dimer. *Phys. Chem. Chem. Phys.* **2000**, *2*, 2227-2234.

115. Bader, R. F., Atoms in Molecules. *Acc. Chem. Res.* **1985**, *18*, 9-15.

116. Bader, R. F. W., *Atoms in Molecules: A Quantum Theory*; Clarendon Press: Oxford, U.K., 1990.

117. Weinhold, F.; Landis, C. R., Valency and Bonding: A Natural Bond Orbital Donor-Acceptor Perspective:. *Cambridge University Press: New York,* **2005**.

118. Reed, A. E.; Curtiss, L. A.; Weinhold, F., Intermolecular Interactions from a Natural Bond Orbital, Donor-Acceptor Viewpoint. *Chem. Rev.* **1988**, *88*, 899-926.

119. Reed, A. E.; Weinhold, F., Natural Bond Orbital Analysis of near-Hartree–Fock Water Dimer. *J. Chem. Phys.* **1983**, *78*, 4066-4073.

120. Laurence, C.; Berthelot, M., Observations on the Strength of Hydrogen Bonding. *Perspect. Drug Discovery Des.* **2000**, *18*, 39-60.

121. Hussein, M.; Millen, D., Hydrogen Bonding in the Gas Phase. Part 1.—Infra-Red Spectroscopic Investigation of Amine–Alcohol Systems. *Journal of the Chemical Society, Faraday Transactions 2: Molecular and Chemical Physics* **1974**, *70*, 685-692.

122. Laurence, C.; Berthelot, M.; Helbert, M.; Sraidi, K., The First Measurement of the Hydrogen Bond Basicity of Monomeric Water, Phenols and Weakly Basic Alcohols. *The Journal of Physical Chemistry* **1989**, *93*, 3799-3802.

123. Laurence, C.; Graton, J.; Berthelot, M.; Besseau, F.; Le Questel, J. Y.; Luçon, M.; Ouvrard, C.; Planchat, A.; Renault, E., An Enthalpic Scale of Hydrogen-Bond Basicity. 4. Carbon Π Bases, Oxygen Bases, and Miscellaneous Second-Row, Third-Row, and Fourth-Row Bases and a Survey of the 4-Fluorophenol Affinity Scale. *J. Org. Chem.* **2010**, *75*, 4105.

124. West, R.; Powell, D. L.; Lee, M. K.; Whatley, L. S., Hydrogen Bonding Studies. Ix. The Thermodynamics of Hydrogen Bonding of Phenol to Ethers and Related Compounds. *J. Am. Chem. Soc.* **1964**, *86*, 3227-3229.

125. Berthelot, M.; Besseau, F.; Laurence, C., The Hydrogen-Bond Basicity Pkhb Scale of Peroxides and Ethers. *Eur. J. Org. Chem.* **1998**, *1998*, 925-931.

126. Nochebuena, J.; Cuautli, C.; Ireta, J., Origin of Cooperativity in Hydrogen Bonding. *Phys. Chem. Chem. Phys.* **2017**, *19*, 15256-15263.

127. Ziółkowski, M.; Grabowski, S. J.; Leszczynski, J., Cooperativity in Hydrogen-Bonded Interactions: Ab Initio and "Atoms in Molecules" Analyses. *J. Phys. Chem. A* **2006**, *110*, 6514-6521.

128. Lee, H. M.; Singh, N. J.; Kim, K. S., Weak to Strong Hydrogen Bonds. *Hydrogen Bonding—New Insights* **2006**, 149-192.

129. Desiraju, G. R., The C-H···O Hydrogen Bond in Crystals: What Is It? *Acc. Chem. Res.* **1991**, *24*, 290-296.

130. Biswal, H. S.; Chakraborty, S.; Wategaonkar, S., Experimental Evidence of O–H—S Hydrogen Bonding in Supersonic Jet. *J. Chem. Phys.* **2008**, *129*, 184311.

131. Biswal, H. S.; Wategaonkar, S., Sulfur, Not Too Far Behind O, N, and C: Sh···Π Hydrogen Bond. *J. Phys. Chem. A* **2009**, *113*, 12774-12782.

132. Sutor, D. J., The C–H… O Hydrogen Bond in Crystals. *Nature* **1962**, *195*, 68-69.

133. Sutor, D. J., 204. Evidence for the Existence of C–H··· O Hydrogen Bonds in Crystals. *Journal of the Chemical Society (Resumed)* **1963**, 1105-1110.

134. Wulf, O. R.; Liddel, U.; Hendricks, S. B., The Effect of Ortho Substitution on the Absorption of the Oh Group of Phenol in the Infrared1. *J. Am. Chem. Soc.* **1936**, *58*, 2287-2293.

135. Yoshida, Z.-i.; Osawa, E., Hydrogen Bonding of Phenol to Π Electrons of Aromatics, Polyolefins, Heteroaromatics, Fulvenes, and Azulenes1. *J. Am. Chem. Soc.* **1966**, *88*, 4019-4026.

136. Feller, D., Strength of the Benzene−Water Hydrogen Bond. *J. Phys. Chem. A* **1999**, *103*, 7558-7561.

137. Matisz, G.; Kelterer, A.-M.; Fabian, W. M. F.; Kunsági-Máté, S., Coordination of Methanol Clusters to Benzene: A Computational Study. *J. Phys. Chem. A* **2011**, *115*, 10556-10564.

138. Jaffe, R. L.; Smith, G. D., A Quantum Chemistry Study of Benzene Dimer. *J. Chem. Phys.* **1996**, *105*, 2780-2788.

139. Chandrasekaran, V.; Biennier, L.; Arunan, E.; Talbi, D.; Georges, R., Direct Infrared Absorption Spectroscopy of Benzene Dimer. *J. Phys. Chem. A* **2011**, *115*, 11263-11268.

140. Von R. Schleyer, P.; West, R., Comparison of Covalently Bonded Electro-Negative Atoms as Proton Acceptor Groups in Hydrogen Bonding. *J. Am. Chem. Soc.* **1959**, *81*, 3164-3165.

141. Biswal, H. S.; Gloaguen, E.; Loquais, Y.; Tardivel, B.; Mons, M., Strength of Nh···S Hydrogen Bonds in Methionine Residues Revealed by Gas-Phase Ir/Uv Spectroscopy. *J Phys Chem Lett* **2012**, *3*, 755-9.

142. Mishra, K. K.; Singh, S. K.; Kumar, S.; Singh, G.; Sarkar, B.; Madhusudhan, M. S.; Das, A., Water-Mediated Selenium Hydrogen-Bonding in Proteins: Pdb Analysis and Gas-Phase Spectroscopy of Model Complexes. *J. Phys. Chem. A* **2019**, *123*, 5995-6002.

143. Pearson, R. G., The Transition-Metal-Hydrogen Bond. *Chem. Rev.* **1985**, *85*, 41-49.

144. Hewlings, S.; Kalman, D., Sulfur in Human Health. *EC Nutrition* **2019**, *14*, 785-791.

145. Komarnisky, L. A.; Christopherson, R. J.; Basu, T. K., Sulfur: Its Clinical and Toxicologic Aspects. *Nutrition* **2003**, *19*, 54-61.

146. Flagg, E. W.; Coates, R. J.; Eley, J. W.; Jones, D. P.; Gunter, E. W.; Byers, T. E.; Block, G. S.; Greenberg, R. S., Dietary Glutathione Intake in Humans and the Relationship between Intake and Plasma Total Glutathione Level. **1994**.

147. Nakajima, T., Roles of Sulfur Metabolism and Rhodanese in Detoxification and Anti-Oxidative Stress Functions in the Liver: Responses to Radiation Exposure. *Medical science monitor: international medical journal of experimental and clinical research* **2015**, *21*, 1721.

148. Mukwevho, E.; Ferreira, Z.; Ayeleso, A., Potential Role of Sulfur-Containing Antioxidant Systems in Highly Oxidative Environments. *Molecules* **2014**, *19*, 19376-19389.

149. Atmaca, G., Antioxidant Effects of Sulfur-Containing Amino Acids. *Yonsei medical journal* **2004**, *45*, 776-788.

150. Kim, J.-H.; Jang, H.-J.; Cho, W.-Y.; Yeon, S.-J.; Lee, C.-H., In Vitro Antioxidant Actions of Sulfur-Containing Amino Acids. *Arabian Journal of Chemistry* **2020**, *13*, 1678-1684.

151. Van De Poll, M. C.; Dejong, C. H.; Soeters, P. B., Adequate Range for Sulfur-Containing Amino Acids and Biomarkers for Their Excess: Lessons from Enteral and Parenteral Nutrition. *The Journal of nutrition* **2006**, *136*, 1694S-1700S.

152. Nimni, M. E.; Han, B.; Cordoba, F., Are We Getting Enough Sulfur in Our Diet? *Nutrition & metabolism* **2007**, *4*, 1-12.

153. Brosnan, J. T.; Brosnan, M. E., The Sulfur-Containing Amino Acids: An Overview. *The Journal of nutrition* **2006**, *136*, 1636S-1640S.

154. Zhou, P.; Tian, F.; Lv, F.; Shang, Z., Geometric Characteristics of Hydrogen Bonds Involving Sulfur Atoms in Proteins. *Proteins* **2009**, *76*, 151-163.

155. Nangia, A.; Desiraju, G. R., Axial and Equatorial Conformations of Penicillins, Their Sulphoxides and Sulphones: The Role of N⍰ H··· S and C⍰ H··· O Hydrogen Bonds. *J. Mol. Struct.* **1999**, *474*, 65-79.

156. Reddi, R.; Singarapu, K. K.; Pal, D.; Addlagatta, A., The Unique Functional Role of the C–H··· S Hydrogen Bond in the Substrate Specificity and Enzyme Catalysis of Type 1 Methionine Aminopeptidase. *Molecular BioSystems* **2016**, *12*, 2408-2416.

157. Platts, J.; Howard, S.; Bracke, B., Directionality of Hydrogen Bonds to Sulfur and Oxygen. *J. Am. Chem. Soc.* **1996**, *118*, 2726-2733.

158. Howard, D. L.; Kjaergaard, H. G., Hydrogen Bonding to Divalent Sulfur. *Phys. Chem. Chem. Phys.* **2008**, *10*, 4113-4118.

159. Allen, F. H.; Bird, C. M.; Rowland, R. S.; Raithby, P. R., Resonance-Induced Hydrogen Bonding at Sulfur Acceptors in R1r2c= S and R1cs2− Systems. *Acta Crystallogr. Sect. B: Struct. Sci.* **1997**, *53*, 680-695.

160. Tursi, A. J.; Nixon, E. R., Infrared Spectra of Matrix-Isolated Hydrogen Sulfide in Solid Nitrogen. *J. Chem. Phys.* **1970**, *53*, 518-521.

161. Tang, S. Y.; Brown, C. W., Raman Spectrum of Matrix Isolated Hydrogen Sulfide. *Journal of Raman Spectroscopy* **1974**, *2*, 209-215.

162. Mishra, K. K.; Borish, K.; Singh, G.; Panwaria, P.; Metya, S.; Madhusudhan, M.; Das, A., Observation of an Unusually Large Ir Red-Shift in an Unconventional S–H··· S Hydrogen-Bond. *J. Phys. Chem. Lett.* **2021**, *12*, 1228-1235.

163. Levy, D. H., Laser Spectroscopy of Cold Gas-Phase Molecules. *Annu. Rev. Phys. Chem.* **1980**, *31*, 197-225.

164. Smalley, R. E.; Wharton, L.; Levy, D. H., Molecular Optical Spectroscopy with Supersonic Beams and Jets. *Acc. Chem. Res.* **1977**, *10*, 139-145.

165. Levy, D. H., The Spectroscopy of Very Cold Gases. *Science* **1981**, *214*, 263-269.

166. Kantrowitz, A.; Grey, J., A High Intensity Source for the Molecular Beam. Part I. Theoretical. *Rev. Sci. Instrum* **1951**, *22*, 4.

167. Kistiakowsky, G.; Slichter, W. P., A High Intensity Source for the Molecular Beam. Part Ii. Experimental. *Rev. Sci. Instrum.* **1951**, *22*, 333-337.

168. Becker, E.; Bier, K., Die Erzeugung Eines Intensiven, Teilweise Monochromatisierten Wasserstoff-Molekularstrahles Mit Einer Laval-Düse. *Zeitschrift für Naturforschung A* **1954**, *9*, 975-986.

169. de Vries, M. S.; Hobza, P., Gas-Phase Spectroscopy of Biomolecular Building Blocks. *Annu. Rev. Phys. Chem.* **2007**, *58*, 585-612.

170. Tubergen, M. J.; Levy, D. H., Spectroscopy of Indole Van Der Waals Complexes: Evidence for a Conformation-Dependent Excited State. *The Journal of Physical Chemistry* **1991**, *95*, 2175-2181.

171. Morse, M. D., Supersonic Beam Sources. *Experimental methods in the physical sciences* **1996**, *29*, 21-47.

172. Valleau, J.; Deckers, J., Supersonic Molecular Beams: Ii. Theory of the Formation of Supersonic Molecular Beams. *Can. J. Chem.* **1965**, *43*, 6-17.

173. LeRoy, R. L.; Govers, T. R.; Deckers, J. M., Supersonic Molecular Beam Intensities. *Can. J. Chem.* **1970**, *48*, 927-933.

174. Pollard, J. E.; Trevor, D.; Lee, Y.; Shirley, D., Photoelectron Spectroscopy of Supersonic Molecular Beams. *Rev. Sci. Instrum.* **1981**, *52*, 1837-1846.

175. Quintella, C. D., Supersonic Molecular Beams in Chemistry. *Quim. Nova* **1996**, *19*, 660-667.

176. Arumainayagam, C. R.; Madix, R. J., Molecular-Beam Studies of Gas-Surface Collision Dynamics. *Prog. Surf. Sci.* **1991**, *38*, 1-102.

177. Dunning, F. B.; Hulet, R. G., *Atomic, Molecular, and Optical Physics: Atoms and Molecules*; Academic press, 1996.

178. Imasaka, T.; Moore, D. S.; Vo-Dinh, T., Critical Assessment: Use of Supersonic Jet Spectrometry for Complex Mixture Analysis (Iupac Technical Report). *Pure Appl. Chem.* **2003**, *75*, 975-998.

179. Anderson, J. B.; Fenn, J. B., Velocity Distributions in Molecular Beams from Nozzle Sources. *The Physics of Fluids* **1965**, *8*, 780-787.

180. Rademann, K.; Brutschy, B.; Baumgärtel, H., Electronic Spectroscopy of Fluorobenzene Van Der Waals Molecules by Resonant Two-Photon Ionization. *Chem. Phys.* **1983**, *80*, 129-145.

181. Page, R. H.; Shen, Y.; Lee; YT, Highly Resolved Spectra of Local Modes of Benzene. *Phys. Rev. Lett.* **1987**, *59*, 1293.

182. Wiley, W. C.; McLaren, I. H., Time-of-Flight Mass Spectrometer with Improved Resolution. *Rev. Sci. Instrum.* **1955**, *26*, 1150-1157.

183. Sorokin, P. P.; Lankard, J., Stimulated Emission Observed from an Organic Dye, Chloro-Aluminum Phthalocyanine. *IBM Journal of Research and Development* **1966**, *10*, 162-163.

184. Duarte, F. J.; Hillman, L. W., Dye Laser Principles, with Applications. **1990**.

185. Liao, P. F. K., P.; Duarte, F. J.; Hillman, L. W., *Dye Laser Principles: With Applications*; Elsevier, 2012.

186. Gerhards, M.; Perl, W.; Kleinermanns, K., Rotamers and Vibrations of Resorcinol Obtained by Spectral Hole Burning. *Chem. Phys. Lett.* **1995**, *240*, 506-512.

187. Page, R. H.; Shen, Y.; Lee, Y.-T., Infrared–Ultraviolet Double Resonance Studies of Benzene Molecules in a Supersonic Beam. *J. Chem. Phys.* **1988**, *88*, 5362-5376.

188. Crews, B. O., *Uv and Ir Double Resonance Spectroscopy of Peptides, DNA Bases and Clusters*; University of California, Santa Barbara, 2007.

189. Frisch, M. J., et al. *Gaussian 09, Revision B.01*, Gaussian, Inc., Wallingford CT, 2009.

190. Schmidt, M. W.; Baldridge, K. K.; Boatz, J. A.; Elbert, S. T.; Gordon, M. S.; Jensen, J. H.; Koseki, S.; Matsunaga, N.; Nguyen, K. A.; Su, S., General Atomic and Molecular Electronic Structure System. *J. Comput. Chem.* **1993**, *14*, 1347-1363.

191. Gordon, M. S.; Schmidt, M. W., Advances in Electronic Structure Theory: Gamess a Decade Later. In *Theory and Applications of Computational Chemistry*, Elsevier: 2005; pp 1167-1189.

192. Lu, T.; Chen, F., Multiwfn: A Multifunctional Wavefunction Analyzer. *J. Comput. Chem.* **2012**, *33*, 580-592.

193. Neese, F., Software Update: The Orca Program System, Version 4.0. *Wiley Interdisciplinary Reviews: Computational Molecular Science* **2018**, *8*, e1327.

194. Grimme, S., Semiempirical Gga-Type Density Functional Constructed with a Long-Range Dispersion Correction. *J. Comput. Chem.* **2006**, *27*, 1787-1799.

195. Grimme, S., Semiempirical Hybrid Density Functional with Perturbative Second-Order Correlation. *J. Chem. Phys.* **2006**, *124*.

196. Zhao, Y.; Truhlar, D. G., The M06 Suite of Density Functionals for Main Group Thermochemistry, Thermochemical Kinetics, Noncovalent Interactions, Excited States, and Transition Elements: Two New Functionals and Systematic Testing of Four M06-Class Functionals and 12 Other Functionals. *Theoretical Chemistry Accounts: Theory, Computation, and Modeling* **2008**, *120*, 215.

197. Cai, X. D.; Liu, Z.; Zhao, S.; Song, C.; Dong, S. L.; Xiao, J. X., A Single Stranded Fluorescent Peptide Probe for Targeting Collagen in Connective Tissues. *Chem. Commun.* **2017**, *53*, 11905-11908.

198. Head-Gordon, M.; Head-Gordon, T., Analytic Mp2 Frequencies without Fifth-Order Storage. Theory and Application to Bifurcated Hydrogen Bonds in the Water Hexamer. *Chem. Phys. Lett.* **1994**, *220*, 122-128.

199. Frisch, M. J.; Head-Gordon, M.; Pople, J. A., Semi-Direct Algorithms for the Mp2 Energy and Gradient. *Chem. Phys. Lett.* **1990**, *166*, 281-289.

200. Head-Gordon, M.; Pople, J. A.; Frisch, M. J., Mp2 Energy Evaluation by Direct Methods. *Chem. Phys. Lett.* **1988**, *153*, 503-506.

201. Lu, T. *Molclus Program*, Version 1.12,.

202. Boys, S. F.; Bernardi, F., The Calculation of Small Molecular Interactions by the Differences of Separate Total Energies. Some Procedures with Reduced Errors. *Mol. Phys.* **1970**, *19*, 553-566.

203. Glendening, E. D.; Landis, C. R.; Weinhold, F., Nbo 6.0: Natural Bond Orbital Analysis Program. *J. Comput. Chem.* **2013**, *34*, 1429-1437.

204. Su, P.; Li, H., Energy Decomposition Analysis of Covalent Bonds and Intermolecular Interactions. *J. Chem. Phys.* **2009**, *131*, 14102-15.

205. Bader, R. F. W., Atoms in Molecules. *Acc. Chem. Res.* **1985**, *18*, 9-15.

206. Cortés-Guzmán, F.; Bader, R. F. W., Complementarity of Qtaim and Mo Theory in the Study of Bonding in Donor–Acceptor Complexes. *Coord. Chem. Rev.* **2005**, *249*, 633-662.

207. Meyer, E. A.; Castellano, R. K.; Diederich, F., Interactions with Aromatic Rings in Chemical and Biological Recognition. *Angew. Chem. Int. Ed.* **2003**, *42*, 1210-1250.

208. Desiraju, G. R., Supramolecular Synthons in Crystal Engineering—a New Organic Synthesis. *Angew. Chem. Int. Ed.* **1995**, *34*, 2311-2327.

209. Cannon, C. G., The Nature of Hydrogen Bonding: A Review of Published Work and Discussion. *Spectrochim. Acta* **1958**, *10*, 341-368.

210. Pimentel, G. C.; McClellan, A. L., *The Hydrogen Bond*; W.H. Freeman: San Francisco ; London, 1960, p xi, 475 p.

211. Desiraju, G. R., C-H···O and Other Weak Hydrogen Bonds. From Crystal Engineering to Virtual Screening. *Chem. Commun.* **2005**, 2995-3001.

212. Steiner, T., C–H–O Hydrogen Bonding in Crystals. *Crystallography Reviews* **1996**, *6*, 1-51.

213. Hansen, A. S.; Du, L.; Kjaergaard, H. G., Positively Charged Phosphorus as a Hydrogen Bond Acceptor. *J. Phys. Chem. Lett.* **2014**, *5*, 4225-4231.

214. Mishra, K. K.; Singh, S. K.; Ghosh, P.; Ghosh, D.; Das, A., The Nature of Selenium Hydrogen Bonding: Gas Phase Spectroscopy and Quantum Chemistry Calculations. *Phys. Chem. Chem. Phys.* **2017**, *19*, 24179-24187.

215. Biswal, H. S.; Bhattacharyya, S.; Bhattacherjee, A.; Wategaonkar, S., Nature and Strength of Sulfur-Centred Hydrogen Bonds: Laser Spectroscopic Investigations in the Gas Phase and Quantum-Chemical Calculations. *Int. Rev. Phys. Chem.* **2015**, *34*, 99-160.

216. Chand, A.; Sahoo, D. K.; Rana, A.; Jena, S.; Biswal, H. S., The Prodigious Hydrogen Bonds with Sulfur and Selenium in Molecular Assemblies, Structural Biology, and Functional Materials. *Acc. Chem. Res.* **2020**, *53*, 1580-1592.

217. Mundlapati, V. R.; Ghosh, S.; Bhattacherjee, A.; Tiwari, P.; Biswal, H. S., Critical Assessment of the Strength of Hydrogen Bonds between the Sulfur Atom of Methionine/Cysteine and Backbone Amides in Proteins. *Journal of Physical Chemistry Letters* **2015**, *6*, 1385-1389.

218. Mundlapati, V. R.; Sahoo, D. K.; Ghosh, S.; Purame, U. K.; Pandey, S.; Acharya, R.; Pal, N.; Tiwari, P.; Biswal, H. S., Spectroscopic Evidences for Strong Hydrogen Bonds with Selenomethionine in Proteins. *J. Phys. Chem. Lett.* **2017**, *8*, 794-800.

219. Dalvit, C.; Invernizzi, C.; Vulpetti, A., Fluorine as a Hydrogen-Bond Acceptor: Experimental Evidence and Computational Calculations. *Chem. Eur. J.* **2014**, *20*, 11058-11068.

220. van Bergen, L. A.; Alonso, M.; Palló, A.; Nilsson, L.; De Proft, F.; Messens, J., Revisiting Sulfur H-Bonds in Proteins: The Example of Peroxiredoxin Ahpe. *Sci. Rep.* **2016**, *6*, 30369.

221. Suzuki, N.; Higuchi, T.; Urano, Y.; Kikuchi, K.; Uekusa, H.; Ohashi, Y.; Uchida, T.; Kitagawa, T.; Nagano, T., Novel Iron Porphyrin− Alkanethiolate Complex with Intramolecular Nh···S Hydrogen Bond: Synthesis, Spectroscopy, and Reactivity. *J. Am. Chem. Soc.* **1999**, *121*, 11571-11572.

222. Steiner, T., S—H··· S Hydrogen-Bond Chain in Thiosalicylic Acid. *Acta Crystallogr. Sect. C: Cryst. Struct. Commun.* **2000**, *56*, 876-877.

223. Yan, B.; Jaeqx, S.; Van Der Zande, W. J.; Rijs, A. M., A Conformation-Selective Ir-Uv Study of the Dipeptides Ac-Phe-Ser-Nh$_2$ and Ac-Phe-Cys-Nh$_2$: Probing the Sh···O and Oh···O Hydrogen Bond Interactions. *Phys. Chem. Chem. Phys.* **2014**, *16*, 10770-10778.

224. Begley, T. P.; Xi, J.; Kinsland, C.; Taylor, S.; McLafferty, F., The Enzymology of Sulfur Activation During Thiamin and Biotin Biosynthesis. *Curr. Opin. Chem. Biol.* **1999**, *3*, 623-629.

225. Lehninger, A. L.; Nelson, D. L.; Cox, M. M.; Cox, M. M., *Lehninger Principles of Biochemistry*; Macmillan, 2005.

226. Daeffler, K. N. M.; Lester, H. A.; Dougherty, D. A., Functionally Important Aromatic-Aromatic and Sulfur-Π Interactions in the D2 Dopamine Receptor. *J. Am. Chem. Soc.* **2012**, *134*, 14890-14896.

227. Zheng, P.; Takayama, S.-i. J.; Mauk, A. G.; Li, H., Hydrogen Bond Strength Modulates the Mechanical Strength of Ferric-Thiolate Bonds in Rubredoxin. *J. Am. Chem. Soc.* **2012**, *134*, 4124-4131.

228. Allen, F. H.; Bird, C. M.; Rowland, R. S.; Raithby, P. R., Hydrogen-Bond Acceptor and Donor Properties of Divalent Sulfur (Ysz and Rsh). *Acta Crystallogr. Sect. B: Struct. Sci.* **1997**, *53*, 696-701.

229. Biswal, H. S.; Wategaonkar, S., Oh⋯X (X = O, S) Hydrogen Bonding in Thetrahydrofuran and Tetrahydrothiophene. *J. Chem. Phys.* **2011**, *135*, 134306.

230. Copley, M.; Marvel, C.; Ginsberg, E., Hydrogen Bonding by Sh. Vii. 1 Aryl Mercaptans. *J. Am. Chem. Soc.* **1939**, *61*, 3161-3162.

231. Gordy, W.; Stanford, S. C., Spectroscopic Evidence for Hydrogen Bonds: Sh, Nh and Nh2 Compounds. *J. Am. Chem. Soc.* **1940**, *62*, 497-505.

232. Menefee, A.; Alford, D.; Scott, C., Hydrogen Bonding of the Thiol Group. *J. Chem. Phys.* **1956**, *25*, 370-371.

233. Plant, D.; Tarbell, D. S.; Whiteman, C., An Infrared Study of Hydrogen Bonding Involving the Thiol Group1. *J. Am. Chem. Soc.* **1955**, *77*, 1572-1575.

234. Silva, W. G.; Evangelisti, L.; van Wijngaarden, J., Internal Motions and Sulfur Hydrogen Bonding in Methyl 3-Mercaptopropionate. *J. Phys. Chem. A* **2019**, *123*, 9840-9849.

235. Saragi, R. T.; Juanes, M.; Pinacho, R.; Rubio, J. E.; Fernández, J. A.; Lesarri, A., Molecular Recognition, Transient Chirality and Sulfur Hydrogen Bonding in the Benzyl Mercaptan Dimer. *Symmetry* **2021**, *13*, 2022.

236. Juanes, M.; Lesarri, A.; Pinacho, R.; Charro, E.; Rubio, J. E.; Enriquez, L.; Jaraiz, M., Sulfur Hydrogen Bonding in Isolated Monohydrates: Furfuryl Mercaptan Versus Furfuryl Alcohol. *Chemistry* **2018**, *24*, 6564-6571.

237. Han, S.; You, H. S.; Kim, S.-Y.; Kim, S. K., Dynamic Role of the Intramolecular Hydrogen Bonding in Nonadiabatic Chemistry Revealed in the Uv Photodissociation

Reactions of 2-Fluorothiophenol and 2-Chlorothiophenol. *J. Phys. Chem. A* **2014**, *118*, 6940-6949.

238. You, H. S.; Han, S.; Yoon, J.-H.; Lim, J. S.; Lee, J.; Kim, S.-Y.; Ahn, D.-S.; Lim, J. S.; Kim, S. K., Structure and Dynamic Role of Conical Intersections in the Πσ*-Mediated Photodissociation Reactions. *Int. Rev. Phys. Chem.* **2015**, *34*, 429-459.

239. Dunitz, J. D.; Taylor, R., Organic Fluorine Hardly Ever Accepts Hydrogen Bonds. *Chem. Eur. J.* **1997**, *3*, 89-98.

240. Li, X.; Jin, Y.; Gou, Q.; Xia, Z.; Feng, G., Microwave Spectrum and Non-Covalent Interactions of the 1, 2, 3, 4-Tetrafluorobenzene-Water Complex. *J. Chem. Phys.* **2018**, *149*.

241. Brendel, K.; Mader, H.; Xu, Y.; Jager, W., The Rotational Spectra of the Fluorobenzene⋯Water and P-Difluorobenzene⋯Water Dimers: Structure and Internal Dynamics. *J. Mol. Spectrosc.* **2011**, *268*, 47-52.

242. Tarakeshwar, P.; Kim, K. S.; Brutschy, B., Fluorobenzene⋯ Water and Difluorobenzene⋯ Water Systems: An Ab Initio Investigation. *J. Chem. Phys.* **1999**, *110*, 8501-8512.

243. Kang; Pratt, D. W.; Schäfer, M., High-Resolution Electronic Spectrum of the P-Difluorobenzene− Water Complex: Structure and Internal Rotation Dynamics. *J. Phys. Chem. A* **2005**, *109*, 767-772.

244. Banerjee, P.; Mukhopadhyay, D. P.; Chakraborty, T., On the Origin of Donor O–H Bond Weakening in Phenol-Water Complexes. *J. Chem. Phys.* **2015**, *143*, 204306.

245. Maity, S.; Patwari, G. N., Hydrogen Bonding to Multifunctional Molecules: Spectroscopic and Ab Initio Investigation of Water Complexes of Fluorophenylacetylenes. *J. Phys. Chem. A* **2009**, *113*, 1760-1769.

246. Singh, P. C.; Maity, S.; Patwari, G. N., Water Complexes of Styrene and 4-Fluorostyrene: A Combined Electronic, Vibrational Spectroscopic and Ab-Initio Investigation. *J. Phys. Chem. A* **2008**, *112*, 9702-9707.

247. Robertson, P. A.; Villani, L.; Dissanayake, U. L.; Duncan, L. F.; Abbott, B. M.; Wilson, D. J.; Robertson, E. G., Halocarbons as Hydrogen Bond Acceptors: A Spectroscopic Study of Haloethylbenzenes (Phch 2 Ch 2 X, X= F, Cl, Br) and Their Hydrate Clusters. *Phys. Chem. Chem. Phys.* **2018**, *20*, 8218-8227.

248. Ruoff, R.; Klots, T.; Emilsson, T.; Gutowsky, H., Relaxation of Conformers and Isomers in Seeded Supersonic Jets of Inert Gases. *J. Chem. Phys.* **1990**, *93*, 3142-3150.

249. Watanabe, T.; Ebata, T.; Tanabe, S.; Mikami, N., Size-Selected Vibrational Spectra of Phenol-$(H_2O)_N$ (N= 1–4) Clusters Observed by Ir–Uv Double Resonance and Stimulated Raman-Uv Double Resonance Spectroscopies. *J. Chem. Phys.* **1996**, *105*, 408-419.

250. Herzberg, G., Electronic Spectra and Electronic Structure of Polyatomic Molecules. *(No Title)* **1966**.

251. Ghosh, S.; Bhattacharyya, S.; Wategaonkar, S., Dissociation Energies of Sulfur-Centered Hydrogen-Bonded Complexes. *J. Phys. Chem. A* **2015**, *119*, 10863-10870.

252. Bhattacharyya, S.; Bhattacherjee, A.; Shirhatti, P. R.; Wategaonkar, S., O-H⋯S Hydrogen Bonds Conform to the Acid-Base Formalism. *J. Phys. Chem. A* **2013**, *117*, 8238-8250.

253. Kreevoy, M. M.; Harper, E. T.; Duvall, R. E.; Wilgus, H. S., III; Ditsch, L. T., Inductive Effects on the Acid Dissociation Constants of Mercaptans1. *J. Am. Chem. Soc.* **1960**, *82*, 4899-4902.

254. Serjeant, E. P.; Dempsey, B., Ionisation Constants of Organic Acids in Aqueous Solution. *IUPAC chemical data series* **1979**, *23*, 160-190.

255. Jencks, W.; Regenstein, J., Handbook of Biochemistry and Molecular Biology. *CRC, Cleveland, OH* **1976**, 338.

256. Ballinger, P.; Long, F. A., Acid Ionization Constants of Alcohols. Ii. Acidities of Some Substituted Methanols and Related Compounds1,2. *J. Am. Chem. Soc.* **1960**, *82*, 795-798.

257. Bjerrum, J.; Schwarzenbach, G.; Sillén, L., Stability Constants, Part Ii: Inorganic Ligands, Chem. *Soc. Spec. Publ* **1958**.

258. Perrin, D. D., *Ionisation Constants of Inorganic Acids and Bases in Aqueous Solution*; Elsevier, 2016.

259. Kubinyi, H., Hydrogen Bonding: The Last Mystery in Drug Design? *Pharmacokinetic optimization in drug research: biological, physicochemical, and computational strategies* **2001**, 513-524.

260. Kuhn, B.; Mohr, P.; Stahl, M., Intramolecular Hydrogen Bonding in Medicinal Chemistry. *J. Med. Chem.* **2010**, *53*, 2601-11.

261. Lu, A.; Wang, Z.; Zhou, Z.; Chen, J.; Wang, Q., Application of "Hydrogen Bonding Interaction" in New Drug Development: Design, Synthesis, Antiviral Activity, and Sars of Thiourea Derivatives. *J. Agric. Food. Chem.* **2015**, *63*, 1378-84.

262. Moller, K. H.; Hansen, A. S.; Kjaergaard, H. G., Gas Phase Detection of the Nh-P Hydrogen Bond and Importance of Secondary Interactions. *J. Phys. Chem. A* **2015**, *119*, 10988-10998.

263. Fang, W.; Chen, J.; Feng, Y.; Li, X.-Z.; Michaelides, A., The Quantum Nature of Hydrogen. *Int. Rev. Phys. Chem.* **2019**, *38*, 35-61.

264. Chand, A.; Biswal, H. S., Hydrogen Bonds with Chalcogens: Looking Beyond the Second Row of the Periodic Table. *J. Indian Inst. Sci.* **2019**, *100*, 77-100.

265. Pal, D.; Charaya, H.; Chakraborty, S., An Experimental Exploration of C-H··· X Hydrogen Bond in [Chcl3-X (Ch3) 2] Complexes (X= O, S, and Se). *ChemPhysChem* **2023**, e202300124.

266. Agrawal, S. K.; Chakraborty, A.; Chakraborty, S., Atmospherically Relevant Halogen-and Hydrogen-Bond Complex [Ccl_4 $(H_2y)_N$] with Y= O and S, N≤ 4: A Computational Study on Rayleigh Scattering Properties. *Computational and Theoretical Chemistry* **2023**, *1229*, 114293.

267. Metya, S.; Das, A., S–H···O Hydrogen Bond Can Win over O–H···S Hydrogen Bond: Gas-Phase Spectroscopy of 2-Fluorothiophenol···H_2o Complex. *J. Phys. Chem. A* **2022**, *126*, 9178-9189.

268. Press, C., *Handbook of Biochemistry and Molecular Biology*; CRC Press, 2010.

269. Oikawa, A.; Abe, H.; Mikami, N.; Ito, M., Solvated Phenol Studied by Supersonic Jet Spectroscopy. *The Journal of Physical Chemistry* **1983**, *87*, 5083-5090.

270. Lipert, R. J.; Colson, S. D., Persistent Spectral Hole Burning of Molecular Clusters in a Supersonic Jet. *The Journal of Physical Chemistry* **1989**, *93*, 3894-3896.

271. Larsen, R. W.; Zielke, P.; Suhm, M. A., Hydrogen-Bonded Oh Stretching Modes of Methanol Clusters: A Combined Ir and Raman Isotopomer Study. *J. Chem. Phys.* **2007**, *126*, 194307-18.

272. Doi, A.; Mikami, N., Dynamics of Hydrogen-Bonded Oh Stretches as Revealed by Single-Mode Infrared-Ultraviolet Laser Double Resonance Spectroscopy on Supersonically Cooled Clusters of Phenol. *J. Chem. Phys.* **2008**, *129*, 154308.

273. Alecu, I.; Zheng, J.; Zhao, Y.; Truhlar, D. G., Computational Thermochemistry: Scale Factor Databases and Scale Factors for Vibrational Frequencies Obtained from Electronic Model Chemistries. *Journal of chemical theory and computation* **2010**, *6*, 2872-2887.

274. Wassermann, T. N.; Suhm, M. A., Ethanol Monomers and Dimers Revisited: A Raman Study of Conformational Preferences and Argon Nanocoating Effects. *J. Phys. Chem. A* **2010**, *114*, 8223-8233.

275. Hunter, E. P.; Lias, S. G., Evaluated Gas Phase Basicities and Proton Affinities of Molecules: An Update. *J. Phys. Chem. Ref. Data* **1998**, *27*, 413-656.

276. Corbin, P. S.; Zimmerman, S. C.; Thiessen, P. A.; Hawryluk, N. A.; Murray, T. J., Complexation-Induced Unfolding of Heterocyclic Ureas. Simple Foldamers Equilibrate with Multiply Hydrogen-Bonded Sheetlike Structures1. *J. Am. Chem. Soc.* **2001**, *123*, 10475-10488.

277. Prins, L. J.; Reinhoudt, D. N.; Timmerman, P., Noncovalent Synthesis Using Hydrogen Bonding. *Angew. Chem. Int. Ed.* **2001**, *40*, 2382-2426.

278. Chang, S.-Y.; Kim, H. S.; Chang, K.-J.; Jeong, K.-S., Efficient Modulation of Hydrogen-Bonding Interactions by Remote Substituents. *Org. Lett.* **2004**, *6*, 181-184.

279. Beno, B. R.; Yeung, K.-S.; Bartberger, M. D.; Pennington, L. D.; Meanwell, N. A., A Survey of the Role of Noncovalent Sulfur Interactions in Drug Design. *J. Med. Chem.* **2015**, *58*, 4383-4438.

280. Pathania, S.; Narang, R. K.; Rawal, R. K., Role of Sulphur-Heterocycles in Medicinal Chemistry: An Update. *European journal of medicinal chemistry* **2019**, *180*, 486-508.

281. Toth, G.; Bowers, S. G.; Truong, A. P.; Probst, G., The Role and Significance of Unconventional Hydrogen Bonds in Small Molecule Recognition by Biological Receptors of Pharmaceutical Relevance. *Current pharmaceutical design* **2007**, *13*, 3476-3493.

282. Adhav, V. A.; Saikrishnan, K., The Realm of Unconventional Noncovalent Interactions in Proteins: Their Significance in Structure and Function. *Acs Omega* **2023**, *8*, 22268-22284.

283. Bhattacharyya, S.; Ghosh, S.; Wategaonkar, S., O–H Stretching Frequency Red Shifts Do Not Correlate with the Dissociation Energies in the Dimethylether and Dimethylsulfide Complexes of Phenol Derivatives. *Phys. Chem. Chem. Phys.* **2021**, *23*, 5718-5739.

284. Bhattacharyya, S.; Ghosh, S.; Wategaonkar, S., O-H Stretching Frequency Red Shifts Do Not Correlate with the Dissociation Energies in the Dimethylether and Dimethylsulfide Complexes of Phenol Derivatives. *Phys Chem Chem Phys* **2021**, *23*, 5718-5739.

285. Biswal, H. S.; Wategaonkar, S., O−H⋯O Versus O−H⋯S Hydrogen Bonding. 3. Ir−Uv Double Resonance Study of Hydrogen Bonded Complexes of P-Cresol with Diethyl Ether and Its Sulfur Analog. *J. Phys. Chem. A* **2010**, *114*, 5947-5957.

286. Aarabi, M.; Gholami, S.; Grabowski, S. J., S− H… O and O− H… O Hydrogen Bonds-Comparison of Dimers of Thiocarboxylic and Carboxylic Acids. *ChemPhysChem* **2020**, *21*, 1653-1664.

287. Fossey, J.; Mourgues, P.; Thissen, R.; Audier, H. E., Proton Affinity of Some Radicals of Alcohols, Ethers and Amines. *Int. J. Mass spectrom.* **2003**, *227*, 373-380.

288. Walters, A.; Müller, H. S. P.; Lewen, F.; Schlemmer, S., Submillimeter-Wave Spectrum of *Anti-Anti* and *Anti-Gauche* Diethyl Ether. *J. Mol. Spectrosc.* **2009**, *257*, 24-28.

289. Medvedev, I.; Winnewisser, M.; De Lucia, F. C.; Herbst, E.; Bialkowska-Jaworska, E.; Pszczólkowski, L.; Kisiel, Z., The Millimeter- and Submillimeter-Wave Spectrum of the *Trans-Gauche* Conformer of Diethyl Ether. *J. Mol. Spectrosc.* **2004**, *228*, 314-328.

290. Galabov, B.; Ilieva, S.; Dudev, T.; Phan, H. V.; Durig, J. R., Interpretation and Prediction of Vibrational Absorption Intensities - Methylethyl Ether and Diethyl-Ether. *Spectrochimica Acta Part a-Molecular and Biomolecular Spectroscopy* **1993**, *49*, 2093-2103.

291. Kisiel, Z.; Pszczólkowski, L.; Medvedev, I. R.; Winnewisser, M.; De Lucia, F. C.; Herbst, E., Rotational Spectrum of *Trans-Trans* Diethyl Ether in the Ground and Three Excited Vibrational States. *J. Mol. Spectrosc.* **2005**, *233*, 231-243.

292. Morita, M.; Matsuda, Y.; Endo, T.; Mikami, N.; Fujii, A.; Takahashi, K., Hyperconjugation in Diethyl Ether Cation Versus Diethyl Sulfide Cation. *Phys. Chem. Chem. Phys.* **2015**, *17*, 23602-23612.

293. Song, C. Y.; Li, R. Q.; Ge, L. X.; Liu, Y., Study on the Fluorescence Characteristic and Mechanism of Ether-Water Solution. *Spectroscopy and Spectral Analysis* **2007**, *27*, 534-538.

294. Rakipov, I. T.; Semenov, K. N.; Petrov, A. A.; Akhmadiyarov, A. A.; Khachatrian, A. A.; Klimovitskii, A. E.; Solomonov, B. N., Ftir Spectroscopy of Intermolecular Interactions of Ethers with Methanol: Cooperativity Effect. *J. Solution Chem.* **2022**, *51*, 1219-1228.

295. Wieser, H.; Laidlaw, W.; Krueger, P.; Fuhrer, H., Vibrational Spectra and a Valence Force Field for Conformers of Diethyl Ether and Deuterated Analogues. *Spectrochimica Acta Part A: Molecular Spectroscopy* **1968**, *24*, 1055-1089.

296. Hayashi, M.; Kuwada, K., The Microwave Spectrum, the Rs Structure and the Dipole Moment of the Tt Isomer of Diethyl Ether. *Bull. Chem. Soc. Jpn.* **1974**, *47*, 3006-3009.

297. Snyder, R. G.; Zerbi, G., Vibrational Analysis of Ten Simple Aliphatic Ethers: Spectra, Assignments, Valence Force Field and Molecular Conformations. *Spectrochimica Acta Part A: Molecular Spectroscopy* **1967**, *23*, 391-437.

298. Galabov, B.; Ilieva, S.; Dudev, T.; Phan, H. V.; Durig, J. R., Interpretation and Prediction of Vibrational Absorption Intensities: Methylethyl Ether and Diethyl Ether. *Spectrochimica Acta Part A: Molecular Spectroscopy* **1993**, *49*, 2093-2103.

299. Sarkar, S.; Ramanathan, N.; Sruthi, P.; Sundararajan, K., Conformations of Diethyl Ether and Its Interaction with Pyrrole at Low Temperatures. *Spectrochimica Acta Part A: Molecular and Biomolecular Spectroscopy* **2019**, *213*, 361-369.

300. Plusquellic, D. F.; Suenram, R.; Mate, B.; Jensen, J.; Samuels, A., The Conformational Structures and Dipole Moments of Ethyl Sulfide in the Gas Phase. *J. Chem. Phys.* **2001**, *115*, 3057-3067.

301. Kusaka, R.; Inokuchi, Y.; Haino, T.; Ebata, T., Structures of (3n-Crown-N)–Phenol (N = 4, 5, 6, 8) Host–Guest Complexes: Formation of a Uniquely Stable Complex for N = 6 Via Collective Intermolecular Interaction. *J. Phys. Chem. Lett.* **2012**, *3*, 1414-1420.

302. Badenhoop, J. K.; Weinhold, F., Natural Bond Orbital Analysis of Steric Interactions. *J. Chem. Phys.* **1997**, *107*, 5406-5421.

303. Kabli, S.; van Beelen, E. S. E.; Ingemann, S.; Henriksen, L.; Hammerum, S., The Proton Affinities of Saturated and Unsaturated Heterocyclic Molecules. *Int. J. Mass spectrom.* **2006**, *249-250*, 370-378.

304 Caminati, W.; Melandri, S.; Rossi, I.; Favero, P. G., The C-F···H-O Hydrogen Bond in the Gas Phase. Rotational Spectrum and Ab Initio Calculations of Difluoromethane-Water. *J. Am. Chem. Soc.* **1999**, *121*, 10098-10101.